STATISTICAL MECHANICAL THEORY OF EQUILIBRIUM STRUCTURE AND MISCIBILITY OF POLYMER NANOCOMPOSITES: EFFECTS OF POLYMER CHEMICAL HETEROGENEITY AND ARCHITECTURE, AND NANOPARTICLE SURFACE CORRUGATION AND SOFTNESS

BY

DEBAPRIYA BANERJEE

DISSERTATION

Submitted in partial fulfillment of the requirements
for the degree of Doctor of Philosophy in Materials Science and Engineering
in the Graduate College of the
University of Illinois at Urbana-Champaign, 2015

Urbana, Illinois

Doctoral Committee:

Professor Kenneth S. Schweizer, Chair
Professor Paul V. Braun
Associate Professor Charles M. Schroeder
Assistant Professor Andrew L. Ferguson

ABSTRACT

Motivated by the persistent interest in different nanoparticles added to various polymer matrices, the Polymer Reference Interaction Site Model (PRISM) theory is extended and applied to study the thermodynamics, statistical structure, and miscibility of diverse polymer nanocomposites (PNCs). Under chemistry-matched conditions and in the absence of interfacial attractions between a spherically smooth nanoparticle and the matrix fluid, the polymer-induced depletion attraction is dominant and induces entropic phase separation. The depletion attraction can be potentially reduced by modifying the nanoparticle surface topography as recently observed in experiments. Two types of surface-modified nanoparticles have been considered in this thesis – (1) spheres with ordered roughness on the surface and (2) soft polymeric nanoparticles with surface fluctuations and fuzziness. Monte Carlo integration and other computational techniques have been developed to compute the effective interactions between such particles. The morphologically diverse particles introduce additional length scales, making the physics non-monotonic, subtle, and rich. The common advantage with using either of the particles is reduced contact aggregation and enhanced miscibility. Optimal surface corrugation and/or particle softness allow monomer penetration resulting in favourable (entropic) mixing. However, high enough degree of corrugation/softness can also result in destabilization by excluding the polymer from its interior.

Another route of developing new nanocomposites is by tuning the polymer-particle interfacial chemistry. Prior work has established three states of spatial organization, namely

depletion, steric stabilization and bridging, depending upon the effective interfacial attraction strengths. Introducing polymer chemical heterogeneity via the use of AB copolymers offers additional control over the equilibrium structure. Specifically, two types of copolymers are considered – (1) random copolymers (RCP) of disordered sequence and (2) ordered, alternating multiblock copolymers (MBCP). Quantum chemical calculations are combined with the polymer liquid state theory to predict structure and miscibility. The chain connectivity, monomer sequence, copolymer composition and differential wettability results in unique frustration in the system leading to novel states of organization of the polymer around the nanoparticles. In the context of strongly attractive nanoscopic fullerenes, this results in improved miscibility relative to the corresponding homopolymers. For some of the systems studied, maximum dispersion is predicted at an intermediate copolymer composition due to packing correlations and differential wetting effects with favourable comparison to experiments.

To Baba, Ma and Rim

ACKNOWLEDGMENTS

My graduate school experience at the University of Illinois Urbana-Champaign would not have as fulfilling and educative without the contribution of so many people. First and foremost, I would like to thank my advisor, Prof. Kenneth. S. Schweizer, for his persistent guidance and continual encouragement. His passion and love for science, and his over-brimming scientific inquisitiveness have motivated me further along this journey. A veritable geyser of ideas, his vast breadth of knowledge makes him stand out as a model mentor and advisor. Additionally, apart from his kindness and his sense of fairness, he has also inculcated in me the need of impeccable discipline that is indispensable for a relaxed and enriching life.

I would like to thank my Prelim and Doctoral Committee members, Prof. Steve Granick, Prof. Andrew Ferguson, Prof. Charles Schroeder, Prof. Paul Braun and Prof. Kenneth Schweizer for their time, support and helpful comments. I am very thankful to Prof. Braun for agreeing to be on my committee at a very short notice, despite his hectic and busy summer schedule. I would also take this opportunity to gratefully acknowledge DOE-BES (via Oak Ridge National Laboratory) for supporting my research.

I cannot stress enough on the importance of being surrounded by intellectually-stimulating and extremely helpful lab-mates (the “Schweizerians”) of both past and present: Dr. Lisa Hall, Dr. Rajarshi Chakrabarti, Dr. Daniel Sussman, Dr. Rui Zhang, Dr. Mukta Tripathy, Dr. Jian Yang, Dr. Umi Yamamoto, Dr. Homin Shin, Dr. Stephen Mirigian, Dr. Ryan Jadrich, Zachary Dell and Anh Duc Phan. From the most inane discussions to bouncing off research

ideas, they have helped create a friendly lab atmosphere that is extremely conducive for fruitful work.

My journey so far, both academically and personally, has also been moulded by people I have known before coming to Urbana-Champaign. To name a few, Mrs. S. Ghosh and Mrs. S. Nath, teachers from high school who have etched an indelible mark on a young mind and who continue to inspire me even today. I would also like to thank my advisor from IIT Madras (India), Prof. P. B. Sunil Kumar, for igniting my interest in research and helping me during my initial foray into soft condensed matter.

Graduate school experience would have been absolutely incomplete and bleak without my friends in Illinois and elsewhere. The innumerable joyful moments shared with my roommates and friends, Shalmoli, Utsav, Piyush, Sreeradha and Kiran, over travel, good food and chai, discussing serious worldly issues, frivolous Bollywood movies and music or even innocuous pranks, are some of the things that I will always treasure for life. Thanks to them, I cannot ever reminisce about my graduate life without a smile on my face. I'd also like to express my heartfelt gratitude to my friends, Ranjini and Sanhita, who with their infinite patience, compassion and good humour, helped me keep my chin up and tide over the unsettling times.

All through the eventful ride of the past six years, books have been a constant companion and I cannot thank the University enough for its vast and well-maintained repository and library. I have never been left wanting.

This thesis is a culmination of all of the above that have defined my graduate school experience, but it would not have been possible without the unwavering love and support of my

family – Baba, Ma, Rim and the rest of “745”. They have supported my education throughout and stood by all my decisions. The values that they have instilled in me continue to give me strength to pursue my dreams so far away from home.

Table of Contents

CHAPTER 1

INTRODUCTION

1.1 Motivation and Goal

Nanoparticles are widely added to polymers to create nanocomposites with improved mechanical, optical, thermal and properties[1-6]. The small size of the nanoscopic fillers results in strongly enhanced interfacial area compared to conventional composites. The interfacial characteristics of the resulting polymer nanocomposite (PNC) are a complex function of the system chemistry, polymer and nanoparticle architecture, temperature, solvent quality, etc. A thorough understanding of the interfacial microstructure is therefore required to control the properties of PNCs.

The study of how polymers mediate effective interactions between particles in a dense liquid or melt is a challenging problem of fundamental interest in statistical mechanics. In its general context of melts and solutions, it is also of high importance for a plethora of technological situations such as in tire manufacturing, oil recovery, paints and cosmetics, as well as in diverse biological systems[7-15]. One of the key hurdles in many applications is the strong direct inter-particle attractions due to unbalanced van der Waals interactions and entropic polymer-mediated depletion attractions which make it very challenging to disperse the particles in the polymer matrices at desired levels of loading. The over-arching aim of this thesis is to

understand the conditions that determine the PNC statistical structure and particle miscibility, and identify the features of the polymer matrix and particle that can be tuned to achieve this goal.

The ability to spatially disperse particles in PNCs in a thermodynamically stable manner is sensitive to structural correlations which depend on controllable features of the macromolecules and nanoparticles. The most obvious parameters that can be varied are the nanoparticle shape, size and polymer-particle interfacial cohesion. Much recent simulation[16-21], experimental[1-3, 22-26] and theoretical[27-33] work has focused on the simplest case of spherical nanoparticles in a homopolymer melt wherein the polymer and particle chemistry and particle size are manipulated to achieve diverse effective interactions, microstructural organizations, and degree of miscibility.

In the absence of adsorption between the polymer and the particle, the polymers induce the nanoparticles to come close spatially in order to gain free volume and maximize their translational and excess packing entropy. This leads to an effective attraction between the nanoparticles known as "depletion" attraction[34-36] leading to particle aggregation and potentially macrophase separation and/or non-equilibrium physical gelation[37]. The pioneering work on depletion by Asakura and Oosawa (AO)[34-36] addressed how a dilute solution of small polymer coils (radius of gyration, R_g) mediate an entropic attraction between two very large hard spheres (diameter D=2R) or surfaces. Polymers were modeled as small spheres with no internal conformational degrees of freedom which can pass through each other but not penetrate the particles. This strongly nonadditive excluded volume model results in an entropic, purely attractive potential of mean force (PMF) between the particles[35, 36] with a strength at contact that

scales linearly with polymer concentration and a range determined by polymer size. The AO model suffers from three major limitations: (i) very dilute polymer solution, (ii) very small polymers compared to the particle size ($R_g << R$), and (iii) neglect of all internal polymer conformational degrees of freedom. One or more of these simplifications very often fails depending on the physical situation. This has motivated the development of improved theories aimed at diverse aspects of the problem which include scaling arguments[38, 39], lattice and continuum mean field approaches[40-42], integral equations[43-46], and density functional theories[47]. Simulations and liquid state theory have long established that at high fluid densities the depletion potential is oscillatory with short range barriers and repulsive regions due to local packing correlations[48], which potentially might "stabilize" particles (presumably kinetically) against aggregation[40, 49].

Due to the presence of strong packing correlations and a wide range of length scales in a dense melt, the theoretical study of depletion effects in polymer nanocomposites is a relatively recent activity. Over the last decade, the microscopic Polymer Reference Interaction Site Model (PRISM) integral equation theory[50, 51] (to be discussed in Chapter 2) has been developed and widely applied for the simplest case of PNCs discussed above. It explicitly takes into account chain connectivity and intermolecular pair correlations over all length scales. Extensive comparisons with scattering experiments and simulations have been performed[20-24].

Despite this progress, much remains to be understood about the elementary depletion problem in polymer melts especially in the regime of large particle-to-monomer size asymmetry ratio and whether there is a uniquely macromolecular component of the effective inter-particle

potential of mean force (PMF). Answers are sought for questions like (1) how do the PMF minima vary with the polymer molecular weight? (2) What is the importance of maintaining realistic constant pressure conditions on depletion? (3) Are the (PMF) features completely local as true for the related problem of a polymer melt confined between two parallel plates?

One far less explored approach of reducing or eliminating depletion-induced clustering is to modify the particle surface by incorporating roughness. In practical materials, the latter is often unavoidable. Since rough spheres present less exclusion volume to the matrix than their smooth analogs, a diminished contact depletion is expected. The fact that particle roughness can attenuate depletion attraction was experimentally demonstrated by Stroock et al for plates and cylinders[52, 53] where they found different states of aggregation as a function of the particle shape, roughness and also the concentration of the depleting solvent. Mason et al exploited this effect and by introducing roughness on only one side of platelets, achieved side-specific attractions between the platelets[54, 55]. They observed that depending upon the surface morphology (shape and height of asperities), the entropic depletion attraction can be either suppressed or enhanced. Others have also tried to "engineer entropy" by exploiting the differences between smooth and rough surfaces to assemble colloidal particles at specific sites[56, 57]. Our interest in heterogeneous surface topography was partially inspired by experiments on the stabilization of phospholipid liposomes in suspensions using charged nanoparticles[58]. Generally liposomes in suspensions tend to fuse rendering many of their applications inefficient. Zhang and Granick[58] showed that by covering 25% of the liposome surface with nanoparticles, improved stability of such particles was achieved. While this class of materials serves as a major motivation, our aim is to investigate a more generic and broader class of ordered surface heterogeneity, e.g. rigid but rough carbon

black nanoparticles[59], nanoparticle-stabilized emulsions (Pickering emulsion – fig 1.1d)[60-62], and raspberry-shaped colloids[63-65]. The surface morphology can be viewed as rigid hemispherical beads on a smooth core. Thus, a multi-scale modeling approach is needed to fully understand the role of surface morphology at roughly the monomer length scale which is most relevant to polymer mediated depletion attraction forces between nanoparticles.

Going beyond the hard bumpy surface morphology, there are other diverse 'soft' particles in materials science and biology. These are generally deformable objects that form an important class of materials at the interface between polymers, and colloids. Examples of such particles are many-armed star polymers[66, 67] (fig 1.1a), polymer-grafted nanoparticles[68-73] (fig 1.1b), cross-linked nano or microgels[2, 74, 75] (fig 1.1c), micellar diblock copolymers[76, 77], etc. The viscoelastic behaviour of such particles is exploited industrially to formulate food or personal care products and to process high performance materials such as films, coatings, solid inks and ceramics. An added advantage of using such particles is the ability to control the particle softness and size by tuning external parameters like temperature, pH, solvent quality, and intrinsic structural characteristics such as the length and density of grafts (for grafted nanoparticles) and crosslinking density (for cross-linked nanogels). It has been long established that thermodynamically stable nanoparticles can be obtained in homopolymer melts when the nanoparticles are densely covered by polymer grafts of molecular weight comparable to or greater than that of the matrix[68-73]. The 'wetting-to-dewetting' transition for such PNCs is therefore a function of the relative graft-to-matrix molecular weight and the surface graft density.

Microgels/nanogels[2, 74, 75] are cross-linked polymeric particles that are receiving increasing attention due to their unique advantages for polymer-based drug delivery system[74].

Their sizes can be tuned from nanometer to micrometers, they offer large surface area and provide an interior network for the incorporation of biomolecules. Microgels have become one of the most popular soft systems to study because of the relative ease of their synthesis as well as the convenience of manipulating their softness by varying the amount of crosslinking or temperature. Recent experiments illustrate the (unexpected) possibility of dispersion of cross-linked polystyrene nanogels in chemically matched dense polymer matrix of linear polystyrene[2]. The particle diameters range from ~ 5 nm to 7 nm depending upon the pre-polymer molecular weight and degree of cross-linking. The Kratky plots obtained from neutron scattering data in solution show a shift towards a hard particle-like nature for heavily cross-linked nanogels (20 mol % crosslinker)[2, 78]. Depending on the cross-linking density, the nanogels can be semi-impenetrable with interfaces that are fuzzy and/or fluctuating. This makes them distinctly different from both hard smooth and rough nanoparticles.

There are multiple length scales associated with nanogel particles, such as the monomer diameter, the solid core diameter and the graded interface of finite width. Concerted efforts towards a systematic characterization of these multi scale particles have been made[75, 79, 80]. Classic soft repulsive Hertzian pair potentials are often used to describe the center-of-mass interactions between two microgels[81] but these do not explicitly take into account the width of the fuzzy corona relative to the core and monomer diameter. This necessitates theoretical/computational techniques to calculate the bare potentials between the particles and between a particle and a monomer, which can then be combined with statistical mechanical approaches such as PRISM theory to predict the equilibrium structure and miscibility of the resulting PNC.

Many theoretical challenges and key questions remain open for the PNCs based on the novel soft fillers described above, some of which are the following. (1) What is the role of different length scales on nanoparticle dispersion in concentrated monomeric solvents and dense polymer melts? (2) On the nanometer scale, does the nanoparticle surface softness perturbatively modify the states of organization and miscibility found for hard fillers, or do qualitatively new and unique behaviors emerge?

The contact depletion attraction can also be countered by incorporating appropriate enthalpic interfacial attraction between the polymer and the particle via tuning system chemistry. Prior work shows that interfacial attraction can either lead to miscibility by forming a stabilizing adsorbed layer around the particle (steric stabilization) or create "bridged" polymer-particle complexes[25, 26, 30, 31, 51]. The polymer architecture or monomer sequence in chemically heterogeneous macromolecules is another knob that can be tuned to yield better control of the equilibrium structure of the PNCs. An AB copolymer of myriad sequences (see fig 1.2) offers physical and/or chemical heterogeneity that can potentially lead to new packing structures. Recent experiments have demonstrated the potential of using AB random copolymers (RCP) to significantly improve the (still non-equilibrium) spatial dispersion of CNTs based on either non-covalent electron donor-acceptor interactions[82, 83] between fillers and polymer or hydrogen-bonding with oxidized carbon nanotubes[84, 85.] Intriguingly, it was found for most systems, but not all, that optimal dispersion is achieved at an intermediate RCP composition corresponding to a subtle "window of miscibility". Also, for spherical, nanoscopic fullerene molecules, recent experimental-computational chemistry studies again suggest that AB random copolymers of intermediate composition can afford for many systems major improvement of dispersion relative

to homopolymer behaviour based on electron donor-acceptor C_{60}-polymer attractions[86]. However, a fundamental statistical mechanical understanding of this behavior is lacking and may be subtle for multiple reasons including: (i) the strong (compared to thermal energy) and spatially short range nature of C_{60}-C_{60} and C_{60}-polymer attractions, and (ii) nonrandom packing and local surface segregation of *A* and *B* monomers around the fullerene which are sensitive to quenched copolymer sequence disorder and (iii) the small nature of the nanoparticle. These interfacial packing effects may mediate subtle PMFs.

Beyond the differential wettability in the RCP context, polymer architecture or monomer sequence offers an additional route for tuning effective interactions and controlling nanoparticle spatial organization. Multi-block copolymers (MBCP) are ubiquitous in natural biopolymers, but precise control of the sequence of synthetic monomers has proven to be more difficult although recent progress has been made[87-89]. Periodically sequenced MBCPs introduce a new parameter – the length of each block. Using a disordered MBCP liquid (i.e., no global micro-phase separation) in lieu of a homopolymer raises numerous questions. (1) What is the role of chemical heterogeneity on the polymer-mediated state of organization of the nanoparticles? (2) Can one achieve better miscibility by replacing the sequence *disorder* in a RCP melt by the tunable sequence *order* in a MBCP melt? (3) What is the effect of the block length of the MBCP relative to the size of the particle? (4) Does the MBCP molecular weight have the same effect on the equilibrium structure and dispersion as that of a RCP or a homopolymer? (5) How do the answers to the above questions change if one were to use a realistic, weakly micro-phase separated MBCP? At present, to the best of our knowledge, there are neither systematic simulations nor experiments on PNCs of hard nanoparticles in MBCP melts.

Simulations are an obvious choice to probe the equilibrium behaviour of PNCs. But brute force Molecular Dynamics or Monte Carlo techniques are often not possible owing to equilibration difficulties presented by dense melts of long chains, the wide range of length scales, and the large particle-monomer size asymmetry ratio. The common tool used in this thesis to predict the thermodynamic structure of the above-mentioned diverse systems is the microscopic PRISM theory. However, depending upon the chemical and physical nature of these systems, this liquid state theory needs to be coupled with additional modeling strategies to (1) render the results chemically predictive and (2) simplify the systems tractability by coarse graining some degrees of freedom. To this end, we have combined computational techniques like quantum chemical calculations, Monte Carlo Integration and coarse-graining methods using experimental scattering information and pure polymer liquid equation of state data, with PRISM theory to achieve quantitative and qualitative predictions of equilibrium structure and miscibility.

1.2 Dissertation Overview

Chapter 2 presents the microscopic PRISM that is central to this thesis. Chapter 2 also briefly presents some of the PRISM-predicted (and experimentally verified) results on the simplest system of dilute smooth nanoparticles in homopolymer melts that is essential background for understanding the more physically and chemically complex systems studied in this thesis. Each subsequent chapter addresses a chemically and physically distinct PNC. Fig 1.3 schematically represents a brief overview of the dissertation.

In Chapter 3 we apply numerical polymer integral equation theory to study the entropic depletion problem for smooth hard spheres dissolved in flexible chain polymer athermal melts

and concentrated solutions over an exceptionally wide range of polymer radius of gyration to particle diameter ratios (R_g/D), particle-monomer diameter ratios (D/d), and chain lengths (N) including the monomer and oligomer regimes[90]. Calculations are performed based on a calibration of the effective melt packing fraction that reproduces the isobaric dimensionless isothermal compressibility of real polymer liquids. Three regimes of the polymer-mediated inter-particle potential of mean force (PMF) are identified and analyzed in depth. A novel finding is a long range (of order R_g) repulsive, exponentially decaying component of the depletion potential emerges when polymer coils are smaller than, or of order, the nanoparticle diameter. A weak long range and N-dependent component of the monomer-particle pair correlation function identified as the origin of the long range repulsive PMF. Implications of our results for thermodynamics and miscibility are discussed.

In Chapter 4 we employ a hybrid Monte Carlo integration plus integral equation theory approach to study, for the first time, how dense fluids of small nanoparticles or polymer chains mediate effective entropic depletion interactions between topographically rough particles where all interactions are pure hard core repulsion[91]. The corrugated particle surfaces are composed of densely packed beads which present variable degrees of topographic roughness and free volume associated with their geometric crevices. This pure entropy problem is characterized by competing ideal translational and both favorable and unfavorable excess entropic contributions. Surface roughness generically reduces particle depletion aggregation relative to the smooth hard sphere case. However, the competition between ideal and excess packing entropy effects in the bulk, near the particle surface, and in the crevices results in a non-monotonic variation of the particle-monomer packing correlation function as a function of the two dimensionless length

scale ratios that are a measure of effective surface roughness. As a result, the inter-particle potential of mean force, second virial coefficient, and spinodal miscibility volume fraction vary non-monotonically with the surface bead to monomer diameter and particle core to surface bead diameter. A miscibility window is predicted corresponding to an optimum degree of surface roughness that destroys depletion attraction entirely. Variation of the (dense) matrix packing fraction can enhance or suppress particle miscibility depending upon the amount of surface roughness.

Chapter 5 studies, for the first time, the effective interactions, spatial organization and miscibility of dilute spherical nanoparticles in non-microphase separating, chemically-heterogeneous, compositionally-symmetric AB multiblock copolymer melts of varying monomer sequence[92]. The dependence of nanoparticle wettability on copolymer sequence and chemistry results in inter-particle PMFs that are qualitatively different from homopolymers. An important prediction is the ability to improve nanoparticle dispersion via judicious choice of block length and monomer adsorption-strengths which control both local surface segregation and chain connectivity induced packing constraints and frustration. The degree of dispersion also depends strongly on nanoparticle diameter relative to the block contour length. Small particles in copolymers with longer block lengths experience a more homopolymer-like environment which renders them relatively insensitive to copolymer chemical heterogeneity and hinders dispersion. Larger particles (sufficiently larger than the monomer diameter) in copolymers of relatively short block lengths provide better dispersion than either a homopolymer or random copolymer. The theory also predicts a novel widening of the miscibility window for large particles upon increasing the overall molecular weight of copolymers composed of relatively long blocks. We

hope that our predictions will motivate further experimental and simulation work for nanoparticles dissolved in sequence-ordered, chemically-heterogeneous, non-microphase separating MBCP melts.

In Chapter 6 we combine PRISM theory and computational chemistry methods to study the interfacial structure, effective interactions, miscibility and spatial dispersion mechanism of fullerenes dissolved in specific *random AB* copolymer melts characterized by strong non-covalent electron donor-acceptor interactions with the nanofiller[93]. A statistical mechanical basis is developed for designing random copolymers to optimize fullerene dispersion at intermediate copolymer compositions. Pair correlation function calculations reveal a strong sensitivity of interfacial packing near the fullerene to copolymer composition and adsorption energy mismatch. The potential of mean force between fullerenes displays rich trends, often non-monotonic with copolymer composition, reflecting a non-additive competition between direct filler attractions and polymer-mediated bridging and steric stabilization. The spinodal phase diagrams are in qualitative agreement with recent solubility limit experimental observations on three systems, and testable predictions are made for other random copolymers[86]. The distinctive non-monotonic variation of miscibility with copolymer composition is found to be primarily a consequence of composition-dependent, spatially short-range attractions between the *A* and *B* monomers with the fullerene and nontrivial pair correlations. A remarkably rich, polymer-specific temperature dependence of the spinodal diagram is predicted which reflects the thermal sensitivity of spatial correlations which can result in fullerene miscibility either increasing or decreasing with cooling. The calculations are contrasted with a simpler effective homopolymer

model and the random structure Flory-Huggins model. Miscibility predictions of fullerenes in RCP are also quantitatively compared to those in MBCP melts discussed in Chapter 5.

The focus of Chapter 7 is cross-linked, soft polymeric nanoparticles that have an irregular, fluctuating surface formed due to loops, strands and chain ends. When dissolved in a chemistry-matched polymer matrix, the soft nanoparticles have demonstrated enhanced miscibility[2] compared to smooth hard spheres which aggregate due to entropy-dominated depletion forces[90]. Modeling such fuzzy particles is challenging due to the disordered and random morphology at the particle interface. The crosslinked nanoparticles of tunable softness are modeled statistically using particle form factors obtained from small angle neutron scattering experiments. The model yields effective interactions between two fluctuating particles, and one fuzzy particle and a monomer. Using these effective interactions, PRISM theory is employed to study the structure and miscibility of soft nanogels in monomer fluids and homopolymer melts. The monomer-particle pair correlations exhibit increasing polymer penetration in the nanogels with increasing surface fuzziness leading to improved dispersion of the particles, contrary to the depletion attraction induced between hard spheres by non-adsorbing polymers. However, beyond a certain degree of fuzziness, the polymers are excluded from the surface and the particles tend to aggregate. The miscibility of soft nanogels is thus a non-monotonic function of both particle softness and size. Increasing the matrix degree of polymerization tends to destabilize the system.

Chapter 8 concludes the dissertation by briefly sketching outstanding open issues and possible future directions.

1.3 References

(1) K. I. Winey, R. A. Vaia, *MRS Bull.*, **32**, 314-319, 2007.

(2) M. E. Mackay, A. Tuteja, P. M. Duxbury, C. J. Hawker, B. V. Horn, Z. Guan, G. Chen, R. S. Krishnan, *Science*, **311**, 1740-1743, 2006.

(3) M. Alexandre, P. Dubois, *Materials Science and Engineering*, **28**, 1-63, 2000.

(4) B. Natarajan, Y. Li, H. Deng, L. C. Brinson, L. S. Schadler, *Macromolecules*, **46**, 2833-2841, 2013.

(5) P. Akcora, S. K. Kumar, S. Lewis, L. S. Schadler, Y. Li, B. C. Benicewicz, A. Sandy, S. Narayanan, J. Ilavsky, P. Thiyagarajan, R. F. Colby, J. F. Douglas, *Macromolecules*, **43**, 1003-1010, 2010.

(6) Z. Wang, J. K. Nelson, H. Hillborg, S. Zhao, L. S. Schadler, *Adv. Mat.*, **24**, 3134-3137, 2012.

(7) C. Matteo, P. Candido, R. Vera, V. Francesca, *Am. J. Applied Sci*. **9**, 784, 2012.

(8) M.-J. Wang, *Rubber Chem. Technol*. **71**, 520, 1998; **72**, 430, 1999.

(9) G. Huber, T.A. Vilgis, *Macromolecules* **35**, 9204, 1999.

(10) S. Vieweg, R. Unger, G. Heinrick, E. Donth, *J. Appl. Polym.Sci*. **73**, 495, 1999.

(11) P. M. Ajayan, L. S. Schadler, P. V. Braun, *Nanocomposite Science and Technology*; KGaA: Weinheim, 2003; p 77.

(12) B. J. Ash, L. S. Schadler, R. W. Siegel, *Mater. Lett*. **55**, 83, 2002.

(13) Y. Lin, A. Boker, J. He, K. Sill, H. Xiang, C. Abetz, X. Li, J. Wang, T. Emrick, S. Long, Q. Want, A. Balazs, T. P. Russell, *Nature (London)* **434**, 55, 2005.

(14) M. E. Mackay, T. T. Dao, A. Tuteja, D. L. Ho, B. Van Horn, H. –C. Kim, C. J. Hawker, *Nature (London) Mater*. **2**, 762, 2003.

(15) D. H. Napper, *Polymeric Stabilization of Colloidal Dispersions* (Academic Press, 1983).

(16) D. Bedrov, G. D. Smith, J. S. Smith, *J. Chem. Phys.*, **119**, 10438, 2003.

(17) J. S. Smith, D. Bedrov, G. D. Smith, *Compos. Sci, Technol.*, **63**, 1599-1605, 2003.

(18) M. Vacatello, *Macromolecules*, **34**, 1946, 2001.

(19) Q. Zhang, L. A. Archer, *J. Chem. Phys.*, 121, 10814, 2004.

(20) L. Zhao, Y. G. Li, C. Zhong, J. Mi, *J. Chem. Phys.*, **124**, 144913, 2006.

(21) J. B. Hooper, K. S. Schweizer, T. G. Desai, R. Koshy, P. Keblinski, *J. Chem. Phys.*, **121**, 6986-6997, 2004.

(22) S. Sen, Y. Xie, S. K. Kumar, H. Yang, A. Bansal, D. L. Ho, L. Hall, J. B. Hooper, K. S. Schweizer, *Phys. Rev. Lett*., **98**, 128302, 2007.

(23) L. M. Hall, B. J. Anderson, C. F. Zukoski, K. S. Schweizer, *Macromolecules*, **42**, 8435–8442, 2009.

(24) S. Y. Kim, L. M. Hall, K. S. Schweizer, C. F. Zukoski, *Macromolecules*, **43**, 10123–10131, 2010.

(25) B. J. Anderson, C. F. Zukoski, *Macromolecules*, **41**, 9326-9334, 2008.

(26) B. J. Anderson, C. F. Zukoski, *Macromolecules*, **40**, 5133-5140, 2007.

(27) N. Patel, S. A. Egorov, *J. Chem. Phys.*, **121**, 4987-4997, 2004.

(28) X. Chen, J. Cai, H. Liu, Y. Hu, *Molecular Simulation*, **32**, 877-885, 2006.

(29) A. Bymaster, S. Jain, W. G. Chapman, *J. Chem. Phys.*, **128**, 164910, 2008.

(30) J. B. Hooper, K. S. Schweizer, *Macromolecules*, **38**, 8858-8869, 2005.

(31) J. B. Hooper, K. S. Schweizer, *Macromolecules*, **39**, 5133-5142, 2006.

(32) J. B. Hooper, K. S. Schweizer, *Macromolecules*, **40**, 6998-7008, 2007.

(33) L. M. Hall, K. S. Schweizer, *J. Chem. Phys.*, **128**, 234901, 2008.

(34) S. Asakura, F. Oosawa, *J. Chem. Phys*., **22**, 1255, 1954.

(35) S. Asakura, F. Oosawa, *J. Polym.Sci*., **33**, 183, 1958.

(36) A. Vrij, *Pure Appl. Chem*., **48**, 471, 1976.

(37) F. Sciortino, *Nat. Mat*., **1**, 145, 2002.

(38) J. F. Joanny, L. Leibler, P. G. deGennes, *J. Polym. Sci.*,*Polym. Phys*. **17**, 1073, 1979.

(39) P. G. de Gennes, *Scaling Concepts in Polymer Physics* (Cornell University Press, Ithaca, 1979).

(40) R. I. Feigin, D. H. Napper, *J. Colloid Interface Sci*., **75**, 525, 1980.

(41) J. M. H. M. Scheutjens, G. J. Fleer, *J. Phys. Chem*., **83**, 1619, 1979.

(42) A. A. Shvets, A. N. Semenov, *J. Chem. Phys*., **139**, 054905, 2013.

(43) S. Ramakrishnan, M. Fuchs, K. S. Schweizer, C. F. Zukoski, *J. Chem. Phys.*, **116**, 2201, 2002.

(44) M. Fuchs, K. S. Schweizer, *Europhys. Lett*., **51**, 621, 2000.

(45) A. P. Chatterjee, K. S. Schweizer, *J. Chem. Phys.*, **109**, 10464, 1998.

(46) A. P. Chatterjee, K. S. Schweizer, *Macromolecules*, **31**, 2353, 1998.

(47) N. Patel, S. A. Egorov, *J. Chem. Phys*., **121**, 4987, 2004.

(48) A. Yethiraj, C. K. Hall, R. Dickman, *J. Colloid Interface Sci*., **151**, 102, 1992.

(49) R. Tuinier, J. Rieger, C. G. de Kruif, *Advances in Colloid and Interface Science*, **103**, 1 2003.

(50) K. S. Schweizer, J. G. Curro, *Adv. Chem. Phys.*, **98**, 1, 1997.

(51) L. M. Hall, A. Jayaraman, K. S. Schweizer, *Curr. Opin. Solid State Mater. Sci.*, **14**, 38, 2010.

(52) S. Badaire, C. Cottin-Bizonne, J. Woody, A. Yang and A. Stroock, *J. Am. Chem. Soc*, **129**, 40-41, 2007.

(53) S. Badaire, C. Cottin-Bizonne and A. Stroock, *Langmuir*, **24**, 11451-11463, 2008.

(54) K. Zhao and T. G. Mason, *Phys. Rev. Lett.*, **101**, 148301, 2008.

(55) K. Zhao and T. G. Mason, *Phys. Rev. Lett.*, **99**, 268301, 2007.

(56) D. J. Kraft, R. Ni, F. Smallenburg, M. Hermes, K. Yoon, D. A. Weitz, A. van Blaaderen, J. Groenewold, M. Dijkstra and W. K. Kegel, *Proc. Natl. Acad. Sci.*, **109**, 10787-10792, 2011.

(57) E. Barry and Z. Dogic, *Proc. Natl. Acad. Sci.*, **107**, 10348-10353, 2010.

(58) L. Zhang and S. Granick, *Nano Lett.*, **6**, 694-698, 2006.

(59) R. Chakrabarti, J. –Y. Delannoy, M. Couty and K. S. Schweizer, *Soft Matter*, **7**, 5397-5407, 2011.

(60) R. F. A. Teixeira and S. A. F. Bon, *Adv. Polym. Sci.*, **233**, 19-52, 2010.

(61) J. W. J. de Folter, M. W. M. van Ruijven and K. P. Velikov, *Soft Matter*, **8**, 6807-6815, 2012.

(62) R. Aveyard, B. P. Binks and J. H. Clint, *Advances in Colloid and Interface Science*, **100**, 503-546, 2003.

(63) Z. Qian, Z. Zhang, L. Song and H. Liu, *J. Mater. Chem.*, **19**, 1297-1304, 2009.

(64) E. C. Cho, Y. K. Hwang and U. Jeong, *Bull. Korean Chem. Soc.*, **35**, 1784-1788, 2014.

(65) S. Jiang, Q. Chen, M. Tripathy, E. Luijten, K. S. Schweizer and S. Granick, *Adv. Mat.*, **22**, 1060-1071, 2010.

(66) G. Grest, K. Kremer, T. A. Witten, *Macromolecules*, **20**, 1376-1383, 1987.

(67) A. Jusufi, M. Watzlawek, H. Lolwen, *Macromolecules*, 32, 4470-4473, 1999.

(68) I. Borukhov, L. Leibler, *Macromolecules*, **35**, 5171-5182, 2002.

(69) S. K. Kumar, N. Jouault, B. Benicewicz and T. Neely, *Macromolecules*, **46**, 3199-3214, 2013.

(70) R. Hasegawa, Y. Aoki and M. Doi, *Macromolecules*, **29**, 6656-6662, 1996.

(71) A. Jayaraman and N. Nair, *Mol. Sim.*, **38**, 751-761, 2012.

(72) V. Ganesan and A. Jayaraman, *Soft Matter*, **10**, 13-38, 2014.

(73) A. Jayaraman and K. S. Schweizer, *Macromolecules*, **42**, 8423-8434, 2009.

(74) J. K. Oh, R. Drumright, D. J. Siegwart, K. Matyjaszewski, *Progress in Polymer Science*, **33**, 448-477, 2008.

(75) D.W. Holley, M. Ruppel, J.W. Mays, V.S. Urban, D. Baskaran, *Polymer*, **55**, 58-65, 2014.

(76) A. Blanazs, S. P. Armes, A. J. Ryan, *Macromol. Rapid Commun.*, **30**, 267–277, 2009.

(77) K. Kataoka, A. Harada, Y. Nagasaki, *Advanced Drug Delivery Reviews*, **47**, 113-131, 2001.

(78) A. Tuteja, M. E. Mackay, C. J. Hawker, B. V. Horn, *J. Polym. Sci. Part B: Polym. Phys.*, **44**, 1930-1947, 2006.

(79) I. Berndt, J. S. Pedersen, W. Richtering, *J. Am. Chem. Soc.*, **127**, 9372-9373, 2005.

(80) J. R. Seth, M. Cloitre, R. T. Bonnecaze, *J. Rheology*, **50**, 353, 2006; **52**, 1241.

(81) G. R. Deen, T. Alsted, W. Richtering, J. S. Pedersen, *Phys. Chem. Chem. Phys.*, **13**, 3108-3114, 2011.

(82) D. Linton, P. Driva, B. Sumpter, I. Ivanov, D. Geohegan, C. Feigerle, M. D. Dadmun, *Soft Matter*, **6**, 2801-2814, 2010.

(83) A. Laiho, R. H. A. Ras, S. Valkama, J. Ruokolainen, R. Osterbacka, O. Ikkala, *Macromolecules*, 39, 7648-7653, 2006.

(84) A. Rasheed, M. D. Dadmun, I. Ivanov, P. F. Britt, D. B. Geohegan, *Chem. Mater*., **18**, 3513-3522, 2006.

(85) A. Rasheed, H. G. Chae, S. K. Kumar, M. D. Dadmun, *Polymer*, **47**, 4734-4741, 2006.

(86) S .Teh, D. Linton, B. Sumpter, M. D. Dadmun, *Macromolecules*, **44**, 7737-7745, 2011.

(87) J. F. Lutz, M. Ouchi, D. R. Liu, M. Sawamoto, *Science*, **341**, 1238149, 2013.

(88) A. Song, K. A. Parker, N. S. Sampson, *J. Am. Chem. Soc*., **131**, 3444-3445, 2009.

(89) C. S. Daeffler, R. H. Grubbs, *Macromolecules*, **46**, 3288-3292, 2013.

(90) D. Banerjee and K. S. Schweizer, *J. Chem. Phys.*, **142**, 214903, 2015.

(91) D. Banerjee*, J. Yang*, K. S. Schweizer, *Soft Matter*, to be submitted, August 2015 (*Equal Contribution).

(92) D. Banerjee and K. S. Schweizer, *J. Polym. Sci. Part B: Polym. Phys*, **53**, 1098-1111, 2015.

(93) D. Banerjee, M. D. Dadmun, B. Sumpter, K. S. Schweizer, *Macromolecules*, 2013, **46**, 8732-8743.

(94) D. Banerjee, K. S. Schweizer, in preparation.

1.4 Figures

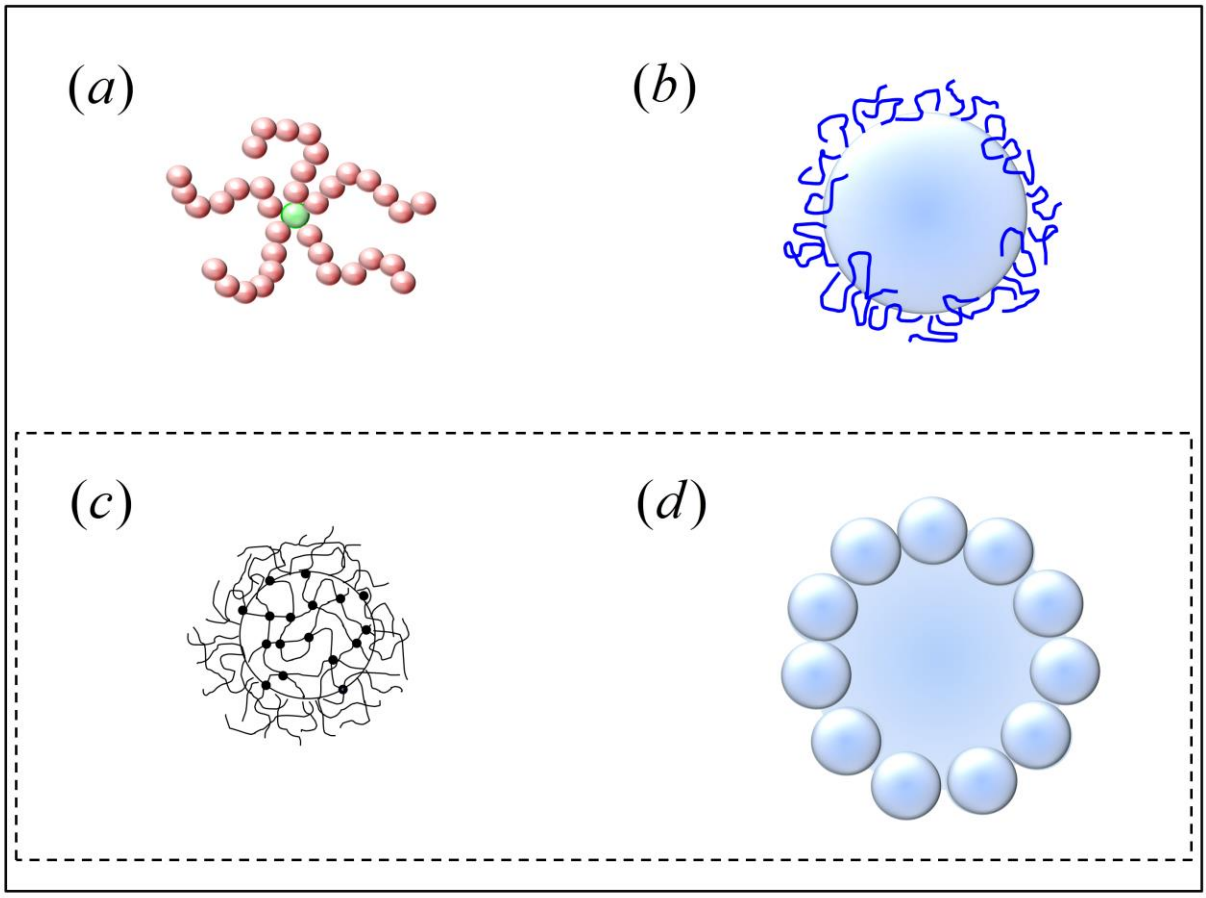

Figure 1.1 Schematic diagram of some members of the soft particle family – (a) Star Polymer, (b) Polymer grafted nanoparticle, (c) Cross-linked nanogel, (d) Particle-stabilized emulsion. The boxed particles are of particular interest in this thesis.

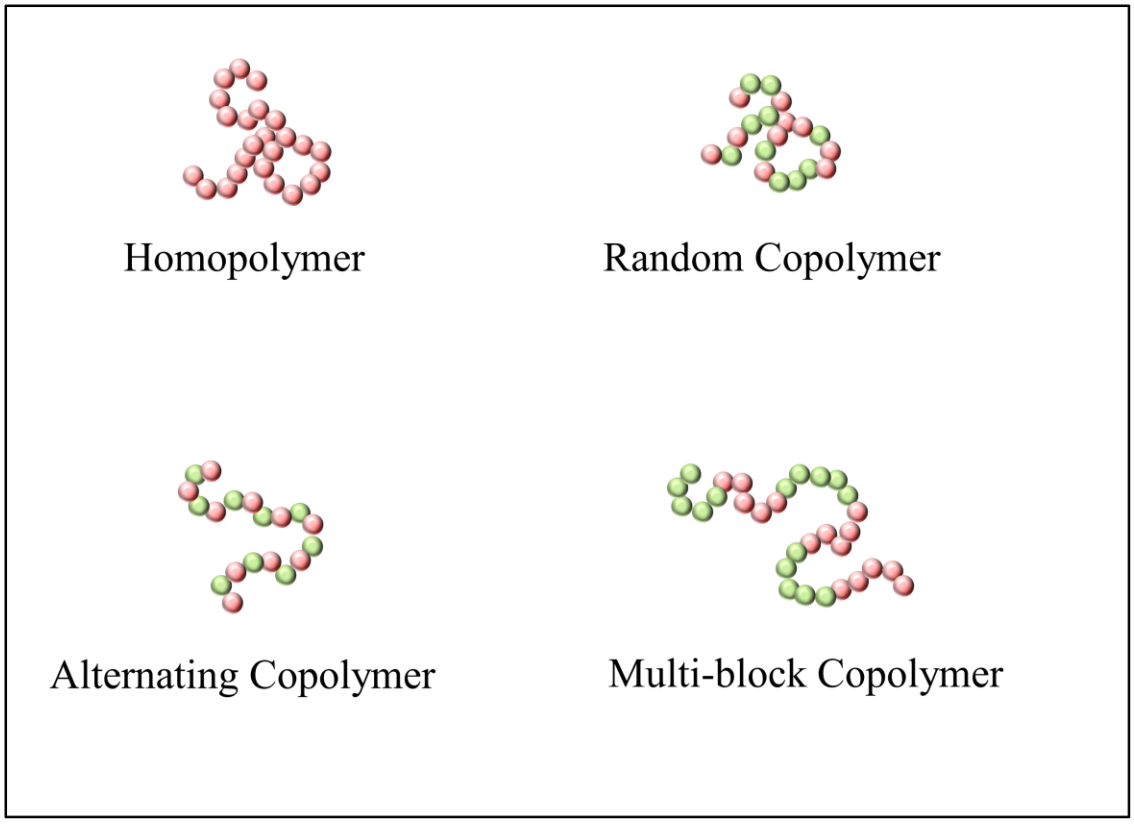

Figure 1.2 Various polymer architecture considered in this thesis.

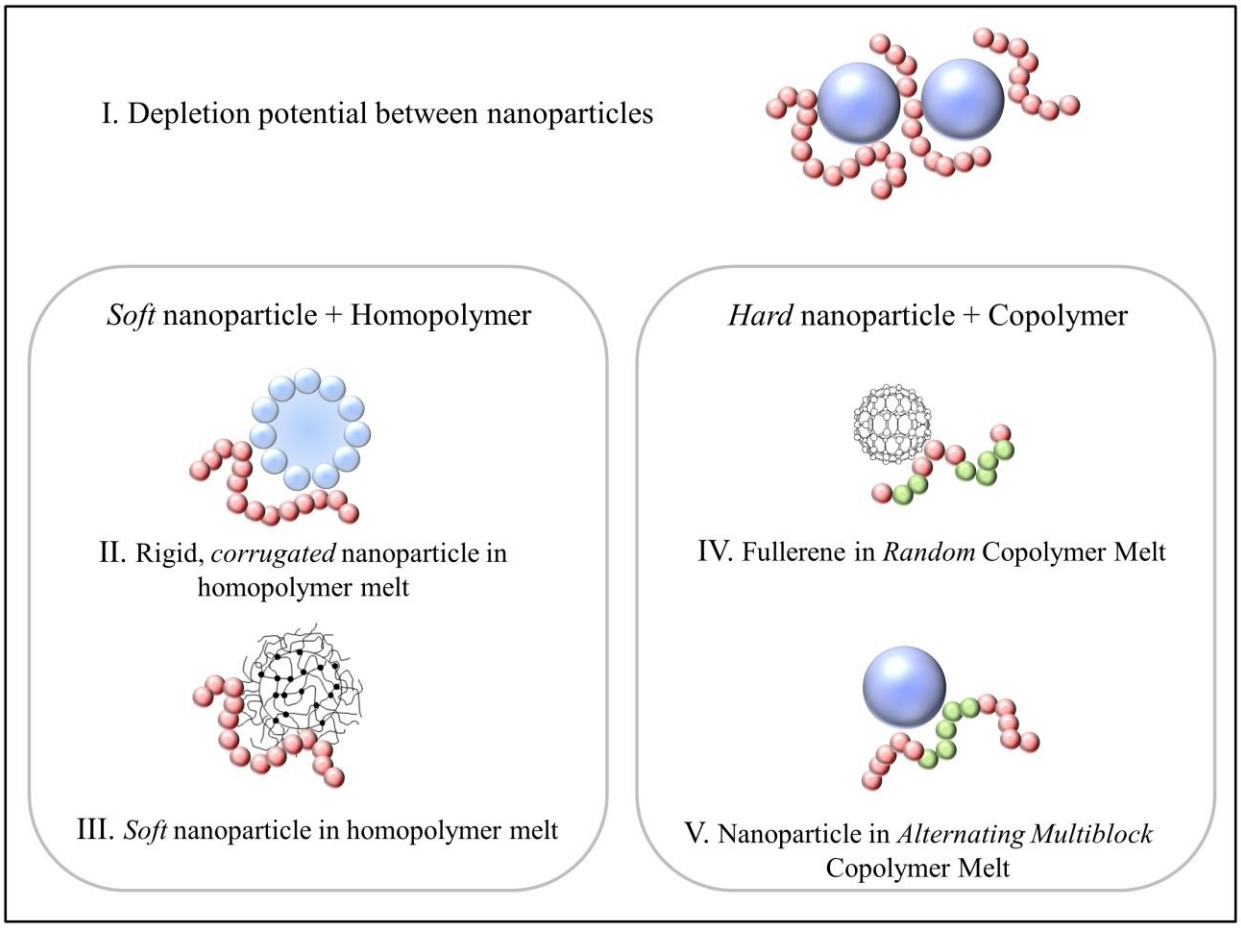

Figure 1.3 Schematic of the dissertation overview.

CHAPTER 2

THEORY AND BACKGROUND

2.1 PRISM Theory

The Polymer Reference Interaction Site Model Theory (PRISM)[1-3] is a statistical mechanical integral equation theory that can be used to numerically predict the pair structure and thermodynamics of polymer nanocomposites (PNC). In this chapter, we review basics for the simplest case studied in great detail previously by others – a binary mixture of homopolymers and structureless smooth spherical nanoparticles.

2.1.1 Model

A polymer is modeled as a conformationally ideal freely jointed chain (FJC) of N spherical interaction sites or monomers of size d and fixed bond length *l* as shown schematically in figure 2.1. Unless otherwise stated, the persistence length is $l = (4/3)d$ which is representative of flexible polymers and the monomer (or segment) diameter $d = 1$ is adopted as the unit of length. Relative to the monomer diameter d, the nanoparticles are spheres of diameter D. In the limit of dilute nanoparticles considered mainly in this thesis, the total system volume (packing) fraction is given by $\eta_t = \frac{\pi}{6}\rho_p d^3$ where ρ_p is polymer site number density. Throughout this thesis, the subscript p denotes a polymer monomer while n denotes a nanoparticle. All

dimensions are in units of monomer diameter unless otherwise mentioned. All energies are in units of the thermal energy $k_B T$.

The mean statistical shape of a molecule composed of multiple sites (labeled *i*) is described by its site-site intramolecular pair correlation function matrix $\omega_{ij}(r)$. For a freely jointed chain, the intramolecular pair correlation function in Fourier space is given by[4]:

$$\omega_p(k) = N^{-1}\sum_{i,j}^{N}\omega_{ij}(k) = (1-f)^{-2}[1-f^2 - 2N^{-1}f + 2N^{-1}f^{N+1}] \tag{2.1}$$

where $f = \sin(kl)/kl$. The chain statistics in the dense melt are taken to be unperturbed (conformational ideality) by the presence of nanoparticles. Possible non-ideal nanoparticle-induced conformational changes have previously been argued to be perturbative[2, 5, 6]. The statistical packing of each polymer segment is taken to be identical corresponding to pre-averaging chain end effects. A chemically heterogeneous AB copolymer is described by three intramolecular correlation functions, one for each type of site and a cross term which describes how the two types of sites are connected. The intramolecular correlation functions for multi-block and random copolymers are given in chapters 5 and 6, respectively. For a structureless spherical nanoparticle, one trivially has $\omega_n(k) = 1$.

2.1.2 Interactions Potentials

Intermolecular interactions are given by pair decomposable site-site potentials $U_{ij}(r)$. Monomer-monomer interactions are taken to be hard-core. For the simplest case of smooth

nanoparticles, the monomer-nanoparticle and particle-particle interactions are hard core with an exponential attraction added for some systems:

$$\begin{aligned} U_{pp}(r) &= \infty, \quad r < d \\ &= 0, \quad r \geq d \end{aligned} \tag{2.2a}$$

$$\begin{aligned} U_{nn}(r) &= \infty, \qquad\qquad r < D \\ &= -\varepsilon_{nn} e^{-(r-D)/\alpha_{nn}}, \quad r \geq D \end{aligned} \tag{2.2b}$$

$$\begin{aligned} U_{pn}(r) &= \infty, \qquad\qquad r < r_c \\ &= -\varepsilon_{pn} e^{-(r-r_c)/\alpha_{pn}}, \quad r \geq r_c \end{aligned} \tag{2.2c}$$

where $r_c = (D+d)/2$ is the monomer-nanoparticle distance of closest approach (contact). The parameters ε_{ij} and α_{ij} are the strength and range of the exponential site-site attractive potentials. For chemically heterogeneous species, the forms of the potentials are the same but the strength or range can be different for different sites. The shape of the exponential attraction is similar to the attraction calculated by Henderson and coworkers between a Lennard-Jones particle and a colloid represented by a continuum of Lennard-Jones particles[9, 16, 17]. The chemistry of the model enters via the ε_{ij} and α_{ij}. Given that the polymer interactions are hard core, ε_{pn} represents the net enthalpic gain of transferring a monomer from the pure melt to the surface of the particle. The shortest range studied, $\alpha_{pn} = 0.25d$, mimics a specific attraction such as hydrogen bonding or charger transfer, while $\alpha_{pn} = 0.5d$ or 1 are relevant to a generic van der Waals attraction[9].

For the rough and soft particles discussed in chapters 4 and 7, respectively, the inter-particle and particle-monomer interactions are computed using different techniques as discussed later.

2.1.3 PRISM Equations for Homopolymer Nanocomposites

PRISM theory is an extension of the Reference Interaction Site Model (RISM) for rigid, small molecules to polymers[2]. Each molecule is composed of sites and given the site densities, interactions and intramolecular correlations, the theory can be used to predict the intermolecular pair correlation functions. The PRISM theory is based on the matrix generalized Ornstein-Zernike[7] or Chandler-Andersen[8] integral equations which relate the site-site intermolecular pair correlations, C, and intramolecular pair correlations, ω, as[2]:

$$\underset{\sim}{H}(k) = \underset{\sim}{\Omega}(k)\underset{\sim}{C}(k)\left[\underset{\sim}{\Omega}(k) + \underset{\sim}{H}(k)\right] \tag{2.3}$$

Here, $h_{ij}(r) = \rho_i \rho_j \left(g_{ij}(r) - 1\right)$, $\Omega_{ij} = \left(\rho_i + \rho_j\right)\omega_{ij}$, and ρ_j is the number density of sites of type *j*. In the dilute particle limit $\rho_p d^3$ is the only relevant dimensionless density. Under the standard PRISM theory approximation[2] for homopolymers of treating all polymer sites as statistically equivalent (no explicit chain end effects), equation 2.3 reduces to three uncoupled, sequentially solvable integral equations[9]:

$$\begin{aligned} h_{pp}(k) &= \omega_p(k) C_{pp}(k)[\omega_p(k) + \rho_p h_{pp}(k)] \\ &\equiv \omega_p(k) C_{pp}(k) S_{pp}(k) \end{aligned} \tag{2.4}$$

$$h_{np}(k) = C_{np}(k) S_{pp}(k) \tag{2.5}$$

$$h_{nn}(k) = C_{nn}(k) + \Delta(k) \tag{2.6}$$

$$\Delta(k) \equiv \rho_p C_{np}^2(k) S_{pp}(k) = \rho_p \frac{h_{np}^2(k)}{S_{pp}(k)} \tag{2.7}$$

One sees from equation 2.6 that the polymer-mediated PMF between particles is determined by polymer correlations around an isolated particle and the pure melt collective density fluctuations.

Hard-core interactions imply exclusion constraints in real space inside the distance of closest approach: $g_{ij}(r) = 0, r \le r_{ij,c}$. Approximate closures relating $h_{ij}(k)$, $C_{ij}(k)$ and the site-site pair potentials, $U_{ij}(r)$, render the theory mathematically solvable. Prior work has established the site-site Percus-Yevick approximation for p-n and p-p correlations, and the Hypernetted Chain approximation for n-n correlations, are good closures for nanocomposites[10]. Outside the distance of closest approach, $r_{ij,c}$, these are given by[11]:

$$C_{ij}(r) = \left(1 - e^{-\beta U_{ij}(r)}\right) g_{ij}(r) \tag{2.8a}$$

$$C_{nn}(r) = -\beta U_{nn}(r) + h_{nn}(r) - \ln g_{nn}(r) \tag{2.8b}$$

where $\beta \equiv (k_B T)^{-1}$ is the inverse thermal energy. The integral equations are solved numerically using the inexact Newton method[12, 13].

Of primary interest is the polymer-mediated interparticle potential of mean force (PMF):

$$\beta W_{nn}(r) = -\ln g_{nn}(r) \tag{2.9}$$

which quantifies the change in system free energy to bring two particles from infinitely far apart to a separation r. Physically, in a dense liquid the PMF is intimately related to changes of the excess free energy of the intervening fluid which is connected with packing correlations. In the dilute particle regime of present interest the virial approach to computing the spinodal phase separation corresponds to a particle miscibility limit volume fraction of[14]:

$$\Phi_c = -\left(8\overline{B_2}\eta_t\right)^{-1} \tag{2.10}$$

where the normalized second virial coefficient is

$$\overline{B_2} = \frac{B_2}{B_{2,bare}} = \frac{\int_0^\infty (e^{-\beta W_{nn}(r)} - 1) r^2 dr}{\int_0^\infty (e^{-\beta U_{nn}(r)} - 1) r^2 dr} \tag{2.11}$$

More rigorous calculations of spinodal demixing curves based on the simultaneous divergence of all k = 0 partial collective structure factors, $S_{MM'}(k=0) \to \infty$, at arbitrary nanoparticle loading have been performed based on established numerical methods[12, 15]. All the miscibility trends discussed in this thesis remain qualitatively the same (and quantitatively similar for $\Phi_c \le 0.2$), and thus the virial results are reliable at the level of accuracy of interest in the present study.

2.2 Background

PRISM theory has been widely applied to study model homopolymer-nanoparticle mixtures[9, 10]. In the absence of any attraction between the polymer and the particle (or when $\beta\varepsilon_{pn} << 1$), the

particles aggregate due to entropic depletion[9, 10, 14] resulting in strong negative PMF minima at contact (figure 2.2). Attractive interactions between the hard sphere and the polymer are important in order to achieve some degree of miscibility. At higher values of $\varepsilon_{pn} (\geq 3k_B T)$, the enthalpy gain of the polymer segments adsorbing on the particle surface will compete with the depletion attraction resulting in "bridging" where a layer(s) of polymer is shared between two nanoparticles forming polymer-particle complexes (figure 2.2). The bridging PMF is repulsive at contact followed by a minimum at a monomer diameter distance. When the polymer-particle attraction strength is intermediate ($\varepsilon_{pn} \sim 1-2k_B T$), the polymers adsorb on the particle forming a repulsive layer that frustrates macro-phase separation. This state is known as steric stabilization and is a compromise between the entropically-driven depletion and high enthalpy-dominated bridging. The corresponding PMFs for these three states of spatial organization as well as their schematic cartoons are shown in figure 2.2.

Figure 2.3 shows the spinodal solubility limit of nanoparticles in a homopolymer melt as a function of interfacial cohesion strength ε_{pn} at fixed range of $\alpha_{pn} = 0.5d$, particle-monomer size asymmetry ratio D/d = 5, polymer chain length N = 100 and total packing fraction $\eta_t = 0.4$. The spinodal solubility limit is computed from the particle PMF using equations (2.9) and (2.10) and is defined as the critical volume fraction beyond which spinodal macro-phase separation is predicted. The two spinodal curves at low and high interfacial adsorption ε_{pn} denote phase separation induced by depletion and bridging, respectively. The window between the two spinodal curves is the miscible region where the particles are sterically stabilized.

It is intriguing that a relatively simple system of hard spheres in homopolymer melt can lead to such complex physics. This suggests that more novel and tunable states of structural organization and miscibility/dispersion strategies can be realized by using more complicated components, like chemically heterogeneous polymers of different architecture or non-smooth nanoparticle surface morphology.

2.3 References

(1) J. G. Curro, K. S. Schweizer, G. S. Grest, K. Kremer, *J. Chem. Phys.*, **91**, 1357–1364, 1989.

(2) K. S. Schweizer, J. G. Curro, *Adv. Chem. Phys.*, **98**, 1–142, 1997.

(3) J. G. Curro, K. S. Schweizer, *Macromolecules*, **24**, 6736–6747, 1991.

(4) K. S. Schweizer, J. G. Curro, *J. Chem. Phys.*, **89**, 3350–3362, 1988.

(5) R. Koshy, T. Desai, P. Keblinski, J. Hooper, K. S. Schweizer, *J. Chem. Phys.*, **119**, 7599–7603, 2003.

(6) A. L. Frischknecht, E. S. McGarrity, M. E. Mackay, *J. Chem. Phys.*, **132**, 204901, 2010.

(7) L. S. Ornstein and F. Zernike, *Proc. Acad. Sci. Amsterdam*, **17**, 793-806, 1917.

(8) D. Chandler and H. C. Andersen, *J. Chem. Phys*., **57**, 1930-1937, 1972.

(9) J. B. Hooper, K. S. Schweizer, *Macromolecules* **38**, 8858, 2005.

(10) L. M. Hall, A. Jayaraman, K. S. Schweizer, *Curr. Opin. Solid State Mater. Sci.* **14**, 38, 2010.

(11) J. P. Hansen, I. R. McDonald, *Theory of Simple Liquids* (Academic Press, London, 1986).

(12) L. M. Hall, L. M.; K. S. Schweizer, *J. Chem. Phys.* **128**, 234901, 2008.

(13) L. M. Hall, Ph.D. Thesis, University of Illinois at Urbana-Champaign, 2009.

(14) J. B. Hooper, K. S. Schweizer, *Macromolecules* **39**, 5133, 2006.

(15) D. Banerjee, M. D. Dadmun, B. Sumpter, K. S. Schweizer, *Macromolecules*, **46**, 8732-8743, 2013.

(16) J. B. Hooper, *Ph.D. Dissertation*, University of Illinois at Urbana-Champaign, 2005.

(17) D. Henderson, D. –M. Duh, X. Chu, D. Wasan, *J. Colloid Int. Sci.*, **185**, 265–268, 1997.

2.4 Figures

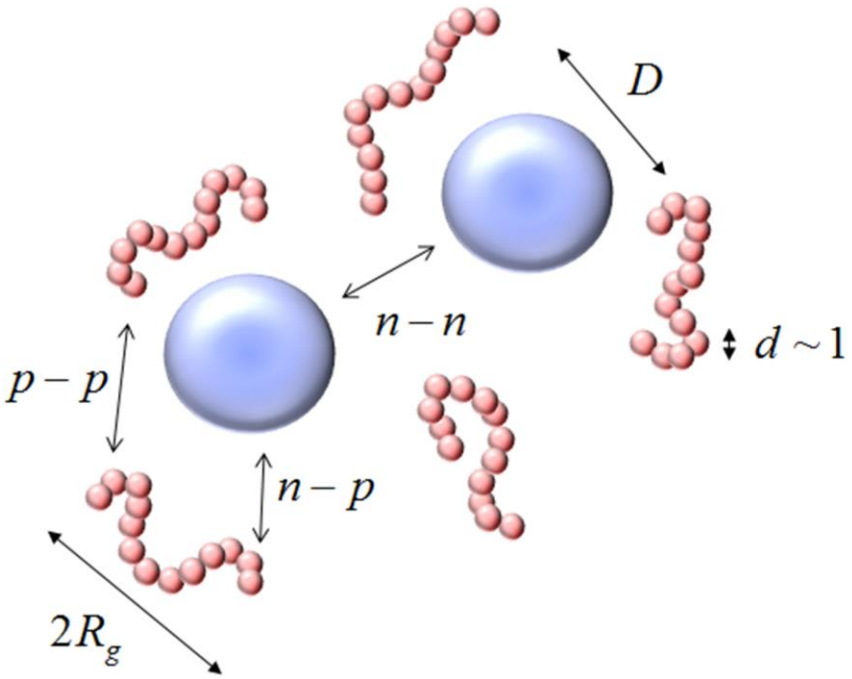

Figure 2.1 Schematic of a polymer nanocomposite (PNC) of smooth hard spheres in a homopolymer melt.

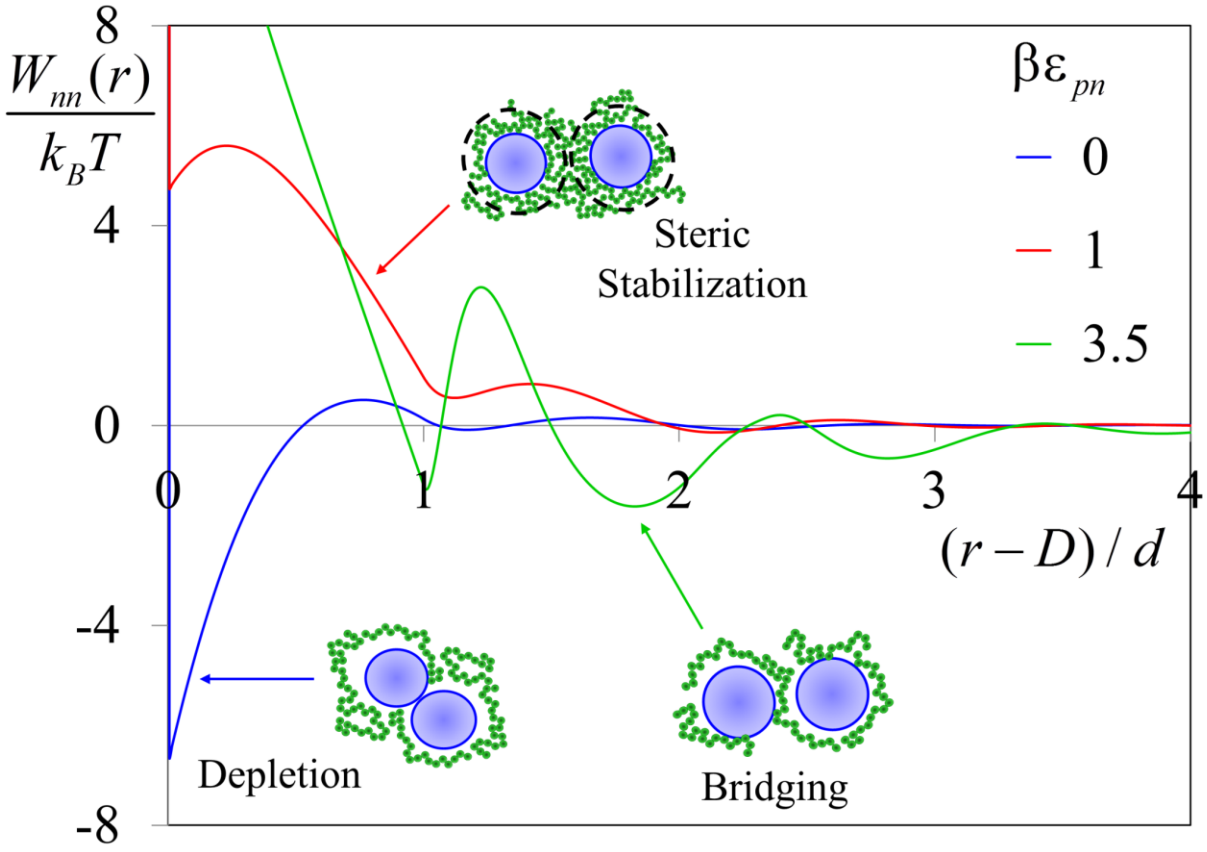

Figure 2.2 Potential of Mean Force (PMF) between dilute hard spheres of size D/d = 5 in a homopolymer melt of N = 100 at a packing fraction of $\eta_t = 0.4$ at various polymer-particle interaction strengths $\beta\varepsilon_{pn}$ and interfacial attraction range of $\alpha_{pn} = 0.5d$.

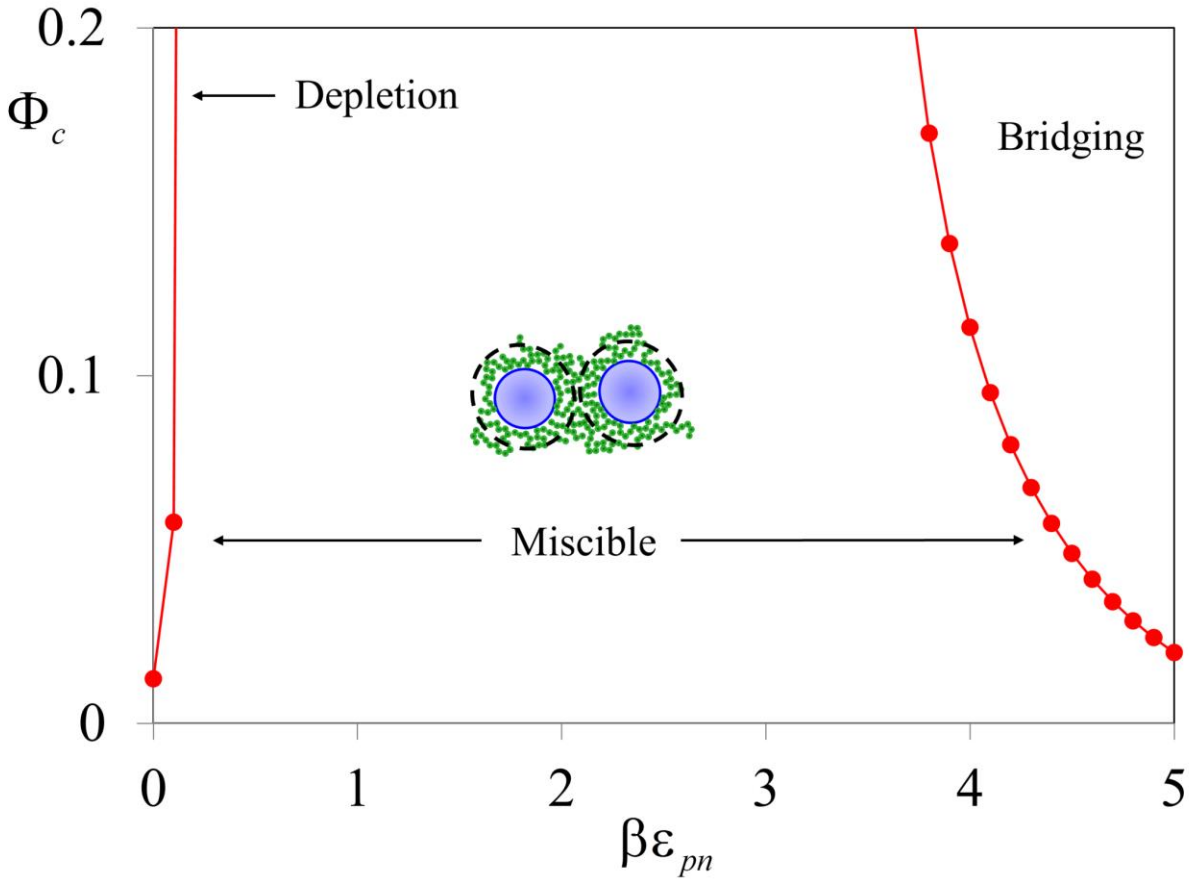

Figure 2.3 Spinodal phase diagram of dilute hard spheres of D/d = 5 in a homopolymer melt of N = 100, packing fraction $\eta_t = 0.4$ and $\alpha_{pn} = 0.5d$ as a function of ε_{pn}.

CHAPTER 3

MULTI-SCALE ENTROPIC DEPLETION PHENOMENON IN OLIGOMER AND POLYMER LIQUIDS[1]

3.1 Introduction

The most elementary question concerning polymer nanocomposites (PNC) is the potential of mean force (PMF) between two dilute hard spheres dissolved in a nonadsorbing polymer liquid. This defines the basic "entropic depletion" problem which has been the subject of many theoretical[1-13], simulation[14-24] and experimental[25-35] investigations, in diverse parameter regimes. For physically distinct reasons, the depletion interaction can be net attractive which induces particle clustering and potentially macrophase separation and/or nonequilibrium physical gelation[36].

We have applied PRISM theory to study the entropic depletion problem in melts and concentrated solutions over an exceptionally wide range of polymer-particle size ratios (R_g/D) (figure 3.1), particle-monomer size ratios ($D/d \sim 1\text{-}100$), and chain lengths ($N=1\text{-}10^6$) or equivalently the ratio R_g/d. Calculations are performed for experimentally relevant ranges of packing fraction (or dimensionless isothermal compressibility) and (flexible) chain persistence lengths. The above range of parameters far exceeds what has been previously studied

[1] This chapter is drawn in its entirety from a previous publication. Reprinted (adapted) with permission from D. Banerjee and K. S. Schweizer, J. Chem. Phys. **142**, 214903. Copyright 2015 American Institute of Physics.

theoretically, and is not feasible using simulation (where typically D/d<5-10, N<100-500) due to equilibration difficulties and system size limitations. Our goal is to perform calculations with models that are consistent with the equation of state (EOS) of real polymer liquids. As we shall show, to properly address the influence (direction and magnitude) of chain length on depletion phenomena under isobaric conditions requires such an approach.

3.2 Model Calibration via the Dimensionless Density Fluctuation Amplitude

Repulsive interactions generically dominate packing correlations in one-component nonassociated liquids, including polymer melts[37, 38]. This motivates the minimalist hard core model of interactions. However, thermodynamic (k=0) properties are sensitive to chemistry-specific attractions. We take this into account in an effective manner and build models consistent with the EOS of polymer liquids by requiring the dimensionless compressibility ($S_{pp}(k=0)=S_0$) to agree exactly with the experimental behavior at fixed pressure. This thermodynamic property is given by[39]:

$$\begin{aligned} S_{pp}(k=0) \equiv S_0 &= \rho_p k_B T \chi_T \\ &= N + \rho_p h_{pp}(k=0) = N + \rho_p \int d\vec{r}\left(g_{pp}(r)-1\right) \end{aligned} \tag{3.1}$$

Here, the above defined S_0 is proportional to the amplitude of the long wavelength density fluctuations of the pure polymer melt, χ_T is the isothermal compressibility directly related to the EOS via:

$$\chi_T = -\frac{1}{V}\left(\frac{\partial V}{\partial P}\right)_T \tag{3.2}$$

and $g_{pp}(r)$ is the interchain site-site pair correlation function which has a long range correlation hole component on the R_g scale[40] due to the combined consequences of chain connectivity and excluded volume. The second line of Eq(3.1) makes explicit how S_0 is determined at high N by a subtle quantitative competition between two very large terms of opposite sign. The negative second term scales linearly with N due to the correlation hole, and nearly cancels the first intrachain contribution resulting in the small value of S_0 typical of a nearly incompressible liquid. (see Fig. 3.2a[41]). Such a near cancellation must be influenced by the value of N since it modifies the correlation hole part of $g_{pp}(r)$ which, in turn, also influences local packing and the magnitude of $g_{pp}(r)$ on the length scale of intermolecular potentials, as seen in Figs. 3.3a and 3.3b. This physical mechanism results in a liquid density that grows with N under isobaric conditions, which experimentally saturates at an approximate chain length of N=100 (see Fig. 3.2b inset).

The density (S_0) is also well known to increase (decrease) modestly with cooling (Fig. 3.2), but S_0 is largely insensitive to N at fixed temperature due to a compensation of growing density and decreasing compressibility under isobaric conditions. This near constancy is illustrated in Fig. 3.2 for chemically diverse polymer liquids: polydimethylsiloxane(PDMS), polystyrene (PS) and polyethylene oxide (PEO). One sees over a wide range of temperature and chemistry that S_0~0.07-0.2. Calculations for moderately higher values of S_0 mimic concentrated polymer solutions[41], and lower values mimic liquids under applied pressure.

The above discussion has motivated our "calibration strategy" for performing experimentally-relevant isobaric-isothermal calculations for different values of N: the effective

("bare") packing fraction of our model, η_t , is adjusted to maintain a fixed S_0. A modest range of the latter is explored to mimic the known experimental variation of S_0 with chemical structure and temperature for diverse polymers. Examples of how the effective packing fraction computed this way varies with N are shown in the main frame of Fig 3.2b. With increasing chain length, higher packing fractions are needed to attain the same dimensionless compressibility. The initial increase is roughly logarithmic before saturating for large N. For increasing values of S_0, the trend is the same but the corresponding packing fractions quantitatively decrease, as they must.

The predicted densification of pure polymer melts with increasing N under iso-S_0 conditions is in qualitative agreement with experiment but is quantitatively too large (inset of Fig. 3.2b)[42]. This over-prediction could have many origins such as the simple chain and/or interaction potential model adopted and/or the theoretical approximations. Based on prior work, the most obvious candidate is the use of an ideal random walk description of polymers which implies the physical volume a chain takes up is smaller than it should be due to self-overlaps[43]. The latter effect increases with N before ultimately saturating. In essence, we are avoiding an a priori treatment of this aspect by adopting the calibration procedure whereby the model effective packing fraction value serves only to reproduce the correct experimental behavior of S_0 of real polymer liquids. Unless stated otherwise, all calculations are performed in this iso-S_0 manner.

As relevant background, Figure 3.3 presents representative calculations of the real space polymer site-site pair correlation function and corresponding collective static structure factor for N=10→10,000. Results based on constant S_0 (Fig 3.3a) and fixed packing fraction (Fig 3.3b) are shown. Qualitatively, the trends with N for structure are identical, but signifcantly weaker for the

more realistic iso-S_0 results. One clearly sees the long range correlation hole deepens and extends in range with N, and emerges at an inter-monomer separation of ~4d[41, 43]. One also sees how the presence of the elongating correlation hole with N and the iso-S_0 constraint conspire to reduce the pair correlation function locally (small r) before the long chain limit is achieved. The inset of Fig. 3.3b shows how fixing the bare packing fraction of the theory results in an unrealistic massive growth (factor of 7) of S_0 with increasing N. Within the framework of PRISM theory and ideal chain models this is additional support for not using constant packing fraction models if one is interested in experimental realism.

3.3 Depletion Potential of Mean Force

In this section we study the polymer-induced PMF over all length scales as a function of D/d, N, S_0 and backbone stiffness. Figure 3.4 shows results for a large nanoparticle of D/d = 80 in a melt of fixed S_0 = 0.2 over a 5 orders of magnitude variation of N, including the monomer limit and the $2R_g$>D long chain regime. The key features of the PMF can be divided into three main regions (as marked in the plot) which we refer to as the contact (I), local or inner barrier (II), and long range (III) regimes. We discuss each region separately, and identify trends as a function of D/d and N. The relatively weak quantitative dependences on S_0 and chain persistence length are briefly discussed.

3.3.1 Contact Attraction

The PMF at contact in Figure 3.4 (lies outside the plot scale) is negative corresponding to an induced attraction between nanoparticles. It quantifies the tendency for particle aggregation,

and plays a dominant role in thermodynamic miscibility. In a melt, this most local feature of the PMF is related to the short monomer or density fluctuation correlation length scale, which grows modestly with increasing polymer density or decreasing S_0[14]. The leading order physical origin of the depletion attraction in melts is not the same as in dilute solutions where polymer translational and/or conformational entropy is a key driving force. Rather, in a dense melt with oscillatory local packing correlations (see Fig. 3.3), when two particles are brought spatially close the preferred local packing of the polymer liquid is frustrated thereby raising the excess free energy (here entropic) of the liquid providing the driving force for particle clustering. As N increases, there are two major changes in the melt: (i) a longer range correlation hole regime, and (ii) a higher density under isobaric conditions. Both suggest a stronger depletion attraction.

The above physical expectation is confirmed in Figure 3.5 which shows in a log-linear format the negative minimum of the PMF at contact normalized by D/d as a function of chain length. There are several interesting trends. (i) The attraction strength significantly grows initially as roughly a logarithmic function of N which is identical to the change of melt density, as verified by cross plotting (not shown) $\beta W_{nn}^{\min}$ versus effective packing fraction under iso-S_0 conditions. (ii) Scaling the PMF minimum by D/d nearly collapses all the curves except in the monomer limit. More quantitatively, such linear scaling holds well provided that the particle-monomer size asymmetry is significant, i.e., D/d $\geq$ 4-5, in accordance with prior findings[11]. Physically, a particle that is large compared to the polymer density-density correlation length appears to the melt *on* the most local scales that defines the contact PMF as a "flat surface". (iii) The slope of the logarithmic regime is nearly independent of D/d, which again suggests its origin

is the logarithmic variation of density. (iv) For high enough N, the PMF minimum logarithmic growth breaks down at N ~ 150 ± 50 , independent of D/d, polymer persistence length, or S_0 value (not shown). This buttresses our argument that melt EOS effects are the origin of this behavior. (v) At high enough N, the scaled PMF contact value saturates at a value roughly independent of D/d.

The dimensionless melt isothermal compressibility was held fixed at S_0=0.2 in Fig. 3.5. Figure 3.6 shows the consequence of varying this polymer-specific parameter over the wide (in practice) range of 0.1 to 0.5. Qualitatively the N-dependent trends remain the same, however, quantitatively the attractive minima are quite different. With decreasing S_0, the local pair correlations in the melt are enhanced resulting in a stronger driving force to aggregate particles. The PMF minima deepen by a factor of 5.3 from low N=1 to high N=10^5, and a factor of 2.3 for S_0=0.1; if we extrapolate our calculations to S_0=0 (i.e., a hypothetical incompressible fluid), this factor attains the near unity value of 1.4. The long chain asymptotic scaling of the PMF minimum with dimensionless compressibility is found to approximately be an inverse power law, ~ $(1/S_0)^{1/2}$. Though the latter is an empirical deduction based on numerical calculations, interestingly it agrees with the analytic thread model analysis in the Appendix A since $S_0^{-1/2} \propto \rho\sigma^3$ which has a clear physical origin.

The dashed curve in Fig. 3.6 shows the effect of increasing chain persistence length on the depletion attraction. Increasing stiffness at fixed packing fraction is known to enhance interchain packing and reduce the dimensionless compressibility[44]. Therefore, to maintain a fixed S_0, the melt density must decrease, resulting in a weaker PMF attraction with increased *l/d*. We

note that polymer chemistry (precise values of *l/d*, S_0) does not affect the universality of the N~150±50 crossover or the general qualitative trends of the PMF.

3.3.2 Local Barriers

In general one expects repulsive barriers in the PMF to emerge in dense liquids when particles are separated by a small distance that is incommensurate with the length scale of the intervening liquid packing correlations (integer multiples of d). Figures 3.4 and 3.7 show that just beyond the contact attractive minimum of the PMF a repulsive "inner" barrier occurs under melt polymer conditions. Even for the N=1 atomic fluid there is a substantial barrier of height F_B ~ 4.5 kT. Strikingly, the barrier height is a non-monotonic function of chain length N, or equivalently the ratio D/R_g. It initially grows with N when $R_g < R/2$, then goes through a shallow maximum, and ultimately saturates as $2R_g >> D$ (see inset of fig 3.7). In Figure 3.4, we note that D/d=80 is commensurate in size with a chain of N=5400, and the repulsive barrier height peaks for N=1000 before its decreases. Note also that for the smallest chain of N=10 there is an increase of $2k_BT$ in the barrier height relative to the N=1 monomer fluid, and this jump more than doubles when N=1000.

Equilibrium thermodynamics and aggregation behavior are undoubtedly controlled by the local (contact) part of the PMF. However, the emergence of repulsive barriers significantly greater than the thermal energy may allow an alternative nonequilibrium kinetic mechansim for avoiding depletion-induced aggregation. Such a repulsive barrier has been discussed in prior diverse studies of (usually) semidilute or concentrated solutions[9, 11, 22, 45, 46, 47]. Experimental evidence for this phenomenon was suggested by Ogden and Lewis[47] who observed improved

suspension stability at low polymer concentration which they attributed to the presence of a repulsive barrier arising before complete exclusion of polymers from the region between two colloids. However, no prior theoretical study we are aware of has found a non-monotonic variation of the barrier height with N or the large logarithmic-like N-dependences predicted by PRISM theory under model isobaric melt conditions.

The non-monotonicity of the repulsive barrier height with N emerges when $R_g \sim R/2$. Thus, while thermodynamic stability is best for the N=1 atomic fluid, kinetic stability is best achieved by a polymer with $R_g \approx R/2$. The physical origin of the non-monotonicity is rather subtle as discussed in the following section. The main frame of figure 3.7 shows the growth of the repulsive barrier with particle diameter at fixed chain length N=1000 and packing fraction $\eta_t = 0.42$ ($S_0 = 0.2$). The barrier height grows almost linearly with the size asymmetry ratio D/d, a well understand trend for the local features of the PMF of large enough particles in a dense liquid[11]. Barriers of significant height emerge at larger interparticle separations as the particle diameter increases. An overall important feature is that barriers become non-negligible in a practical sense ($>k_BT$) only when the size asymmetry reaches D/d=10 corresponding to a ~10 nm nanoparticle.

The inset of figure 3.7 shows the primary barrier height, F_B, normalized by particle size as a function of $2R_g/D$. Two physical regimes are seen corresponding to roughly $2R_g/D > 1$ and $2R_g/D < 1$. In the $N \rightarrow \infty$ limit, the particle can sense only the interior of self-similar polymer coils leading to a collapse of the primary barrier if $D/d > 10$. In the limit where the particles are much larger than the polymer, the primary barrier decreases from its maximum value as the

polymer-particle size ratio decreases. This $2R_g/D$ dependent non-monotonicity is manifested in a slight shift of the location of the barrier peak with decreasing $2R_g/D$. The non-monotonic barrier height change and the concomitant peak in the inset are absent for particles smaller than of order D/d=10.

3.3.3 Long Range Repulsion

The idea of a long range (R_g scale) component of the depletion potential under equilibrium dense, nearly incompressible, melt conditions has historically not been expected. For example, deGennes[48] argued that for the seemingly related problem of a polymer melt confined between two parallel plates, the range of fluid density oscillations orthogonal to the confining surface is of the order of the liquid density correlation length. This implies the solvation pressure or surface force (analog of the PMF) is short range. However, replacing curved nanoparticles by surfaces is only a priori valid, even qualitatively, if $R_g<<R$. This question of a long range component of the PMF in melts would not seem to be amenable to resolving via simulation since it requires very long chain melts and very large particles relative to the monomer size.

Figure 3.4 shows we do find a long-ranged repulsive tail of the PMF (regime III) of amplitude that is nearly a constant for $2R_g \leq D$. Rescaling the horizontal axis in Fig. 3.4 by R_g demonstrates that its range is of the order of R_g for all chain lengths (Fig 3.8a).Figure 3.8b shows the functional form is a simple exponential:

$$\beta W_{nn}^{long}(h) \approx \alpha \frac{D}{d} e^{-\frac{h}{2\lambda R_g}} \tag{3.3}$$

where h=r-2D is the inter-particle surface-to-surface separation, and α and λ are numerical factors. The log-linear plot as a function of $h/2R_g$ for D/d=34.4 shows linear behavior to a good approximation with a nearly universal slope of ~0.2-0.25 for the different curves implying a constant λ; numerically, this corresponds to a range of $2\lambda R_g \sim R_g/2$, only modestly larger than the pure melt correlation hole range. The overlap of the PMF curves for D/d=80 and D/d=34.4 implies the following four important facts. (i) The amplitude of the long ranged part the PMF scales with D/d, the same scaling found for local features of the PMF. (ii) The amplitude of the tail appears to be nearly independent of N ($\ln \alpha \approx -3.5$) as long as $2R_g \leq D$. (iii) For chains much larger than the particle size ($2R_g >> D$), the amplitude becomes extremely small and effectively disappears on the scale of the plot; in detail, we find (not shown) the tail amplitude decreases strongly as $(D/2R_g)^4 \sim N^{-2}$. (iv) For the atomic fluid and short polymers ($N \leq 20$), the PMF is spatially short-ranged and oscillatory with no long-ranged repulsive feature given the lack of separation between local and polymer size scales.

We now can return to the question of why the inner repulsive barrier (regime II) is a non-monotonic function of $2R_g/D$ (see Fig. 3.7). The reason is that this feature occurs on an intermediate length scale that falls between the local contact regime I and the long range repulsive tail (regime III), and thus its behavior reflects the interplay of their different underlying physics. Specifically, the EOS effects that control the most local regime I is the leading order reason why the barrier height initially grows logarithmically with chain length. However, for long enough chains the EOS effects saturate, and given the inner repulsive barrier "rides" on top of the long range tail of the PMF, the barrier then gradually decreases at very high N due to the reduced amplitude of the long range tail when $2R_g > D$.

In summary, we have found a coupling between the local and macromolecular scale effects in the depletion potential of hard spheres dissolved in dense polymer melts. A repulsive tail of the PMF of range of order R_g exists for all chain lengths but its amplitude becomes negligibly small when the polymer is much larger than the particle size ($2R_g >> D$). Recall that we have pre-averaged explicit chain end effects, and the chains are conformationally ideal. A speculative physical interpretation of the long range tail is that it is as if a droplet of the liquid of size R_g (correlation hole scale) is mediating an effective repulsion between the larger particles (fig 3.1). On the other hand, when $2R_g>>D$, the particle "sees" only the interior of such a droplet where the individual polymer chains, and their interchain pair correlations, obey self-similar (~1/r) spatial correlations. In this regime, the long range tail amplitude is negligibly small. Mathematically, within PRISM theory this tail feature must arise from the cross correlation function, $h_{pn}(r)$, which enters the polymer-mediated depletion potential. From eqns (2.6) and (2.7), one sees the essential quantity is the monomer-particle direct correlation function. It is this object that enforces the impenetrability constraint that the connected sites of polymer chains cannot be in the interior of the hard sphere. This suggests a search for the precise technical origin of the long range part of the PMF should focus on this quantity, as done in section 3.4. Finally, consistent with physical expectations, we have found that the long-ranged PMF tail is not affected by the EOS calibration strategy (not shown) and remains qualitatively unchanged under fixed melt packing fraction conditions.

3.4 Polymer-Nanoparticle Interfacial Correlations

We now briefly study how polymers statistically pack around isolated particles as quantified by the site-site monomer-particle pair correlation function, $g_{pn}(r)$. This quantity is of general interest, and is the origin of the N-dependences of the PMF predicted by PRISM theory.

We have examined in detail the nonrandom part of the pair correlation function, $h_{pn}(r) = g_{pn}(r) - 1$. As an example, we present calculations for D/d = 80 at fixed S_0=0.2 as a function of polymer chain length, N. Generically, $g_{pn}(r)$ has a contact peak followed by local oscillations on the monomer diameter scale (not shown). For any chain length, we find that the curves seem to collapse, but the first peak is a weakly non-monotonic function N with a maximum value when $R_g < D/2$. The latter is a consequence of melt EOS effects.

Figure 3.9 shows that at larger monomer-particle separations there is a long-ranged tail of the interfacial correlation. We have verified that its range is set by R_g with an amplitude that varies non-monotonically with N or equivalently $2R_g/D$. The amplitude appears very weak on the scale of Fig. 3.9, but it is well known that small changes in the polymer-particle pair correlations can have strong consequences on the particle-particle PMF[3, 9, 11, 13]. This long range tail in nearly incompressible melts is a new discovery, and at a technical level is the origin within PRISM theory of the long range tail in the PMF. Physically, it presumably reflects the fact that there is a weak macromolecular component to the constraint of impenetrability of a monomer with a curved hard sphere due to chain connectivity. The sharp drop of the amplitude when $2R_g > D$ is identical to what was found in section 3.3.3 for the PMF, and the physical reason is presumably the same as suggested there.

It is natural to ask whether the long range feature in the interfacial correlation function (and consequently the interparticle PMF) is unique to a dense polymer melt. To answer this, we have studied this problem for semidilute solutions (see Appendix A) based on two levels of chain modeling: (1) the analytic Gaussian thread model, and (2) full numerical PRISM calculations for nonzero monomer diameter chains. The thread model by construction sets the monomer diameter to zero resulting in a vanishing contact value of the polymer-particle correlation function and no density oscillations in the collective structure factor. The thread model does *not* predict the weak long range repulsion in the PMF in semidilute solutions. In contrast, full numerical PRISM theory *does* predict a nonzero polymer density at the particle surface *and* a long range repulsive tail in the PMF; the latter ultimately vanishes continuously only as the polymer density approaches zero. These results are discussed in detail in the Appendix A. Our analysis establishes the common physical origin of the long range PMF repulsion in melts and semidilute solutions is a nonzero polymer density at the nanoparticle surface and the long range component of the polymer-particle pair correlation function associated with chain connectivity.

3.5 Miscibility and Thermodynamics

We now present a few calculations of the particle second virial coefficient $\overline{B}_2 = B_{2,nn} / B_{2,HS}$ which determines the miscibility limit volume fraction under dilute conditions. We also discuss the possible relevance of kinetic stabilization via repulsive barriers.

Figure 3.10 presents calculations of the normalized second virial coefficient for particles of size D/d=5 in a polymer matrix of chains with persistence length l/d = 4/3. Results are shown

at various fixed dimensionless melt compressibilities. Recall that negative values of the second virial coefficient imply phase separation will occur and positive values imply complete miscibility. Following the PMF calculations trend, the $\overline{B}_2$ curves have a sigmoidal-like dependence on chain length. For very short polymers and a "high" concentrated-solution-like value of S_0=0.5, the miscibility decreases very slowly up to N~10. It then decreases much faster with increasing (intermediate) N, eventually saturating in the long chain limit. This trend is amplified for a less compressible melt of S_0=0.2 or 0.1. The massive difference in the second virial coefficients for different S_0 values stems primarily from the difference in the polymer packing fractions required to maintain the constant dimensionless compressibility constraint.

For the least compressible system of S_0=0.1, the negative second virial coefficient at N=1 hints that the system is never completely miscible, unlike when S_0=0.2 and 0.5. The second virial coefficient changes sign at N=10 for S_0=0.5, implying that for very short polymers, the particles are completely miscible. For S_0=0.2, $\overline{B}_2$ is positive only for N=1 and 2 and becomes negative for $N \geq 3$. The transition from positive to negative B_2 depends not only on the dimensionless compressibility S_0, but also on D/d since the PMF grows with this quantity.

In terms of numbers, the spinodal volume fraction in the long chain limit is ~6% and 1% for S_0=0.5 and 0.2, respectively, for the D/d=5 system of Fig. 3.10. Alternatively, if one asks at what chain length is 1% miscibility attained we find N~60 and 20 for S_0=0.2 and 0.1, respectively. Recall that S_0 is a nonuniversal function of polymer chemistry and temperature. Increasing D/d greatly decreases the solubility limits given the exponential connection between the second virial coefficient and the PMF.

The monotonic dependence of $\overline{B}_2$ on N emphasizes that thermodynamic miscibility is dominated by the local (contact) contribution of the PMF. While regimes II and III of the PMF also, in principle, contribute to the quantification of dispersion, their weak non-monotonic dependence on N is masked by the strong primary attractive minimum.

An interesting question is nonequilibrium stability and dispersion. Recall that for big enough particles in dense long chain melts, large repulsive barriers are predicted in the PMF at short interparticle separations (Fig. 3.7). These could potentially kinetically frustrate aggregation and phase separation, stabilizing the dispersion in analogy with charge stabilization in colloidal suspensions. For example, from Fig. 3.7 we find that in the long chain limit the primary repulsive barrier height is ~ 0.12 D/d in thermal energy units. Thus, given a typical monomer size of d~1 nm, for a 100 nm particle there is a high ~12 k_BT barrier. This raises the striking idea that by *increasing* polymer chain length one might kinetically achieve particle stabilization. Note that, in analogy with charged colloids that also experience a very strong van der Waals attraction, the contact attraction strength is even larger; from Fig. 3.6, we find W_{min}/k_BT~ -D/d for S_0~0.25. Of course, in real long chain melts there are potential complications such as entanglements and adsorption.

A prior simulation study of spherical particles (D/d~5) in a (largely) nonadsorbing bead-spring polymer melt under isobaric conditions was performed by Smith et al[20]. They found that the tendency for particle aggregation was enhanced with increasing chain length. Their systems were simulated initially in the NPT ensemble that yielded equilibrium reduced densities of $\rho_p d^3$ = 0.63, 0.68 and 0.70 for N = 5, 10 and 20, respectively; in all cases they found a negative second

virial coefficient. Given the simulation and theoretical models are not identical, to make a fair qualitative comparison of the N-dependences we normalize the second virial coefficient with the shortest chain (N=5) value as: $B_{2,nn}(N) = \overline{B}_2(N) / \overline{B}_2(N=5)$. The simulation values of $B_{2,nn}(N)$ are given in Table 3.1 along with our predicted values. We do not want to over-emphasize the quantitative comparison but rather the similar qualitative, even semi-quantitative, variation of the second virial coefficient with N under melt-like conditions found in simulation and theory.

3.6 Summary

We have employed PRISM theory to study polymer-mediated entropic depletion interactions between two hard spheres dissolved in a dense polymer melt or concentrated solution. Our new insights derive from studying this problem within the context of model isobaric conditions, and over an unprecedented wide range of polymer-particle size ratios (R_g/D), particle-monomer size ratios (D/d), and chain lengths (N, up to 10^6) or equivalently R_g/d. Given a typical segment size of d~ 1-1.5 nm, our calculations are relevant to nanoparticles as large as ~100 nm, and polymers with end-to-end mean distances as large as ~2 microns. Such length scales are far beyond the ability of direct simulation, but are highly relevant to experiment, including systems of biophysical relevance.

Motivated by the desire to mimic the experimental equation of state behavior of real polymer liquids at atmospheric pressure, we have formulated an iso-dimensionless compressibility calibration procedure for selecting the polymer packing fraction that enters the

theory. We find that this "calibration" or mapping procedure is essential to realistically capture chain length effects in polymer melts and the depletion problem in real nanocomposites.

We have identified and analyzed three key features of the PMF on different length scales. On the most local scale of the contact value of the PMF that dominates the second virial coefficient and thermodynamic miscibility, we find the well-known and understood near universal linear scaling of the strength of depletion attraction with D/d, and a nonperturbative logarithmic increase up to N~ 100 which ultimately saturates in the long chain limit. The latter increase is due to the growth with N of the effective packing fraction under iso-S_0 conditions. It implies that even in dense melts with their short density correlation lengths, the isobaric constraint and corresponding liquid densification results in a major loss of miscibility as polymers become longer, an equation of state effect. Polymer chemistry (and to zeroth order, temperature) enters via the value of S_0. As the latter decreases, the depletion contact attraction quantitatively increases, but there are no qualitative changes of any of the dependences on D/d or N; a similar invariance of the qualitative aspects to chain persistence length is found. Qualitative consistency of the predicted chain length dependence (N=5-20) of the 2^{nd} virial coefficient with a simulation[20] has been demonstrated.

The second key feature of the PMF is just beyond contact there is a repulsive entropic barrier of height that again grows linearly with D/d for the same physical reasons the contact minimum does. The barrier can attain values far in excess of thermal energy for experimentally relevant (large) nanoparticle sizes and polymer chain lengths. This raises the possibility of entropic kinetic stabilization of nanoparticles. Moreover, for relatively large nanoparticles

(D/d>10) the barrier is a non-monotonic function of chain length which becomes quantitatively more pronounced with increasing D/d. The barrier initially grows significantly and roughly logarithmically with N for all particle sizes at a rate that is nearly independent of D/d. A maximum is attained when the geometric criterion $R_g \sim R/2$ is reached, and beyond that the barrier height decreases weakly and ultimately saturates when $2R_g >> D$. Non-negligible secondary barriers can emerge for large enough particles and long enough chains. New physics beyond just EOS effects underlie this non-monotonic variation of the repulsive barrier height with $2R_g/D$.

The third key feature of the PMF is perhaps the most striking given it was not apparently anticipated in dense melts. A long range (of order R_g) repulsive component of the depletion potential emerges when the polymers are smaller than, or of order, the particle diameter. This feature is also present in semidilute solutions (see Appendix A1) although the Gaussian thread model misses it completely[49]. Hence, this tail requires both particle curvature relative to macromolecular size, and nonzero monomer volume that results in a nonzero contact value of both g_{pp} and g_{pn}. On general grounds, and based on its exponential dependence of interparticle separation with a decay length of order R_g, we speculate there is a qualitative connection to the melt correlation hole idea as generalized to the problem of how polymers pack around hard particles. As the polymer becomes larger than the particle, this long range feature decreases extremely rapidly and becomes negligible. Its origin within the theory is traced back to a weak R_g-scale component of the monomer-particle pair correlation function associated with how chain connectivity influences this packing problem. The predictions of PRISM theory for this long

range repulsion in semidilute solutions, and the similarities and differences compared to the melt behavior, is addressed in the Appendix A2.

The practical consequences of the long range repulsive PMF feature seem very small for equilibrium thermodynamics, but might be relevant to dynamics. Concerning its technical reliability to the approximations of the version of PRISM theory we employ, our largest concern is that the theory does not allow polymer conformation to vary in a spatially inhomogeneous manner for that part of the melt near or between the particles. This approximation is difficult to avoid in any integral equation approach for nanocomposites formulated at the level of pair correlations[9], and represents an open future direction of research. However, a priori we cannot think of an argument for why this effect would qualitatively modify the prediction of PRISM theory for the long range feature of the PMF.

Concerning experimental implications, we see two major ones. First, the dispersability of nanoparticles in polymer melts clearly decreases with growing chain length under isobaric conditions[50, 51]. Whether this involves nonequilibrium effects (adsorption, entanglements, gelation) or is an equilibrium phenomenon is not well understood. Our calculations establish what is expected based on isobaric equilibrium conditions for the foundational problem of nonadsorbing polymers and a model nanocomposite controlled entirely by entropic packing effects. Second, the prediction that large repulsive barriers can emerge for big enough nanoparticles and long chains suggests the idea that spatial dispersion might be achieved kinetically by increasing the size of polymers and particles, counter to what happens under equilibrium conditions. This would be a new strategy that complements the now well known

strategies for dispersion based on controlling the polymer-particle adsorption strength[9, 11, 12, 13] or coating particle surfaces with grafted brushes[52-54].

3.7 References

(1) A. Yethiraj, *Adv. Chem. Phys*. **121**, 89 (2002).

(2) A. Yethiraj, C. K. Hall, *J. Chem. Phys*. **95**, 3749 (1991).

(3) N. Patel, S. A. Egorov, *J. Chem. Phys*. **121**, 4987 (2004).

(4) J. F. Joanny, L. Leibler, P. G. deGennes, *J. Polym. Sci.,Polym. Phys*. **17**, 1073 (1979).

(5) J. M. H. M. Scheutjens, G. J. Fleer, *Adv. Colloid Interface Sci*. **16**, 361 (1982).

(6) E. Eisenriegler, *J. Chem. Phys*. **113**, 5091 (2000); *Phys. Rev. E* **55**, 3116 (1997).

(7) T. Odijk, *J. Chem. Phys*. **106**, 3402 (1997).

(8) L. M. Hall, L. M.; K. S. Schweizer, *J. Chem. Phys.* **128**, 234901 (2008).

(9) L. M. Hall, A. Jayaraman, K. S. Schweizer, *Curr. Opin. Solid State Mater. Sci.* **14**, 38 (2010).

(10) L. M. Hall, K. S. Schweizer, *Macromolecules* **44**, 3149 (2011).

(11) J. B. Hooper, K. S. Schweizer, *Macromolecules* **38**, 8858 (2005).

(12) J. B. Hooper, K. S. Schweizer, *Macromolecules* **39**, 5133 (2006).

(13) L. M. Hall, K. S. Schweizer, *Soft Matter* **6**, 1015 (2010).

(14) J. B. Hooper, K. S. Schweizer, T. G. Desai, R. Koshy, P. Keblinski,. *J. Chem. Phys*. **121**, 6986 (2004).

(15) S. Salaniwal, S. K. Kumar, J. F. Douglas, *Phys. Rev. Lett.* **89**, 258301 (2002).

(16) F. W. Starr, T. B. Schroeder, S. C. Glotzer, *Macromolecules* **35**, 4481 (2002); *Phys. Rev. E* **64**, 021802 (2001).

(17) F. W. Starr, J. F. Douglas, *J. Chem. Phys*. **119**, 1777 (2003).

(18) M. Vacatello, *Macromolecules* **34**, 1946 (2001); **35**, 8191 (2002).

(19) M. Doxastakis, Y. L. Chen, O. Guzman, J. J. dePablo, *J. Chem. Phys*. **120**, 9335 (2004).

(20) J. S. Smith, D. Bedrov, G. D. Smith, *Compos. Sci. Technol*. **63**, 1599 (2003).

(21) D. Bedrov, G. D. Smith, J. S. Smith, *J. Chem. Phys*. **119**, 10438 (2003).

(22) A. Yethiraj, C. K. Hall, R. Dickman, *J. Colloid Interface Sci*. **151**, 102 (1992).

(23) R. Dickman, A. Yethiraj, *J. Chem. Phys*. **100**, 4683 (1994).

(24) P. G. Khalatur, L. Zherenkova, A. R. Khoklov, *Physica A* **247**, 205 (1997).

(25) B. J. Ash, L. S. Schadler, R. W. Siegel, *Mater. Lett*. **55**, 83 (2002).

(26) Y. Lin, A. Boker, J. He, K. Sill, H. Xiang, C. Abetz, X. Li, J. Wang, T. Emrick, S. Long, Q. Want, A. Balazs, T. P. Russell, *Nature (London)* **434**, 55 (2005).

(27) M. E. Mackay, T. T. Dao, A. Tuteja, D. L. Ho, B. Van Horn, H. –C. Kim, C. J. Hawker, *Nature (London) Mater*. **2**, 762 (2003).

(28) L. M. Hall, B. J. Anderson, C. F. Zukoski, K. S. Schweizer, *Macromolecules* **42**, 8435 (2009).

(29) S. Sen, Y. Xie, S. K. Kumar, H. Yang, A. Bansal, D. L. Ho, L. M. Hall, J. B. Hooper, K. S. Schweizer, *Phys. Rev. Lett*. **98**, 128302 (2007).

(30) S. Y. Kim, L. M. Hall, K. S. Schweizer, C. F. Zukoski, *Macromolecules* **43**, 10123 (2010).

(31) B. J. Anderson, C. F. Zukoski, *Macromolecules* **41**, 9326 (2008).

(32) B. J. Anderson, C. F. Zukoski, *Macromolecules* **40**, 5133 (2007).

(33) K. I. Winey, R. A. Vaia, *MRS Bull.* **32**, 314 (2007).

(34) M. E. Mackay, A. Tuteja, P. M. Duxbury, C. J. Hawker, B. V. Horn, Z. Guan, G. Chen, R. S. Krishnan, *Science* **311**, 1740 (2006).

(35) M. Alexandre, P. Dubois, *Materials Science and Engineering* **28**, 1 (2000).

(36) F. Sciortino, *Nat. Mat*. **1**, 145 (2002).

(37) J. D. Weeks, D. Chandler, H. C. Andersen, *J. Chem. Phys.* **54**, 5237 (1971).

(38) D. Chandler, *Introduction to Statistical Mechanics* (Oxford Univ Press, 1987).

(39) J. P. Hansen, I. R. McDonald, *Theory of Simple Liquids* (Academic Press, London, 1986).

(40) P. G. de Gennes, *Scaling Concepts in Polymer Physics* (Cornell University Press, Ithaca, 1979).

(41) K. S. Schweizer, J. G. Curro, *Adv. Chem. Phys.* **98**, 1 (1997).

(42) P. Zoller and D. J. Walsh, *Standard Pressure-Volume-Temperature Data for Polymers* (Technomic, Lancaster, 1995).

(43) K. S. Schweizer, J. G. Curro, *Macromolecules* **21**, 3070 (1988).

(44) K. G. Honnell, J. G. Curro, K. S. Schweizer, *Macromolecules* **23**, 3496 (1990).

(45) R. I. Feigin, D. H. Napper, *J. Colloid Interface Sci*. **75**, 525 (1980).

(46) A. A. Shvets, A. N. Semenov, *J. Chem. Phys*. **139**, 054905 (2013).

(47) A. L. Ogden, J. A. Lewis, *Langmuir* **12**, 3413 (1996).

(48) P. –G. de Gennes, *C. R. Acad. Sci. (Paris)* **305**, 1181 (1987).

(49) A. P. Chatterjee, K. S. Schweizer, *J. Chem. Phys.* **109**, 10464 (1998).

(50) B. J. Anderson, C. F. Zukoski, *Langmuir* **26**, 8709 (2010).

(51) B. J. Anderson, C. F. Zukoski, *Macromolecules* **42**, 8370 (2009).

(52) S. K. Kumar, N. Jouault, B. Benicewicz, T. Neely, *Macromolecules* **46**, 3199 (2013).

(53) A. Jayaraman, N. Nair, *Mol. Sim.* **38**, 751 (2012).

(54) P. Akcora, H. Liu, S. K. Kumar, J. Moll, Y. Li, B. C. Benicewicz, L. S. Schadler, D. Acehan, A. Z. Panagiotopoulos, V. Pryamitsyn, V. Ganesan, J. Ilavsky, P. Thiyagarajan, R. H. Colby, J. F. Douglas, *Nat. Mat.* **8**, 354 (2009).

3.8 Figures

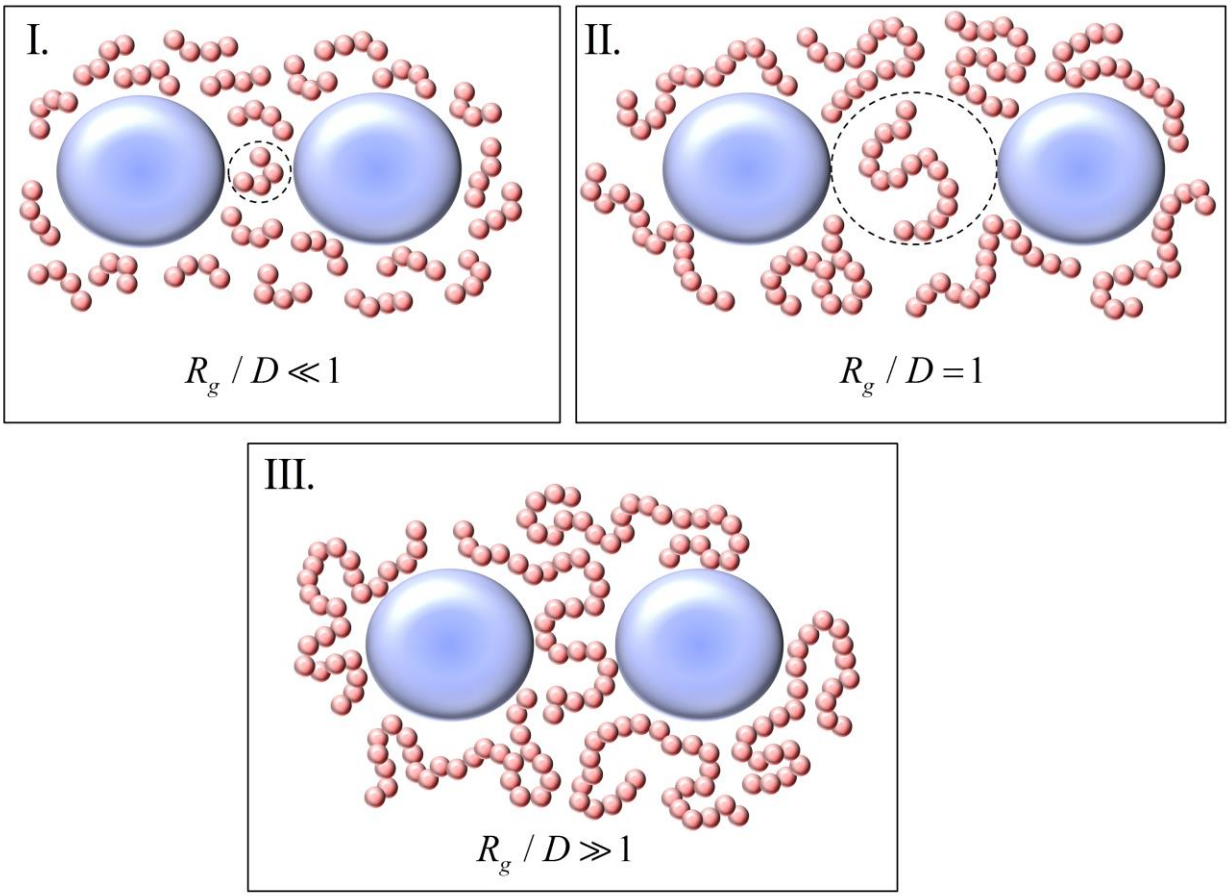

Figure 3.1 Cartoon of the three physical regimes based on the ratio R_g/D.

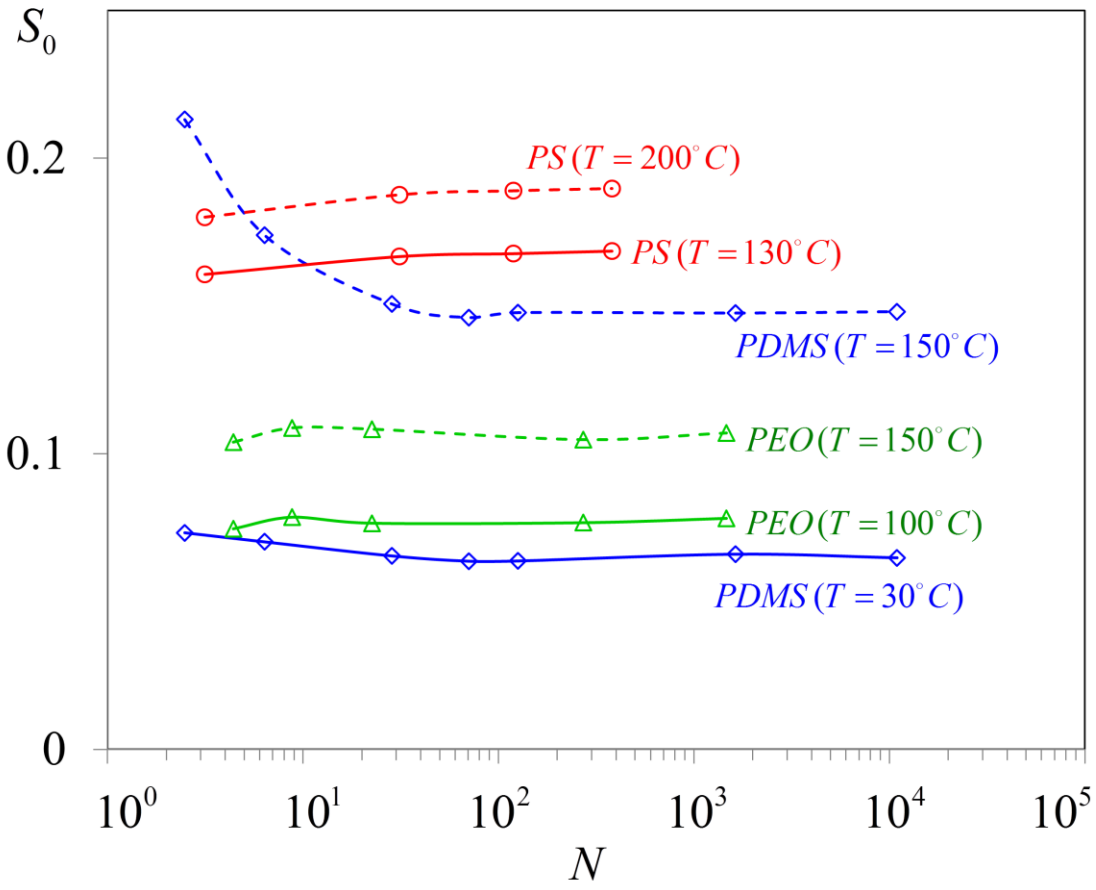

Figure 3.2a Experimental dimensionless isothermal compressibility[67] as a function of chain degree of polymerization (N) for PDMS, PS and PEO melts at the indicated temperatures and 1 atm pressure.

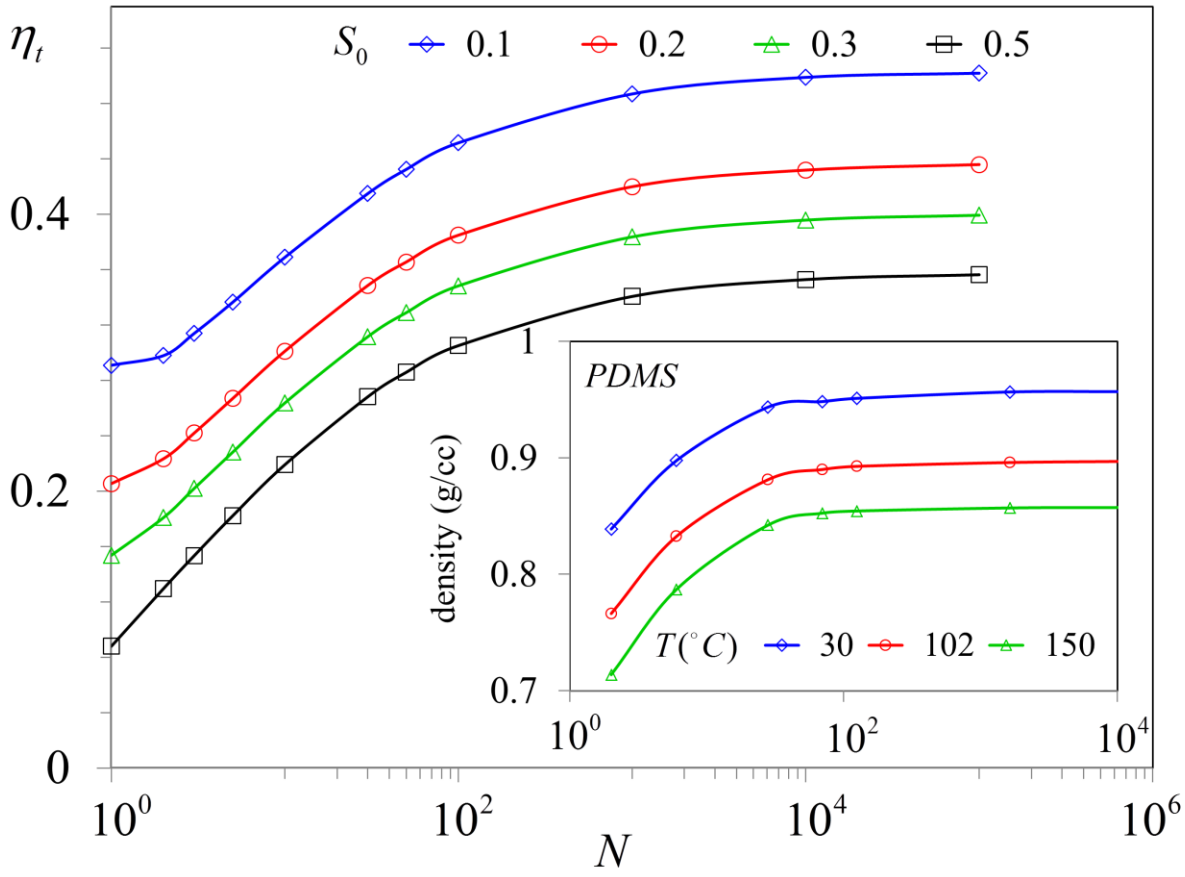

Figure 3.2b (Main) PRISM-predicted pure polymer melt packing fraction as a function of N required to maintain the indicated constant dimensionless compressibilities. (Inset) Experimental change of density of a PDMS melt with molecular weight at different temperatures and 1 atm[67].

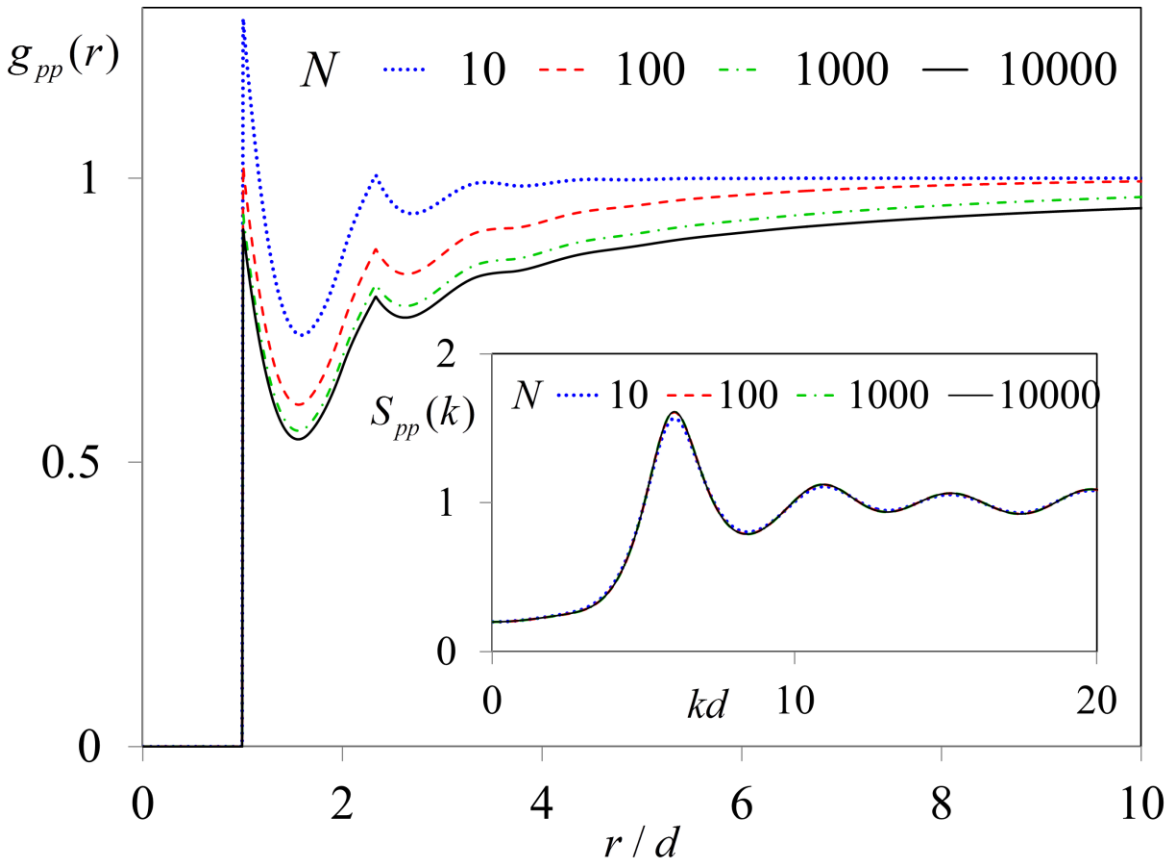

Figure 3.3a (Main) Polymer melt interchain site-site pair correlation function, $g_{pp}(r)$, for various chain lengths based on the "calibration strategy" for S_0 = 0.2. (Inset) The corresponding dimensionless collective static structure factors.

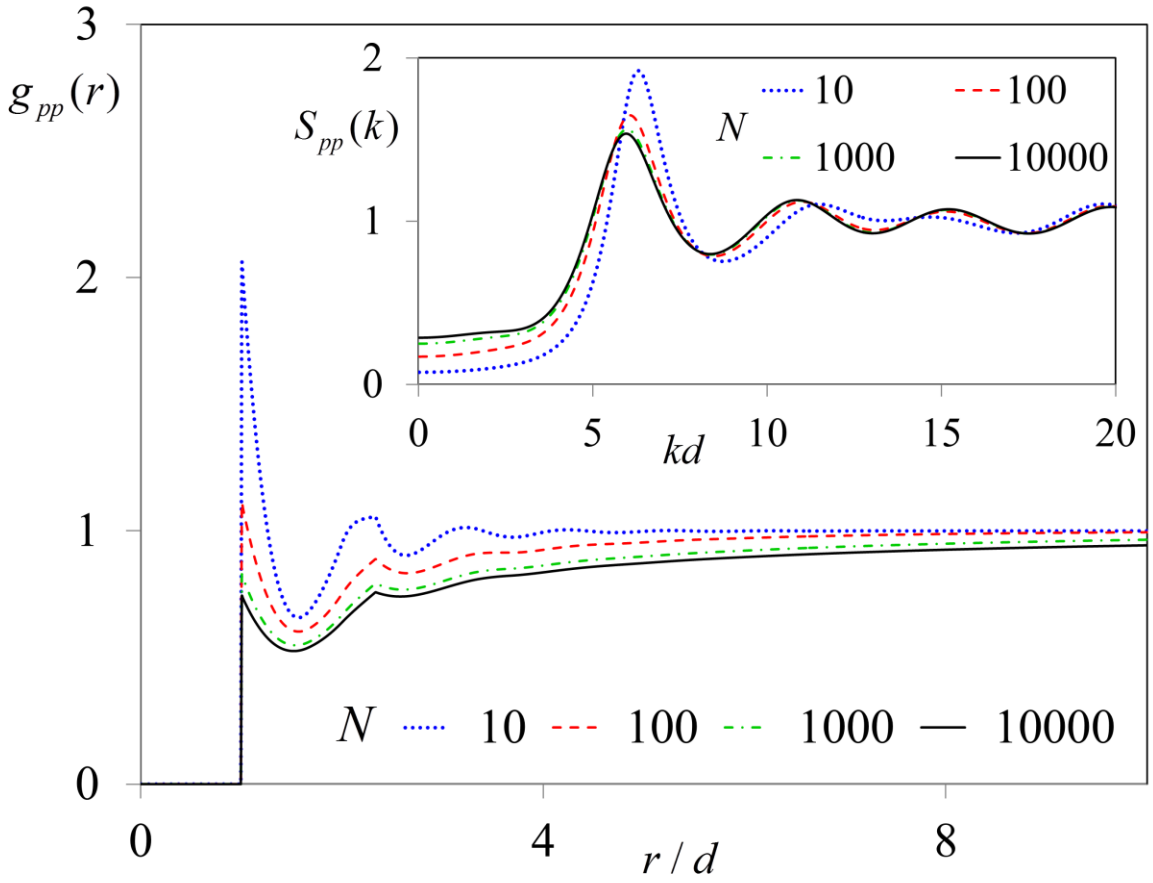

Figure 3.3b Analog of Fig.3a but at a fixed melt total packing fraction of η_t = 0.4 (no calibration).

.

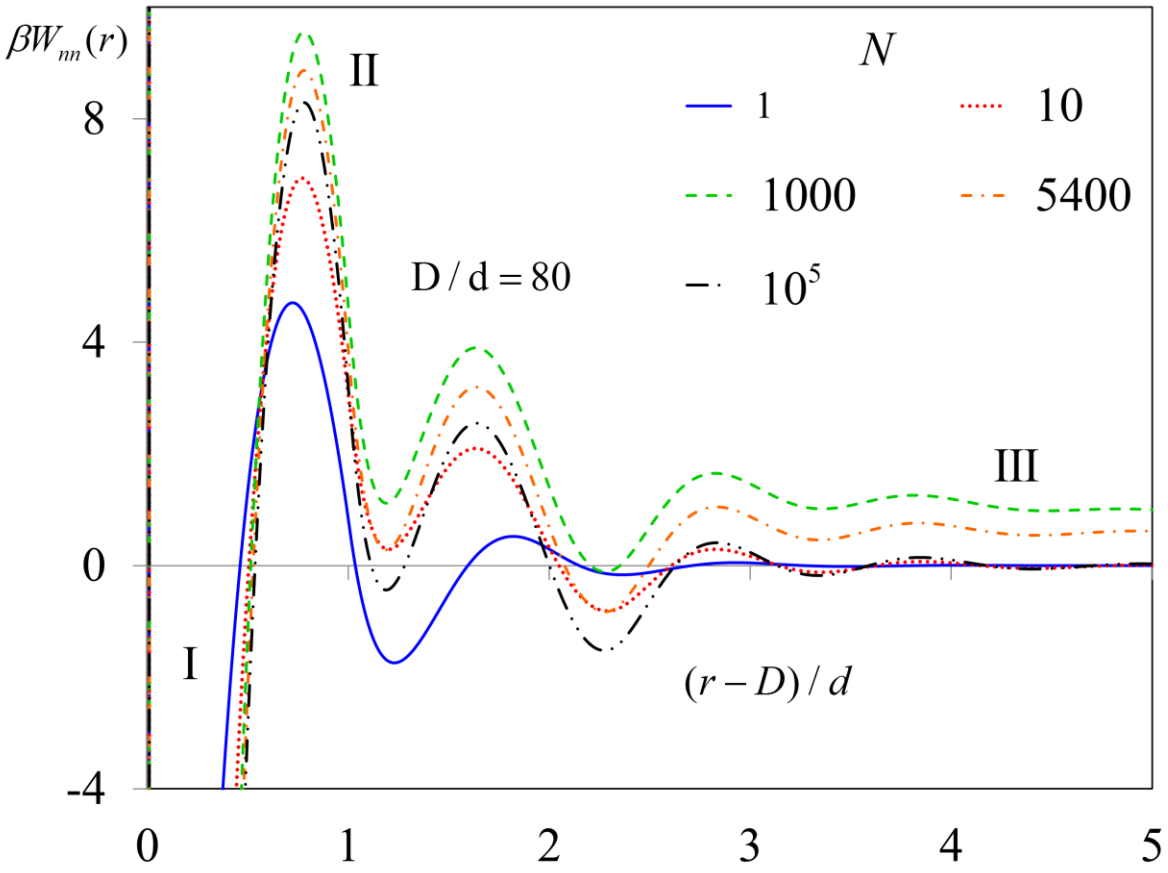

Figure 3.4 Potential of mean force (units of thermal energy) between two particles of size asymmetry ratio D/d = 80 at the indicated chain lengths and fixed S_0=0.2. The attractive minima at contact (off scale) in units of the thermal energy are -39 (N = 1), -67 (N = 10), -95(N = 1000), -99 (N = 5400) and -101 (N = 10000), respectively.

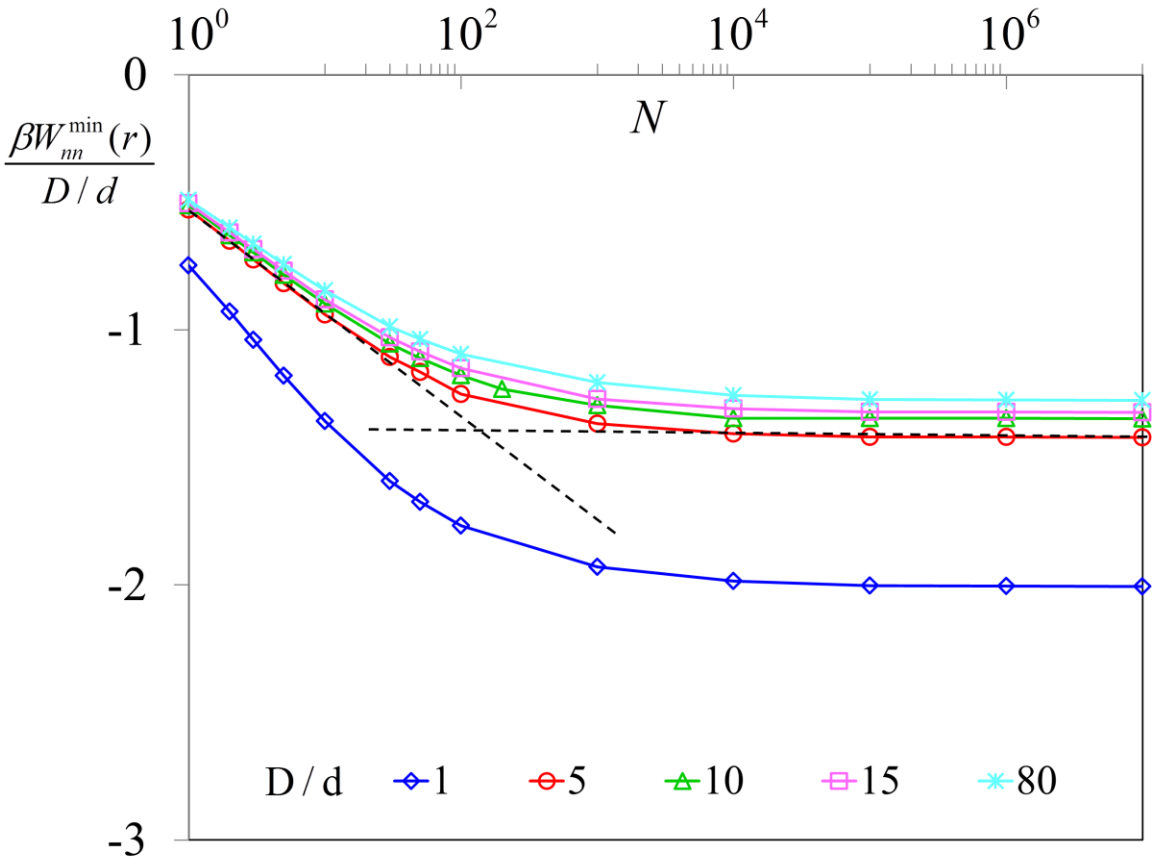

Figure 3.5 Potential of mean force contact minimum normalized by the size asymmetry ratio as a function of N and various values of D/d with S_0=0.2.

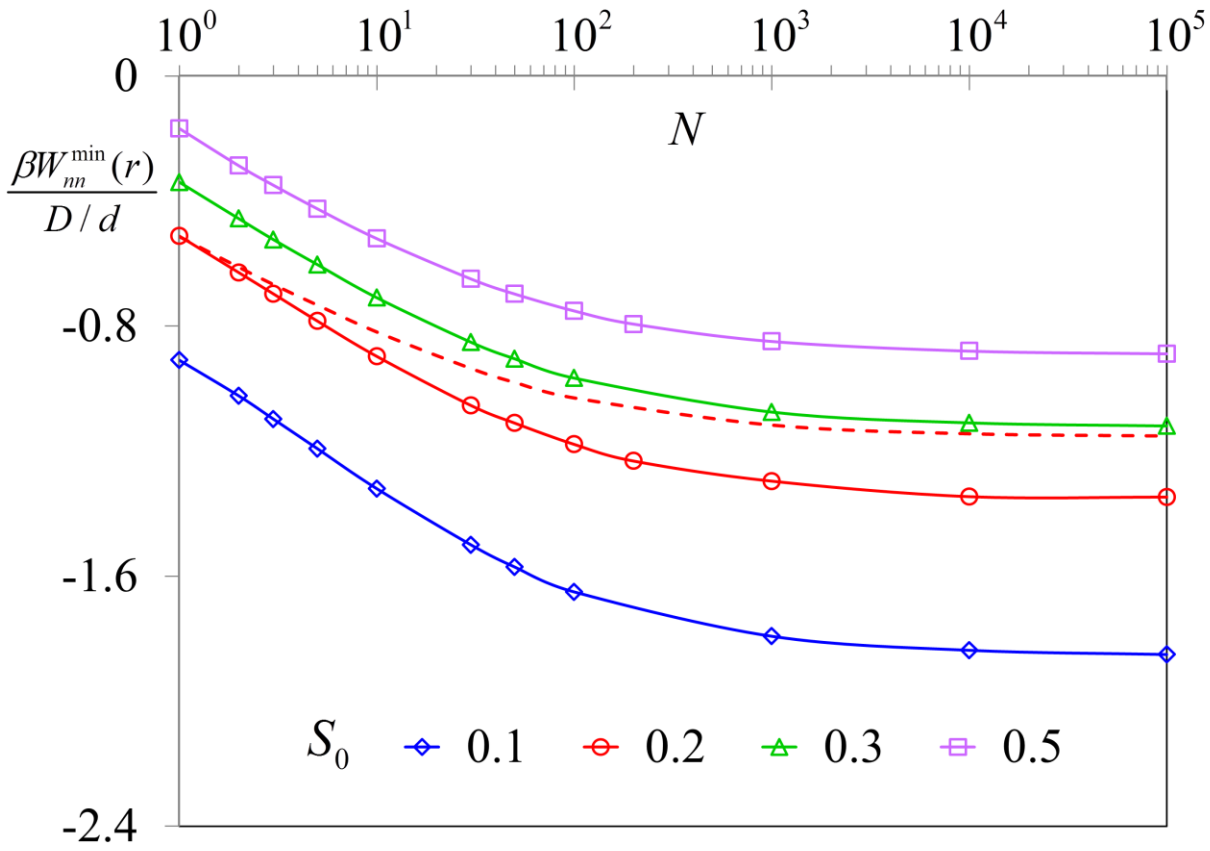

Figure 3.6 Potential of mean force contact minimum for fixed D/d=10 and chain persistence lengths of *l/d* = 1.333 (solid) and 1.5 (dashed) as a function of N at various values of dimensionless compressibility S_0.

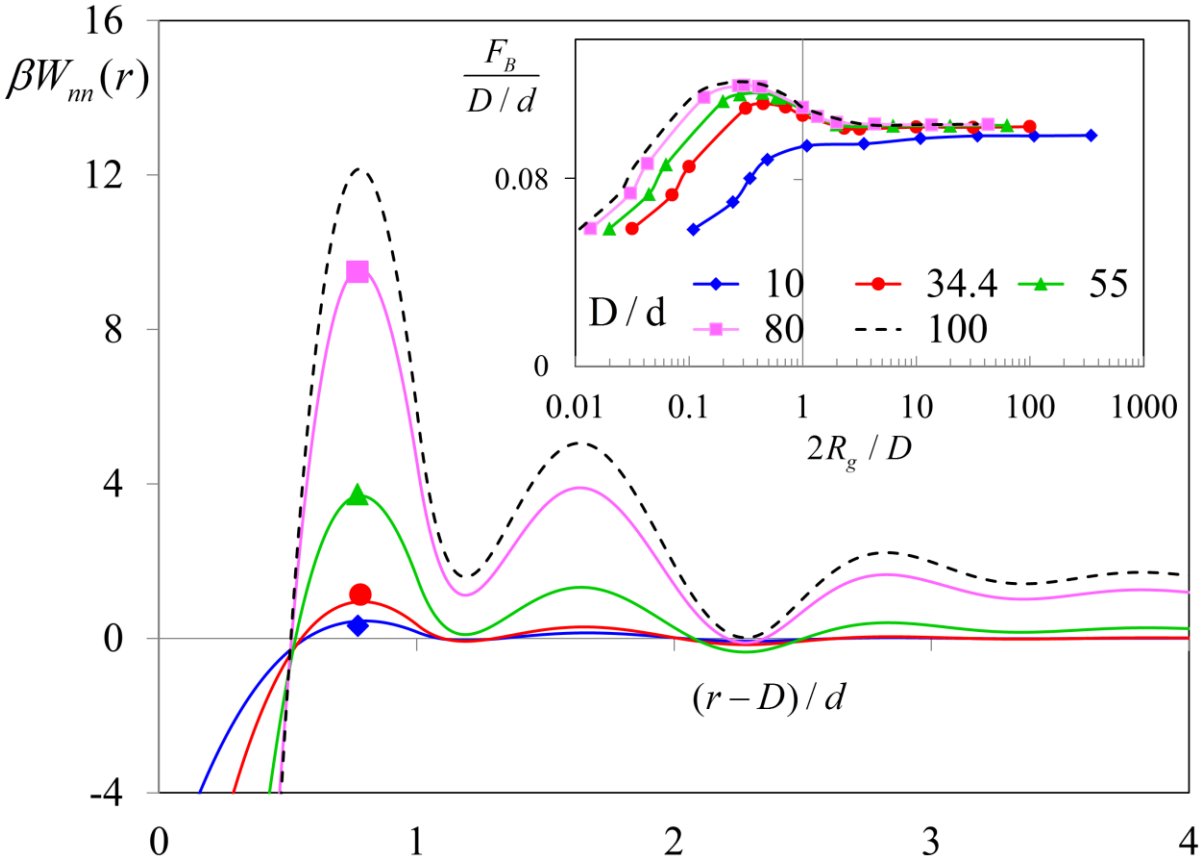

Figure 3.7 (Main) Potential of mean force for N = 1000 and S_0=0.2 at the indicated values (see inset legend) of D/d which range from 10 to 100. (Inset) Primary barrier height (regime II) normalized by the particle diameter as a function of $2R_g/D$ for various values of the size asymmetry ratio D/d.

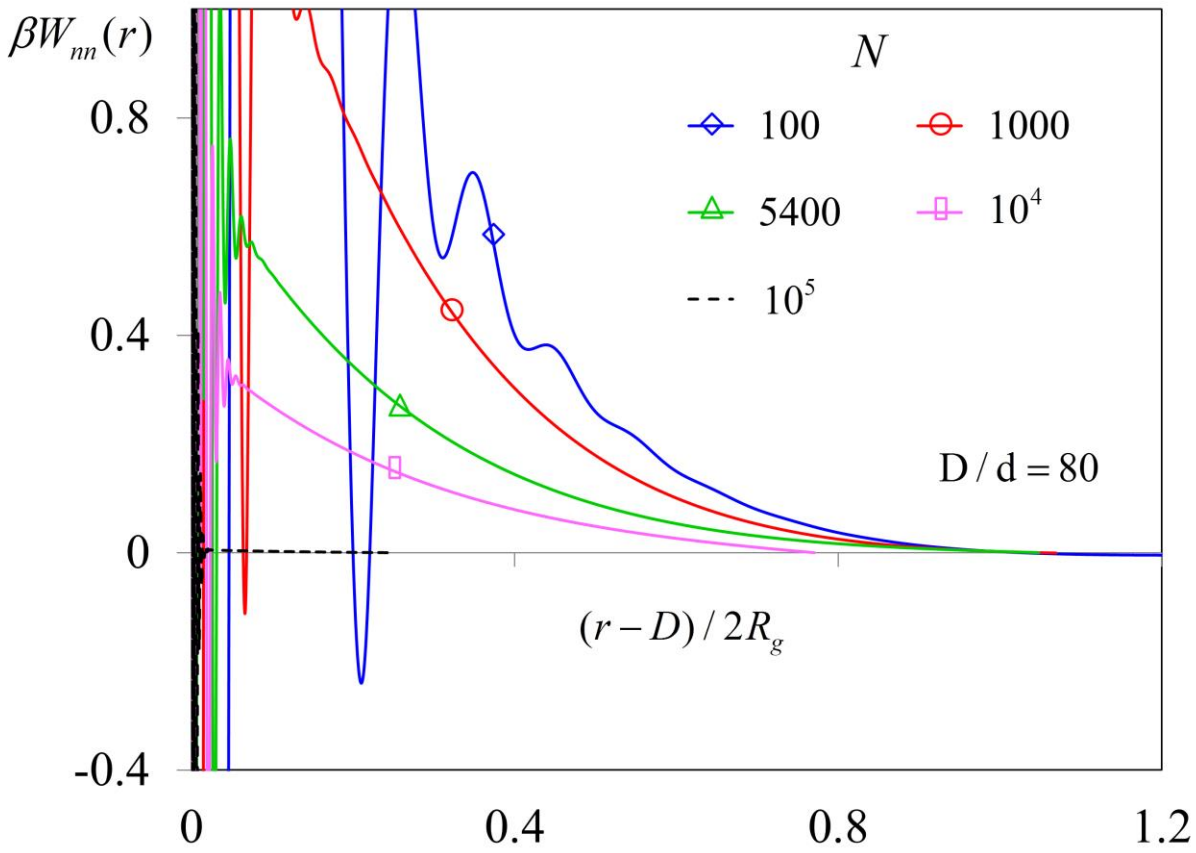

Figure 3.8a The long-ranged repulsive tail of the potential of mean force (regime III) for D/d=80 and S_0=0.2 at the indicated chain lengths.

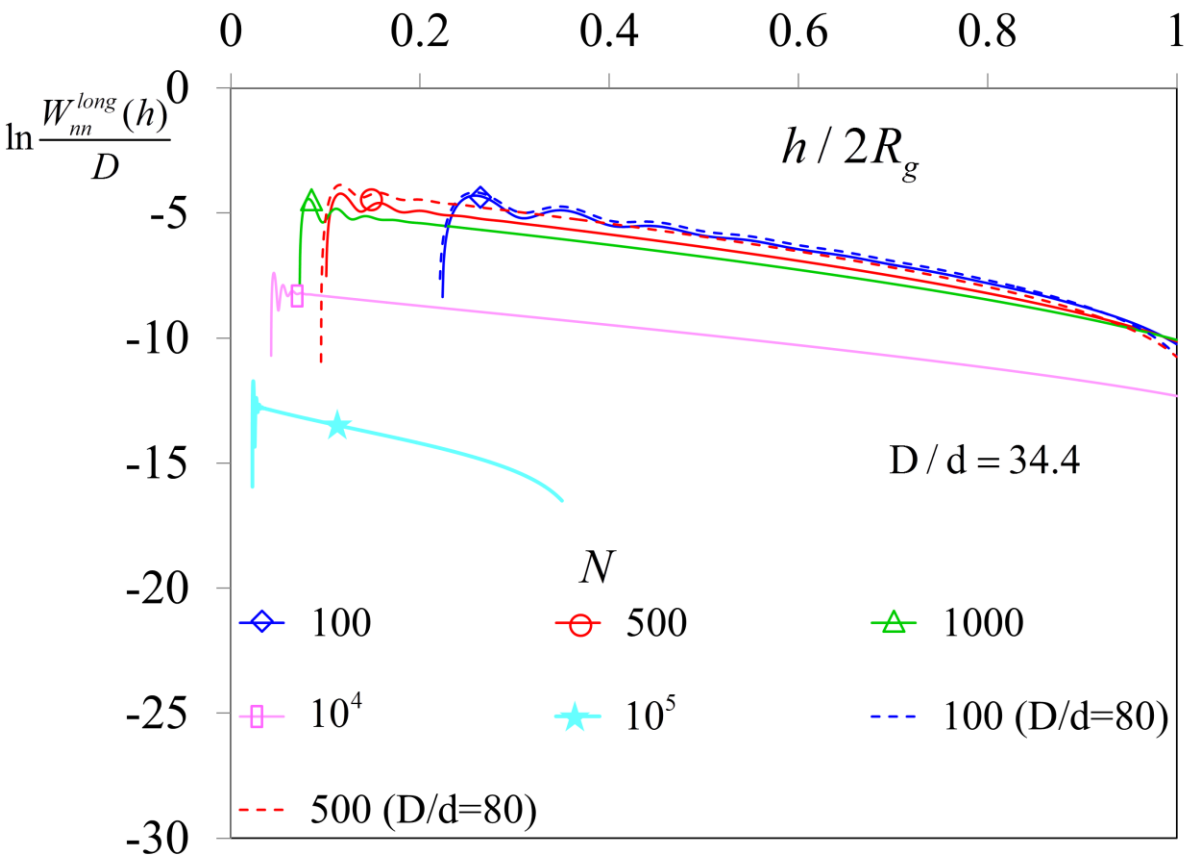

Figure 3.8b Log-linear plot of the normalized long-ranged part of the PMF as a function of the interparticle surface-to-surface separation at the indicated chain lengths for D/d=34.4 (solid) and 80 (dashed) and S_0=0.2.

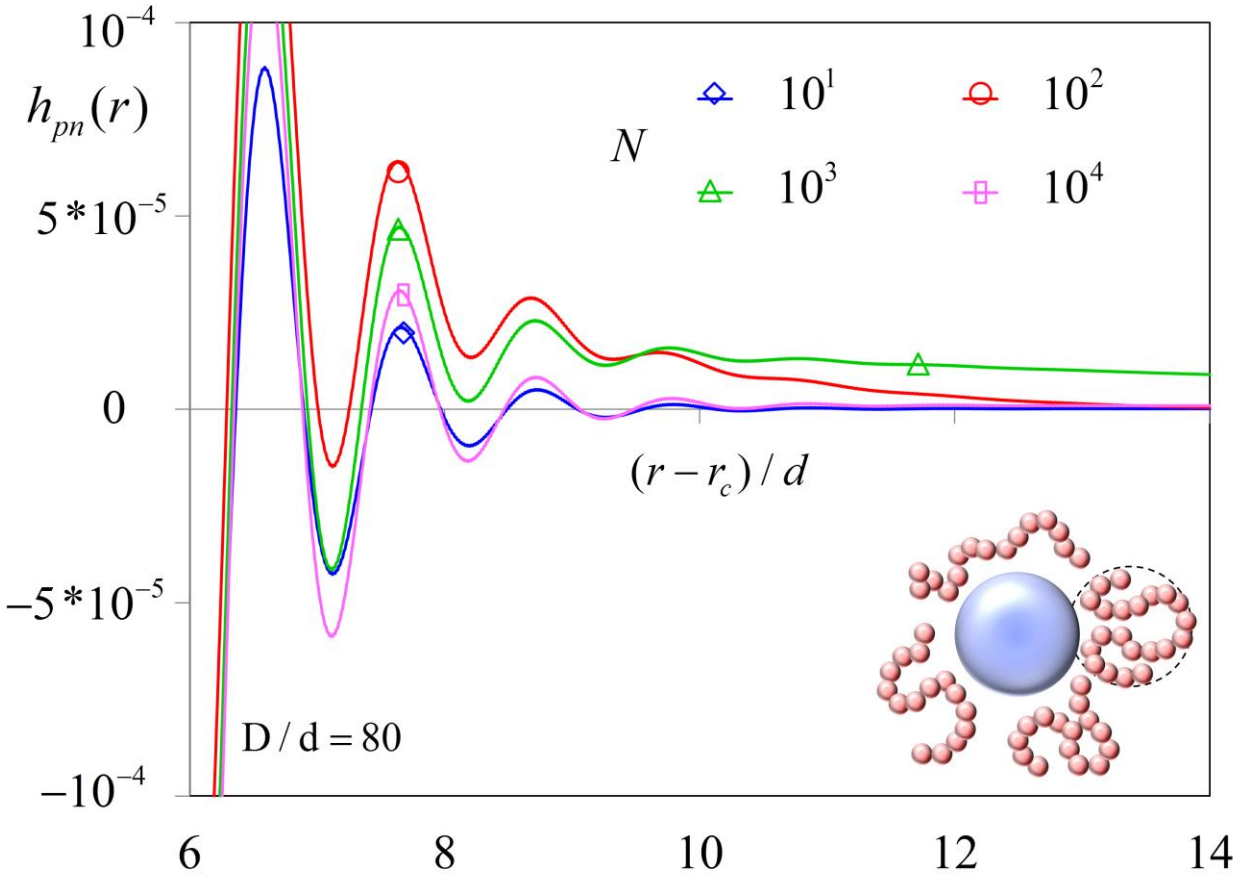

Figure 3.9 Non-random part of the site-site polymer-particle pair correlation function for D/d=80 and S_0=0.2 at the indicated chain lengths. Note that the result for $N=10^4$ is long-ranged but the amplitude is extremely small. For the N=1000 ($2R_g$ ~ 34.4) system, the curve goes to zero at an inter-surface separation of ~ 35*d*.

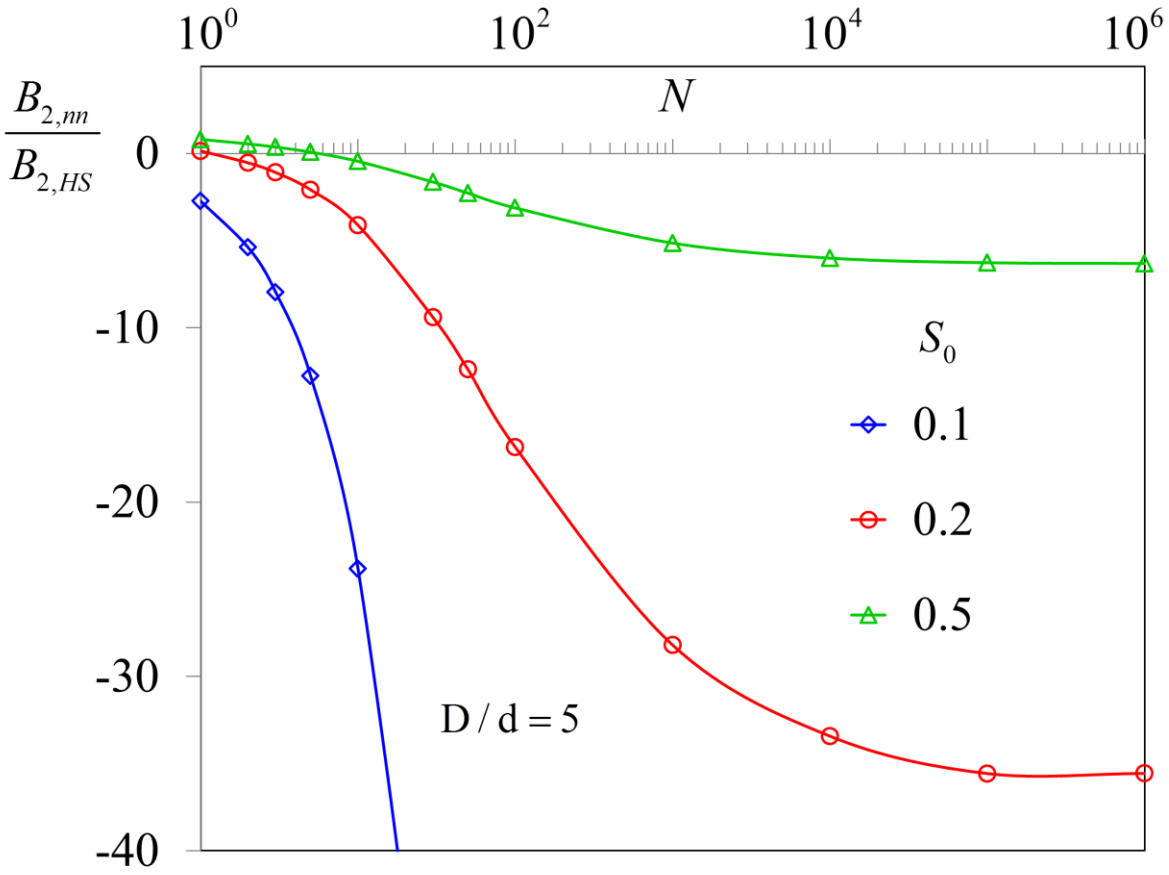

Figure 3.10 Normalized second virial coefficient for D/d=5 as a function of chain length N for different dimensionless compressibilities S_0.

N	(Simulation[20]) $B_{2,nn}$	(PRISM) $B_{2,nn}$
5	1	1
10	1.9	1.95
20	3	3.4

Table 3.1 Comparison of Theory and Simulation Virial Coefficients as a Function of N. The normalized second virial coefficient defined as $B_{2,nn}(N) = \overline{B}_2(N) / \overline{B}_2(N=5)$. Simulation results are from ref. [20]. For the PRISM calculations, *l/d* = 1.333 and S_0 = 0.2. The individual $\overline{B}_2(N)$ are all negative.

CHAPTER 4

ENTROPIC DEPLETION IN COLLOIDAL SUSPENSIONS AND POLYMER LIQUIDS: ROLE OF NANOPARTICLE SURFACE TOPOGRAPHY

4.1 Introduction

The study of how small nanoparticles or polymers mediate effective entropic depletion interactions between particles or colloids in liquid media is a problem of enduring relevance to colloid science, polymer science, materials science, and biological systems[1-4]. The most elementary question concerns the potential of mean force (PMF) between two dilute spheres in non-adsorbing media where all interactions are repulsive hard core. This is a pure entropy problem, and the nonideal aspects vary depending on the system and concentration regime. The basic problem is theoretically well understood for large smooth hard spheres dissolved in a fluid of smaller hard spheres[5-7] as discussed in Chapter 3. If the matrix is a dense polymer solutions or melts, the physics is much richer and depends on additional length scales[8-16]. Though there are some surprises in polymeric media regarding the non-contact form of the depletion potential, much recent progress has been made using a variety of theoretical methods and the problem is now well understood. If excluded volume interactions are additive, excess entropy favors contact aggregation of the large spheres. However, often depletion attraction leads to macroscopic phase

separation which is undesirable. Multiple complementary strategies have been developed to counteract this including tuning chemistry to favor limited matrix-particle adsorption[17-20], attaching chain molecules to provide steric stabilization[21-24], and introducing frustration based on sequence-designed AB copolymers[25-29].

The other avenue to avoid clustering of fillers is to modify the surface morphology of the particles by incorporating roughness compared to the conventional smooth spheres. Some recent experiments have demonstrated the fact that particle roughness can attenuate depletion attraction[30-36]. Studying the effect of surface roughness on the depletion interaction between two fillers in a solvent or polymer solution/melt is a relatively recent phenomenon. In reality, the surfaces of colloidal particles fabricated via different techniques are not exactly smooth on the molecular level. This provides the motivation to study the effect of the surface imperfection or disorder on the classical depletion force. Rough spheres have less overlapping volumes than smooth hard spheres and are therefore potential candidates to diminish the strong attractive force at contact. Examples of 'rough' particles include rough carbon black nanoparticles[37], nanoparticle-stabilized emulsions (Pickering emulsion)[38-40], and raspberry-shaped colloids[41-43].

The above discussion motivates our present theoretical work which is aimed at systematically exploring how regular surface roughness modifies the pure entropic packing problem underlying depletion phenomena. The problem is subtle and rich due to the presence of multiple excess entropy contributions which compete and can vary widely (even in sign) depending on length scales. Figure 4.1 shows the model we study - regularly surface corrugated colloids dissolved in "monomer" (or nanoparticle) suspensions and polymer melts. Beyond the

translational and packing entropic effects present for smooth hard spheres, for such structured colloids (or "raspberry" particles) the presence of surface crevices introduces new physical considerations associated with placement entropy (matrix particles exploring the crevices), changes (frustration) of fluid packing in the confined crevice space, and possible non-additive effects associated with the overlap of crevices on two colloids close in space. Per Figure 4.1, the corrugated systems are characterized by two dimensionless length scales, D/σ and σ/d. For a minimalist model of a polymer liquid, two additional length scale ratios enter (in units of the monomer diameter), R_g/d and l/d, where R_g is the polymer radius of gyration and l the chain persistence length. Our goal is to study all these realizations with a single theoretical approach.

There are rather limited prior theoretical and simulation studies of entropic depletion for colloids with non-smooth surfaces. Kostoglou and Karabelas[44] calculated the effective potential between two rough surfaces by considering the surface topography to be sinusoidal with a specific amplitude and wavelength. Others[45-47] have computed the interaction force between a rough spherical particle and a smooth flat surface but the focus was on how roughness reduces van der Waals attraction. Our interest differs from these studies in that we focus on dense nanoparticle matrix fluids and polymer melts. For such systems, simulation is extremely difficult because of long equilibration times or very low acceptance probabilities due to the high total packing fraction, large size asymmetry between monomers and fillers, and/or polymer connectivity constraints. We thus adopt well-established integral equation theory (IET) methods. However, using IET to treat the entire problem is also difficult computationally, and for asymmetric systems as in Fig. 4.1 numerical solutions are sometimes unattainable. Thus, for this reason, and given our desire to broadly explore the relevant parameter space, we adopt a coarse

grained hybrid approach. Specifically, Monte Carlo integration is employed to construct colloid-colloid and colloid-monomer effective potentials at the center-of-mass level, which are then used in IET to compute liquid structural correlations and miscibility limits. This hybrid approach has been successfully used recently in the very different context of statistical fractal aggregates dissolved in polymer melts[37].

4.2 Model and Effective Pair Potentials

Figure 4.1 shows the model studied. The rough colloids are characterized by a core diameter, D, and the diameter of densely packed spherical bumps is σ. A pair of such particles are dissolved in a monomer fluid of hard spheres of diameter d, or a liquid of flexible polymers of degree of polymerization N composed of these same monomers. Thus, depending upon the choice of the solvent, there are either 3 or 4 length scales, and hence 2 or 3 dimensionless ratios, that characterize the packing problem. In addition, the matrix fluid packing fraction η_t enters, which is taken to be a value representative of dense melts or concentrated solutions.

We first construct a coarse-grained model which removes the explicit surface bump degrees of freedom in the spirit of prior studies of soft colloids, e.g. many arm stars, crosslinked microgels, block copolymer micelles, and fractal aggregates[37, 48-52]. We determine the effective pair potentials that incorporate colloid roughness in an average manner. The well-established integral equation methods are employed to predict the equilibrium structure.

4.2.1 Particle Model and Effective Pair Potentials

The corrugated "raspberry" particle of Figure 4.1 is composed of N_b surface spherical interaction sites of diameter σ centered on, and densely covering, the core (diameter D) surface. The ratio D/σ characterizes the static corrugation, while the relative roughness perceived by a monomer of diameter d is quantified by the ratio σ/d. Due to geometrical constraints, there are only a limited set of options for D/σ such that the surface is densely covered[53]. We study here N_b = 72, 128, 282 and 650, corresponding to D/σ = 5, 7.8, 10 and 15, respectively[53]. Standard Monte Carlo integration is employed to determine the effective pair potential between the centers of two particles, $U_{nn}(r)$, and between a monomer and a rough particle, $U_{mn}(r)$, by fixing their center-to-center distance and averaging over all orientational degree of freedom. All elementary site-site potentials are pure hard core. The technical and computational details are identical to prior work for disordered fractal aggregates[37].

The nanoparticles can rotate and adopt different orientations characterized by two angles θ and φ. The conditional configurational partition function for two particles at fixed CM separation r is written as an integral over the two angles of rotations of each particle, where the energy is a function of these angles:

$$Z(r) = \frac{1}{(4\pi)^2} \int \sin\theta_1 \sin\theta_2 d\theta_1 d\varphi_1 d\theta_2 d\varphi_2 e^{-\beta E(r,\theta_1,\theta_2,\varphi_1,\varphi_2)} \tag{4.1}$$

which is computed using standard multi-dimensional integration methods akin to an elementary Monte Carlo integration:

$$Z(r) \cong \frac{1}{(4\pi)^2}\prod_{i=1}^{2}(\theta_{i,\max}-\theta_{i,\min})(\varphi_{i,\max}-\varphi_{i,\min}).\frac{1}{M}\sum_{n=1}^{M}\sin\theta_{1,n}\sin\theta_{2,n}e^{-\beta E(r,\theta_{1,n},\theta_{2n},\varphi_{1,n},\varphi_{2,n})}$$
$$= \frac{\pi^2}{4}\frac{1}{M}\sum_{n=1}^{M}\sin\theta_{1,n}\sin\theta_{2,n}e^{-\beta E(r,\theta_{1,n},\theta_{2n},\varphi_{1,n},\varphi_{2,n})} \quad (4.2)$$

where $(\theta_{1,n},\theta_{2,n},\varphi_{1,n},\varphi_{2,n})$ are uniform random numbers that fall in the permissible integral limits.

The probability to find two particles separated by a distance in the interval r and r+dr is $P(r) \propto 4\pi r^2 e^{-\beta U_{nn}(r)}dr \propto 4\pi r^2 Z(r)dr$ where $\beta U_{nn}(r)$ is the desired effective potential between the two corrugated particles. Exploiting the spherical symmetry in our model, the potential can then be written as:

$$U_{nn}(r) = -k_B T \ln Z(r)$$
$$= -k_B T \ln\left[\frac{\pi^2}{4}\frac{1}{M}\sum_{noc}\sin\theta_1\sin\theta_2\right] \quad (4.3)$$

where ‘‘noc” stands for ‘‘non-overlapping configurations’’. We use the following rule to define overlapping configurations: any part of particle 1 (core or bead) overlaps with any part of particle 2 (core or bead). Here the summation is equivalent to counting “noc” because $E=0$ for ‘noc’ and $E=\infty$ otherwise. The effective interaction between the rough particle and the monomer/solvent molecule $U_{mn}(r)$ is similarly computed using the same procedure as described above.

The main frame of Figure 4.2 presents the effective particle-monomer potentials for fixed core size D/σ at various bead-to-monomer ratios, σ/d. Their general functional form is a finite range, soft repulsion which depends on σ/d. The repulsion onset shifts to smaller

separations as the surface beads become larger relative to the monomers, and the potential shape approaches a bare hard-core interaction as the monomer size grows. Increasing the bead size relative to the monomer provides more interstitial space for monomers to explore without violating the non-overlap criterion, and thus the effective interactions become softer with increasing σ / d.

Figure 4.3 shows the particle-monomer pair potentials at two ratios $\sigma / d = 1$ and 4 for three core sizes. At a fixed σ / d, as D / σ grows from 5 to 10 the repulsion become less soft since the surface topography is smoother. From the cross potentials of Figs. 4.2 and 4.3, the distance of closest approach between the rough particle and monomer, r_c^{eff}, can be deduced. For a smooth hard sphere, this is trivially $r_c^{eff} = r_c = (D + d)/2$. For a rough sphere, its value reflects the degree to which a monomer can penetrate the particle surface layer. From the $U_{mn}(r)$ plots, we find that r_c^{eff} for $\sigma / d = 4$ is 10.515, 16.05 and 20.5d for $D / \sigma = 5$, 7.8 and 10, respectively.

The inset to Fig. 4.2 shows the particle-particle pair interactions for three core sizes. The effective interaction becomes zero when the two outer shells (an imaginary sphere enveloping the surface bumps) first touch. Then, as the two particles approach closer, the beads on one particle can explore to some degree the crevice of the other particle, and a soft repulsion grows. Eventually with decreasing inter-particle separation $U_{nn}(r)$ diverges.

4.2.2 Coarse-grained Model

We adopt a center-of-mass (CM) description where the surface bumps enter only via the effective potentials described above which are then employed in the relevant IET. For polymers, monomers are connected into chains using the same $U_{mn}(r)$ determined for the monomer fluid.

There are several reasons for adopting this coarse graining approach versus numerically using IET for colloids that explicitly retain the surface beads as distinct interaction sites. First, implementing the latter involves a minimum of six nonlinear integral equations which prior work[37, 43, 54] has found are very difficult to numerically solve, and sometimes it is impossible (no convergence) due to the high degree of interaction size and packing asymmetry. Second, the adoption of a reduced degree of freedom model is generalizable to even more complex colloidal particles.

Structural pair correlations thus follow from solving three integral equations for the pair correlation functions, $g_{ij}(r)$. In our notation, the subscript 'p' and 'm' denote a polymer and monomer site, respectively, while 'n' labels a rough nanoparticle. For the monomer fluid, we employ standard Ornstein-Zernike (OZ) theory[55, 56] with the Percus-Yevick (PY) closure for m-m and m-n correlations and the hypernetted chain (HNC) closure for n-n correlations[57]. Use of the latter has been shown to be successful for soft repulsive colloids and polymer nanocomposites[48, 58]. It also guarantees the positivity of the n-n pair correlation function which can becomes an issue in packing problems that have entropic dewetting aspects, as is relevant here. For polymer melts, we employ the Polymer Reference Interaction Site Model (PRISM) theory.

4.3 Monomer Solvent : Structural Correlations

Much of the new physics that emerge from excess packing entropy effects for rough colloids is present in the monomer liquid or small nanoparticle suspension (N=1) case. Thus, we first study

this system in detail in sections 4.3 (correlation functions) and 4.4 (miscibility limit). With this foundation, the consequences of polymer connectivity are established in section 4.5.

A key variable is the total matrix fluid packing fraction, η_t. Increase of the latter is known to enhance depletion for smooth particles. Our interest is dense polymer melts (including the monomer and oligomer regimes) and concentrated nanoparticle suspensions. Thus, we perform calculations for two values of packing fraction: 0.4 (melt) and 0.226 (concentrated solution). More generally, reducing packing fraction significantly weakens the local packing short range order in the suspending fluid, which is of interest to explore with regards to its consequences for depletion attraction between rough colloids.

4.3.1 Competing Entropic Effects

To place our new results for rough particles in context, we first recall basics of the problem for smooth particles. For both monomeric and polymer fluids, the depletion attraction strength at contact grows with increasing particle size as ~ D/d and also with increasing fluid packing fraction. The latter trend is deeply related to the origin of depletion attraction in dense melts which is optimization of excess packing entropy of the correlated matrix fluid. For polymers, contact depletion attraction monotonically and significantly grows with chain length due to conformation restrictions on packing, ultimately saturating for long enough chains.

To set the stage for physically interpreting our numerical results, we discuss the various competing excess entropic packing effects one expects due to the surface protrusions or roughness associated with the crevices (Fig. 4.1). The crevices present extra space for the matrix

particles to explore. Consequently, the gain in "free volume" of the depletants realized by clustering the larger particle is smaller relative to a smooth particle. This translational entropy argument implies that surface roughness can be harnessed to reduce depletion. The importance of this source of entropy obviously depends on the relative sizes of the surface bumps and fluid particles, and to some extent the particle core radius. If translational entropy was the only consideration, then increasing the surface bump size would monotonically improve miscibility. However, we shall show that interfacial roughness can enhance or inhibit depletion depending upon system variables. This indicates the presence of a competing entropic effect which is the matrix fluid packing in the crevices. The frustration of the ability of the fluid particles to layer in a bulk-like manner due to their confinement in the crevice can hinder dispersion. Additionally, close to the particle surface, the solvent particles perceive the colloid as a sterically 'patchy' surface composed of alternating hard bumps and relatively softer, solvent-filled crevices. The packing of the matrix particles near these two types of surface regions will be different and their manifestations for miscibility cannot be a priori guessed.

The three spatial regions of matrix packing near a rough particle surface discussed above are sketched in Fig. 4.1c to highlight the complexity of the packing problem relative to the smooth particle case. The packing frustration of the matrix particles in the curved and confined space of the crevices costs excess entropy relative to matrix particles remaining in the bulk. This can result in a type of "entropic de-wetting" which enhances depletion. Physically, we argue that the competition of favorable and unfavorable consequences of crevices raises the possibility of a non-monotonic dependence of entropy-driven clustering tendency on the relative length scale ratios. Trivial limits would seem to be when the matrix fluid particles are vanishingly small (a

continuum solvent limit) and the opposite case whence fluid particles for steric reasons do not "see" the crevices and the rough particle appears as effectively smooth. The above discussion is largely focused on the most elementary problem of how the matrix fluid packs around a single colloid. For the PMF question, the two rough particles are held at fixed (close) separation and the combined translational and crevice-related packing entropies may lead to subtle and unexpected non-monotonic excess entropy effects.

The rich competing physics in monomer fluids remains present in polymer melts, but the extra constraints of chain connectivity might be expected to result in stronger depletion attraction will increasing with N, as found for smooth hard spheres. This indeed is the qualitative trend we find below based on our numerical calculations. However, there are subtle aspects that emerge concerning precisely how chain connectivity impacts the favorable and unfavorable crevice entropy effects.

4.3.2 Monomer-Particle Interfacial Correlations

The statistical packing around an isolated particle is quantified by the monomer-particle cross correlation function, $g_{mn}(r)$. For a smooth hard sphere, it peaks at the distance of closest approach $r_c (=(D+d)/2)$ followed by oscillations on the monomer scale indicating layering. Figure 4.4 shows results for $D/\sigma = 10$ rough particles at $\eta_t = 0.4$(main) and 0.226 (inset). The effective distance of closest approach, r_c^{eff}, for each surface bead size can be read off from the corresponding monomer-particle pair potential discussed in section 4.2.1. When the monomer is larger than the bead ($\sigma/d = 0.5$), $g_{mn}(r)$ looks similar to that of a smooth hard sphere except

that the first peak occurs at an inter-surface separation of 0.125*d*. As the bead size is increased to $\sigma / d = 2$, the packing correlation becomes much more diffuse and the fluid locally dewets as indicated by the first peak of $g_{mn}(r)$ significantly shifting outwards, broadening, and decreasing in amplitude; there is a small hint of a non-zero value at contact ($r = r_c^{eff}$). As the surface beads become even larger, $g_{mn}(r)$ at contact increases, implying enhanced accessibility of the crevices to the monomers, and the non-contact first maximum decreases even further for $\sigma / d = 3$.Therefore, the primary $g_{mn}(r)$ peak (both contact and non-contact) changes non-monotonically with σ / d indicating that, in contrast to a smooth hard sphere with well-developed layering, for rough spheres the pure solvent packing entropy in the crevice ($r_c^{eff} \le r \le (D+\sigma)/2$) and beyond ($r > (D+\sigma)/2$) competes with free volume entropy in a complex manner .

The inset of Fig. 4.4 shows analogous results at the lower fluid packing fraction $\eta_t = 0.226$. Qualitatively, the subtle non-monotonic trends are still present But quantitatively the peak heights are lower, and again decrease with increasing σ / d .

Figure 4.5 compares the interfacial correlation functions of a smooth sphere with a rough sphere of $D/\sigma = 10$ for two surface bead sizes $\sigma / d = 0.5$ (main) and $\sigma / d = 7$ (inset). A hard sphere analogous to a raspberry particle of $\sigma / d = 0.5$ has a diameter of D/d=5, and its $g_{mn}(r)$ peaks at contact followed by monomer scale oscillations. The latter features remain for rough particles when the surface bumps are smaller than the monomers, at both fluid packing fractions (solid and dashed lines). However, the peak for the raspberry particle occurs at $r = (D+\sigma+d)/2$ which is greater than the effective closest distance of approach r_c^{eff} .

Effectively, the monomers which are larger than the surface beads "see" the particles as a smooth sphere of diameter $(D+\sigma)/2$ and do not probe the tiny crevices. Differences between $g_{mn}(r)$ of a smooth hard sphere and a rough particle of $\sigma/d=7$ are much starker (inset). The peak occurs at the distance of closest approach in both cases, but for the rough sphere, the peak height is significantly reduced due to the lack of accessible free space and monomer length scale oscillations beyond contact are totally absent. Here the combined packing entropy dominates over the excess free volume. The rough sphere $g_{mn}(r)$ also exhibits a correlation hole feature (local density less than bulk value) of spatial range ~ $\sigma/2$. At $r-r_c^{eff}=\sigma/2$, $g_{mn}(r)$ displays a small peak followed by very weak oscillations on the scale of density fluctuation correlation length of the bulk liquid. The non-zero contact value at r_c^{eff} indicates that the monomers do explore to a limited extent the surface corrugation. This effect is concomitant with the near-destruction of the monomer scale layering. Thus, rough particles introduce geometric packing frustration in the packing of the monomer fluid near its surface which is sensitive to crevice size relative to monomer diameter.

4.3.3 Inter-Particle Potential of Mean Force

A representative example of the PMF for smooth hard spheres in a fluid of $\eta_t=0.226$ is shown by the blue dotted curve on Figure 4.6a. Strong contact aggregation occurs, with well defined oscillatory features on the monomer size scale. The PMF minima $\beta W_{nn}^{\min}$ scale linearly with particle size D/d[11, 17] as indicated by the triangular points in the inset. The main frame of Figure 4.6a also shows the PMF between rough particles of $D/\sigma=10$ where the surface corrugation is less than or equal to monomer diameter, i.e. $\sigma/d\le 1$. When the monomer is twice

the bead diameter ($\sigma / d = 0.5$), the rough particle appears as a near-smooth hard sphere with an attraction well of -2.6k_BT at 1.091D that is quantitatively close to its smooth hard sphere analog; corrugation effects are still essentially absent. When $\sigma / d = 1$, the monomer effectively still perceives the rough particle as smooth but now with a larger diameter compared to the case of $\sigma / d = 0.5$, which explains the more attractive PMF.

Increasing the roughness to $\sigma / d > 1$, monomers begin to strongly sense the ordered surface topography as indicated by the PMFs in Fig. 4.6b. To maximize free volume, monomers now explore the crevices leading to a reduction of the depletion contact attraction when $\sigma / d \geq 2$. Remarkably, for $\sigma / d = 4$ the depletion attraction is completely destroyed leading to a purely repulsive PMF! This behavior is intimately related to the interfacial correlations in Fig. 4.4 where one sees that for $\sigma / d = 3$ the monomers pack in a much more disordered fashion around the particle. However, this effective repulsion does not persist with further increase of the corrugation. Rather, for $\sigma / d \geq 5$, we find that the PMF trend reverses again, and contact-like depetion attraction re-emerges and grows in depth as σ / d varies from 6 to 8. For such high bead-to-monomer ratios, this enhanced crevice accessibility is countered by the lack of bulk-like layering in the crevice as seen in the $g_{mn}(r)$ curves in the inset of Fig. 4.5. This effect of non-layering in the crevice presumably favors tighter interparticle contacts leading to more depletion attraction.

The PMFs in Figs. 4.6 discussed above are for a matrix fluid $\eta_t = 0.226$. The green dashed curve in Fig. 4.6b shows the corresponding PMF for $\sigma / d = 6$ if $\eta_t = 0.4$. Increasing η_t results in a very different PMF which is now weakly repulsive. This massive reduction of

depletion attraction is a consequence of the enhanced exploration of the crevices by monomers, as indicated in the pair correlation functions in Fig. 4.4.

The inset of Fig. 4.6a provides a clearer picture of the non-monotonic changes of the PMF with σ / d by plotting the attractive well depth as a function of σ / d for rough particles and versus D/d for the corresponding smooth hard spheres. The latter displays stronger attractions that grow linearly with particle diameter. In sharp contrast, the attractive strength of the raspberry particles is a doubly non-monotonic function of corrugation, first intensifying from $\sigma / d = 0.5$ to 1, then weakening up to $\sigma / d = 5$, and then reversing again. This complex behavior arises from the non-monotonic variation of the interfacial pair correlation function with σ / d.

Figure 4.7 shows the PMF for three core sizes at two different surface bead sizes. When the bead and monomer diameters are equal, increasing the core size results in a monotonically deepening of the attractive PMF akin to depletion in smooth hard sphere systems[5, 11, 17]. On the other hand, in the $\sigma / d = 5$ corrugated regime (inset), the trend is non-monotonic. Decreasing the bead size relative to the core implies an increase of D / σ and the particle appears smoother to the monomer. Therefore, as D / σ is decreases from 15 to 10, the attractive strength between the particles is reduced from -4.3k_BT to -0.41k_BT. One would expect that decreasing D / σ further would continue this trend. However, we find that the PMFs for $D / \sigma = 10$ and 7.8 are roughly the same, with very weak depletion attractions, but then becomes more attractive for $D / \sigma = 5$. This non-monotonic PMF variation occurs in the window $2 \le \sigma / d \le 10$ with effective attractions between the rough spheres minimized when $D / \sigma = 7.8$ or 10. The non-monotonicity for

$5 \le D/\sigma \le 10$ can be traced back to the behavior of the interfacial pair correlation function behavior where maximum penetration of solvent monomers into the crevices is predicted when $D/\sigma = 7.8$ or 10 depending upon the specific value of σ/d (not shown). Thus, the multiple competing entropies in the problem result in an optimum amount of roughness that maximizes particle dispersion.

The variation of the primary PMF attraction minimum as a function of core size, bead size and fluid packing fraction is summarized in Fig. 4.8. Per Fig. 4.6a, these minima for rough particles are a doubly non-monotonic function of bead size, and the dependence on core size depends on σ/d. At $\eta_t = 0.226$, in the classic depletion regime ($\sigma/d \le 1$), the PMF minima decrease with increasing D/σ, but it varies non-monotonically in the $\sigma > d$ corrugated regime. For $\sigma/d \ge 2$, the minima become more shallow upon increasing $D/\sigma = 5$ to 7.8, attain a minimum depth at either $D/\sigma = 7.8$ or 10, and then become more attractive again for $D/\sigma = 15$ (not shown). Thus, the PMF minimum is a non-monotonic function of both surface roughness and core size. For denser liquids ($\eta_t = 0.4$), the changes of the PMF minima depend on bead size. In the near-smooth particle limit ($\sigma/d \le 1$), increasing packing fraction leads to a more attractive PMF in a manner similar to smooth hard spheres (see inset). However, in the rough sphere regime for $D/\sigma = 5$ (dashed blue curve), increasing the fluid density weakens the PMF attraction, even resulting in a transition from an attractive to repulsive PMF in the window of $3 \le \sigma/d \le 7$. These variations of the PMF attraction depth are vastly different than the simple behavior predicted for smooth hard spheres in the inset of Fig. 4.8.

4.4 Monomer Solvent: Miscibility

We now present representative calculations of the particle second virial coefficient which determines the miscibility limit volume fraction under dilute conditions. Spinodal phase separation is controlled by the PMF. Thus, all the trends discussed in section 4.3 provide a physical basis for understanding the miscibility behavior discussed below.

Figure 4.9 shows the non-dimensionalized second virial coefficient at $\eta_t = 0.226$ (main frame) and 0.4 (inset). For a fixed core size of $D/\sigma < 10$ in the less dense solvent, the second virial coefficient initially decreases as the bead size grows from 0.5 to 1*d*. Beyond $\sigma/d = 1$, miscibility increases until $\sigma/d \approx 6$. The rough particles are completely miscible in the window of $2 \le \sigma/d \le 6$ where $\bar{B}_2$ is positive and nearly equal to the pure hard sphere value of unity. The virial coefficient also appears to be independent of the core-to-bead ratio in this window. For $\sigma/d > 6$, the miscibility trend reverses, and the virial coefficient becomes negative for the smaller core particle. For particles with a large core ($D/\sigma = 10$), the behavior is qualitatively similar but the miscibility window is wider since second virial coefficient becomes negative only for $\sigma/d > 8$.

Taken as a whole, the main frame of Fig. 4.9 establishes three regimes determined by the size of the bead relative to the monomer. (i) If $\sigma/d \le 1$, the monomer does not perceive the corrugation, and the smooth particle trend of increasing particle size enhancing depletion attraction occurs resulting in destabilization[11, 17, 59]. (ii) An intermediate regime, $2 \le \sigma/d \le 6$. Here, surface beads are large enough to allow monomers to explore particle crevices leading to enhanced stability or positive $\bar{B}_2$. (iii) Large asymmetry regime, $\sigma/d \ge 7$, where strong particle clustering re-emerges via a new mechanism that appears to be a subtle competition of opposing

effects. Here the large crevices are accessible to monomers, but beads on different particles can effectively inter-digitate (in an average statistical sense). Figure 4.9 also shows that the miscibility window after first widening as D/σ grows from 5 to 10, undergoes a dramatic narrowing for $D/\sigma = 15$. This non-monotonic variation of $\bar{B}_2$ with D/σ and σ/d is a subtle consequence of the particle PMF, which in turn is related to the spatial organization of the solvent around the rough particles, as discussed in section 4.3.

The inset of Fig. 4.9 shows analogous results in the denser $\eta_t = 0.4$ fluid. An increase of solvent density has opposing effects determined by the bead-to-monomer size ratio. When $\sigma/d \le 1$(off scale), the second virial coefficient becomes exceedingly negative with $\bar{B}_2$ = -13, -60, -229 for $\sigma/d = 0.5$, and -214, -2039, -45361 for $\sigma/d = 1$, for the three core sizes of $D/\sigma = 5$, 7.8 and 10, respectively. This trend is in accordance with prior studies[5, 6, 11, 14, 15, 60]. On the other hand, increasing η_t from 0.226 to 0.4 necessarily leads to more solvent particles in the crevices, which provides a more repulsive contribution to the PMF that explains the predicted widening of the miscibility window when $\sigma/d = 10$ for $D/\sigma = 7.8$ and 10.

The virial spinodal volume fractions of the rough ($D/\sigma = 5$) and smooth particles are reported in Table 4.1 at the two liquid packing fractions. Our virial-level estimates are expected to be reliable only up to $\Phi_c \approx 0.2 - 0.25$. At lower fluid density, total dispersion ($\bar{B}_2 > 0$) of the rough particles is predicted if $\sigma/d \le 6$, after which miscibility drops. For the analogous smooth spheres, complete miscibility is observed only until $D/d \le 5$. Upon further increase of particle size, we find that miscibility decreases. Interestingly, in contrast to smooth hard spheres, the

effect of the total packing fraction on the rough sphere systems depends upon their surface topography. When the bead size is small compared to the monomer, i.e., the depletion-like regime, one sees from the Table 4.1 that increasing fluid density decreases the spinodal volume fraction. Contrary to this smooth hard sphere like behavior, miscibility improves with increased packing fraction for the rough particles with sufficiently large bead-to-monomer diameter ratios. These trends are qualitatively similar for core sizes of D/σ = 7.8, 10 and 15 (not shown). Thus, we conclude that adding ordered roughness to the particle surface improves dispersion provided the corrugation scale is larger than the monomer diameter, $\sigma/d > 1$. Also, unlike conventional depletion for smooth particles, increasing the liquid density can impart more miscibility to the raspberry composites.

4.5 Polymer Melts

In this section we employ the identical iso-dimensionless-compressibility calibration method to mimic isobaric-isothermal melt conditions[11]. A realistic melt dimensionless compressibility of $S_0 \equiv S_{mm}(k=0) = 0.17$ is used, and the corresponding packing fractions for N=1, 10, 10^3, 10^4 and 10^5 are 0.226, 0.317, 0.4, 0.4355 and 0.4475, respectively.

Representative calculations of the second virial coefficient as a function of chain length are shown in Fig. 4.10 for $D/\sigma = 5$ and $2 \le \sigma/d \le 6$. The most obvious trend is that the rough particles become less dispersed as N increases. This is the expected conformational frustration effect whereby increasing chain length hinders the ability of polymers to penetrate the interstices of the particles and pack in an efficient manner. For a polymer as short as N=10, the window of

miscibility (or, positive $\bar{B}_2$) shrinks to $3 \le \sigma / d \le 5$ compared to the monomeric solvent where there is complete miscibility for $2 \le \sigma / d \le 6$. In the near hard sphere limit of $\sigma / d < 2$, the virial coefficients monotonically decrease with N and assume large negative values that lie outside the scale of the plot.

Figure 4.11 shows the effect of chain length when the bead size relative to the core is reduced to $D / \sigma = 10$. At a fixed σ / d, the second virial coefficient again decreases with N. Similarly as before, the window of miscibility narrows from $2 \le \sigma / d \le 8$ for N=1, to $4 \le \sigma / d \le 5$ for N=10^3. Strikingly, even for chains as long as N=10^4 ($R_g / d \approx 54.4$), there is one bead-to-monomer ratio $(\sigma / d = 4)$ for which total miscibility is predicted. This establishes the fundamentally local nature of the excess entropy effects that lead to this striking non-monotonic behavior.

We emphasize that all the qualitative trends discussed above persist without the iso-compressible calibration strategy (not shown). Quantitatively, upon repeating the above calculations at fixed $\eta_t = 0.4$ for all values of N, we find the virial coefficients again decrease with N but quantitatively more rapidly than the corresponding iso-compressible case.

Since the second virial coefficient is calculated from the particle PMF, it is instructive to examine how the latter changes with N. For a particle with $D / \sigma = 10$, the PMFs for N=1, 10, 100, 1000 are shown in Figure 4.12 at fixed $\sigma / d = 1$ (main) and 4 (inset). The $\sigma / d = 1$ result is in the depletion-like regime where the PMF minima decrease logarithmically with N[11]. The attractive minimum is followed by monomer scale oscillations indicating liquid layering. On the

other hand, the variation of the PMF with chain length at $\sigma / d = 4$ (inset) is very different. From Fig. 4.11, we know that this is the bead size at which the system is completely miscible for all chain lengths. In the solvent (N=1) limit, the PMF does not look much different from the bare particle potential, $U_{nn}(r)$, implying that no work or free energy penalty is required to bring the particles from infinitely far apart to a separation r. Increasing N from 1 to 100 results in the emergence of a weak barrier of spatial range roughly proportional to the polymer radius of gyration. Increasing the chain length further, a weak attractive minimum in the PMF emerges, followed by a long-ranged repulsive barrier. In contrast, the attractive component of the PMF of rough particles for $D / \sigma = 5$ and $\sigma / d = 4$ deepens monotonically with N (not shown) which leads to a monotonic decrease of $\bar{B}_2$ with chain length.

4.6 Summary

We have developed a hybrid Monte Carlo plus integral equation theory approach to study the interfacial packing correlations, potentials of mean force, and thermodynamic miscibility of rough raspberry particles dissolved in chemically-matched concentrated monomeric fluids and polymer melts controlled entirely by entropic considerations. Broadly, our results provide a basis for understanding, and potentially exploiting in materials applications, the subtle ability to counter entropic depletion attraction and phase separation by introducing surface roughness. Dramatic qualitative changes of the packing correlations are predicted relative to smooth hard spheres as a consequence of competing translational and crevice packing entropic effects. The changes in statistical spatial organization vary non-monotonically with the two dimensionless length scale ratios: surface bead to monomer diameter, and particle core to surface bead

diameter. Connecting monomers into chains results in large quantitative, but not qualitative, changes of trends, with depletion attraction always enhanced with growing chain length.

For certain windows of parameter space or length scale ratios, surface corrugation and excess free volume result in a favorable driving force for mixing which can effectively compete with the unfavorable depletion attraction, resulting in a major enhancement of nanoparticle dispersion, and even in complete miscibility and a repulsive PMF. Overall, miscibility as quantified by the second virial coefficient is a complex, non-monotonic function of the two dimensionless length scales ratios in monomer fluids, resulting in "miscibility windows" that optimize particle dispersion. Increasing the monomeric packing fraction from $\eta_t = 0.226$ to 0.4 diminishes the solubility in the depletion-like regime where particles tend to aggregate, but widens the miscibility window in the rough particle regime where monomers sense crevices.

To the best of our knowledge, this is the first systematic theoretical study of the role of nanoparticle static surface corrugation on packing correlations, potentials of mean force, and miscibility in the purely athermal entropic regime. We focused here on very dense liquid-like matrices, and nanoparticles that have close-packed and regularly arranged bumps. Lower surface coverage particles can be easily studied, and represents another knob to tune miscibility, effective interactions, and assembly. A natural extension of our work is to include surface fluctuation (coherent/incoherent fluctuation) of the beads, which is relevant to systems like intra-molecularly crosslinked polymer nanoparticles. Another direction is to break chemical symmetry and allow a local interfacial attraction between the surface beads and monomers. Finally, the ability to compute structural correlations for these rough particles can provide crucial input to

developing force-level theories for the slow dynamics and kinetic arrest in suspensions composed non-smooth surface particle suspensions.

4.7 References

(1) R. Tuinier, J. Rieger, C. G. de Kruif, *Advances in Colloid and Interface Science*, 2003, **103**, 1-31.

(2) L. M. Hall, A. Jayaraman and K. S. Schweizer, *Curr. Opin. Solid State Mater. Sci.*, 2010, **14**, 38-48.

(3) H. –X. Zhou, G. Rivas and A. P. Minton, *Annual Review of Biophysics*, 2008, **37**, 375-397.

(4) A. Syrbe, W. J. Bauer and H. Klostermeyer, *Int. Dairy Jour.*, 1998, **8**, 179-193.

(5) S. Asakura and F. Oosawa, *J. Chem. Phys*., 1954, **22**, 1255-1256.

(6) S. Asakura and F. Oosawa, *J. Polym.Sci*., 1958, **33**, 183-192.

(7) A. Vrij, *Pure Appl. Chem*., 1976, **48**, 471-483.

(8) J. F. Joanny, L. Leibler and P. G. deGennes, *J. Polym. Sci.,Polym. Phys*., 1979, **17**, 1073-1084.

(9) J. M. H. M. Scheutjens and G. J. Fleer, *Adv. Colloid Interface Sci*., 1982, **16**, 361-380.

(10) R. I. Feigin and D. H. Napper, *J. Colloid Interface Sci*., 1980, **75**, 525-541.

(11) D. Banerjee and K. S. Schweizer, *J. Chem. Phys.*, 2015, **142**, 214903.

(12) A. Trokhymchuk and D. Henderson, *Current Opinion in Colloid & Interface Science*, 2015, **20**, 32-38.

(13) A. L. Ogden and J. A. Lewis, *Langmuir*, 1996, **12**, 3413-3424.

(14) N. Patel and S. A. Egorov, *J. Chem. Phys*., 2004, **121**, 4987-4997.

(15) J. S. Smith, D. Bedrov and G. D. Smith, *Compos. Sci. Technol*., 2003, **63**, 1599-1605.

(16) A. A. Shvets and A. N. Semenov, *J. Chem. Phys*., 2013, **139**, 054905.

(17) J. B. Hooper and K. S. Schweizer, *Macromolecules*, 2005, **38**, 8858-8869.

(18) L. M. Hall, B. J. Anderson, C. F. Zukoski and K. S. Schweizer, *Macromolecules*, 2009, **42**, 8435-8442.

(19) B. J. Anderson and C. F. Zukoski, *Macromolecules*, 2008, **41**, 9326-9334.

(20) B. J. Anderson and C. F. Zukoski, *Macromolecules*, 2007, **40**, 5133-5140.

(21) S. K. Kumar, N. Jouault, B. Benicewicz and T. Neely, *Macromolecules*, 2013, **46**, 3199-3214.

(22) R. Hasegawa, Y. Aoki and M. Doi, *Macromolecules*, 1996, **29**, 6656-6662.

(23) A. Jayaraman and N. Nair, *Mol. Sim.*, 2012, **38**, 751-761.

(24) V. Ganesan and A. Jayaraman, *Soft Matter*, 2014, **10**, 13-38.

(25) L. M. Hall and K. S. Schweizer, *Macromolecules*, 2011, **44**, 3149-3160.

(26) D. Banerjee, M. D. Dadmun, B. Sumpter, K. S. Schweizer, *Macromolecules*, 2013, **46**, 8732-8743.

(27) D. Banerjee and K. S. Schweizer, *J. Polym. Sci. Part B: Polym. Phys*, 2015, DOI: 10.1002/polb.23752.

(28) S. –L. Teh, D. Linton, B. Sumpter and M. D. Dadmun, *Macromolecules*, 2011, **44**, 7737-7745.

(29) T. Martin, C. McKinney and A. Jayaraman, *Soft Matter*, 2013, **9**, 155-169.

(30) S. Badaire, C. Cottin-Bizonne, J. Woody, A. Yang and A. Stroock, *J. Am. Chem. Soc*, 2007, **129**, 40-41.

(31) S. Badaire, C. Cottin-Bizonne and A. Stroock, *Langmuir*, 2008, **24**, 11451-11463.

(32) K. Zhao and T. G. Mason, *Phys. Rev. Lett.*, 2008, **101**, 148301.

(33) K. Zhao and T. G. Mason, *Phys. Rev. Lett.*, 2007, **99**, 268301

(34) D. J. Kraft, R. Ni, F. Smallenburg, M. Hermes, K. Yoon, D. A. Weitz, A. van Blaaderen, J. Groenewold, M. Dijkstra and W. K. Kegel, *Proc. Natl. Acad. Sci.*, 2011, **109**, 10787-10792.

(35) E. Barry and Z. Dogic, *Proc. Natl. Acad. Sci.*, 2010, **107**, 10348-10353.

(36) L. Zhang and S. Granick, *Nano Lett.*, 2006, **6**, 694-698.

(37) R. Chakrabarti, J. –Y. Delannoy, M. Couty and K. S. Schweizer, *Soft Matter*, 2011, **7**, 5397-5407.

(38) R. F. A. Teixeira and S. A. F. Bon, *Adv. Polym. Sci.*, 2010, **233**, 19-52.

(39) J. W. J. de Folter, M. W. M. van Ruijven and K. P. Velikov, *Soft Matter*, 2012, **8**, 6807-6815.

(40) R. Aveyard, B. P. Binks and J. H. Clint, *Advances in Colloid and Interface Science*, 2003, **100**, 503-546

(41) Z. Qian, Z. Zhang, L. Song and H. Liu, *J. Mater. Chem.*, 2009, **19**, 1297-1304.

(42) E. C. Cho, Y. K. Hwang and U. Jeong, *Bull. Korean Chem. Soc.*, 2014, **35**, 1784-1788.

(43) S. Jiang, Q. Chen, M. Tripathy, E. Luijten, K. S. Schweizer and S. Granick, *Adv. Mat.*, 2010, **22**, 1060-1071.

(44) M. Kostoglou and A. J. Karabelas, *J. Colloid Interface Sci.*, 1995, **171**, 187-199.

(45) L. Suresh and J. Y. Walz, *J. Colloid Interface Sci.*, 1996, **183**, 199-213.

(46) M. A. Bevan and D. C. Prieve, *Langmuir*, 1999, **15**, 7925-7936.

(47) J. Czarnecki and T. Dabros, *J. Colloid Interface Sci.*, 1980, **78**, 25-30.

(48) J. Yang and K. S. Schweizer, *Europhys. Lett.*, 2010, **90**, 66001.

(49) W. R. Chen, F. Mallamace, C. J. Glinka, E. Fratini and S. H. Chen, *Phys. Rev. E: Stat. Phys.*, 2003, **68**, 041402.

(50) J. R. Seth, M. Cloitre and R. T. Bonnecaze, *J. Rheol.*, 2006, **50**, 353–376.

(51) F. Ozon, G. Petekidis and D. Vlassopoulos, *Ind. Eng. Chem. Res.*, 2006, **45**, 6946-6952.

(52) C. N. Likos, H. Lowen, M. Watzlawek, B. Abber, O. Jucknischke, J. Allgaier and D. Richter, *Phys. Rev. Lett.*, 1998, **80**, 4450-4453.

(53) R. H. Hardin, N. J. A. Sloane and W. D. Smith, Tables of spherical codes with icosahedral symmetry, published electronically at http://www.research.att.com/~njas/icosahedral.codes/.

(54) A. Jayaraman and K. S. Schweizer, *Macromolecules*, 2009, **42**, 8423-8434.

(55) L. S. Ornstein and F. Zernike, *Proc. Acad. Sci. Amsterdam*, 1917, **17**, 793-806.

(56) D. Chandler and H. C. Andersen, *J. Chem. Phys*. 1972, **57**, 1930-1937.

(57) J. P. Hansen and I. R. McDonald, *Theory of Simple Liquids* (Academic Press, London, 1986).

(58) H. Jacquin and L. Berthier, *Soft Matter*, 2010, **6**, 2970-2974.

(59) J. B. Hooper and K. S. Schweizer, *Macromolecules*, 2006, **39**, 5133-5142.

(60) A. Yethiraj, C. K. Hall and R. Dickman, *J. Colloid Interface Sci*., 1992, **151**, 102-117.

4.8 Figures

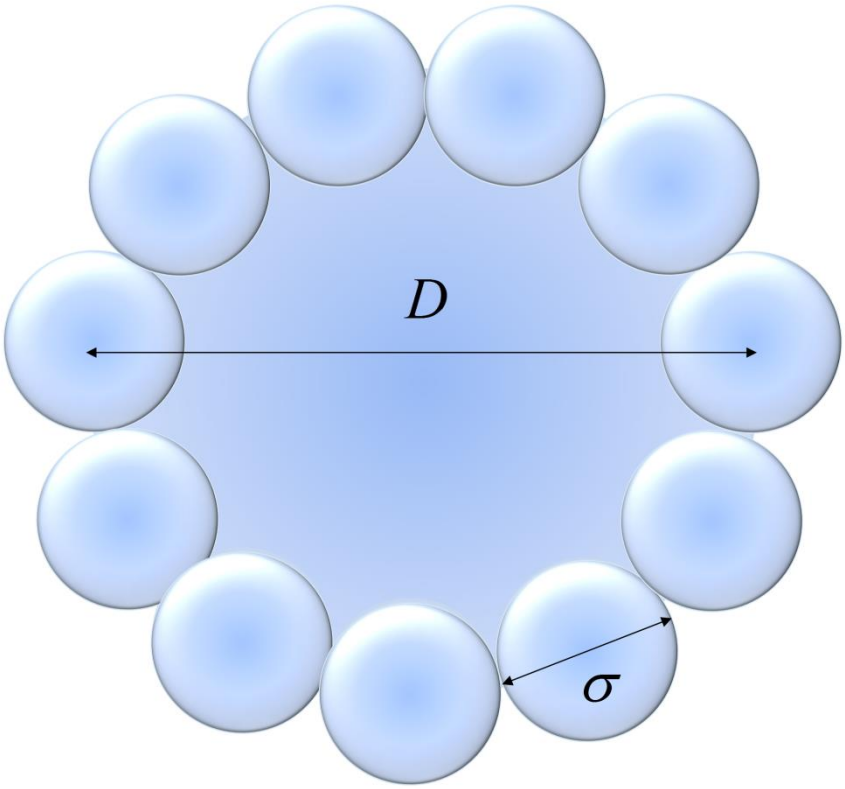

Figure 4.1a Schematic of the corrugated raspberry particle with a core diameter of D and bead (corrugation) diameter of σ.

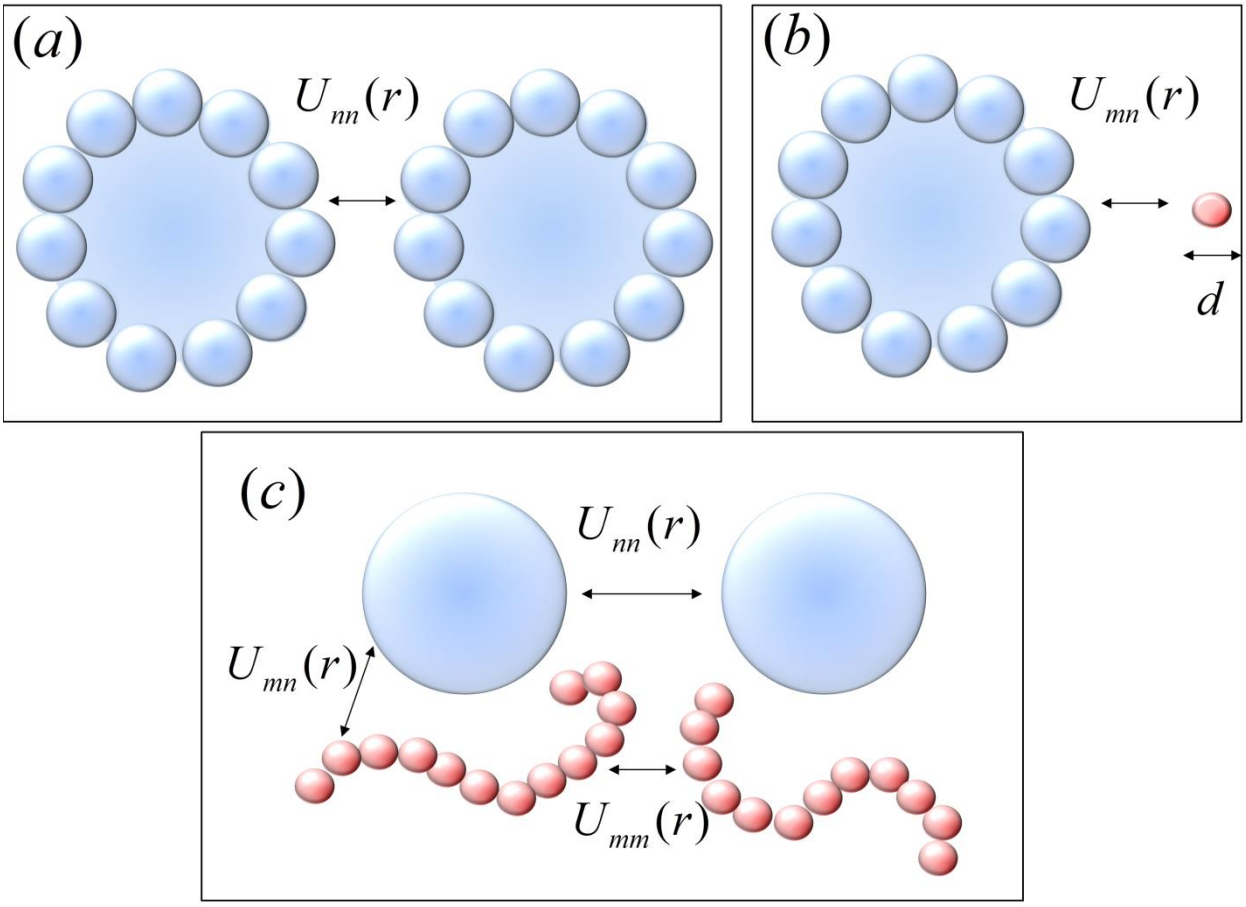

Figure 4.1b Schematic depicting the three step hybrid computational approach for raspberry particles in a polymer liquid. (a) CM level effective interaction between particles (b) CM level effective interaction between a particle and a monomer, and (c) the effective, coarse-grained two-component system.

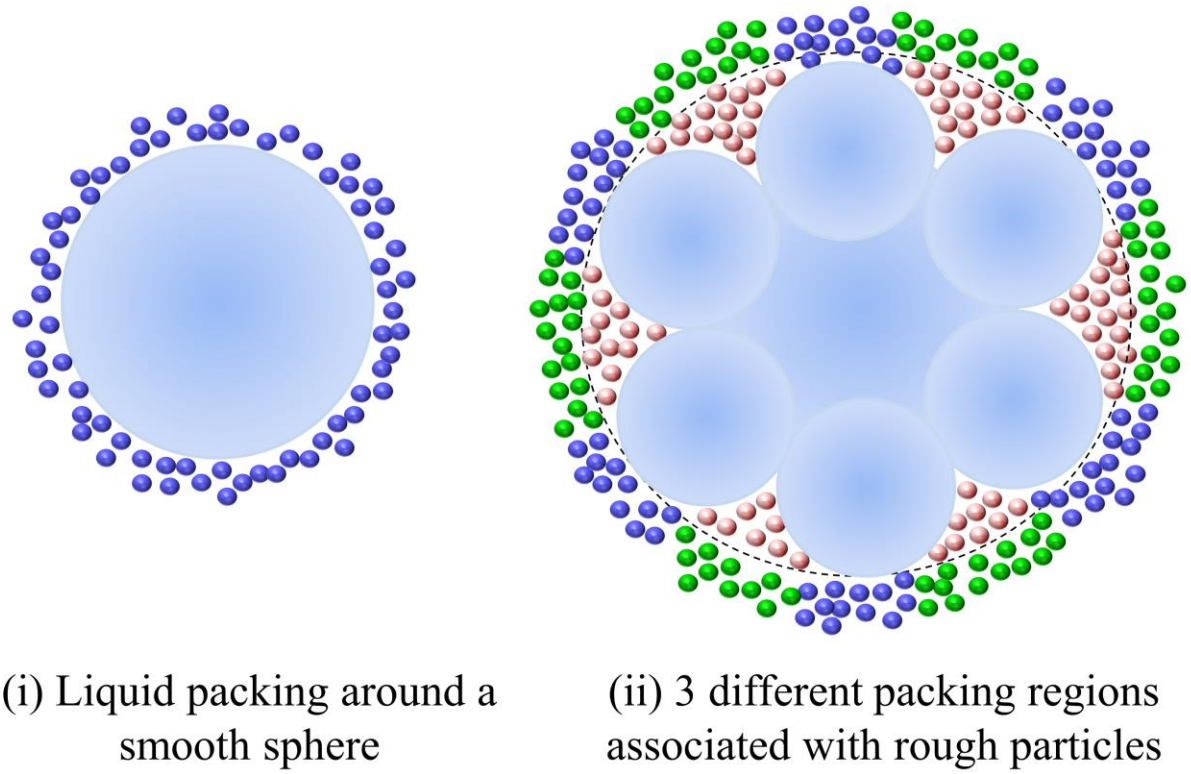

Figure 4.1c Schematic depicting distinct solvent packing states near a (i) smooth sphere and (ii) a rough particle. The red spheres represent the matrix particles that can explore the rough particle crevice. The blue and green spheres indicate fluid particles that feel the solid smooth bump and the softer solvent-filled interface, respectively.

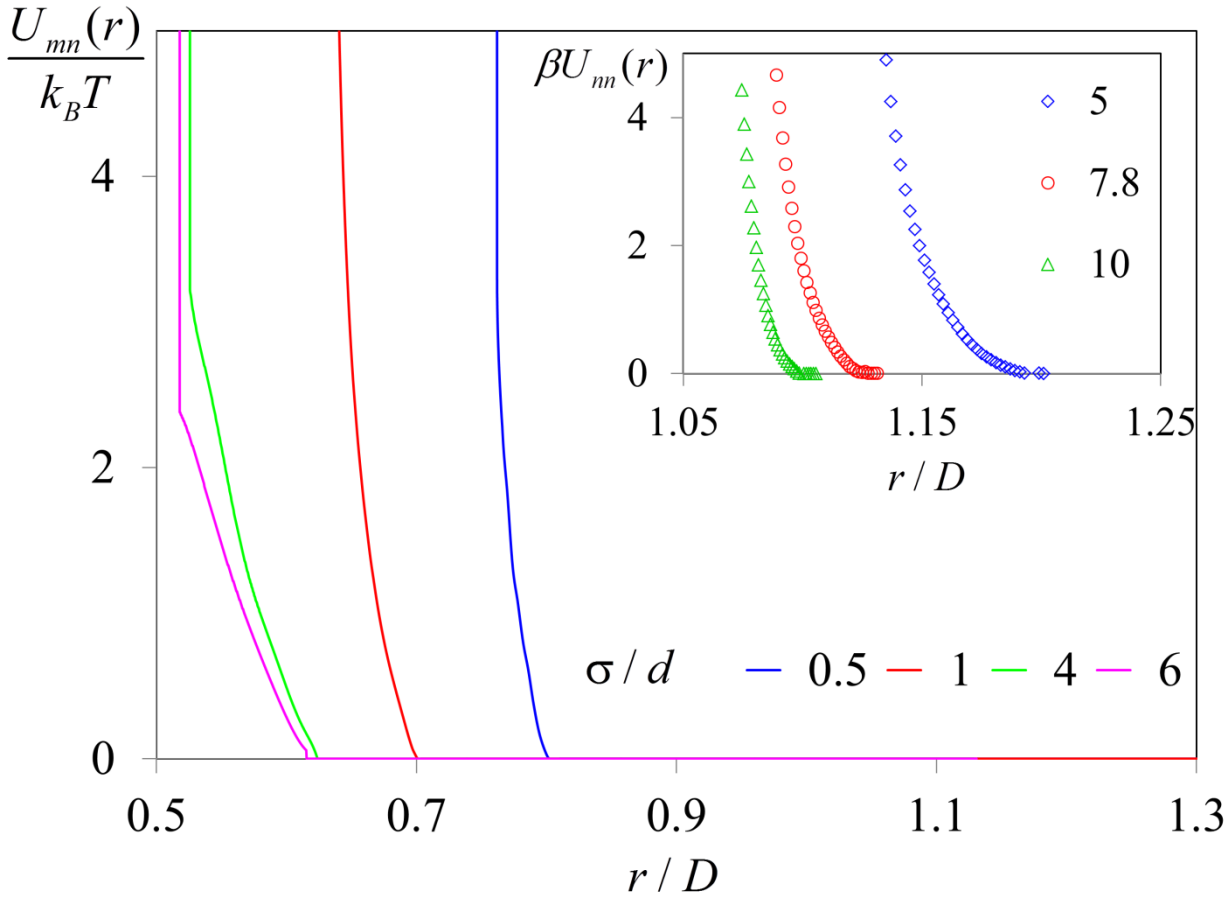

Figure 4.2 (Main) Effective interaction between a monomer and a rough particle for various bead sizes σ / d at a fixed core of $D / \sigma = 5$. (Inset) Effective interaction between two rough particles of core sizes $D / \sigma = 5$, 7.8 and 10.

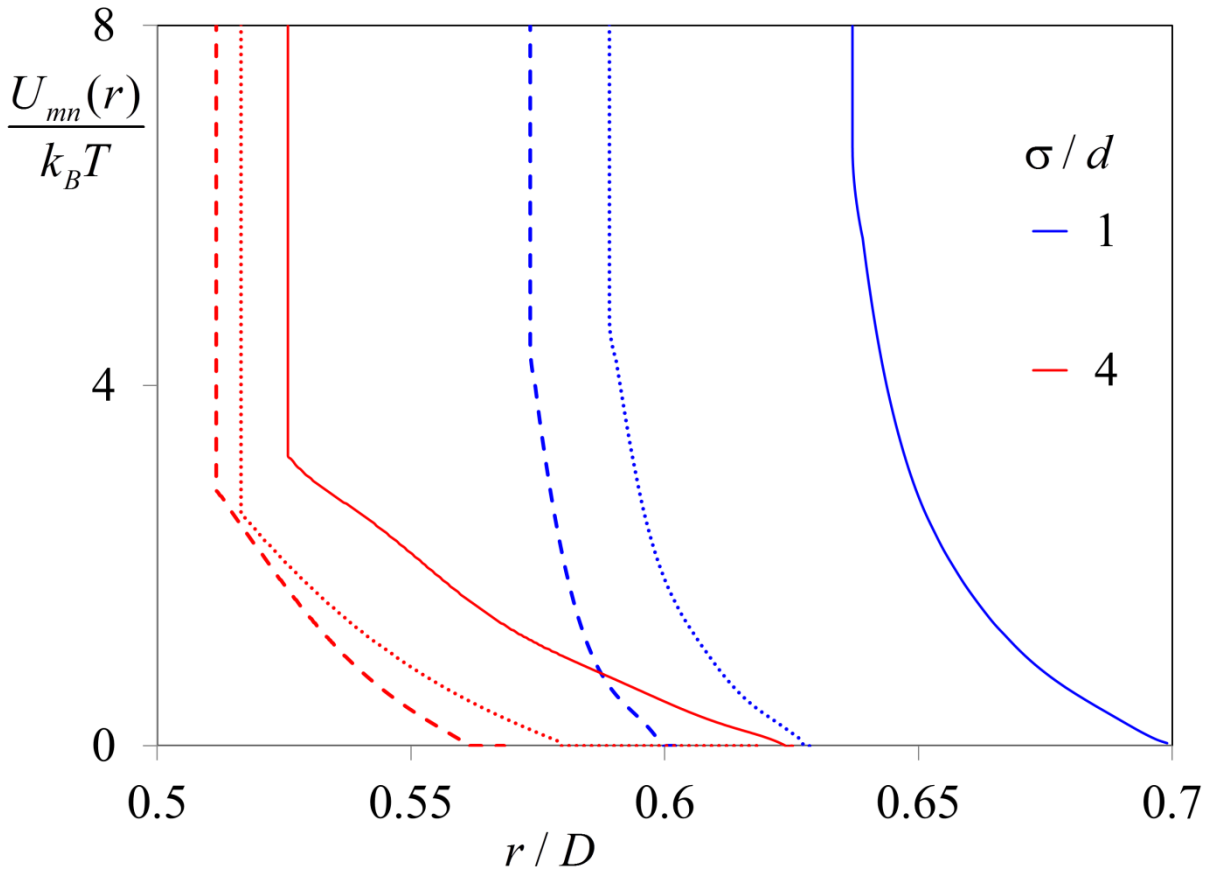

Figure 4.3 Effective interaction between a monomer and a rough particle of core size $D/\sigma = 5$ (solid), 7.8 (dotted) and 10 (dashed) at the indicated surface bead sizes.

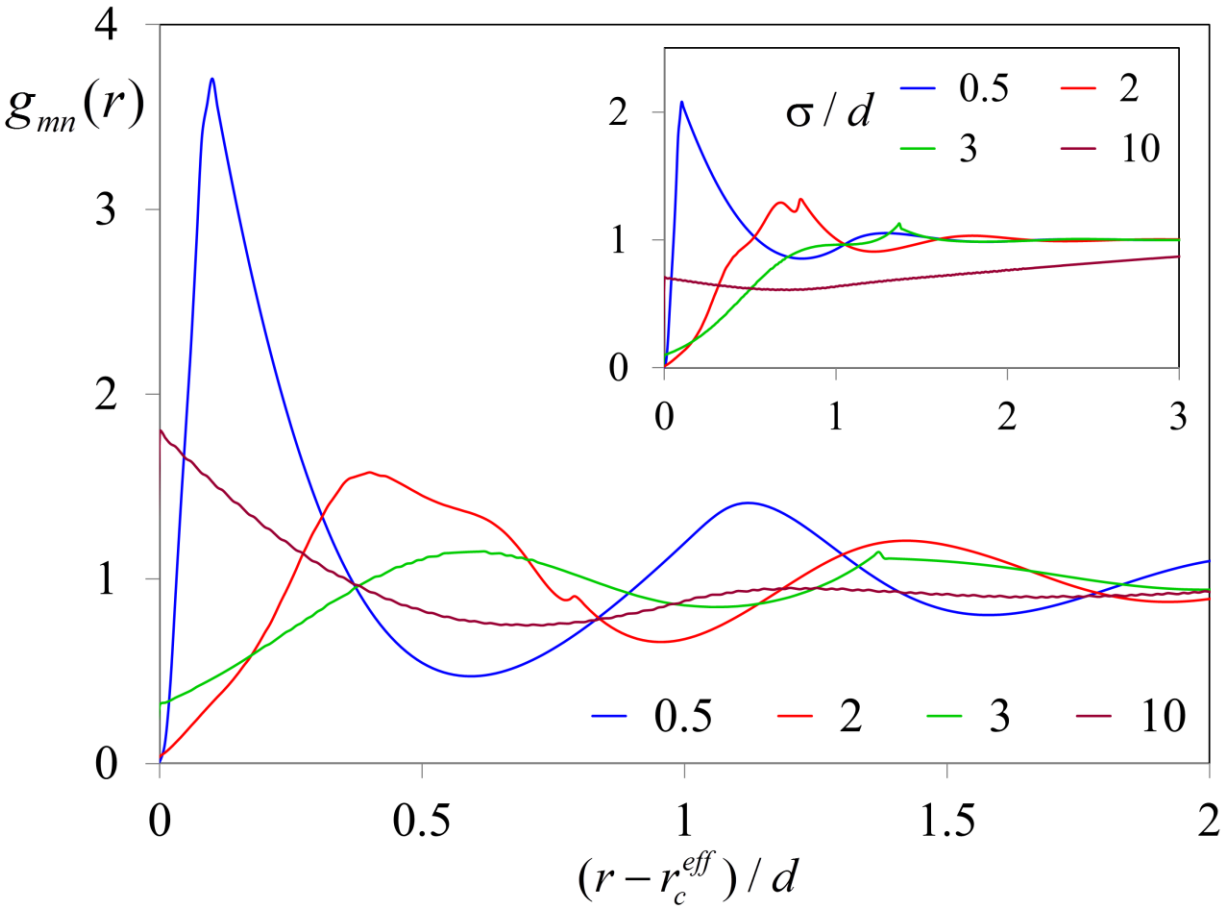

Figure 4.4 Cross correlation function for dilute rough particles of size $D/\sigma = 10$ in a monomeric solvent (N=1) of total packing fraction $\eta_t = 0.4$ (main) and 0.226 (inset). The axes labels for the inset are the same as the main plot.

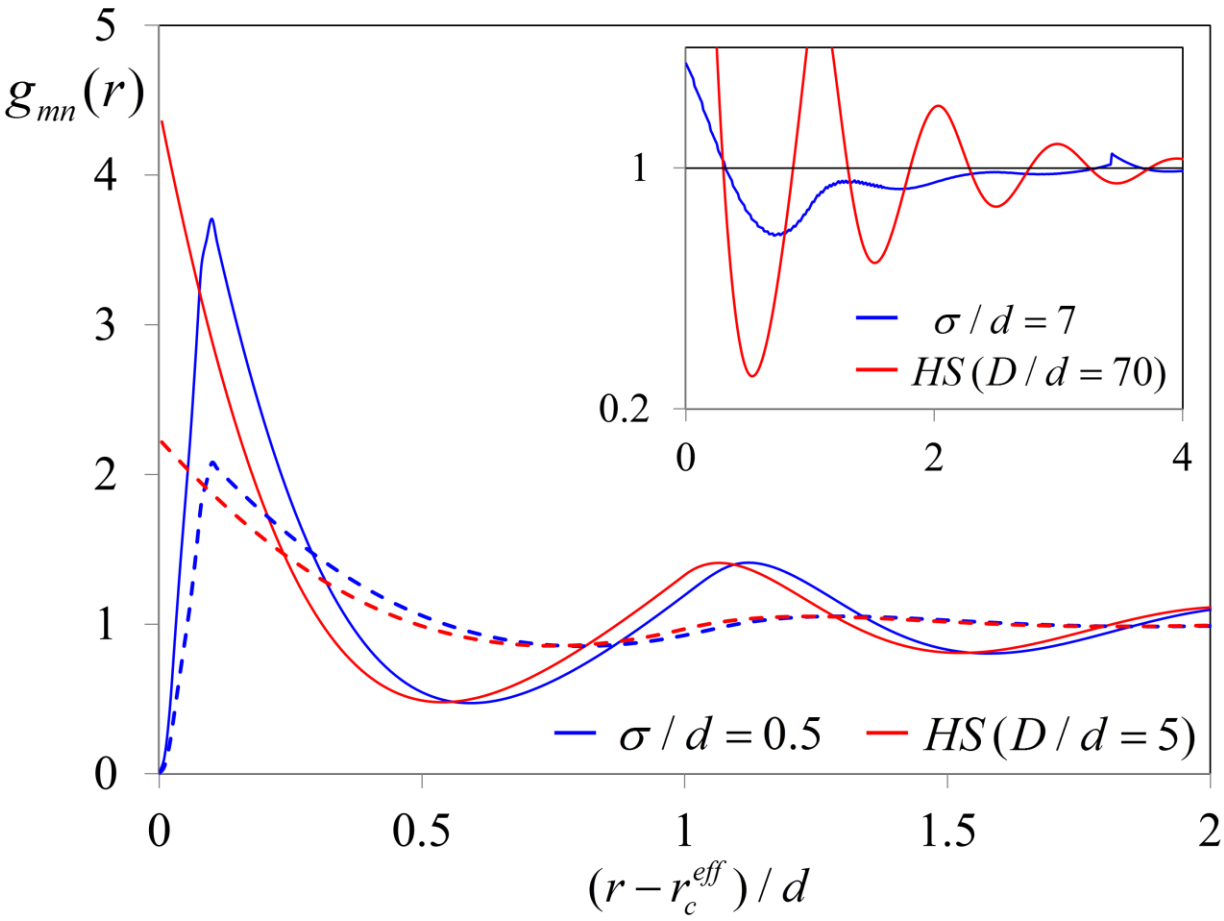

Figure 4.5 Cross correlation function for dilute rough particles of size $D/\sigma = 10$ in a monomeric solvent (N=1) of total packing fraction $\eta_t = 0.4$ (solid) and 0.226 (dotted) for bead sizes $\sigma / d = 0.5$ (main) and $\sigma / d = 7$ (inset) and their corresponding hard spheres. The peak value of $g_{mn}(r)$ for D/d=70 is 4.85. The axes labels for the inset are the same as the main plot.

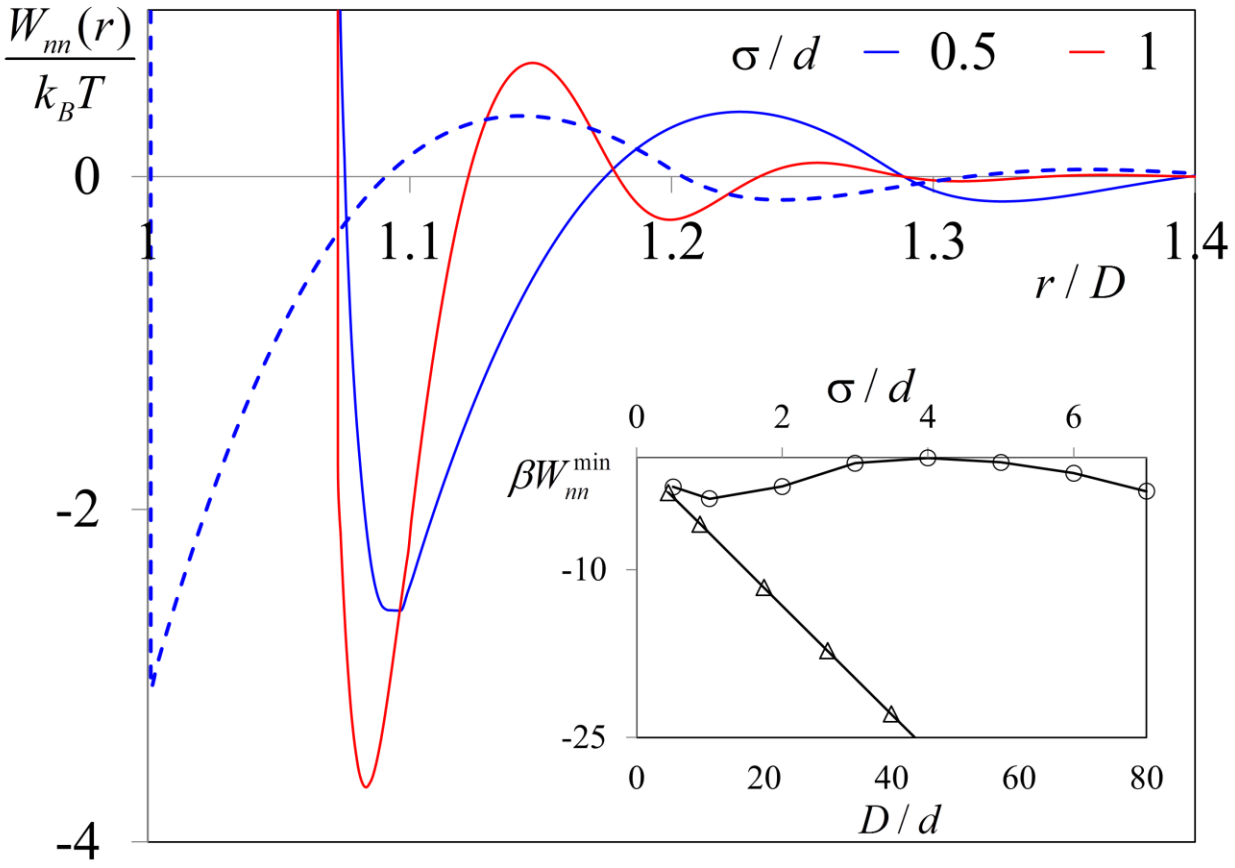

Figure 4.6a (Main) Potential of mean force between dilute rough spheres of size $D/\sigma = 10$ at the indicated surface bead sizes (less than the monomer diameter) in a monomeric solvent of total packing fraction $\eta_t = 0.226$. Dotted curve is the corresponding PMF of dilute hard spheres of size D/d=5. Inset shows the PMF minima of corrugated particles as a function of bead size σ/d (circles) and for smooth hard spheres as a function of particle diameter D/d (triangles).

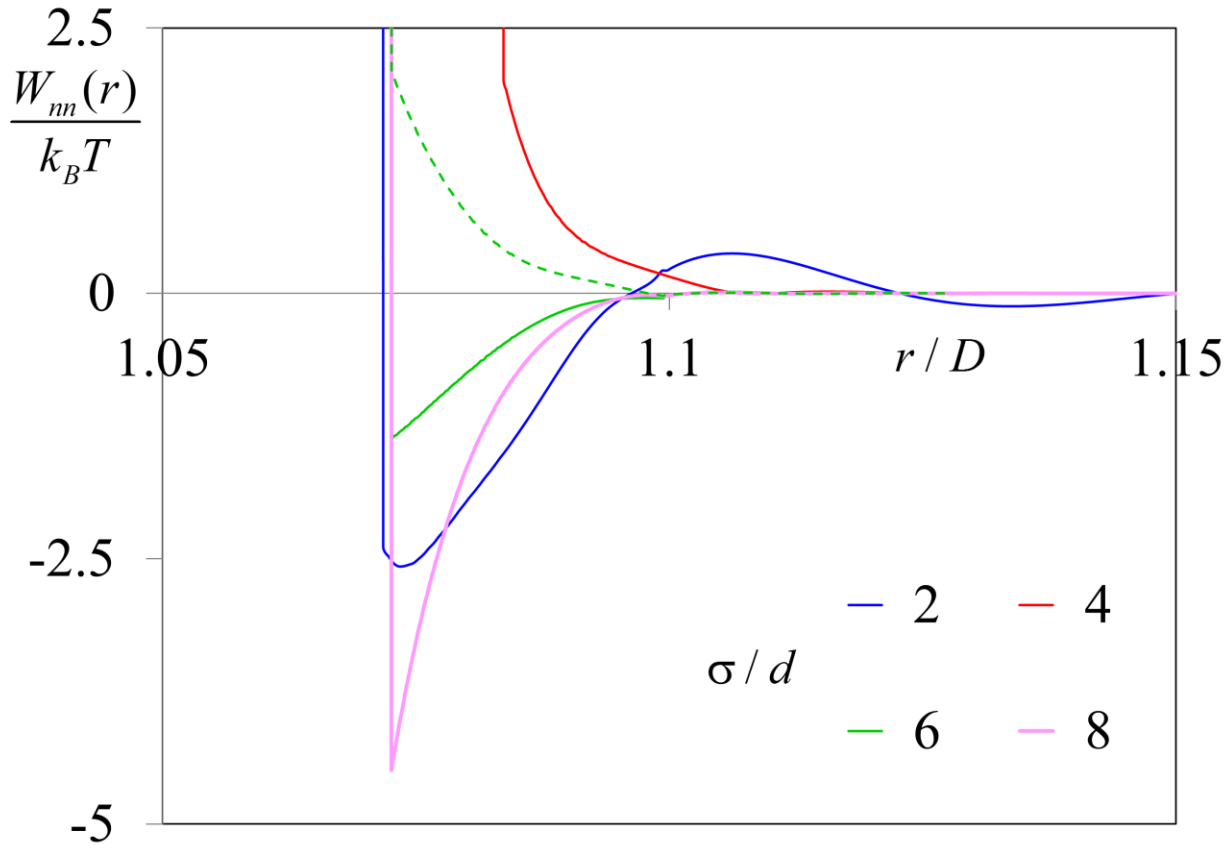

Figure 4.6b Potential of mean force between dilute rough spheres of size $D/\sigma = 10$ at the indicated surface bead sizes (greater than the monomer diameter) in a monomeric solvent of total packing fraction $\eta_t = 0.226$ (solid) and 0.4 (dashed).

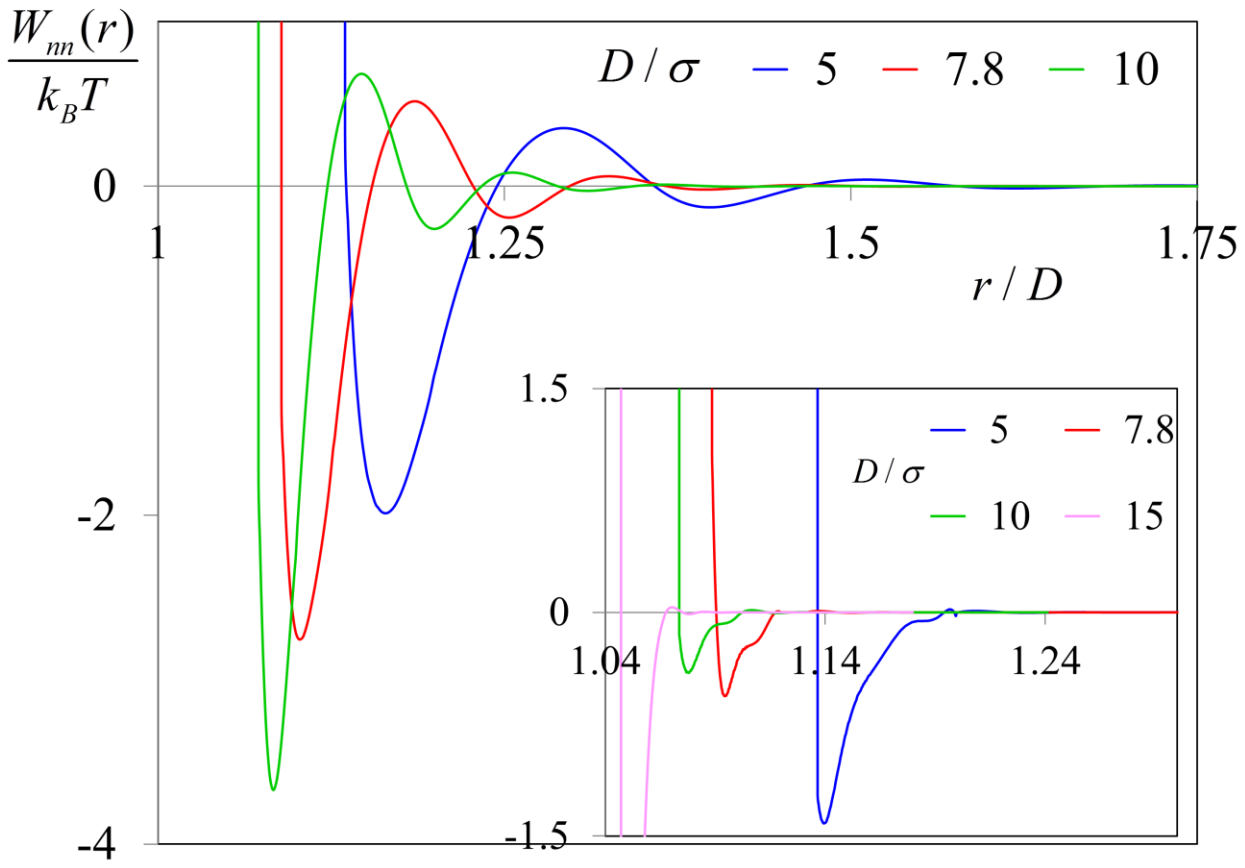

Figure 4.7 Potential of mean force between dilute rough spheres of surface bead size $\sigma/d=1$(main) and 5 (inset) at different core diameters in a monomeric solvent of total packing fraction $\eta_t=0.226$. The axes labels for the inset are the same as the main plot.

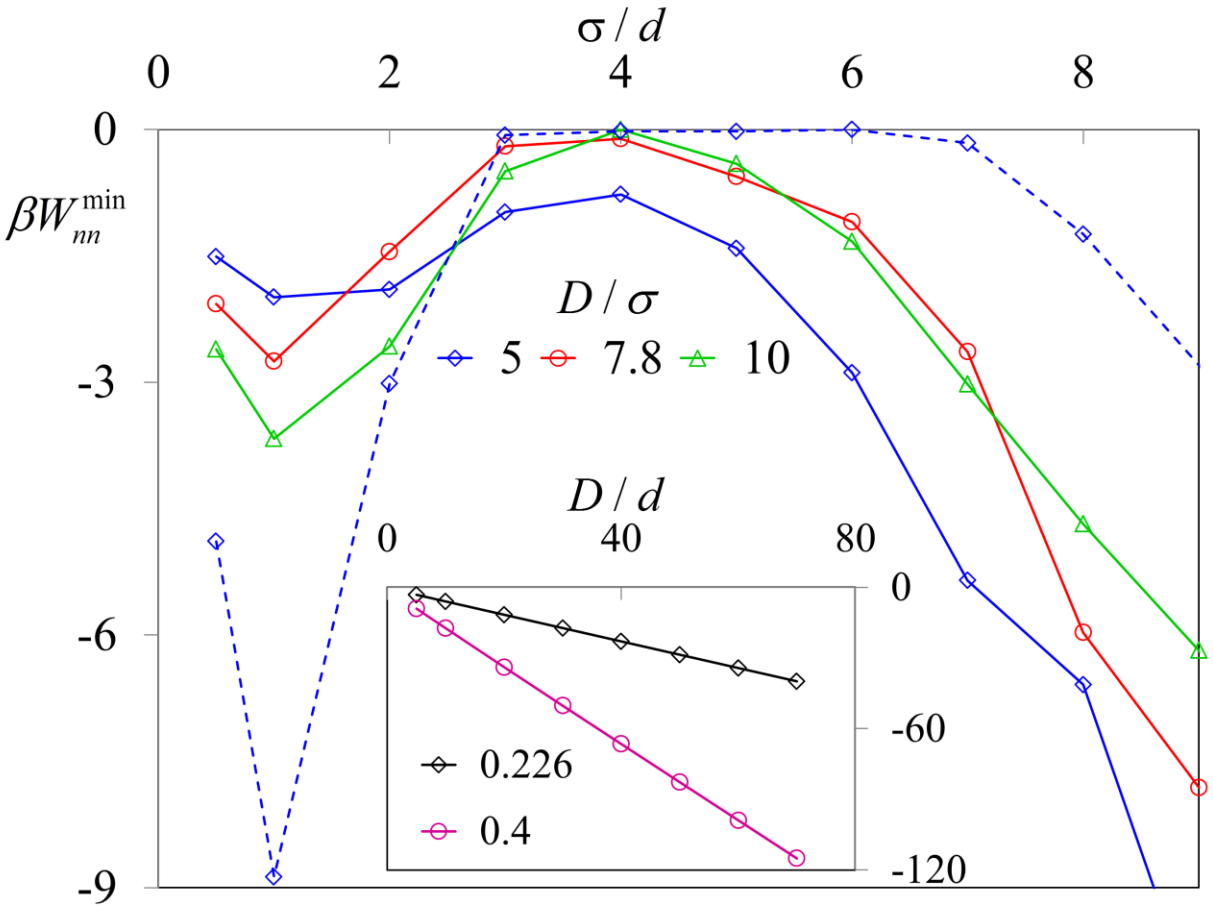

Figure 4.8 (Main) PMF minima (units of thermal energy) of corrugated particles as a function of bead size and different core diameters in a monomeric solvent of total packing fraction $\eta_t = 0.226$ (solid) and 0.4 (dashed). Inset shows PMF minima of smooth hard spheres at the indicated packing fractions. The axes labels for the inset are the same as the main plot.

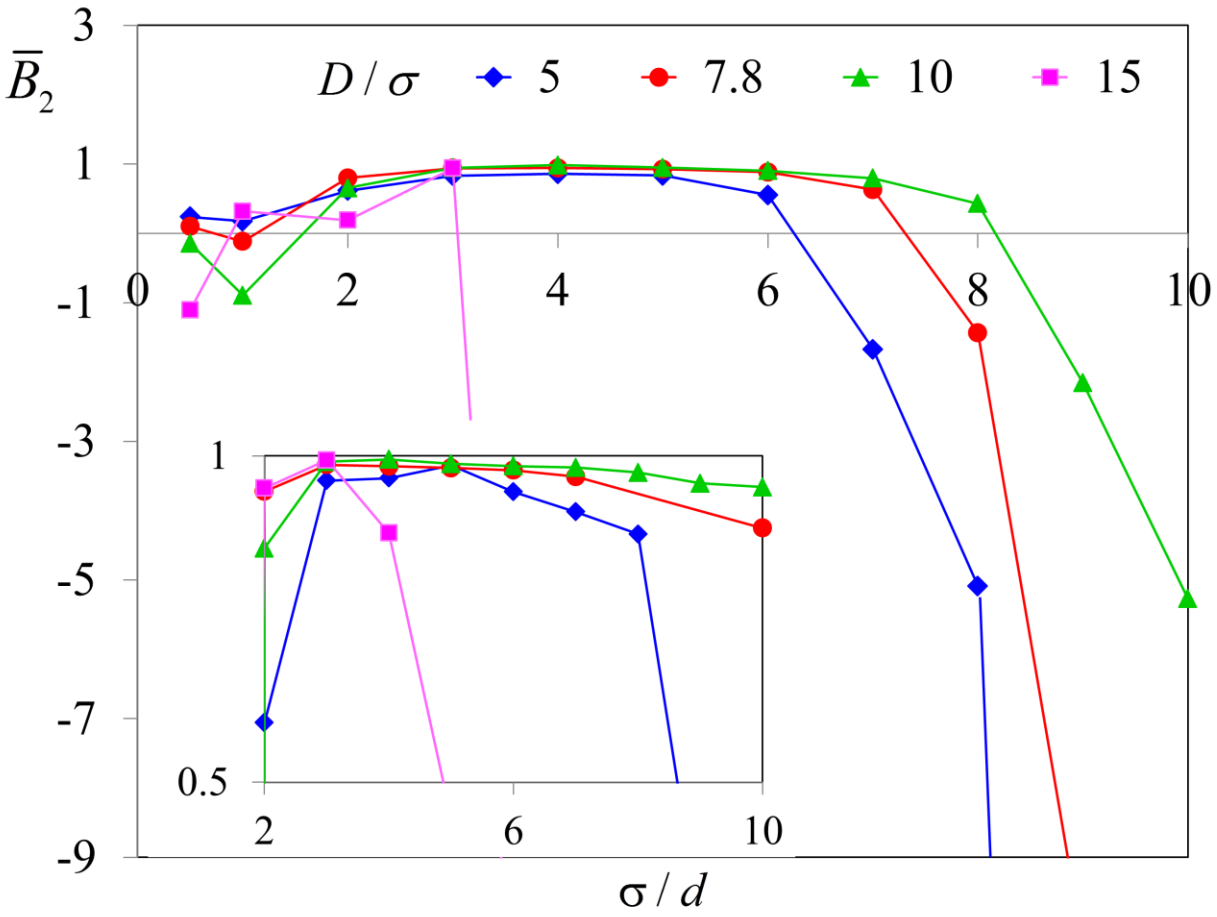

Figure 4.9 Normalized second virial coefficient for rough particles of different core sizes in a monomeric solvent (N=1) of total packing fraction $\eta_t = 0.226$ (main) and 0.4 (inset). The axes labels for the inset are the same as the main plot.

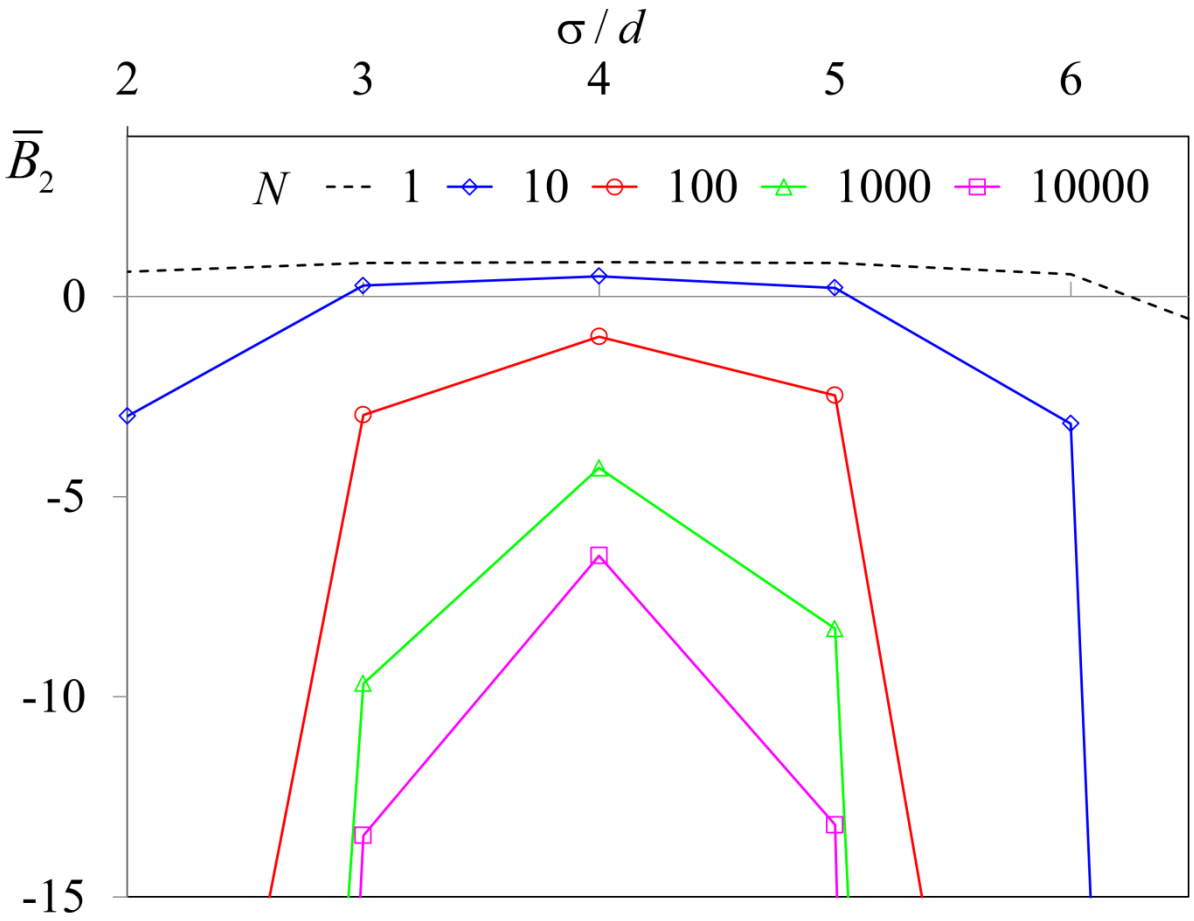

Figure 4.10 Normalized second virial coefficient for rough particles of size $D/\sigma = 5$ as a function of surface bead size in a polymer melt of various chain lengths and fixed $S_0 = 0.17$.

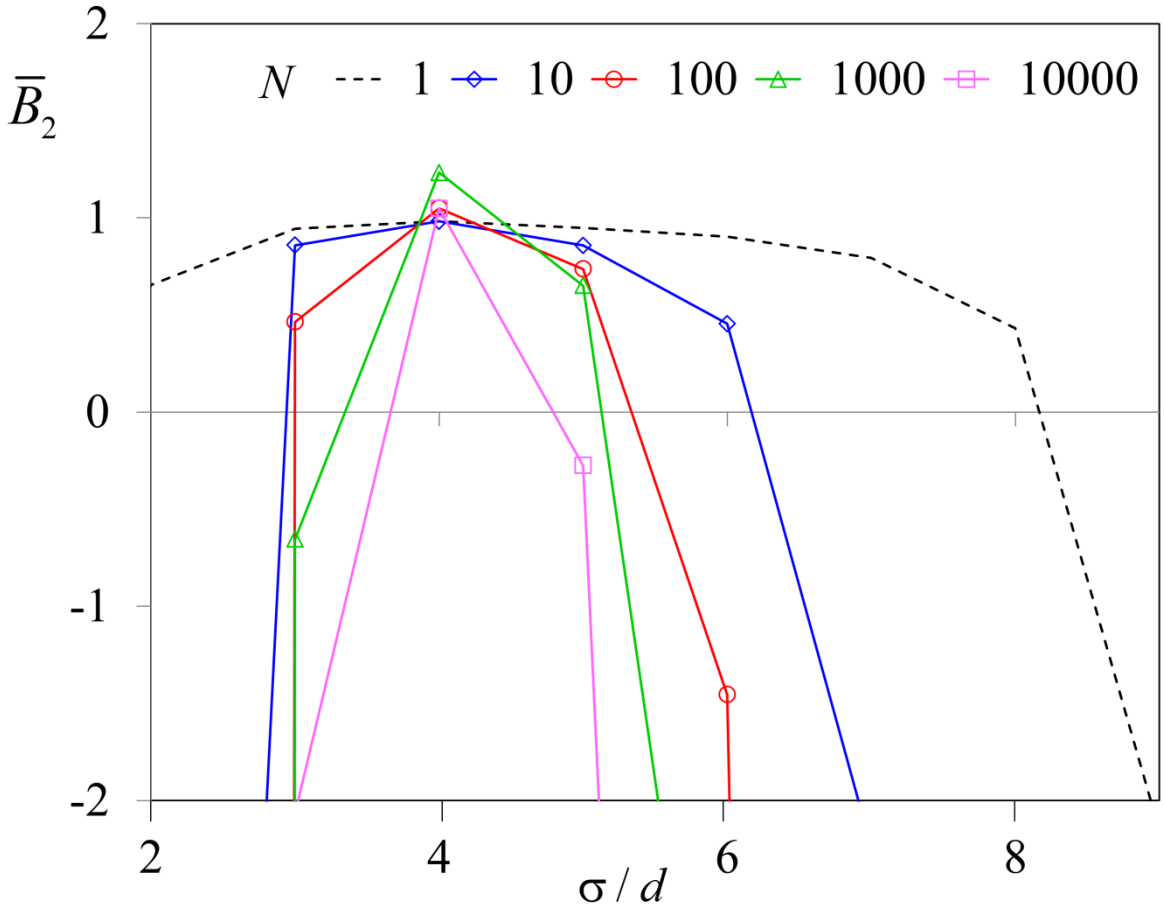

Figure 4.11 Analog of Fig. 4.10 for particles of size $D/\sigma = 10$.

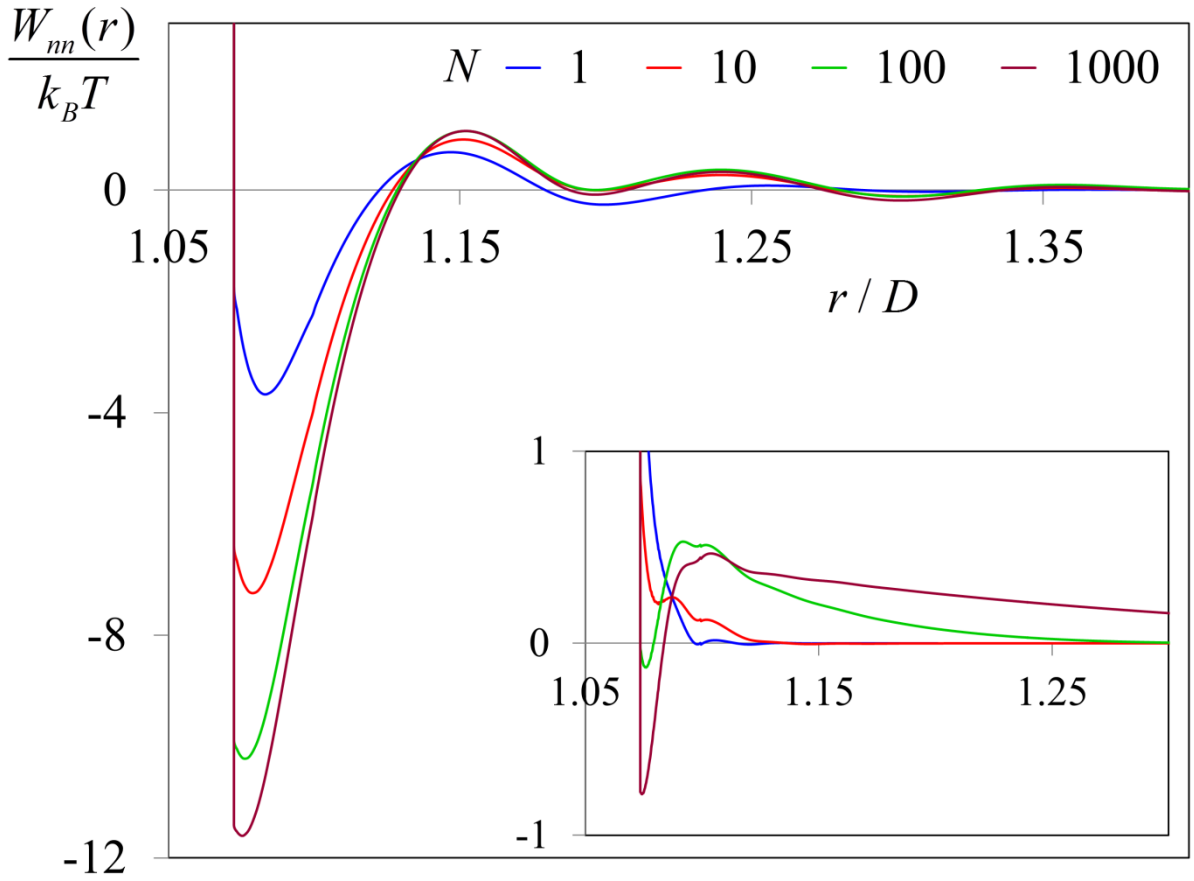

Figure 4.12 Potential of mean force between dilute rough spheres of size $D/\sigma = 10$ at surface bead size $\sigma/d = 1$(main) and 4 (inset) in a polymer melt of various chain lengths and fixed $S_0 = 0.17$. The axes labels for the inset are the same as the main plot.

D/σ	σ/d	D/d	Φ_c			
			$\eta_t = 0.226$		$\eta_t = 0.4$	
			Raspberry	HS	Raspberry	HS
5	0.5	2.5	Miscible	Miscible	0.024	0.059
	1	5			0.001	0.003
	2	10		0.12	Miscible	Immiscible
	3	15		0.013		
	4	20		0.001		
	5	25		Immiscible		
	6	30				
	7	35	0.33			
	8	40	0.11			

Table 4.1 Comparison of the rough and smooth sphere spinodal solubility limits Φ_c in solvents of packing fraction $\eta_t = 0.226$ and 0.4. Systems with solubility limit of < 10^{-4} are deemed immiscible while those with > 0.5 are assumed miscible.

CHAPTER 5

CONTROLLING EFFECTIVE INTERACTIONS AND SPATIAL DISPERSION OF NANOPARTICLES IN MULTIBLOCK COPOLYMER MELTS[1]

5.1 Introduction

In the context of polymer nanocomposites, a recent experimental discovery is that improved particle dispersion can be achieved by using chemically heterogeneous, amorphous copolymers[1]. Specifically, AB *random* copolymers (RCP) of intermediate composition, where the A and B monomers display different wettability with the particle, results in major improvement of the dispersion of fullerenes relative to both the corresponding pure homopolymers.

Beyond chemical heterogeneity in the RCP context, polymer architecture or monomer sequence offers an additional route of tuning effective interactions and controlling nanoparticle spatial organization. Periodically sequenced block copolymers are ubiquitous in natural biopolymers, but high synthetic control of the monomer sequence has proven to be difficult although recent progress[2-4] have opened up a new vista in biology and nanotechnology. Traditionally, nanoparticles of different sizes have been added to diblock copolymers that form

[1] This chapter is drawn in its entirety from a previous publication. Reprinted (adapted) with permission from D. Banerjee and K. S. Schweizer, J. Polym. Sci. Part B: Polym. Phys, **53**, 1098-1111. Copyright 2015 Wiley Periodicals, Inc., A Wiley Company.

well-defined microdomains in order to achieve unique structures and properties that depend upon the preferential segregation of the particles in one of the microdomains[5-8]. Most theoretical efforts in this area have focused on the order-disorder transition and crystalline BCP morphologies[9-11].

The goal of this article is to address a different problem that to the best of our knowledge has not been studied. Specifically, how do dense disordered liquids of MBCP's mediate effective interactions between nanoparticles of significant size as a function of differential and absolute wettability, particle versus monomer size ratio, and block length. We will show that multiple new physical behaviors emerge as the latter experimentally-relevant variables are changed which are *qualitatively* different than that found previously for tiny particles in RCP melts[12].

5.2 Multi-block Copolymer Model

For a *AB* copolymer based on the standard pre-averaging of chain end and junction effects[13], there are two types of chemically inequivalent sites, and hence three intramolecular probability distribution functions or partial structure factors, $\omega_{ij}(k)$. Each copolymer is an ordered sequence of alternating A and B blocks of equal length, R, corresponding to the fraction of *A* sites in a chain of f_A= 0.50, with *Q* blocks such that the chain degree of polymerization is $N = QR$. For example, a MBCP of R=2 implies a chain of A-A-B-B-A-A-B-B-… sequenced-monomers. Per prior work[14-17], the polymer is modeled as a freely-jointed-chain (FJC) of (unless stated otherwise) N = 100 segments where each site has a hard core diameter d and the chain

persistence length $l = 4d/3$, a typical value for flexible polymers[13]. The total packing fraction is fixed at a dense melt-like value of $\eta_t = 0.4$.

We consider composition symmetric MBCP melts of various block lengths of R = 1 (alternating copolymer), 5 and 10, which correspond to 100, 20 and 10 blocks, respectively (figure 5.1). The corresponding block contour lengths are 1*d*, 5*d* and 10*d* respectively. Previous work found that even longer blocks (fewer blocks Q) yield reduced stability in the pure melt[18, 19]. The corresponding $\omega_{ij}(k)$, are[20] :

$$\omega_{ii}(k) = \frac{1}{4}\sum_{\tau=1}^{Q-1}(Q-\tau)(1+(-1)^{\tau})\left(\frac{\sin(kl)}{kl}\right)^{R(\tau-1)}\sum_{i=0}^{R-1}\left(\frac{\sin(kl)}{kl}\right)^{i}\sum_{j=1}^{R}\left(\frac{\sin(kl)}{kl}\right)^{j} + \frac{1}{2}Q\left(R+2\sum_{i=0}^{R-1}(R-i)\left(\frac{\sin(kl)}{kl}\right)^{i}-2R\right) \tag{5.1}$$

$$\omega_{AB}(k) = \frac{1}{4}\sum_{\tau=1}^{Q-1}(Q-\tau)(1+(-1)^{\tau+1})\left(\frac{\sin(kl)}{kl}\right)^{R(\tau-1)}\sum_{i=0}^{R-1}\left(\frac{\sin(kl)}{kl}\right)^{i}\sum_{j=1}^{R}\left(\frac{\sin(kl)}{kl}\right)^{j} \tag{5.2}$$

Particle-particle and monomer-monomer pair potentials are taken as purely hard core. Thus, in the absence of nanoparticles, the copolymer is equivalent to an athermal homopolymer melt. This choice precludes the possibility of polymer microphase separation, thereby cleanly isolating the effects of the monomer-particle differential adsorption. All enthalpic effects then enter only via the effective polymer-particle site potential, modeled as hard core repulsion with an exponential attraction:

$$U_{jn}(r) = -\varepsilon_{jn}e^{-(r-r_c)/\alpha_{jn}}\ ,\ r > r_c \tag{5.3}$$

where j = A or B and $r_c = (D+d)/2$ is the closest distance of approach between the species j and a nanoparticle. The parameter ε_{jn} is the attraction strength between a monomer of type j and filler and quantifies the net effective change in energy when a monomer is transferred from the bulk melt to the surface of the nanoparticle.

Of course, for typical experimentally realizable polymers the interactions between the like and unlike monomers cannot be exactly the same. However, the "full" problem would involve at a minimum 6 different energy parameters, ε_{ij}, along with other dissimilar polymer chain structural parameters such as the persistence length and monomer diameter[12]. To render the large parameter space manageable, we study the consequences of differential polymer adsorption on nanoparticle organization based on a minimalist model which has been shown to successfully predict the miscibility of C_{60} in RCP melts[1] as discussed in chapter 6. In that work, the ranges of the interfacial attraction of A and B monomers are set equal, a simplification shown to be reliable as long as the absolute range is chosen to be representative of real systems[12]. This success is physically plausible when the A and B monomers are chemically quite similar but experience very different attractions with the nanoparticle. The simplified model may also be valid if the particle-monomer attraction strength is much larger than the differences in monomer-monomer interactions, and local clustering of A and B monomers is weak in the pure melt, as recently found for the C_{60}-RCP systems[1, 12].

The A-B interactions were set to zero on purpose to allow us to focus entirely on the consequences of differential nanoparticle surface segregation on nanoparticle dispersion and

miscibility without any interference of microdomain formation in the pure copolymer melt. We briefly study the influence of microdomain formation on our results in section 5.6.

5.3 Interfacial Correlations

This section presents representative calculations of the monomer-particle pair correlations in MBCP melts of different copolymer block lengths R in three different regimes, (D,B), (D,S) and (B,S), for distinct ranges of attractions and large (D/d = 10) and small (D/d = 1) particles. Two monomer-nanoparticle pair correlation functions, g_{An} and g_{Bn}, quantify how A and B monomers statistically organize and locally segregate around a particle in the copolymer melt. Calculations for D/d=10 hard spheres in a multiblock melt of $\beta\varepsilon_{An}$ = 0.1 and $\beta\varepsilon_{Bn}$ = 3 (D-B regime) and α_{pn} = 0.25d at different block lengths R are shown in Figure 5.2a. For any block length, the contact value is greater for the more strongly adsorbing B monomers, with peak heights that grow significantly from 14.8 to 20.8 with increasing R. The trend is opposite for the A monomers where, despite being dewetting, A monomers are still constrained to be close to the particle surface because of chain connectivity. The fact that the g_{An} contact values are much less than the corresponding g_{Bn} contact values (for R=10 less than unity) imply that A monomers are preferentially depleted from the immediate vicinity of the nanoparticles. One can quantify this proximal environment by calculating the number of nearest neighbors (i.e., number of A and B monomers) in the first solvation shell around the particle. The number of B-neighbors can be calculated from the cross pair correlation function g_{Bn} as:

$$N_B = 4\pi\rho_B \int_{r_c}^{r_{solv}} r^2 g_{Bn}(r) dr \tag{5.4}$$

where $\rho_B = \frac{6}{\pi d^3}\eta_t f_B = \frac{3}{\pi d^3}\eta_t$ is the bulk number density of the B monomers, r_c is the distance of closest approach between the particle and monomer, and r_{solv} is the location of the first minima in $g_{Bn}(r)$. The analogous value of N_A can be calculated similarly from g_{An}. For the parameters of Fig. 5.2a (D/d=10, $\beta\varepsilon_{An}$ = 0.1, $\beta\varepsilon_{Bn}$ = 3), B monomers in the first solvation shell comprise 60, 81 and 95 percent for R=1, 5 and 10, respectively. Therefore for R=1, there is nearly an equal mix of A and B monomers around the particle, while when R=10 an almost "pure" B-type environment exists in the immediate proximity of the particle. For all block lengths, as the monomer-particle surface separation increases beyond contact, the g_{An} and g_{Bn} curves cross, and then re-cross, after characteristic distances. This signifies that while B monomers are preferentially found near the surface, the block length R constrains the A monomers to necessarily be "close" to the sequence connected B monomers. The curve crossing separation grows with block length, occurring at 0.18, 0.38 and 1.4*d* for R = 1, 5 and 10, respectively, implying that a "purer" local environment of only B monomers extends farther from contact as R grows.

The analogous cross-correlation results for the two corresponding homopolymers with attraction strengths of $\beta\varepsilon_{pn}$ = 0.1 and 3 are plotted in the inset of Fig. 5.2a, which provide a "reference state" to understand the effect of multiblock architecture on the spatial correlations. The g_{pn} curves are qualitatively similar to the MBCP systems discussed above, but the contact

peaks in MBCP are quantitatively very different with peak heights now of 2.5 and 13.3, respectively. The latter value for the bridging case is much less than the corresponding g_{Bn} values of any of the MBCP systems studied, while the pure depletion contact value of 2.5 is only slightly greater than all the MBCP g_{An} peaks shown in Fig. 5.2a. These quantitative differences imply that the large differential adsorption of monomers in a MBCP results in the near dewetting of A monomers, effectively pushing the attractive B monomers closer to the particle surface relative to a bridging homopolymer.

Fig. 5.2b shows analogous results for very small particles of size D/d = 1. The g_{pn} trends are qualitatively similar as found in Fig. 5.2a for D/d =10, but both contact values are strongly reduced as a consequence of the much smaller nanoparticle surface area, and the crossing of the g_{An} and g_{Bn} profiles occurs at distances farther from the particle surface. The percentage of B monomers in the first solvation shell is 64, 92 and 100 for R=1, 5 and 10, respectively. Thus, achieving a "mixed" or "pure" environment in the immediate vicinity of the particles is a function of the size asymmetry ratio D/d and copolymer block length, R. The larger D/d is, the more "mixed" is the local environment around a particle. This trend will be shown to be important in understanding particle miscibility.

5.4 Nanoparticle Potential of Mean Force

We now study the MBCP mediated PMFs for the systems discussed in section 5.3 as a function of polymer-particle interactions ε_{pn} (in the regimes of D, S, B). Recall this quantity is determined

by how the polymer layering around an isolated particle is changed as two nanoparticles are brought to a surface-to-surface separation of h = r-D[14, 15].

5.4.1 Role of Chemical Heterogeneity

Figure 5.3 shows the PMF between two hard spheres of size D/d = 10 in a MBCP melt where the A and B monomers are attracted to the particle with strengths $\beta\varepsilon_{An}$ = 0.1 and $\beta\varepsilon_{Bn}$ = 3 (i.e., D-B) and α_{pn} = 0.25d. The abundance of B monomers near the surface leads to a large repulsion (6 – 10k_BT) at contact followed by a bridging minimum at an interparticle surface separation of one monomer diameter. However, with increasing separation the usual monomer scale oscillations observed for a pure homopolymer bridging system in Chapter 2 (Fig. 2.2) are replaced by a large amplitude, broad repulsive barrier or shoulder that extends over several monomer diameters, the range of which is controlled by the block length. This long range repulsion arises from the difference in the layering tendencies of A and B monomers. From enthalpic considerations, the particles prefer to be surrounded by B monomers, while entropy favors spatially randomizing the 'dewetting' A monomers. However, the steric constraints of A-B block connectivity frustrate this packing state resulting in the repulsion at longer distances. Smaller block lengths MBCP's experience less adsorption of the sticky monomer, resulting in a shallower bridging minimum which completely vanishes for the R=1 alternating copolymer. Thus, for a R = 1 copolymer in the D-B regime, both the depletion aggregation and bridging minimum attraction features disappear resulting in an effective sterically-stabilized repulsive PMF.

A higher value of R also implies that the more sticky B monomers are followed in close spatial proximity by a larger number of 'nearly-dewetting' A-type monomers which intensifies both the range and amplitude of the longer range repulsive feature of the PMF. If the range of the barrier is defined as the distance at which the repulsion equals $1k_BT$, then we find that the range scales as the ratio of the block end-to-end distance, $\frac{\alpha(R_1)}{\alpha(R_2)} \approx \sqrt{\frac{R_1 - 1}{R_2 - 1}}$, for block lengths greater than unity. A direct correlation between the barrier height and block length is, however, not found, and the barrier heights are 3.4, 5.6 and 6.9 in thermal energy units for R = 1, 5 and 10, respectively. Physically, the attractive B monomers try to maximally cover the particle surface. Chain connectivity induces the R depleting A monomers to follow the adhesive B monomers, but the former do not spread spatially to allow the immediately-following attractive block to get closer to the particle surface and wet maximum area. The regions of aggregated dewetting A monomers give rise to the broad repulsive barriers in the PMF, thereby explaining the correlation of its range with the block radius of gyration. These features render the PMFs in the MBCP melt very different from those in homopolymer melts of $\beta\varepsilon_{pn}$ = 0.1 or 3. The dashed black curve in Fig. 5.3 further emphasizes this point by showing the PMF between the two particles in a hypothetical 'average' homopolymer melt of attraction strength $\varepsilon_{pn} = (\varepsilon_{An} + \varepsilon_{Bn})/2$. At separations less than $1d$, the average homopolymer PMF closely follows the R = 1 alternating copolymer curve. However, it bridges more strongly than the alternating polymer and at larger separations the repulsive barriers present for the MBCP systems vanish, and are replaced by weak monomer scale oscillations as expected for a homopolymer.

As a secondary trend in Figure 5.3, we note that for the R=10 multiblock copolymer the second barrier becomes higher than the first barrier. Qualitatively, this is a consequence of the simultaneous presence of strong bridging and a longer-ranged repulsive barrier in the copolymer-mediated PMF. We also note that the high barriers in MBCP melts of intermediate block lengths R = 5 and 10 might kinetically prevent particles from forming bridged complexes and frustrate equilibrium demixing.

When the attraction strengths of A and B monomers with the filler are $\beta\varepsilon_{An}$ = 1.5 and $\beta\varepsilon_{Bn}$ = 3 we find that the PMF is a competition between bridging and steric stabilization (B-S). A plot is not shown for this case since the PMFs are qualitatively the same as that found in the D-B regime (Fig. 5.3), albeit with modest quantitative differences. Specifically, the repulsive barrier is quantitatively reduced because the A monomers are now more wetting, the approximate relation between barrier range and block radius of gyration observed for the D-B case no longer accurately holds, and the barrier range for R=10 is ~10% smaller because the stabilizing A monomers, unlike the depleting ones, prefer to layer around the particles to cover maximum surface. The barrier heights for R = 5 and 10 are now reduced to 1.6 and 4.5, respectively, compared to 5.6 and 6.9 for the D-B system of Fig. 5.3.

When $\beta\varepsilon_{An}$ = 0.1 and $\beta\varepsilon_{Bn}$ = 1.5, the depleting A monomers compete with the steric stabilizing (or optimally adsorbing) B monomers (D-S regime) as shown in the inset of Figure 5.4. At short distances, the B monomers preferentially layer around the particles. The PMF at contact is very weak, in strong contrast with the corresponding homopolymers (Fig. 2.2). A broad repulsive barrier is again present, but is much weaker with a height ~1.5 - 2 k_BT. Contact

aggregation is slightly reduced, while the bridging minima deepen with increasing R. The presence of the weak bridging feature is surprising given the monomer energetics are in the D-S regime. Qualitatively unlike the D-B system the repulsive shoulder does not grow monotonically with block length given the barrier height for R=10 is less than that for R=5.

The main plot in Figure 5.4 establishes the role of attraction range on the PMF keeping all the parameters from the inset the same. When the range is increased from 0.25 to 0.5*d*, many (not all) of the features previously discussed above are magnified by roughly a factor of 2 or more. However, the attractive bridging minima at 1*d* for R=1 and 5 vanishes, while for R=10 it is reduced in depth from -1.66 to -1 kT. The physical reason is that by increasing block length, the copolymer can more effectively induce both steric stabilization and entropic depletion. Enhanced stabilization increases the contact repulsion of the PMF, and enhanced depletion results in a larger non-contact repulsive barrier. The reduction of the bridging-like minimum is a subtle consequence of these simultaneous and competing changes.

5.4.2 Role of particle radius of curvature

The calculations above were performed for D/d=10 (Figs 5.3 and 5.4) and D/d=5 (not shown but qualitatively identical to the D/d=10 results) where the particle surface is close to a flat wall on the most local scale of the monomer diameter and short melt density correlation length. To explore the role of particle size and surface area, the main panel of Figure 5.5 shows the PMF between two small hard spheres of D/d = 1 for $\beta\varepsilon_{An} = 0.1$ and $\beta\varepsilon_{Bn} = 3$ (D-B case). For each of the three block lengths shown, large and nearly equal contact and bridging minima are observed. A long-ranged attraction is present out to a distance of 2*d* for R=5 and 10, and an

extremely weak repulsive shoulder emerges beyond this separation for R ≥ 5. The average homopolymer curve in this case is also quite different compared to any of the MBCP results. The physical basis for these differences compared to the large particle case is suggested in Figure 5.6. Specifically, two small nanoparticles can come very close in space to increase the resulting surface area for the bridging B monomer adsorption. The polymer can then pack around the two particles held at contact. Increasing the block length allows polymers to effectively "wrap" around the particles even more strongly, thereby deepening the minima at contact and at a separation of 1*d*. However, this effect is expected to saturate when copolymers of longer block lengths are used because of the relative insensitivity of the small particles to the longer block lengths. This trend of increasing contact aggregation of particles with R is in *sharp contrast* to what we find for large particles (Fig. 5.3) of D/d ≥ 5 where increasing the block length enhances repulsion at contact and induces a strong and long-ranged repulsive barrier. Therefore, the particle size relative to the block length is a key factor in understanding the PMF of nanoparticles in a MBCP melt.

For $\beta\varepsilon_{An}$ = 0.1 and $\beta\varepsilon_{Bn}$ = 1.5 (D-S regime), the PMFs in the inset of Figure 5.5 indicate weak contact aggregation followed by weak attractive minima that extend to a distance of nearly 2*d* for the larger block lengths. Increasing the block length results in deeper attractions, which again is qualitatively opposite to what is found for the larger particle. Though not shown, this is a recurrent observation even in the B-S regime where $\beta\varepsilon_{An}$ = 1.5 and $\beta\varepsilon_{Bn}$ = 3.

5.5 Miscibility and Chain Length Effects

We now compute spinodal phase diagrams at the virial level which follows from Eqs (2.10) and (2.11) and the particle PMF. Figure 5.7 shows results in the representation of the critical particle volume fraction versus the A-monomer-particle attraction strength $\beta\varepsilon_{An}$, where $\beta\varepsilon_{Bn}$ is fixed at 1.5 and D/d=10. The inset (main frame) shows calculations for an attraction range α_{pn} = 0.25*d* (0.5d). As $\beta\varepsilon_{An}$ is varied widely from 0 to 5, our primary interest is the low $\beta\varepsilon_{An}$ (D-S) and high $\beta\varepsilon_{An}$ (B-S) regimes. The black dashed curve is the spinodal curve of the corresponding homopolymer nanocomposite as a function of polymer-particle interfacial attraction strength where now $\varepsilon_{An} \to \varepsilon_{pn}$.

The absence of any colored solid curves in the low $\beta\varepsilon_{An}$ range indicates that a MBCP of block lengths R = 1, 5 and 10 provides complete miscibility when one of the monomers is dewetting and the other is stabilizing. Thus, incorporating 50% steric stabilizing monomer dramatically improves dispersion and prevents phase separation that would otherwise be induced in a pure depleting homopolymer melt. The regime of high $\beta\varepsilon_{An}$ where bridging competes with steric stabilization leads to more complex trends that are a function of the MBCP block length and attraction range. For the shorter attraction range R = 5 system, the spinodal curve shifts to the right relative to the homopolymer, implying improved dispersion. In contrast, the longer R=10 block length system exhibits reduced miscibility relative to the homopolymer, although the presence of a large repulsive barrier for this system might kinetically prevent the particles from accessing the deep attractive bridging minimum in the PMF (see Fig 5.3). The R=1 alternating copolymer is conspicuous by the absence of a spinodal curve implying *no phase separation* for

any $0 \le \beta\varepsilon_{An} \le 5$ provided $\beta\varepsilon_{Bn}$ = 1.5. However, it is important to remember that this is the virial calculation and applicable only for Φ_c < 0.2-0.25. Thus, for the attraction range α_{pn} = 0.25*d*, a MBCP of any block length $R \le 10$ provides more nanoparticle miscibility than a homopolymer in the D-S regime. In contrast, in the B-S regime, the block length determines whether nanoparticle dispersion is enhanced or reduced relative to the homopolymer, with R=5 showing improved miscibility, R=10 worse, and the alternating block copolymer maximum miscibility.

The phase behavior in the D-B regime (not shown) is qualitatively the same as in the B-S regime discussed above. Though perhaps surprising, it is expected based on the PMF calculations and conclusively demonstrates that adding 50% depleting monomers to a bridging system drastically improves miscibility compared to a homopolymer-based nanocomposite provided the block length is judiciously chosen.

Figure 5.7 also shows miscibility results for a random copolymer. Relative to the homopolymer, miscibility increases in the D-S region, but is reduced in the B-S regime. The differential wettability and chain connectivity constraints that results in improved miscibility for the MBCP has the opposite effect for a 50-50 RCP where even in the presence of sequence disorder there exist locally blocky segments of A or B monomers. We surmise that these random blocks generate a more locally "pure" environment comparable to the R=10 MBCP, and therefore less miscibility is predicted in the B-S region. Even in the D-B regime (not shown), the RCP yields less miscibility than both the homopolymer and MBCP.

The main frame of Figure 5.7 shows results for large particles (D/d=10) at fixed $\beta\varepsilon_{Bn}$ = 1.5 but with a longer attraction range of α_{pn} = 0.5*d*. Increasing the spatial range improves dispersion for homopolymers, i.e., widens the miscibility window[15], and similar behavior is found for a MBCP. Recall that for α_{pn} = 0.25*d*, only the R=1 MBCP provided complete miscibility in the range of $0 \le \beta\varepsilon_{An} \le 5$. But if α_{pn} is increased to 0.5*d*, *both* R=1 and 5 provide complete dispersion in the same range of $\beta\varepsilon_{Bn}$, while the RCP and R=10 multiblock still display less miscibility relative to the homopolymer. Overall, increasing the attraction range only quantitatively magnifies the generic miscibility trends.

Figure 5.8 illustrates the influence of nanoparticle size (D/d=1 vs. 10) on spinodal phase boundaries for the MBCP and homopolymer at fixed $\beta\varepsilon_{Bn}$ = 1.5 and α_{pn} = 0.25*d*. For homopolymers the miscibility window narrows as the particle-monomer size asymmetry ratio grows. This behavior is in *complete contrast* to that of the multiblock copolymer of any block length where increasing the particle size from D/d = 1 to 10 leads to widening of the miscibility window. This trend reflects physics unique to sequence ordered multiblock copolymers where chain connectivity creates “mixed” or “pure” local environments around the nanoparticles depending upon the particle-monomer size asymmetry ratio. Increasing the particle size leads to a more “mixed” environment of A and B monomers between two nanoparticles close in space which further frustrates the preferential packing of one of the monomers on the particle surface thereby yielding improved miscibility. Maximum surface heterogeneity is achieved by R=1, and thus the difference in the miscibility for the two particle sizes is the largest for this block length and gradually decreases with increasing R.

The miscibility results in Figures 5.7 and 5.8 were calculated for a fixed chain length of N=100 and η_t=0.4. One can ask what is the effect of chain length on miscibility under experimentally realistic isobaric conditions, or equivalently to a good approximation, at constant dimensionless polymer melt isothermal compressibility $S_0 = S_{pp}(k=0)$ (proportional to the amplitude of the long wavelength density fluctuations)[22]. Equation of state effects dictate that the polymer density ρ_p must change with N in order to hold S_0 fixed, however, the incremental change in density N for N>100 is small[22]. To hold S_0 fixed at a realistic melt value of 0.17, η_t is changed from 0.4 to 0.4355 when N increases from 100 to 1000.

Figure 5.9 shows the miscibility of particles of size D/d=10 in MBCP melt (fixed $\beta\varepsilon_{Bn}$=1.5) of various molecular weights. For high values of $\beta\varepsilon_{An}$, i.e., in the B-S regime, increasing N from 100 to 1000 can have a dramatic effect depending upon the polymer architecture. For the alternating copolymer of R=1, increasing N reduces miscibility. This trend of destabilization with increasing molecular weight has been observed in melts of homopolymer[15, 22] as well as random copolymer[12]. In sharp contrast, increasing chain length from N=100 to 1000 in melts of MBCP of length R=5 and 10 *enhances* miscibility. This increase of spatial dispersion for particles with $D/d \geq 3$ and R=5 or 10 is due to the enhanced repulsion at contact and reduced bridging minimum at a monomer distance separation in the PMF (plot not shown). This increased stability for longer polymer chains appears to be a new finding. However, as N increases beyond ~ 10^3-10^4, the miscibility trend reverses and the critical volume fraction Φ_c decreases with N. We find these N-dependent miscibility trends are qualitatively similar in all three differential wetting regimes (DB, DS, SB). However, for a small nanoparticle

of D/d=1, the miscibility decreases with N irregardless of the polymer sequence and architecture (homopolymer, RCP, MBCP). This is consistent with the idea that longer block lengths provide a homopolymer-like "pure" environment to small particles; prior studies established that increasing homopolymer molecular weight reduces miscibility for any particle size[15, 22].

5.6 Effect of Finite Repulsion between Unlike Monomers

Our desire to minimize parameter space, and focus solely on the consequences of differential surface segregation of copolymers near nanoparticles, led us to removing microdomain formation from the problem via setting all $\varepsilon_{MM'}$ to zero. In practice, an experimentally more realistic choice is to introduce a weak repulsion between the unlike A and B monomers to mimic a positive chi-parameter. This enlarges parameter space and presumably introduces additional richness to the problem. In this section we perform sample calculations that address this aspect using a weak $\beta\varepsilon_{AB}$ repulsion of -0.2 (negative implies repulsion per equation 5.3) and compare the results to the analogous behavior when $\beta\varepsilon_{AB} = 0$. The spatial range of the AB repulsion is identical to that of the monomer-particle attractions.

The main plot of Figure 5.10 compares the polymer-polymer (A-A or B-B since they are identical by symmetry) structure factors for MBCPs melts of block lengths R=5 and 10 to those of the corresponding homopolymer. The tendency for forming microdomains is indicated by the peak at small wavevectors. One sees that the homopolymer melt structure factor has ordering only on the local monomer diameter scale (kd ~ 6). In contrast, the MBCP melt with $\beta\varepsilon_{AB} = -0.2$ show tendencies of weak microphase separation. This low wavevector peak for

R=10 is more than double in height than that of the R=5 system and is slightly shifted to a lower wave vector. Though not shown, increasing the repulsion between A and B enhances the peak height at a fixed block length, as expected.

The inset of Fig. 5.10 shows the real space site-site pair correlation functions of the MBCP melt compared to the reference homopolymer analog. The $g_{AA}(r) = g_{BB}(r)$ correlation function is modestly more peaked than the homopolymer due to clustering of like monomers. For this same reason, the peak of the cross correlation $g_{AB}(r)$ is smaller than that of the homopolymer.

Figure 5.11 shows miscibility results when nanoparticles of D/d=10 are dissolved in the weak microdomain forming copolymer melt of block length R=10. Here, ε_{Bn} is fixed at $0.1k_BT$ and $\beta\varepsilon_{An}$ is varied to span the three regimes of depletion, steric stabilization and bridging. For the MBCP melt with finite repulsion, the miscibility window is shifted to the left compared to the case of $\beta\varepsilon_{AB} = 0$, implying enhanced solubility or dispersion in the D-D regime; however, miscibility is reduced in the D-B regime as well as the S-B (not shown) regime. Changing the particle size from D/d=10 to 1 does not qualitatively alter any of these trends. Thus, increasing the repulsion between A and B monomers only serves to modestly exaggerate quantitatively the miscibility trends obtained in prior sections.

To understand the origin of the shift of the miscibility window, we study the effect of $\beta\varepsilon_{AB}$ on the nanoparticle PMF shown in Fig. 5.12 for (i) $\beta\varepsilon_{An} = 0.5$, $\beta\varepsilon_{Bn} = 0.1$(main) and (ii) $\beta\varepsilon_{An} = 2.5$, $\beta\varepsilon_{Bn} = 0.1$(inset). In the D-D regime where the interfacial attractions of both A and

B are weak corresponding to the depletion regime (though unequal in magnitude), the added energetic frustration associated with a nonzero $\beta\varepsilon_{AB}$ reduces the attraction between the particles at contact. This leads to an overall increase of miscibility in the limit of low $\beta\varepsilon_{An}$ as seen in fig. 5.11. On the other hand, when one of the monomers is in the bridging regime, A-B monomer repulsion results in an enhanced repulsion at contact of the particle PMF, a larger amplitude and long-ranged repulsive shoulder, and a stronger bridging minimum at a monomer diameter separation. This implies that compared to the case of $\beta\varepsilon_{AB}=0$, the stronger adsorbing A monomers are preferentially segregated more towards the particle surface leading to enhanced bridging attraction. This diminishes the thermodynamic miscibility of the nanocomposites. However, the slight increase in the height of the long-ranged barrier could lead to greater kinetic stabilization of the particles. The analogs of Figures 5.11 and 5.12 have also been computed for the shorter block lengths of R=1 and 5 (not shown), and the results are qualitatively similar to that shown for R=10.

5.7 Summary

Polymer integral equation theory has been applied to study the structure, effective interactions and miscibility of nanoparticles in ordered sequence blocky MBCP melts where one monomer is more strongly adsorbing than the other. Chemical heterogeneity associated with differential nanoparticle wettability coupled with tunable MBCP architecture results in qualitative changes of effective interactions and the degree of spatial dispersion compared to homopolymer or sequence-disordered RCP systems. A key determining factor for miscibility is the size of the particle relative to the block contour length.

Beyond the effect of differential adsorption, interfacial packing correlations of the MBCP is sensitive to both nanoparticle size and block length. Smaller particles (D/d = 1) with larger block lengths exhibit a "purer", more homopolymer-like local environment, making them relatively insensitive to the inherent chemical heterogeneity of the copolymer matrix. On the other hand, a more "mixed" environment is obtained around the larger particles (D/d = 10), forcing the particles to be differentially wetted by the adsorbing blocks. Chain connectivity introduces frustration in the sense that the non-adsorbing monomer block is always close in space to the adsorbing block resulting in a large amplitude, long-ranged repulsive barrier in the PMFs.

The highly variable local environment around the particles has strong implications for dispersion. The chemical heterogeneity of the alternating polymer (R=1) is most strongly sensed by the particle, resulting in high solubility. Increasing the block length shrinks the miscibility window. Qualitatively *unlike* a homopolymer, increasing particle size by a factor of 10 in a MBCP melt can lead to *improved* miscibility in both the S-B and D-B regimes. The most dramatic effect is seen in the D-S regime where spinodal demixing is completely destroyed. The tighter adsorption of B and weaker layering of A around the nanoparticle leads to local surface segregation, but the steric constraint of the less adsorbing A segment attached to every B segment frustrates the preferential packing of the B block on the surfaces of the two nanoparticles close in space leading to the dramatic enhancement of miscibility. Increasing the overall MBCP chain length for block lengths of R=5 and 10 results in a surprising initial widening of the miscibility window for the larger particles. This trend is opposite to what is observed for the R=1 alternating copolymer, the RCP, and homopolymers when $D/d \geq 3$.

The effect of introducing a weak repulsion between the A and B monomers which mimics the tendency for microdomain clustering was briefly studied. The latter can lead to either reduction or improvement of thermodynamic miscibility depending upon the strengths of the competing A-n and B-n polymer- particle interfacial attractions.

The overarching outcome of our work has been to provide physical insight into the rich and complex interplay of particle size, block length, and the absolute and differential monomer-particle adsorption energetics on interfacial packing correlations, the copolymer-mediated nanoparticle PMF, and miscibility. Many of the trends are not easily "guessed" due to the nonadditive interplay of coupled entropy-enthalpy correlation effects. As one specific example to further emphasize this point, consider a particle of size D=10d where the A and B monomer attractive interaction parameters are: $\alpha = 0.25d, \beta\varepsilon_{An} = 0.1, \beta\varepsilon_{Bn} = 3.$ The corresponding "reference" homopolymer PMFs are dominated by either depletion or bridging attraction, with a low solubility limit nanoparticle volume fractions, Φ_c , of essentially zero or 0.07, respectively. If these monomers are arranged into copolymers of different architecture at fixed 50/50 composition we predict Φ_c values of: 10^{-5} (random copolymer), fully miscible (R=1 and 5 multiblock copolymers), and 0.001 (R=10). This complex, many order of magnitude variability with copolymer architecture seems impossible to a priori guess, and reflects the complex thermodynamics and competing packing correlations discussed above.

The present work is an initial study, and utilizes a simple model that precludes microphase domain formation, although this aspect can be treated using PRISM theory[13]. All the calculations presented have been in the dilute nanoparticle limit, and future studies are required

to explore in detail the role of many-body effects on structure and thermodynamics. It remains to be determined how the strong coupling between the block length, particle size and chemical heterogeneity is modified when there is a strong direct attraction between the particles. Finally, it would be interesting to study how a copolymer of variable sequence and chemical heterogeneity mediates interactions between non-spherical particles like rods and disks[23].

5.8 References

(1) S. Teh, D. Linton, B. Sumpter, M. D. Dadmun, *Macromolecules*, **44**, 7737-7745, 2011.

(2) J. F. Lutz, M. Ouchi, D. R. Liu, M. Sawamoto, *Science*, **341**, 1238149, 2013.

(3) A. Song, K. A. Parker, N. S. Sampson, *J. Am. Chem. Soc.*, **131**, 3444-3445, 2009.

(4) C. S. Daeffler, R. H. Grubbs, *Macromolecules*, **46**, 3288-3292, 2013.

(5) J. J. Chiu, B. J. Kim, E. J. Kramer, D. J. Pine, *J. Am. Chem. Soc.*, **127**, 5036-5037, 2005.

(6) Q. Zhang, T. Xu, D. Butterfield, M. J. Misner, D. Y. Ryu, T. Emrick, T. P. Russell, *Nano Lett.*, **5**, 357-361, 2005.

(7) W. A. Lopes, H. M. Jaeger, *Nature*, **414**, 735-738, 2001.

(8) J. J. Chiu, B. J. Kim, G. R. Yi, J. Bang, E. J. Kramer, D. J. Pine, *Macromolecules*, **40**, 3361-3365, 2007.

(9) E. Reister, G. H. Fredrickson, *Macromolecules*, **37**, 4718-4730, 2004.

(10) R. B. Thompson, V. V. Ginzburg, M. W. Matsen, A. C. Balazs, *Science*, **292**, 2469, 2001.

(11) R. B. Thompson, V. V. Ginzburg, M. W. Matsen, A. C. Balazs, *Macromolecules*, **35**, 1060-1071, 2002.

(12) D. Banerjee, M. D. Dadmun, B. Sumpter, K. S. Schweizer, *Macromolecules*, **46**, 8732-8743, 2013.

(13) K. S. Schweizer, J.G. Curro, *Adv. Chem. Phys.*, **98**, 1-142, 1997.

(14) J. B. Hooper, K. S. Schweizer, *Macromolecules*, **38**, 8858-8869, 2005.

(15) J. B. Hooper, K. S. Schweizer, *Macromolecules*, **39**, 5133-5142, 2006.

(16) L. M. Hall, K. S. Schweizer, *J. Chem. Phys.*, **128**, 234901, 2008.

(17) L. M. Hall, A. Jayaraman, K. S. Schweizer, *Curr. Opin. Solid State Mater. Sci.*, **14**, 38-48, 2010.

(18) A. M. Mayes, M. Olvera de la Cruz, *J. Chem. Phys.*, 91, 7228–7235, 1989.

(19) H. Benoit, G. Hadziioannou, *Macromolecules*, 21, 1449-1464, 1988.

(20) B. J. Sung, A. Yethiraj, *Macromolecules*, 38, 2000-2008, 2005.

(21) J. B. Hooper, K. S. Schweizer, T. G. Desai, R. Koshy, P. Keblinski, *J. Chem. Phys.*, 121, 6986-6997, 2004.

(22) D. Banerjee and K. S. Schweizer, *J. Chem. Phys.*, **142**, 214903, 2015.

(23) L. M. Hall, K. S. Schweizer, *Soft Matter*, **6,** 1015, 2010.

5.9 Figures

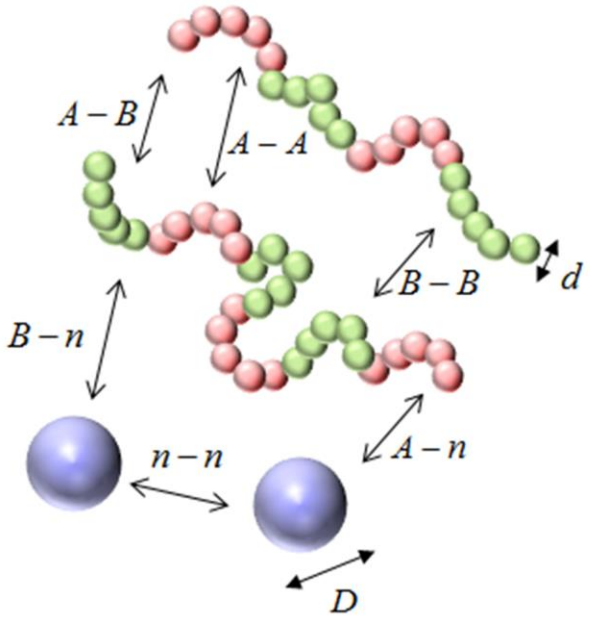

Figure 5.1 Conceptual cartoon of dilute particles in a alternating AB multiblock copolymer melt.

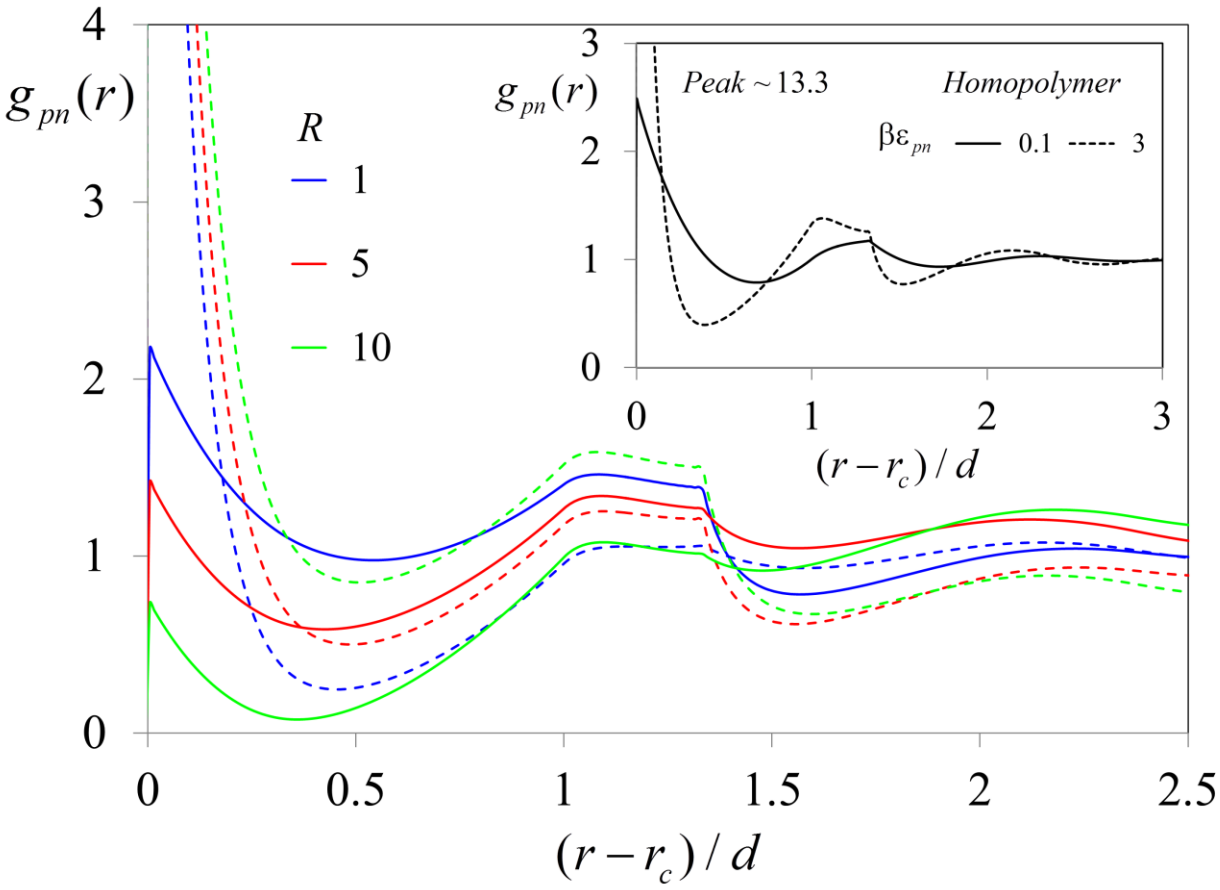

Figure 5.2a A (solid) and B (dashed) monomer – particle cross correlation functions for dilute hard spheres of D/d=10 in a MBCP melt with $\beta\varepsilon_{An}=0.1$, $\beta\varepsilon_{Bn}=3$ and $\alpha_{pn}=0.25d$ at the indicated values of block lengths R = 1, 5 and 10. The g_{Bn} contact values are at 14.8 (R=1), 18.1 (R=5) and 20.8 (R=10), respectively. The g_{pn} contact values for the reference homopolymers of $\beta\varepsilon_{pn}$ = 0.1(solid) and 3(dashed) are shown in inset.

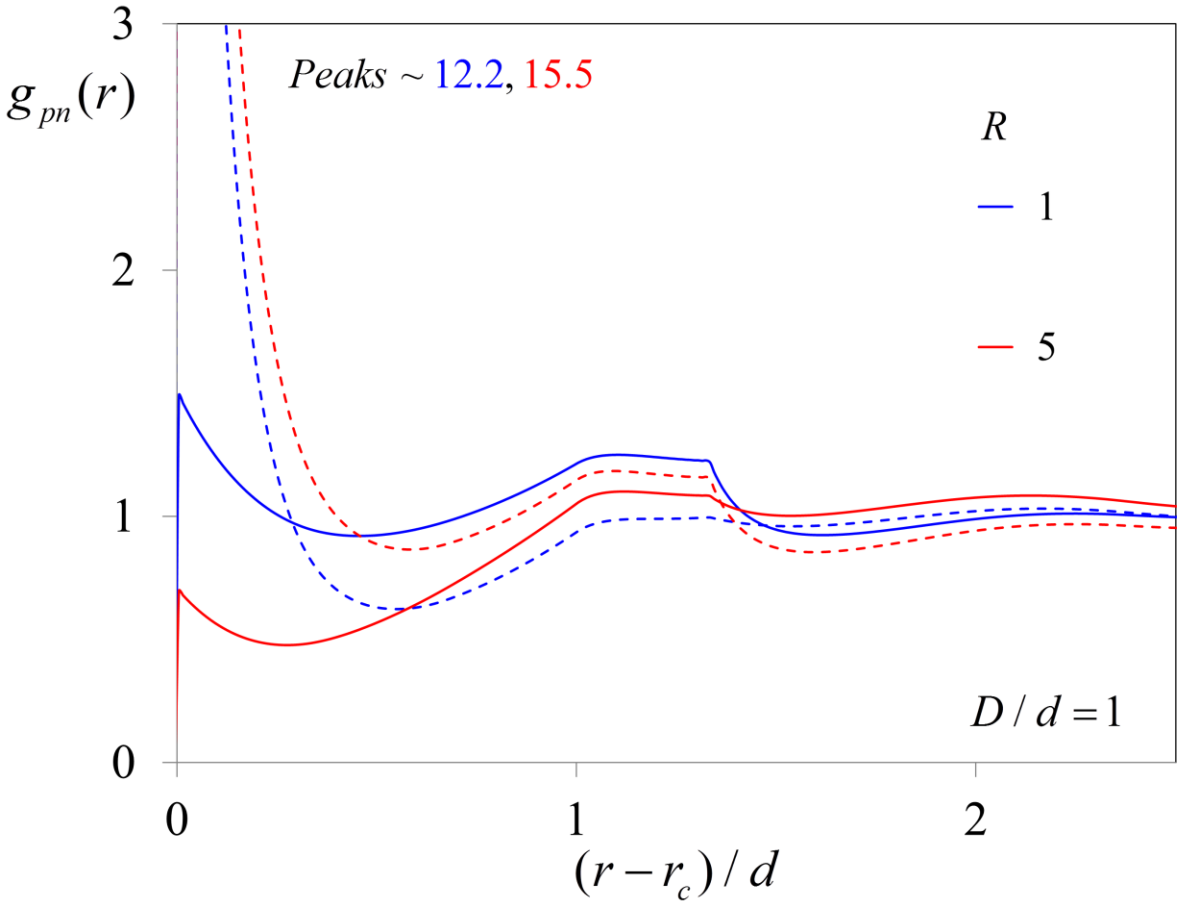

Figure 5.2b A (solid) and B (dashed) monomer – particle cross correlation functions for dilute hard spheres of D/d=1 in a MBCP melt with $\beta\varepsilon_{An}=0.1$, $\beta\varepsilon_{Bn}=3$ and $\alpha_{pn}=0.25d$ at the indicated values of block lengths R = 1 and 5.

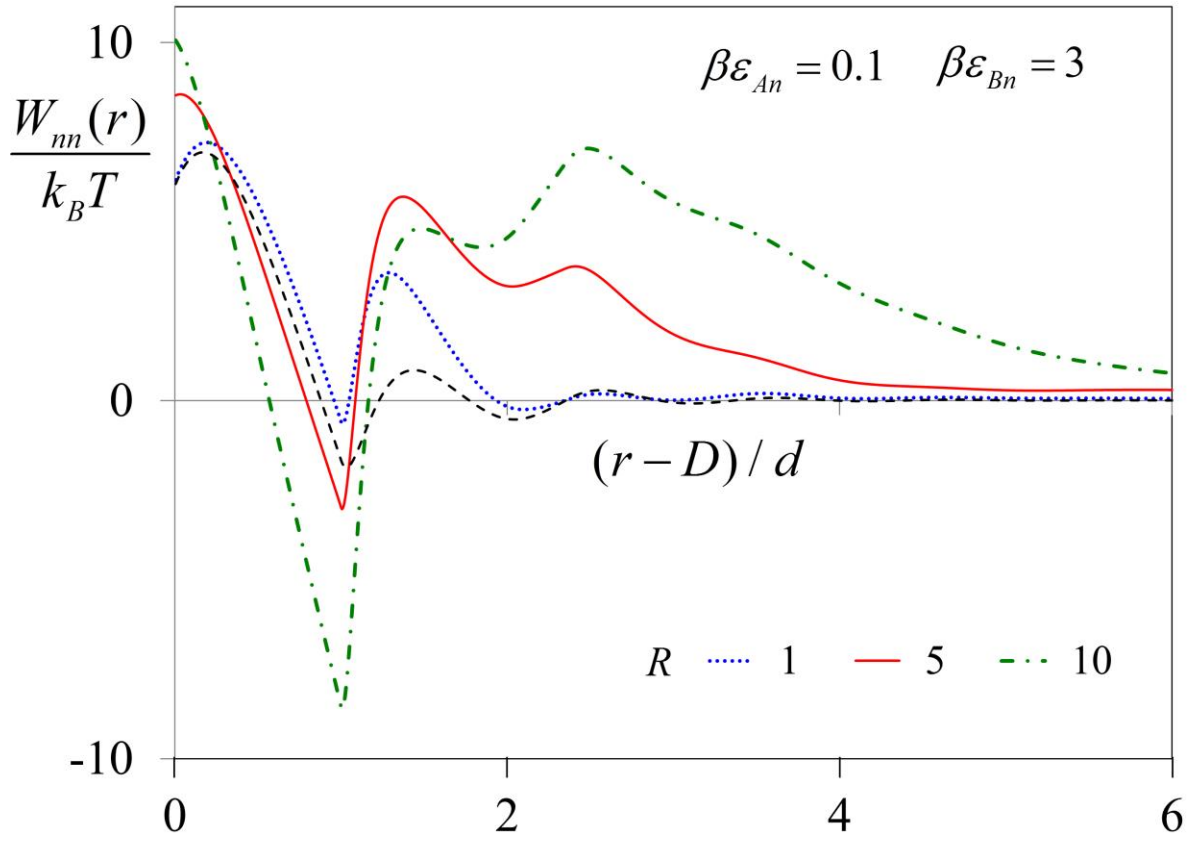

Figure 5.3 Particle potential of mean force for dilute hard spheres of D/d = 10 in a MBCP melt with $\beta\varepsilon_{An} = 0.1$, $\beta\varepsilon_{Bn} = 3$ (D-B) and $\alpha_{pn} = 0.25d$ at the indicated values of block lengths R = 1(dot), 5(solid), and 10(dash-dot) and homopolymer (dash) of average strength $\varepsilon_{pn} = (\varepsilon_{An} + \varepsilon_{Bn})/2$.

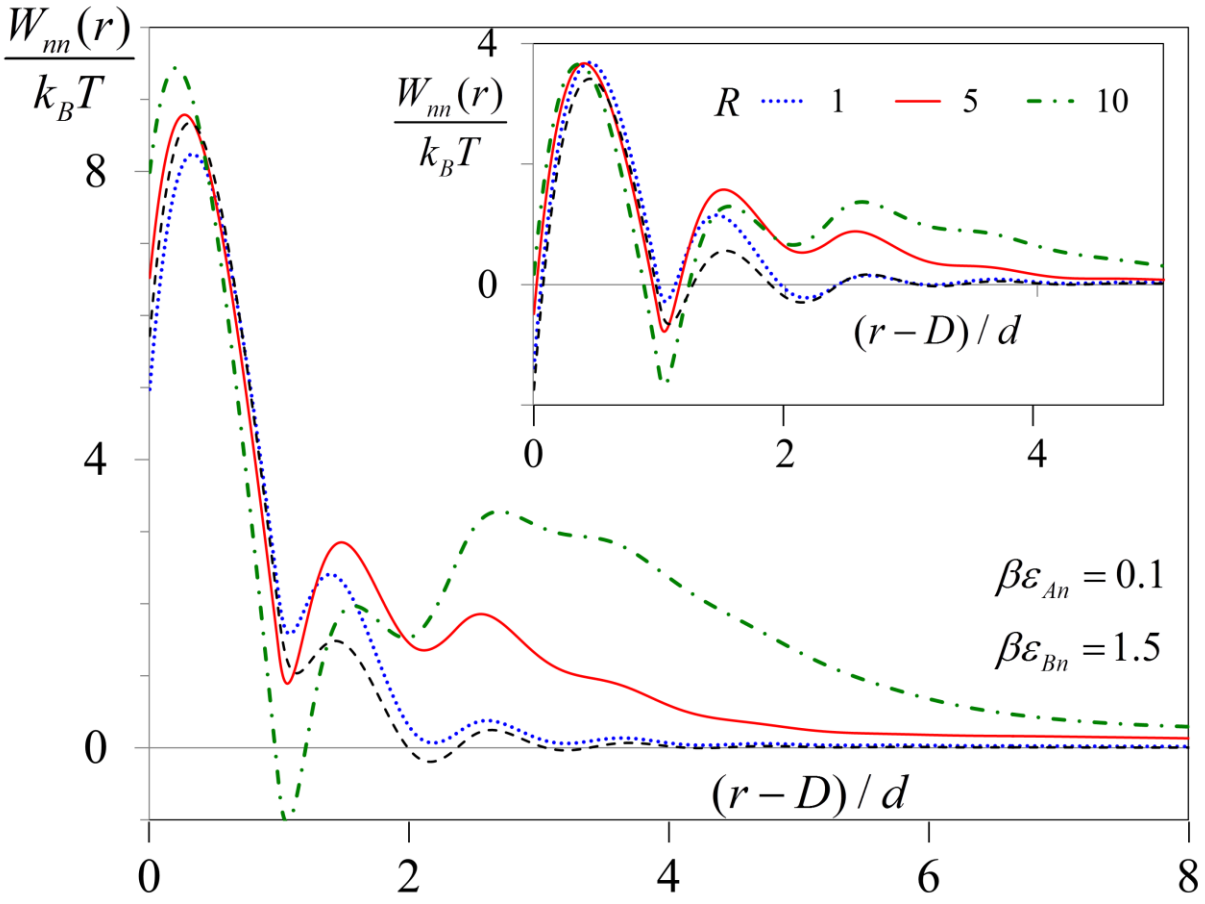

Figure 5.4 (Inset) Particle PMF for dilute hard spheres of D/d = 10 in a MBCP melt with $\beta\varepsilon_{An} = 0.1$, $\beta\varepsilon_{Bn} = 1.5$ (D-S) and $\alpha_{pn} = 0.25d$ at the indicated values of block lengths R = 1(dot), 5(solid), and 10(dash-dot) and a homopolymer (dash) of average strength $\varepsilon_{pn} = (\varepsilon_{An} + \varepsilon_{Bn})/2$. (Main) PMF for the same systems as the inset but with $\alpha_{pn} = 0.5d$.

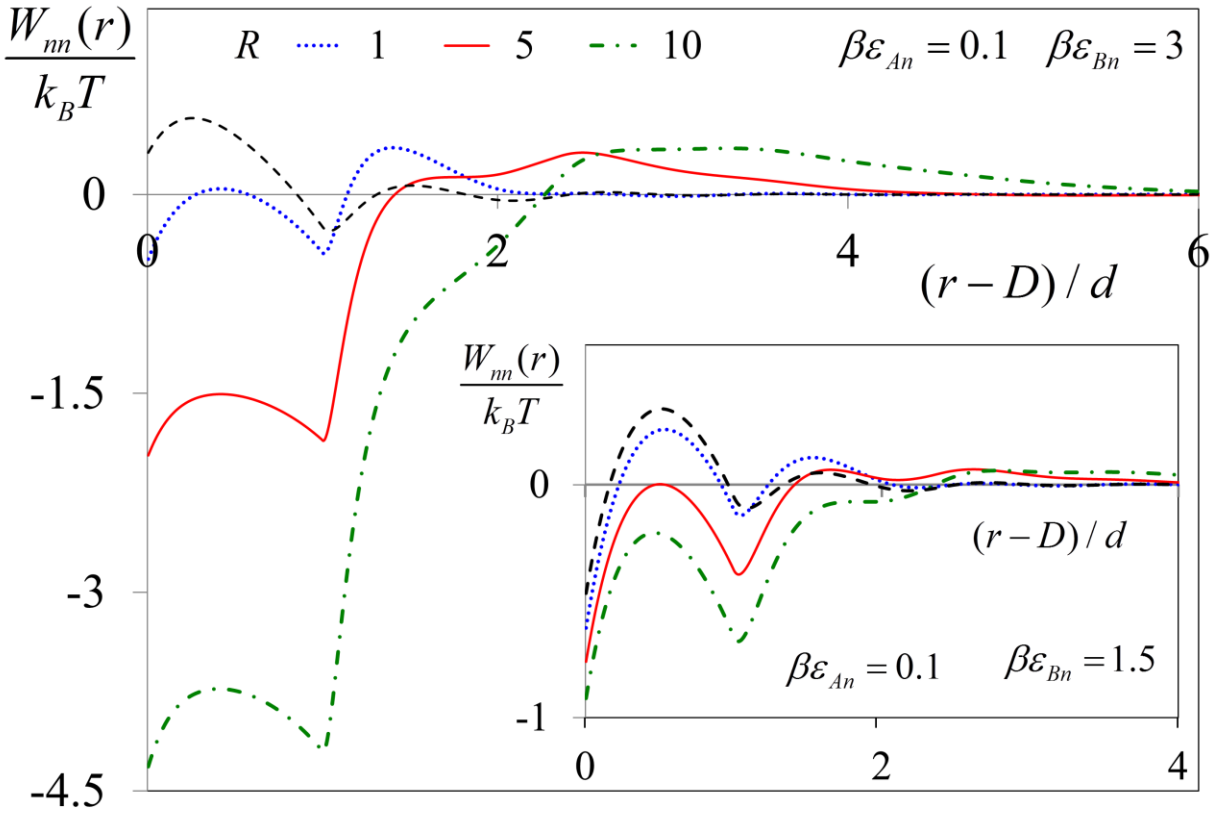

Figure 5.5 (Inset) Particle PMF for dilute hard spheres of D/d = 1 in a MBCP melt with $\beta\varepsilon_{An} = 0.1$, $\beta\varepsilon_{Bn} = 1.5$ (D-S) and $\alpha_{pn} = 0.25d$ at the indicated values of block lengths R = 1(dot), 5(solid), and 10(dash-dot) and a homopolymer (dash) of average strength $\varepsilon_{pn} = (\varepsilon_{An} + \varepsilon_{Bn})/2$. (Main) PMFs for D/d = 1 in a MBCP melt with $\beta\varepsilon_{An} = 0.1$, $\beta\varepsilon_{Bn} = 3$ (D-B) and $\alpha_{pn} = 0.25d$ at the indicated values of block lengths R = 1(dot), 5(solid), and 10(dash-dot) and a homopolymer (dashed) of average strength $\varepsilon_{pn} = (\varepsilon_{An} + \varepsilon_{Bn})/2$.

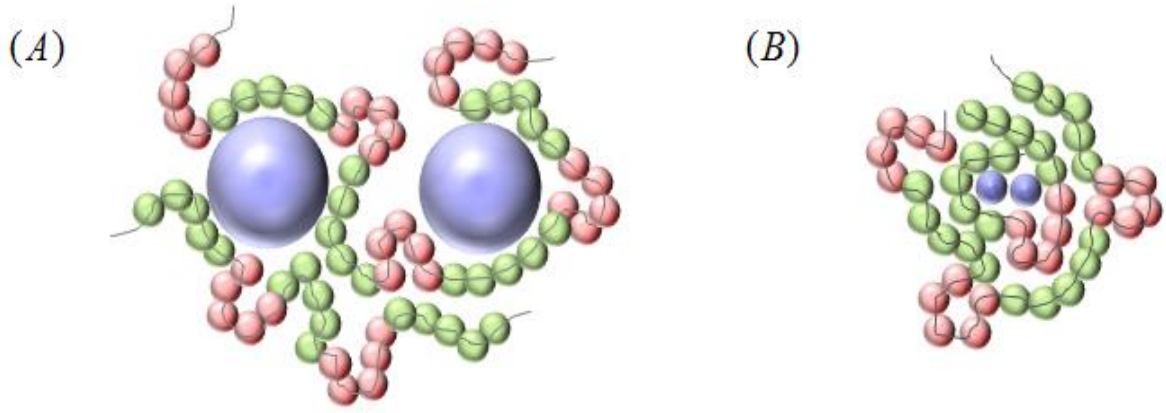

Figure 5.6 Schematic of the probable equilibrium structure of nanoparticles of (A) D/d = 10 , and (B) D/d = 1 in a MBCP melt of R = 5. Black curves show backbone bonds for clarity.

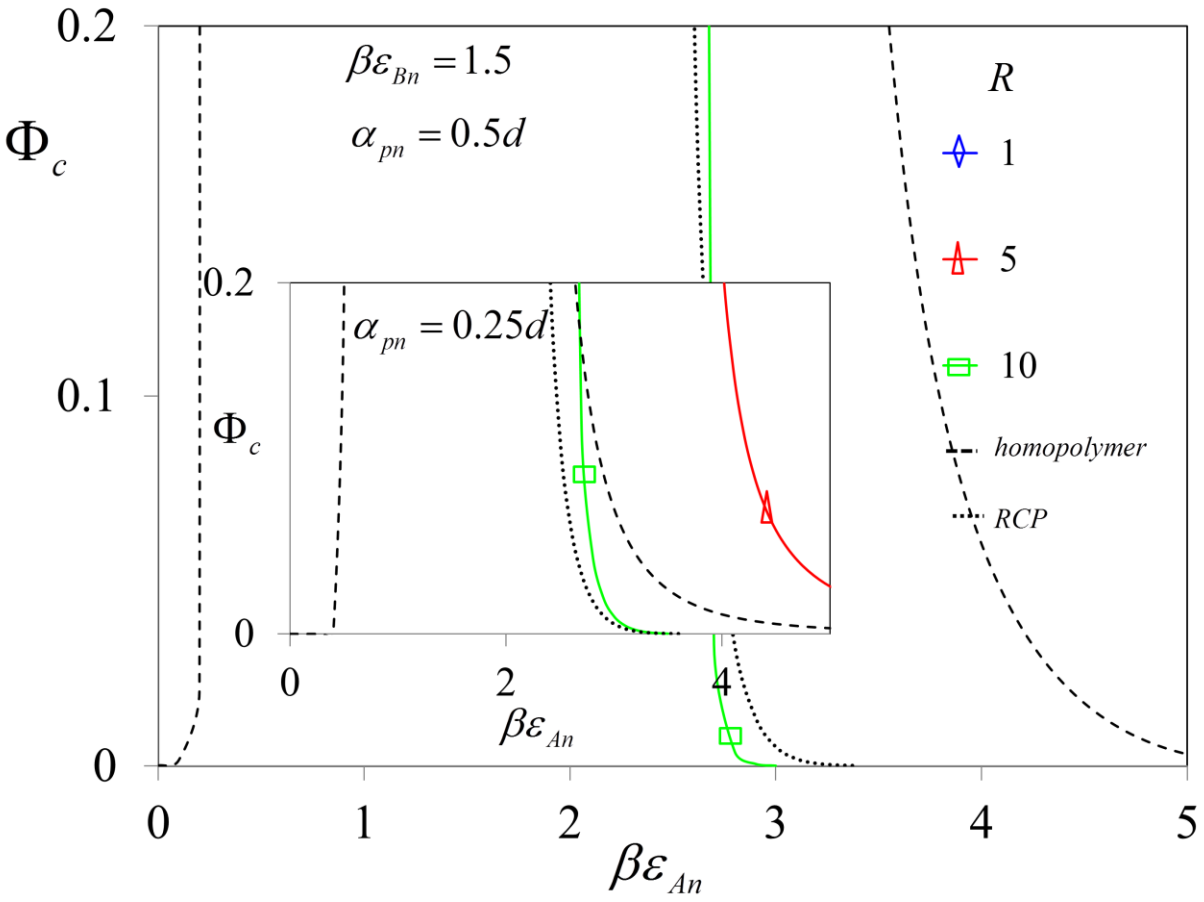

Figure 5.7 (Inset) Spinodal phase diagram of dilute hard spheres of D/d = 10 in a MBCP melt with $\beta\varepsilon_{Bn} = 1.5$ and $\alpha_{pn} = 0.25d$ at the indicated values of block lengths R against that of homopolymer (dashed) and a RCP (dotted) as reference. (Main) Spinodal phase diagram for the same system as the inset but with $\alpha_{pn} = 0.5d$.

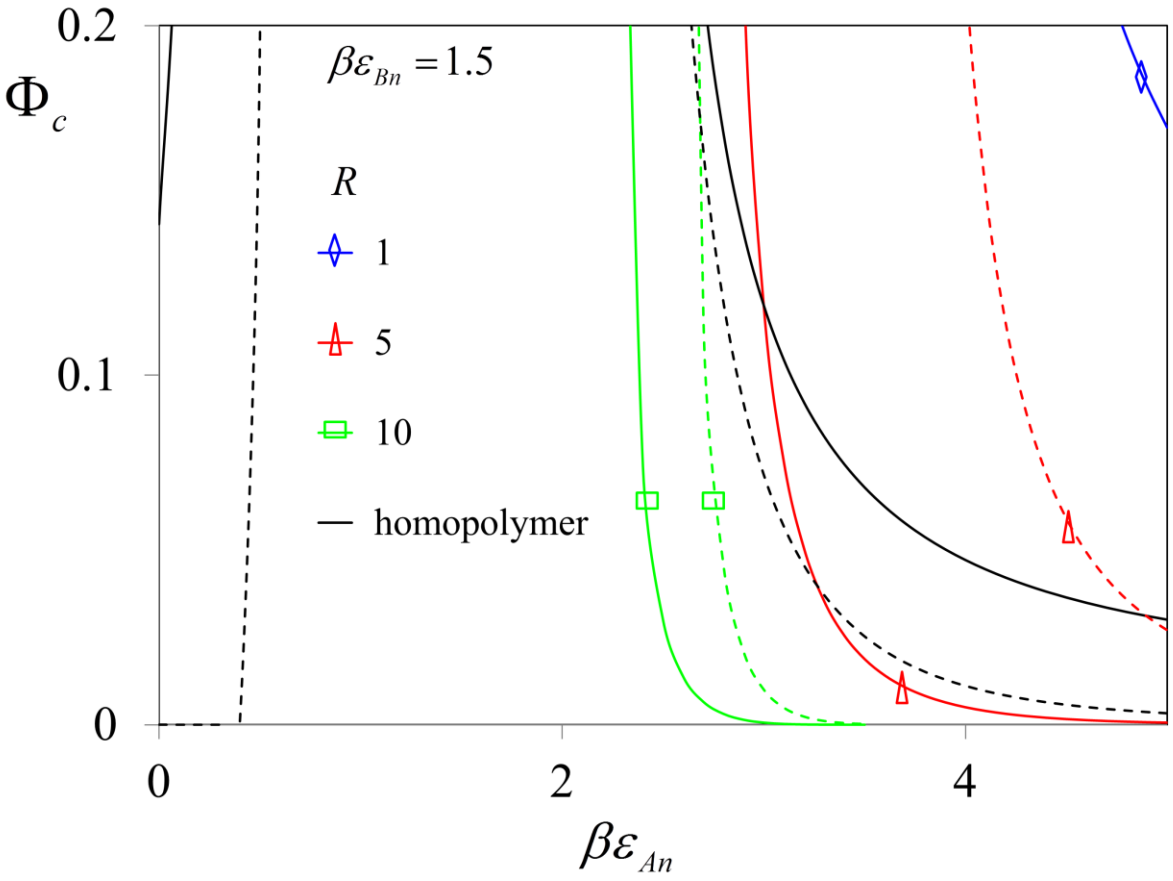

Figure 5.8 Spinodal phase diagram of dilute hard spheres of D/d = 1 (solid) and 10 (dashed) in a MBCP melt with $\beta\varepsilon_{Bn} = 1.5$ and $\alpha_{pn} = 0.25d$ at the indicated values of block lengths R against that of homopolymer as reference.

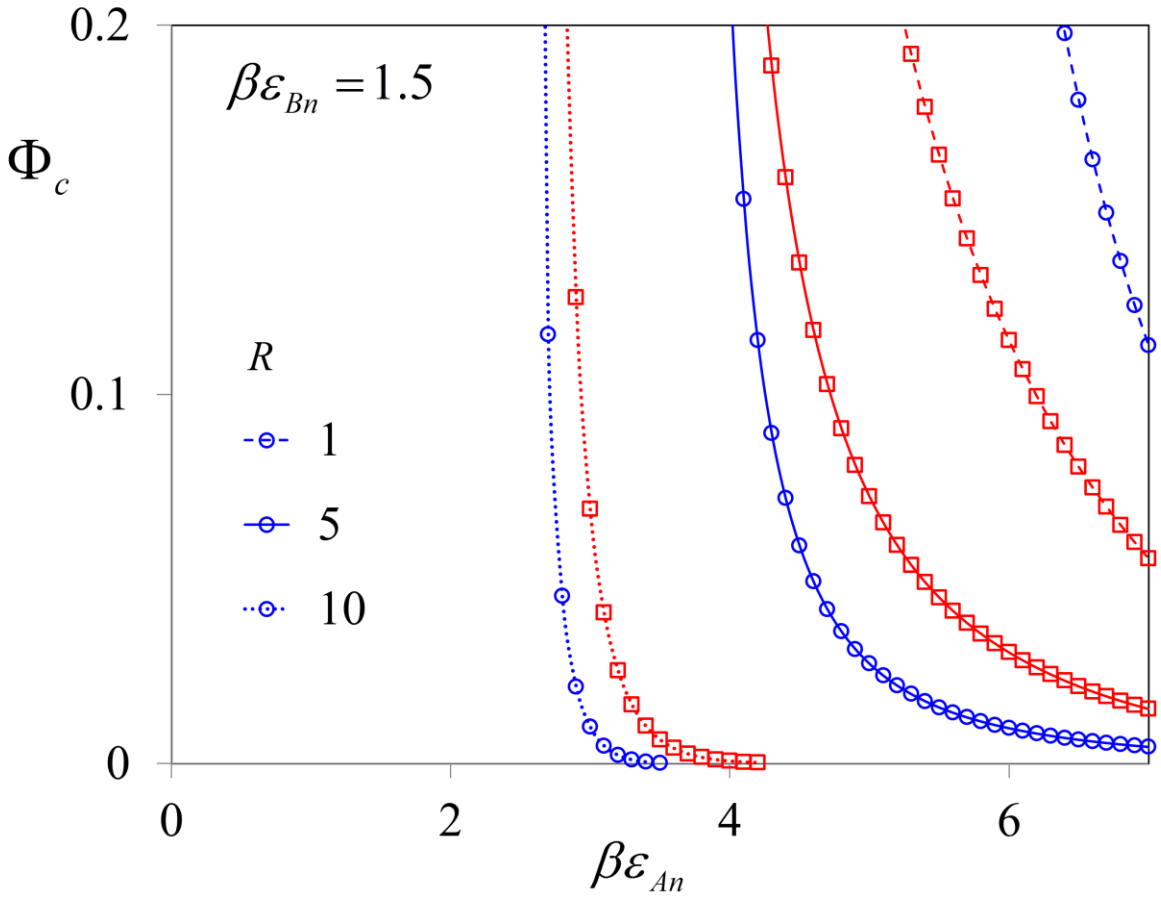

Figure 5.9 Spinodal phase diagram of dilute hard spheres of D/d = 10 in a MBCP melt with $\beta\varepsilon_{Bn} = 1.5$ and $\alpha_{pn} = 0.25d$ at the indicated values of block lengths R for two chain lengths N = 100 (circle) and 1000 (square). Total packing fraction η_t for N=100 and 1000 are 0.4 and 0.4355, respectively, to maintain a constant polymer melt dimensionless isothermal compressibility of $S_0 = 0.17$.

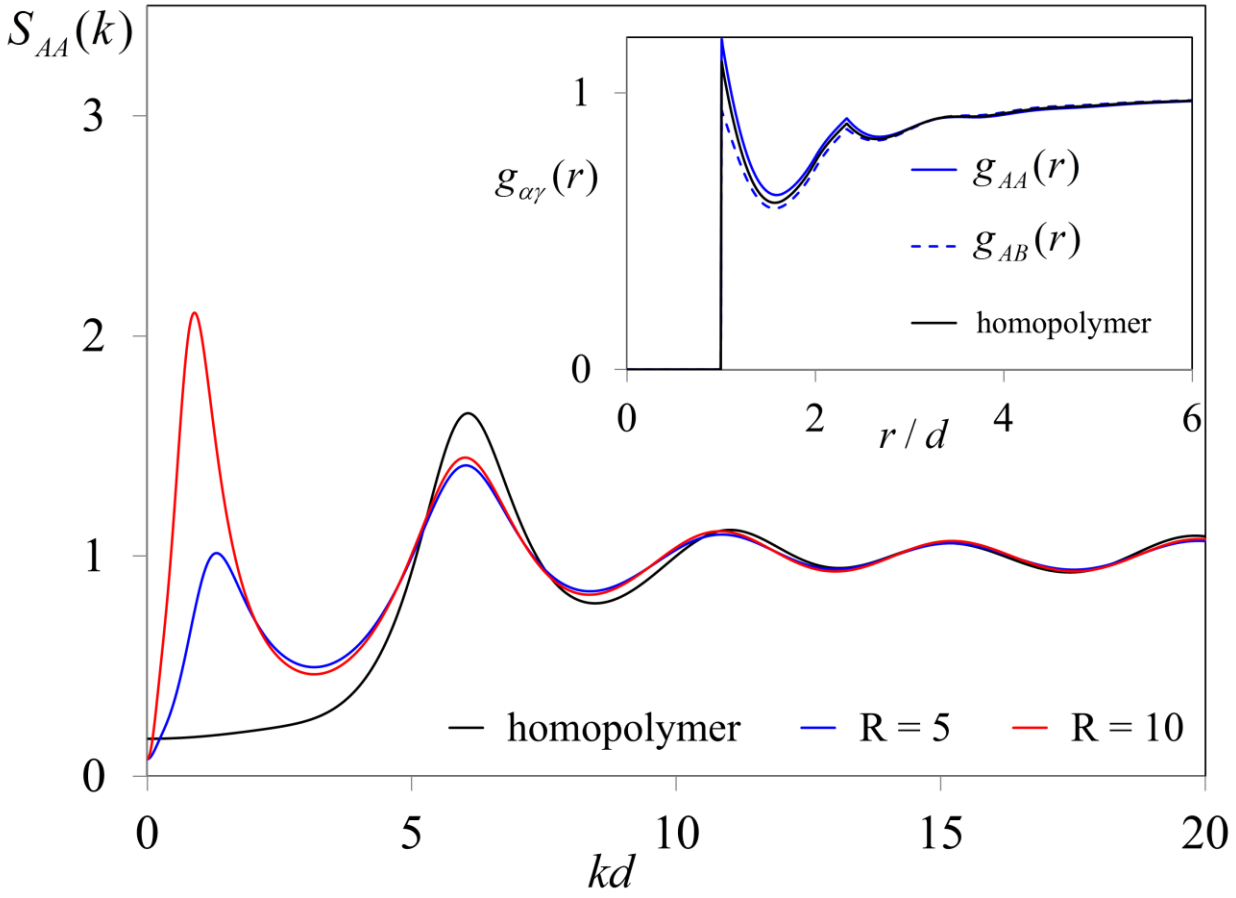

Figure 5.10 (Main) Comparison of the polymer partial structure factor (A-A=B-B) for a MBCP melt with $\beta\varepsilon_{AB} = -0.2$ and block lengths R=5 and 10 with the corresponding homopolymer result. (Inset) The like ($g_{AA}(r)$) and unlike ($g_{AB}(r)$) site-site pair correlation functions for a MBCP of $\beta\varepsilon_{AB} = -0.2$ and R=10 compared to the analogous homopolymer case ($\beta\varepsilon_{AB} = 0$).

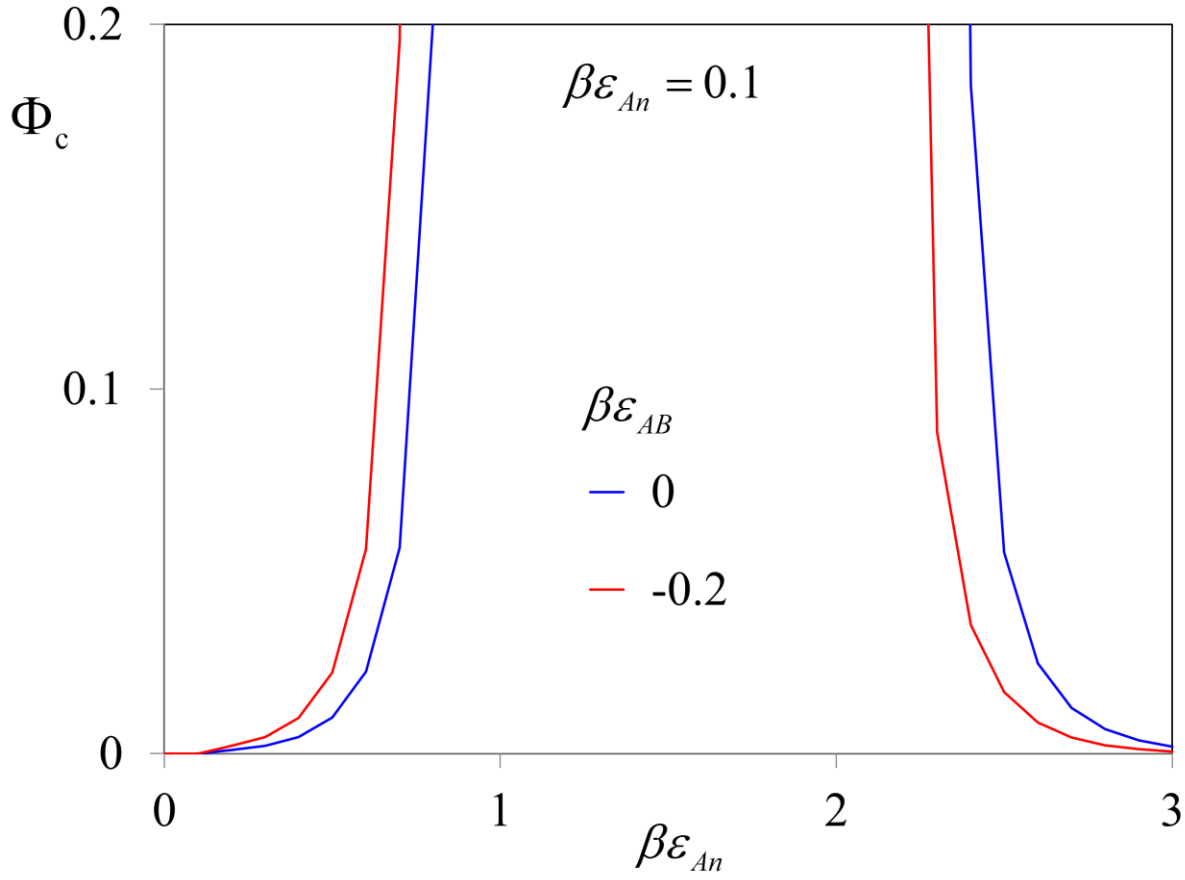

Figure 5.11 Spinodal phase diagram of dilute hard spheres of D/d = 10 in a MBCP melt with $\beta\varepsilon_{Bn} = 0.1$and block length R=10 for $\beta\varepsilon_{AB} = -0.2$ (red) and $\beta\varepsilon_{AB} = 0$ (blue).

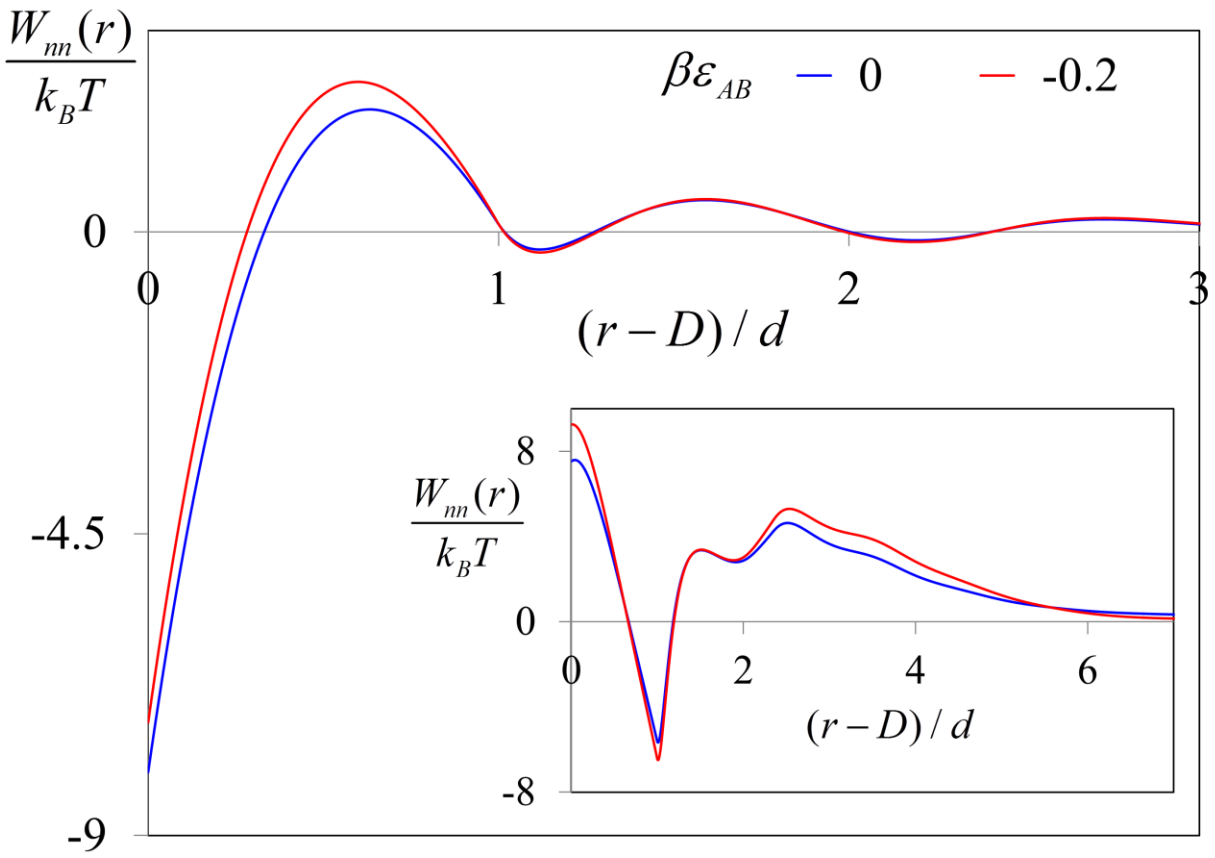

Figure 5.12 Particle PMF for dilute hard spheres of D/d = 10 in a MBCP melt with $\beta\varepsilon_{AB} = -0.2$ and block length R=10 for (i) $\beta\varepsilon_{An} = 0.5$, $\beta\varepsilon_{Bn} = 0.1$(main) and (ii) $\beta\varepsilon_{An} = 2.5$, $\beta\varepsilon_{Bn} = 0.1$(inset).

CHAPTER 6

THEORY OF THE MISCIBILITY OF FULLERENES IN RANDOM COPOLYMER MELTS[1]

6.1 Introduction

Nanoparticles or "fillers" are widely added to polymers to create nanocomposites with improved properties[1,2,3]. Carbon nanotubes (CNTs) and fullerenes (C_{60}) are specific functional particles that have found increasingly large applications as mechanical reinforcers and in optoelectronics due to their pi-conjugated nature and excellent electrical, optical and charge conduction properties[3-9]. However, both nanoparticles experience strong direct intermolecular attractions, which make it challenging to disperse them in polymer matrices at desired levels of loading. This difficulty is especially pronounced for carbon nanotubes due to their high aspect ratio. Recent experiments illustrate the advantage of using chemically heterogeneous AB random copolymers to improve the spatial dispersion of CNTs[10-13].

The focus of this theoretical article is fullerenes, which have attracted much recent attention as active elements for fabricating heterojunction solar cells[7,8,14,15]. In contrast to carbon nanotubes, these nanoparticles are small and spherical, but strong attractions due to delocalized

[1] This chapter is drawn in its entirety from a previous publication. Reprinted (adapted) with permission from D. Banerjee, M. D. Dadmun, B. Sumpter and K. S. Schweizer, Macromolecules, **46**, 8732-8743. Copyright 2013 American Chemical Society.

electrons still render them difficult to disperse in polymers. In photovoltaic applications, controlling polymer packing around fullerenes is also important for charge transfer and the subsequent separation of electrons and holes. One might hope that their smaller size will allow the exploitation of equilibrium thermodynamic principles to achieve better spatial dispersion than CNTs. Just like the CNTs, it was experimentally observed that AB random copolymers of intermediate composition can afford for many, but not all, systems major improvement of dispersion relative to homopolymer behavior based on electron donor-acceptor C_{60}-polymer attractions[16].

The goal of this chapter is to combine the polymer reference interaction site model (PRISM) statistical mechanical theory of packing and thermodynamics in nanocomposites[17-25] with computational chemistry input for the interactions to study specific RCP-fullerene mixtures. To the best of our knowledge, this is the first time such a hybrid approach has been attempted. This problem has been studied in a generic manner with PRISM theory for hard sphere fillers much larger than polymer monomers, and changing from a homopolymer to a RCP appears to *diminish* miscibility relative to the homopolymer limits[24]. However, this conclusion cannot be naively applied to the fullerene systems due to their ultra-small nature, the presence of strong direct attractions, and chemically-specific aspects of the donor-acceptor interactions between C_{60} and polymers.

6.2 Theory and Model

6.2.1 Theory

In the following chapter, the subscript *p* denotes any polymer segment, *A* and *B* labels the two types of polymer segments, and *n* denotes the nanoparticle, as schematically shown in Figure 6.1. For a AB copolymer there are two types of inequivalent sites, and hence three intramolecular probability distribution functions or partial structure factors $\omega_{ij}(k)$. We consider a completely random sequence of *A* and *B* sites, subject only to the constraint of what fraction, f_A, of the *N* total sites of a single chain are of type *A*. Per prior work[18, 19, 22, 23], the polymer is modeled as a freely-jointed-chain (FJC) of N = 100 segments where the *A* and *B* sites have a hard core diameter *d* and bond (persistence) length *l*. The corresponding $\omega_{ij}(k)$ are[26] :

$$\omega_{ii}(k) = \frac{1}{N_i} N f_i + \frac{2}{N_i} \sum_{\tau=1}^{N+1} (N-\tau) f_i^2 \left(\frac{\sin(kl)}{kl} \right)^{\tau} \tag{6.1}$$

$$\omega_{AB}(k) = \frac{2}{N} \sum_{\tau=1}^{N+1} (N-\tau) f_A f_B \left(\frac{\sin(kl)}{kl} \right)^{\tau} \tag{6.2}$$

where f_i is the fraction of *i* sites, and $l = 1.2d$ which is a typical value for flexible polymers[17].

6.2.2 Model

Even by adopting a simple FJC model and an (additive) hard core plus exponential tail model of site-site potentials as discussed in Chapter 2, 18 material-specific parameters are required which can be parsed into two categories. There are 6 length scales: filler diameter *D*, monomer diameters d_A and d_B, bond lengths (or homopolymer persistence lengths) l_A and l_B, and polymer radius-of-gyration or chain length (*N*). The tail potential is defined by a contact strength and spatial range

$$U_{ij}(r) = -\varepsilon_{ij} e^{-(r-r_{ij,c})/\alpha_{ij}} \ , \ r > r_{ij,c} \tag{6.3}$$

where $r_{ij,c}$ is the closest distance of approach between the species i and j , which equals D for n-n and (D+d)/2 for p-n interactions. Given there are 6 pairs (AA, AB, BB, An, Bn, nn), 12 interaction parameters must be specified.

The direct fullerene interaction is often modeled using the analytic expression[27]:

$$U_{nn}(r) = -A\left[\frac{1}{s(s-1)^3} + \frac{1}{s(s+1)^3} - \frac{2}{s^4}\right] + B\left[\frac{1}{s(s-1)^9} + \frac{1}{s(s+1)^9} - \frac{2}{s^{10}}\right] \tag{6.4}$$

where A and B are known constants and $s = r/D$. Figure 6.2 shows this potential is well approximated by a hard core (diameter D = 0.7 nm) plus an exponential attractive tail of strength ε_{nn} and short range α_{nn}, where $\varepsilon_{nn} = 7.3 k_B T$ at the temperature of prime (experimental[10,16]) interest here (T = 440K) and $\alpha_{nn} = 0.15D$, which we adopt in the PRISM calculations. In a dielectric medium, the attraction strength is reduced. We crudely estimate this effect by treating the fullerene as a homogeneous dielectric sphere with a Hamaker constant, A_H, which based on the classic Lifshitz theory of van der Waals interactions is given by[28]:

$$A_H = \frac{3}{4} k_B T \left(\frac{\varepsilon_1 - \varepsilon_2}{\varepsilon_1 + \varepsilon_2}\right)^2 + \frac{3h\nu_e}{16\sqrt{2}} \frac{\left(n_1^2 - n_2^2\right)^2}{\left(n_1^2 + n_2^2\right)^{3/2}} \tag{6.5}$$

Here ε is the medium dielectric constant, n the refractive index, h is Planck's constant and ν_e an absorption frequency typically of order 2-3*10^{15} s^{-1} [28]. The dielectric constant and refractive index of a fullerene is[29] $\varepsilon_1 \approx 4.4$ and $n_1 \approx 2.2$. As a relevant example, consider

polystyrene for which[28] $\varepsilon_2 \approx 2.55$ and $n_2 \approx 1.557$. Using these values, the fullerene Hamaker constant relative to its vacuum value is reduced by a factor of ~ 0.285, which implies $\varepsilon_{nn} \approx 2.1 k_B T$ at T = 440*K*. With these estimates as motivation, we fix $\varepsilon_{nn} = 2.5 k_B T$ in all subsequent PRISM calculations unless stated otherwise.

To specify the polymer model and the p-p and p-n interactions requires 15 parameters. We study five monomers: Acrylonitrile (AN), Styrene (Sty), Cyanostyrene (CNSty), Methylmethacrylate (MMA), di-methyl-amino-ethyl-methacrylate (DMAEMA). Their persistence lengths and monomer diameters have been estimated and differ only modestly. Moreover, beyond a rather low value the chain length only slightly influences particle miscibility in melts[19]. Hence, a minimalist "reference" parameter set is employed corresponding to N = 100, common bond lengths and monomer diameters for A and B of $l = 1.2d$ and $d = 0.7nm$, respectively, and a polymer melt packing fraction (dimensionless compressibility) of[17, 22] η_t = 0.4352 ($S_{pp}(q=0) \equiv S_0 = 0.25$). Note that a fullerene diameter of $D = 0.7nm$ implies the monomer and nanoparticle are the same size, i.e., D/d = 1. The modest sensitivity of our miscibility predictions to variations of these parameters is discussed in section 6.4.2 and Appendix B.

The chemistry of the model now enters via the 5 attraction strength parameters, ε_{AA}, ε_{BB}, ε_{AB}, ε_{An}, ε_{Bn}, and their corresponding spatial ranges. Computational chemistry calculations of these energies have been performed based on standard methods[30]; see Appendix B for a brief discussion. Table 6.1 shows these energies in units of k_BT (at 440*K*). First note that the monomer-fullerene attraction is "strong" in all cases, varying from ~ 5.3 to 10.7. The monomer-monomer attractions vary over an even wider range, from ~ 2.3 to 7.7. However, in all cases the *AB*

monomer exchange energy, $\Delta\varepsilon \equiv \left(\varepsilon_{AA} + \varepsilon_{BB} - 2\varepsilon_{AB}\right)/2$, is small in the sense $|\Delta\varepsilon| \ll \varepsilon_{jj}$. This suggests there will be little local clustering of A and B monomers in the pure RCP melt. In a microscopic approach, especially if attractions are strong relative to thermal energy, the attraction range is important. Full potentials have been computed and a representative example is shown in the inset of Figure 6.2. For all systems of interest, we find that the range is short and very similar, on the order of an Angstrom. Our reference model fixes $\alpha_{pn} = 0.12d$.

Our focus is on understanding the role of interfacial n-p attractions, both in absolute and relative (*A* versus *B*) terms. To achieve this in the simplest way possible, all prior PRISM theory work on PNCs adopted an athermal hard core model of the pure polymer melt[18, 19, 22, 23, 24, 25]. As a consequence, p-p and p-n attractions enter in a combined manner as an *effective* monomer-filler attraction. This significantly reduces the number of energy parameters, simplifies closure selection, and allows a simpler physical interpretation. We adopt the same approach here, which corresponds to modeling the pure RCP melt as an athermal homopolymer liquid. Given that the net tendency for like monomers to cluster in RCP liquids is weak, we believe this is a reasonable simplification, and it corresponds to $g_{AA}(r) = g_{BB}(r) = g_{AB}(r)$ in the absence of fillers. Thus, the monomer-nanoparticle attraction physically corresponds to an energy lowering upon transfer of a monomer from the pure RCP melt environment to the fullerene surface given by

$$\varepsilon_{An}^{eff} = \varepsilon_{An} - f_A\varepsilon_{AA} - (1 - f_A)\varepsilon_{AB} \tag{6.6}$$

$$\varepsilon_{Bn}^{eff} = \varepsilon_{Bn} - (1 - f_A)\varepsilon_{BB} - f_A\varepsilon_{AB} \tag{6.7}$$

Using the above equations and the energy parameters of Table 6.1, the effective monomer-filler attraction strengths as a function of composition for the 4 sets of random copolymers that are studied in depth are plotted in Figure 6.3. One sees that the effective transfer energies are (of course) different for the *A* and *B* monomers, and typically change by 2-3 thermal energy units as copolymer composition varies from *A*-rich to *B*-rich. These values are used in eqn (6.3) to model polymer-particle interactions of strength ε_{pn}^{eff} with $\alpha_{pn} = 0.12d$.

6.2.3 Goals and Approach

We emphasize that our primary goal is to combine statistical mechanical theory with computational chemistry calculations of interaction parameters to study the structure and miscibility of fullerenes dissolved in a specific class of *AB* random copolymers. Most of our results will be based on the reduced "reference system" set of parameters described above. Given the complexity of the problem, the uncertainty in quantum chemical input, and the model simplifications, let alone the approximate nature of the statistical mechanical theory, our goal is not quantitative predictability. Rather we aim to gain insight concerning how RCP chemistry and composition determines miscibility trends, dispersion mechanisms and effective interactions between fullerenes. By comparing our calculations with Flory-Huggins theory and a simpler effective homopolymer PRISM approach, based on the *same* input parameters, the role of correlation effects and copolymer sequence disorder captured in PRISM theory is established. We initially fix temperature to 440*K* in sections 6.3 and 6.4 per recent experimental studies[16]. The surprisingly complex effect of changing temperature is explored in section 6.5.

6.3 Structural Correlations

6.3.1 Interfacial Packing

The monomer-nanoparticle pair correlation function quantifies how *A* and *B* monomers statistically pack and locally segregate around a filler in the melt. Figure 6.4 shows results for CNSty-MMA as a representative example. The inset shows that as the fraction of CNSty (*A* monomer) increases, the effective attraction of both monomers with the fullerene monotonically decreases, which results in a reduction of the pair correlations near contact. For all compositions less than ~65% we find $\varepsilon_{An}^{eff} > \varepsilon_{Bn}^{eff}$, and hence $g_{An} > g_{Bn}$ for $f_A < 0.65$. Local surface segregation can be dramatic, e.g., the contact value of g_{An} is more than twice that of g_{Bn} for $f_A = 0.1$. For 70% composition, the two g_{pn} curves coincide almost exactly due to the equal propensity of both monomers to adsorb, and for $f_A > 0.7$ one has $g_{Bn} > g_{An}$. The strong sensitivity of interfacial structure to RCP composition is present only at small filler-monomer separations, reflecting the short-range attraction and packing frustration associated with a quenched random sequence.

6.3.2 Filler Potential of Mean Force

Figure 6.5 shows the PMF between two fullerenes dissolved in the same CNSty-MMA RCP studied in Figure 6.4. At 10% CNSty, the effective adsorption energies of both monomers are large (see inset of Fig. 6.4), sufficiently so that if they were homopolymers one expects bridging. Qualitatively, the latter is seen since the PMF displays a modest (since the filler is small) bridging minimum of 0.84 k_BT at a separation of one monomer diameter, along with a stronger contact attraction of ~1.83 k_BT due to the direct fullerene attraction. Note, however, that

the PMF at contact is significantly less attractive than the bare strength of 2.5 k_BT, a reflection of its reduced probability due to the tendency to form particle separated bridging configurations.

As the copolymer composition is increased and MMA becomes the minority species, both effective interfacial attraction strengths decrease significantly but remain well in excess of the thermal energy (inset of Fig. 6.4). Hence, the PMF is expected to acquire some features characteristic of the presence of adsorbed layers and a repulsive steric stabilization type of organization[18, 25]. This effect is manifested in Figure 6.5 as a weakening of the bridging minimum, essentially the same contact aggregation minimum, and the emergence of a small repulsive barrier of ~0.235k_BT at a fullerene surface-to-surface separation of roughly one half a monomer diameter. However, at 90% MMA, although the bridging minimum is further suppressed, the repulsive barriers *do not grow* beyond what is obtained for 70% composition, and the contact attraction deepens. Hence, importantly, the PMF is a *non-monotonic* function of RCP composition. The intermediate composition 70% MMA system has the weakest attractive features and hence is the most soluble system.

We now turn to the solubility question, and given the above findings we expect subtle non-monotonic variation of fullerene miscibility depending on the specific monomers chemistries and RCP composition. The origin of this behavior is the non-additive competition between the direct fullerene attraction and polymer-mediated bridging, steric stabilization and depletion.

6.4 Isothermal Miscibility

6.4.1 PRISM predictions and Comparison to Experiment

Figure 6.6 shows the spinodal phase diagram in the representation of the critical nanoparticle volume fraction as a function of (A-B) RCP composition (f_A) for Acrylonitrile-Styrene (AN-Sty), Cyanostyrene-Styrene (CNSty-Sty), Methyl Methacrylate-Styrene (MMA-Sty) and Cyanostyrene–MMA (CNSty-MMA). The critical volume fraction is defined as the volume fraction of nanoparticles beyond which the system spinodally phase separates. As a reference, the miscibility limit volume fraction of C_{60} in the pure homopolymer melts are 18.5%, 16.3%, 18.7% and 11.9% for Sty, AN, CNSty and MMA, respectively. For both the AN-Sty and MMA-Sty copolymers, as the fraction of *A* monomer increases from zero the miscibility increases until a critical composition after which the trend reverses. For both copolymers, the maximum dispersion occurs at ~40% composition. The maximum soluble fullerene volume fraction is 24% for AN-Sty and 40% for MMA-Sty, which are greater than the values achieved in the parent homopolymer melts.

Figure 6.6 also shows the miscibility trends exhibit qualitative changes if the RCP chemistry is changed to CNSty-Sty and CNSty-MMA. As the *A* monomer composition is increased, solubility in CNSty-MMA first decreases compared to the pure MMA melt, then reverses around $f_A = 0.1$, after which it grows to a large maximum value at ~ 75%, before again decreasing. Such complexity is absent for CNSty-Sty and there is no clear optimum copolymer composition, with the miscibility limit fullerene volume fraction ~ 17-19% for all compositions.

The miscibility trends predicted by PRISM theory for AN-Sty and CNSty-Sty can be compared to recent experiments[16] and the estimated solubility limits are shown in Figure 6.7. The highest miscibility of C_{60} (12 wt%) in the AN-Sty melt occurred at 45% AN copolymer, and

is far above the ~4% value for pure polystyrene. For CNSty-Sty there was no clear optimal composition with a C_{60} miscibility of ~ 4-5 wt%, significantly lower than in the AN-Sty copolymer. These observations are in good qualitative agreement with the theoretical calculations in Figure 6.6. Our results for CNSty-MMA and MMA-Sty are testable predictions.

Finally, a RCP melt of di-methyl-amino-ethyl-methacrylate (DMAEMA)–MMA was studied. In contrast with the qualitative agreement between theory and experiment discussed above, our initial calculations did not agree with the observation[16] that the miscibility limit of C_{60} in 50/50 DMAEMA-MMA is *at least* 20%, higher than any other system studied. Rather, PRISM calculations based on the same modeling of interaction potentials as above predicts very poor dispersion, almost zero (0.24% for a 50/50 composition). However, we believe there is a qualitative chemical difference for this polymer since DMAEMA is electron donating, while AN-Sty and Sty-CNSty are electron withdrawing. Although C_{60} is an amphoteric molecule, it is a better electron acceptor than donor. This suggests that DMAEMA-based RCP's are very different due to a transfer of the lone pair electrons of the amino N atom leading to a "partial charge" on the fullerene which qualitatively alters the C_{60}-C_{60} interaction by introducing repulsion between fullerenes, an effect not accounted for in our calculations.

We now quantitatively include the above donor-acceptor partial charge transfer ($DMAEMA^{+}$-C_{60}^{-}) effect which results in an effective dipole-dipole potential. The intermolecular interaction was computed using density functional tight binding theory (DFTB)[31] where the $DMAEMA^{+}$ cations were placed "behind" each C_{60}^{-} anion at the optimized distance of ~3.5 Angstroms from the C_{60} surface. The interaction of two of the C_{60} anion-cation pairs as a

function of the separation was then explicitly computed using DFTB. A homogeneous dielectric screening corresponding to DMAEMA was added based on classical electrostatics via the standard multiplicative factor of $1/\varepsilon^{DMAEMA}$, where $\varepsilon^{DMAEMA} = 6$. The resulting interaction potential is shown in the inset of Figure 6.8, and using it PRISM theory calculations were repeated. Figure 6.8 shows the results based on both ignoring and including this special effect. Including it results in a miscibility curve that remains concave upwards, but the amount of dispersion predicted is dramatically enhanced and reaches 20% miscibility at an A-monomer composition of ~55%. The latter specific and quantitative trend is in rough agreement with experimental observations[16].

Numerically-intensive calculations of spinodal curves based on the simultaneous divergence at zero wavevector of all partial structure factors at arbitrary filler loading have also been performed. In contrast to findings for large fillers[22], the many body effects contained in the beyond virial analysis tend to increase, not decrease, miscibility. However, this appears to be a modest effect, and even if a relatively high Φ_c is predicted using eqn (2.10) we find the results are reliable for the qualitative elucidation of trends at the level the present work aims for[32].

6.4.2 Role of Non-Universal Parameters

One can ask how sensitive the results presented in the previous section are to changes of material structural or interaction potential parameters. This is admittedly a difficult question and is quantitatively explored in Appendix B. In this section we summarize our conclusions.

We relaxed the following seven simplifications of our "reference model": (a) fixed melt packing fraction (0.4352) or, equivalently, fixed polymer melt dimensionless compressibility, S_0 = 0.25, for all copolymer compositions, (b) fixed local aspect ratio of l/d = 1.2, (c) equality of the monomer and fullerene hard core diameters (D/d = 1), (d) fixed interfacial attraction range of 0.12d, (e) copolymer-composition-dependent interfacial attraction energies, (f) N = 100, and (g) ε_{nn} = 2.5 for the direct fullerene attraction. This exercise provides insight on the relative importance of these parameters, which are likely to vary with RCP composition, and how sensitive the results are to absolute values within chemically reasonable bounds.

Relaxing the assumption of constant l/d, S_0 and η_t values for every copolymer composition, or changing their fixed values consistent with known equation-of-state and conformational statistics data, does not qualitatively change the miscibility trends found in section 6.4.1 (points (a), (b)). The sizes of the studied monomers vary between d ~ 0.6–0.8 *nm*, so D/d need not be exactly unity. However, reasonable variation of this ratio does not change qualitatively the miscibility predictions (point (c)). The absolute fullerene solubility limit results are sensitive to the magnitude of the direct attraction between nanoparticles, but the key prediction that an intermediate RCP composition can result in optimum miscibility is robust to variations of the direct attraction within the chemically reasonable window of $2 \le \beta\varepsilon_{nn} \le 4$ (point (g)). Increasing N = 100 to N = 10,000 results in very little changes of the spinodal curves (point (f)), in analogy with classic polymer-solvent systems at "low" solvent volume fractions[33].

On the other hand, the downward concavity of the spinodal miscibility plots in Figure 6.6 reverses to an upward concavity form when effective attraction strengths are not varied with

composition (point (e)). The choice of interfacial attraction range, which modifies packing correlations[18, 19, 22], also seems of major importance as the non-monotonic trend of miscibility is predicted only when $0.1d \leq \alpha_{pn} \leq 0.15d$ (point (d)); the latter range of values is consistent with our quantum chemical calculations. The spatial ranges of *A* and *B* attractions need not be exactly the same, and our results are robust to a realistic variability. Hence, we conclude the "essential parameters" at zeroth order are the composition-dependent strength and spatial range of effective polymer-fullerene attractions.

6.4.3 Understanding Correlation Effects on Miscibility

Our finding that the essential parameters that result in the non-monotonic miscibility curves are the composition–dependent effective polymer-fullerene short range attractions, which result in composition-dependent polymer-particle packing and PMFs, suggests that to develop an intuitive understanding of miscibility trends one should closely examine the energetics. To pursue this we adopt the AN-Sty system as a representative case that illustrates the general principles underlying the optimum dispersion occurring at an intermediate RCP composition.

One sees from Figure 6.6 that in the AN-Sty melt the miscibility peaks at f_A = 0.4 corresponding to a 40% AN random copolymer. At this composition, the effective interaction strengths of Sty and AN are 2.2 and 1.6 k_BT, respectively. What is the significance of these numbers? To answer this, Figure 6.9 shows the fullerene PMF in a *homopolymer* melt at various polymer-particle attraction strengths with all other parameters kept the same as for the reference model RCP studies. When $\beta\varepsilon_{pn}$ = 0.1, the direct attraction reinforces entropic depletion, resulting

in strong contact aggregation with a PMF minimum of ~ 4 k_BT. As ε_{pn} is increased, the polymers adsorb on the filler leading to a decrease in contact aggregation due to steric stabilization. A small bridging minimum then emerges when $2 \leq \beta\varepsilon_{pn} \leq 3$. The spinodal curve for this homopolymer system is shown in the inset, and a miscibility peak is seen at ε_{pn} = $2.1k_BT$. This suggests that when the interfacial attraction reaches the latter value there is an onset of bridging. This is relevant to RCP systems because AN-Sty melt miscibility is optimized when the majority Sty species composition is such that its attraction strength just crosses $2.1k_BT$.

To provide further support for the above interpretation, we consider the CNSty-MMA melt where maximum miscibility is achieved at 80% *A*-composition. The effective interaction of CNSty (the *A* monomer) varies from 2.3 to 2.04 k_BT when f_A increases from 0.7 to 0.8. Miscibility thus peaks at 80% composition since the majority species (CNSty) composition has just crossed the onset of bridging at $2.1k_BT$ while the corresponding homopolymer-fullerene attractions for CNSty and MMA (1.48 and $3.18k_BT$, respectively) are far from this optimally mixed state value. This is the fundamental reason and mechanism for why random copolymers can result in better miscibility as compared to the two limiting homopolymers. The fact that optimum miscibility in both AN-Sty and CNSty-MMA melts is obtained at 40% and 80% compositions implies that spatial dispersion is maximum when the majority composition monomer is present at a level such that it begins to bridge. The location of the latter at $\varepsilon_{pn}=2.1k_BT$ is for α_{pn} = $0.12d$ and is not universal. However, the shift is modest for the attraction ranges relevant to the systems studied where $0.1d \leq \alpha_{pn} \leq 0.15d$.

6.4.4 Average Homopolymer Results

It is interesting to ask how sensitive the key aspects of Figure 6.6 are to differential adsorption of *A* and *B* monomers on the fullerene. The fact that the maximum miscibility is attained when the monomer with higher composition reaches or crosses the point of the onset of bridging in the PMF hints that perhaps a weighted "average homopolymer" model might result in similar behavior. To study this, we define an effective homopolymer that interacts with the filler via a single interfacial attraction energy equal to a weighted mean of Equations (6.6) and (6.7):

$$\varepsilon_{pn}^{homo,eff} = f_A \varepsilon_{An}^{eff} + (1 - f_A)\varepsilon_{Bn}^{eff} \tag{6.8}$$

where $\varepsilon_{\alpha n}^{eff}$ is a function of f_A per equations (6.6) and (6.7).

Calculations based on Equation (6.8) are shown in Figure 6.10 for AN-Sty, CNSty–Sty and CNSty–MMA, and contrasted with the full RCP results of Figure 6.6. For AN-Sty, the highest miscibility occurs at a ~50% composition where $\varepsilon_{pn}^{homo,eff} \approx 2.1 k_B T$. The high miscible filler volume fraction of ~ 44% is nearly twice that obtained based on the RCP model. The difference in miscibility between the latter and the average homopolymer for CNSty–Sty and CNSty–MMA are quantitatively less pronounced than found for AN-Sty, and the qualitative trends agree for the two models.

We conclude that the "average homopolymer" simplification is qualitatively reliable, but can incur significant system-specific errors. For example, the miscibility of the 3 RCP systems analyzed in this section based on the full RCP description are smaller at all compositions than

what is predicted based on the average homopolymer description. This is as expected since in a real RCP system with unequal A and B attractions with the filler there is always packing frustration and differential adsorption due to sequence disorder, which prior PRISM studies have shown results in a less thermodynamically stable mixture[23].

6.4.5 Flory – Huggins Theory Predictions

We now apply the simplest mean field incompressible lattice Flory-Huggins (FH) model[32] to our systems treated as a ternary mixture of nanoparticles *n*, and a random copolymer of *A* and *B* monomers. An elementary analysis yields the Helmholtz free energy of mixing per lattice site of

$$\Delta\overline{F}_{mix} = \Delta\overline{U}_{mix} - T\Delta\overline{S}_{mix} = k_B T\left[\chi\varphi(1-\varphi) + \frac{\varphi}{N}\ln\varphi + (1-\varphi)\ln(1-\varphi)\right] \tag{6.9}$$

where $\varphi((1-\varphi))$ is the total polymer (nanoparticle) volume fraction, and χ is the Flory interaction parameter

$$\chi \equiv \frac{z}{2}\left[\frac{2f_A\varepsilon_{An} + 2(1-f_A)\varepsilon_{Bn} - \varepsilon_{nn} - f_A^2\varepsilon_{AA} - (1-f_A)^2\varepsilon_{BB} - 2f_A(1-f_A)\varepsilon_{AB}}{k_B T}\right] \tag{6.10}$$

and z is the lattice coordination number. The spinodal curve follows as $\frac{1}{N\varphi} + \frac{1}{(1-\varphi)} = 2\chi$, which in the long chain, dilute filler limit of interest $(N\varphi \gg (1-\varphi))$ becomes

$$\Phi_c = \frac{1}{2\chi} \tag{6.11}$$

The FH critical filler volume fractions as a function of RCP composition are shown in Figure 6.11 for T = 440*K*, z = 12 and $\beta\varepsilon_{nn}$ = 2.5. The miscibility limit is a weak and (basically) monotonically increasing or decreasing function of composition, contrary to experiment and PRISM theory. The absolute magnitude of C_{60} solubilities are usually very small (~1%-2.7%) compared to both experiment and PRISM theory. This suggests FH theory is inadequate due to its neglect of spatial correlations and the effect of chain connectivity on enthalpy. How one might try to empirically "correct" the FH approach to account for the latter correlation effects is unclear to us.

6.4.6 Fullerenes in Multiblock Copolymer Melts

Adopting the same model and methods as outlined in chapter 5, we ask how the multi-block copolymer (MBCP) architecture affects fullerene miscibility to make testable comparison between a RCP and MBCP melt as well as establish the effect of order on the monomer sequence.

Using the same models and interactions as above (composition f_A is now fixed at 0.5), we make testable predictions of the spinodal demixing volume fraction of fullerenes in MBCP melts. Table 6.2 shows the results for four sets of copolymers of different architecture: random copolymer, and MBCPs of block lengths R = 1, 5 and 10, at 440K and 370K. There are three notable trends. (1) For every MBCP, the nanoparticle miscibility decreases very weakly, if at all, with increasing block length R. We suspect this is because the energetic chemical heterogeneity for most of these copolymers is modest at 50% composition resulting in both A and B monomers being in the same homopolymer organizational regime (D, S, B) thereby rendering it difficult for

the small fullerenes to distinguish the blocks. The most discernible change of miscibility with block length is observed for AN-Sty at 370K for which the energy difference $\Delta\beta\varepsilon = \left|\beta\varepsilon_{An} - \beta\varepsilon_{Bn}\right| = 0.72$ is the largest among all the copolymers studied. (2) The MBCPs show different variations of miscibility with temperature. For all block lengths, fullerene solubility in AN-Sty, MMA-Sty and CNSty-MMA decreases with cooling, while for CNSty-Sty it increases. The physical reason for the latter trend is qualitatively identical to that discussed in depth in 6.4.3. Briefly, upon cooling from 440K to 370K, the net energetics of the CNSty-Sty copolymer shifts towards the point of maximum miscibility at an effective adsorption energy of ~ 2.1kT; in contrast, such cooling leads to the opposite behavior for the other chemical systems studied, i.e. they move away from the maximum miscibility condition. (3) For nearly all copolymers studied greater fullerene miscibility is predicted in MBCPs compared to the RCP. As shown in figure 6.6, the miscibility obtained in these 50-50 RCPs is mostly higher than the corresponding homopolymers. Hence, we conclude that, within the purview of our study, fullerenes can be best dispersed by multiblock copolymers of block lengths $R \leq 10$. We do not claim that this is universal as the chemistry of the specific polymers in the melt is the most important determinant of miscibility.

6.5 Complex Effect of Temperature

All the above calculations were performed at $440K$ per recent experiments[16]. One can ask what is the effect on miscibility if the temperature is varied, even over a relatively narrow range? The most obvious and direct consequence of varying temperature is a rescaling of all energies by the same factor, i.e., $\beta\varepsilon_{ij}$. According to Flory-Huggins theory, the χ parameter varies as the inverse

temperature and one expects miscibility decreases with cooling corresponding to UCST behavior (Figure 6.11). Does this hold based on PRISM theory? Given the importance of temperature-sensitive spatial correlations, the answer is unclear. Of course, when temperature is varied other parameters change, such as the melt packing fraction, compressibility and chain backbone stiffness. However, these variations are very small, and the analysis in Appendix B suggests they are not important. Hence we ignore them, and focus on the direct effect associated with $\beta\varepsilon_{ij}$.

Figure 6.12a shows PRISM theory spinodal calculations at several temperatures for MMA-Sty. Three features stand out: (i) miscibility of C_{60} in a pure Styrene homopolymer melt (f_A = 0) *decreases* with heating, (ii) miscibility in a pure MMA homopolymer melt (f_A = 1) *increases* with heating, and (iii) the optimum composition (miscibility peak) significantly changes with temperature. The inset of Figure 6.12a shows that upon heating from 370K to 500K, the effective C_{60}-Sty interaction strength decreases from 1.75 k_BT to 1.3 k_BT, and the system moves away from the miscibility peak centered at ~2.1k_BT. This explains why the solubility decreases if temperature is raised. On the other hand, ε_{pn}^{eff} for MMA decreases from 3.8 k_BT to 2.8 k_BT, i.e., shifts from the bridging regime towards the steric stabilizing peak as temperature grows. Thus, the dispersion trend for this monomer is exactly the opposite of Sty. When temperature is varied, the ε_{pn}^{eff} for the intermediate compositions also change and, thus, the point at which the monomer with the greater composition reaches an effective attraction strength of 2.1k_BT also changes resulting in a shift of the miscibility peaks.

Figure 6.12b shows the effect of variable temperature on fullerene miscibility in AN-Sty (inset) and CNSty-Sty melts. As the temperature drops from 500 to 440K, there is no qualitative

change of the spinodal curves for the CNSty-Sty melt, and no clear optimum copolymer composition. At 370K, the miscibility curve becomes concave upwards, which means better dispersion is obtained in the parent homopolymer melts than for any random copolymer composition. The inset shows the temperature dependence in the AN-Sty melt. As found for the CNSty-MMA case, the composition at which the highest miscibility occurs changes as well as the miscibility in the two limiting homopolymer matrices. At 370*K*, the non-monotonic behavior disappears completely with the *B* homopolymer (Sty) yielding the best dispersion.

The above results demonstrate a remarkably rich sensitivity to changing temperature. The predicted behavior does not correspond to either simple UCST or LCST behavior. For a specific random copolymer, at fixed composition the filler miscibility can either increase or decrease with cooling or heating. Hence, PRISM theory with quantum chemical input for polymers that interact with fullerenes via strong, short range specific attractions suggests a material-specific complex dependence of miscibility on temperature in qualitative contrast with Flory-Huggins theory. The key physics that underlies this complexity is nonrandom packing, differential surface segregation, and competition between steric stabilization and bridging, which in turn are intimately related to the composition-dependent polymer-filler energetics. The predicted complex thermal behavior of miscibility is amenable to experimental and simulation tests.

6.6 Summary

We have combined polymer integral equation theory and computational chemistry methods to study the interfacial packing, effective nanoparticle interactions, liquid demixing, and spatial dispersion mechanism of fullerenes dissolved in random copolymer melts which interact with the

nanofiller via strong, short range, and tunable non-covalent electron donor-acceptor interactions. A statistical mechanical basis has been formulated for using random copolymers to optimize fullerene dispersion at an intermediate composition. Key general features, typically not present in PNCs composed of larger fillers which interact non-specifically with polymers, include the strong and spatially very short range nature of C_{60}-polymer attractions, and the nonrandom packing and surface segregation of *A* and *B* monomers around the fullerene which is sensitive to chemistry, chain connectivity, and the small nature of the nanoparticle.

Theoretical pair structure calculations reveal a strong sensitivity of interfacial packing close to the fullerene surface to RCP composition and adsorption energy mismatch. The PMF between fullerenes also displays rich trends, often non-monotonic with copolymer composition, reflecting a competition between direct filler attractions and polymer-mediated bridging and steric stabilization. The spinodal phase diagrams are in good qualitative agreement with the very different observations[16] on AN-Sty and CNSty-Sty melts. Testable predictions are made for MMA-Sty and CNSty-MMA which are potential future targets to further improve dispersion.

A physical understanding of the isothermal miscibility predictions has been achieved in two steps. First, the role of nonuniversal material parameters was investigated, and the distinctive non-monotonic variation of miscibility with copolymer composition is found to be primarily a consequence of composition-dependent, short range attractions between the *A* and *B* monomers with the fullerene which induce nonrandom and composition-dependent interfacial packing correlations and polymer-mediated filler interactions. Second, a connection to the non-monotonic

miscibility behavior in homopolymer systems has been elucidated based on the idea that effective energetics can be tuned to maximize the steric stabilization features of the filler PMF.

The PRISM RCP miscibility calculations were contrasted with an effective homopolymer PRISM model and the Flory-Huggins model. The former appears to be qualitatively reasonable but can incur large quantitative errors since it misses preferential packing of *A* and *B* monomers near nanoparticles. The latter appears to fail qualitatively due to its neglect of spatial correlations.

A remarkably rich temperature dependence of the phase behavior is predicted which depends on the chemical system and reflects the thermal sensitivity of spatial correlations. Simple UCST or LCST behavior is often not found, but rather for a specific random copolymer at fixed composition the fullerene miscibility can either increase or decrease with cooling or heating, which is not predicted by the Flory-Huggins model for the polymer systems studied.

We also studied the dispersion trends of fullerenes in specific multiblock copolymer melts of experimental interest, and made comparisons with the behavior in a RCP melt of the same bare chemistry. For all the polymers studied, a MBCP composed of short blocks affords better miscibility than either a RCP or the corresponding homopolymer, making the MBCP a potentially novel option to strongly disperse small, strongly attractive particles.

Finally, we emphasize much remains to be done. For example, studying the full spatial mixture structure at high fullerene loading, in real and Fourier (scattering) space, or the role of polymer grafts attached to fullerenes on miscibility and structure, are interesting directions. Since

fullerenes readily crystallize, generalizing the theoretical phase behavior analysis to treat this aspect, as opposed to the present liquid-liquid demixing analysis, is also a worthy future task.

6.7 References

(1) Winey, K. I.; Vaia, R. A. *MRS Bull.* **2007**, 32, 314-319.

(2) Mackay, M. E.; Tuteja, A.; Duxbury, P. M.; Hawker, C. J.; Horn, B. V.; Guan, Z; Chen, G; Krishnan, R. S. *Science* **2006**, 311, 1740-1743.

(3) Alexandre, M.; Dubois, P. *Materials Science and Engineering* **2000**, 28, 1-63.

(4) Shinar, J., Vardeny, Z. V., Kafafi, Z. H., editors, *Optical and electronic properties of fullerenes and fullerene-based materials*; Marcel Dekker: New York, 2000.

(5) Moniruzzaman, M.; Winey, K. I. *Macromolecules* **2006**, 39, 5194-5205.

(6) Kropka, J. M.; Putz, K. W.; Pryamitsyn, V.; Ganesan, V.; Green, P. F. *Macromolecules* **2007**, 40, 5424-5432.

(7) Guralnick, B. W.; Kirby, B. J.; Majkrzak, C. F.; Mackay, M. E. *Applied Phys. Lett.* **2013**, 102, 083305.

(8) Kiel, J. W.; Eberle, A. P. R.; Mackay, M. E. *Phys. Rev. Lett.* **2010**, 105, 168701.

(9) Harris, P. J. *Carbon Nanotube Science : Synthesis, Properties and Applications*; Cambridge: New York, 2009.

(10) Linton, D.; Driva, P.; Sumpter, B.; Ivanov, I.; Geohegan, D.; Feigerle, C.; Dadmun M. D. *Soft Matter* **2010**, 6, 2801-2814.

(11) Laiho, A.; Ras, R. H. A.; Valkama, S.; Ruokolainen, J.; Osterbacka, R.; Ikkala, O. *Macromolecules* **2006**, 39, 7648-7653.

(12) Rasheed, A.; Dadmun M. D.; Ivanov, I.;Britt, P. F.; Geohegan, D. B. *Chem. Mater.* **2006**, 18, 3513-3522.

(13) Rasheed, A.; Chae, H. G.; Kumar, S.; Dadmun, M. D. *Polymer* **2006**, 47, 4734-4741.

(14) Davenas, J.; Alcouffe, P.; Ltaief, A.; Bouazizi, A. *Macromol. Symp.* **2006**, 233, 203-209.

(15) Ratner, M. *Nature Nanotech.* **2013**, 8, 378-381.

(16) Teh, S.; Linton, D.; Sumpter, B.; Dadmun, M. D. Macromolecules *2011*, **44**, 7737-7745.

(17) Schweizer, K. S.; Curro, J. G. *Adv. Chem. Phys.* **1997**, 98, 1-142.

(18) Hooper, J. B.; Schweizer, K. S. *Macromolecules* **2005**, 38, 8858-8869.

(19) Hooper, J. B.; Schweizer, K. S. *Macromolecules* **2006**, 39, 5133-5142.

(20) Hall, L. M.; Schweizer, K. S. *Soft Matter* **2010**, 6, 1015-1025.

(21) Zhao, L.; Li, Y.; Zhong, C.; Mi, J. *J. Chem. Phys.* **2006**, 124, 144913.

(22) Hall, L. M.; Schweizer, K. S. *J. Chem. Phys.* **2008**, 128, 234901.

(23) Hall, L. M.; Jayaraman, A.; Schweizer, K. S. *Curr. Opin. Solid State Mater. Sci.* **2010**, 14, 38-48.

(24) Hall, L. M.; Schweizer, K. S. *Macromolecules* **2011**, 44, 3149-3160.

(25) Hall, L. M.; Anderson, B. J.; Zukoski, C. F.; Schweizer, K. S. *Macromolecules* **2009**, 42, 8435-8442.

(26) Sung, B. J.; Yethiraj, A. *Macromolecules* **2005**, 38, 2000-2008.

(27) Girifalco, L. A. *J. Phys. Chem.* **1992**, 96, 858-861.

(28) Israelachvili, J. *Intermolecular and Surface Forces*; Academic Press: London, 1991.

(29) https://sesres.com/PhysicalProperties.asp

(30) Sherrill, C. D.; Sumpter, B.; Sinnokrot, M. O.; Marshall, M. S.; Hohenstein, E. G.; Walker, R. C.; Gould, I. R. *J. Computational Chemistry* **2009**, 30, 2187-2193.

(31) Elstner, M.; Porezag, D.; Jungnickel, G.; Elsner, J.; Haugk, M.; Frauenheim, T.; Suhai, S.; Seifert, G.; *Phys. Rev. B* **1998**, 58, 7260-7268.

(32) More rigorous calculations of spinodal demixing curves based on the simultaneous divergence of all k = 0 partial structure factors at arbitrary filler loading have been performed for the systems analyzed in the main text based on established numerical PRISM theory methods[22]. We recall that for large hard sphere fillers, $D/d \geq 5$, in a homopolymer melt, it has been previously shown that particle many body effects result in a net destabilisation beyond a filler volume fraction of ≈ 0.2[22]. Contrary to this, for very small attractive particles of the

present work, $D/d = 1$, we find that the selected full many-body calculations predict a higher miscibility compared to virial calculations for all $\Phi_c \geq 0.2$. For the cases where our virial-based miscibility limit volume fractions are large, this quantitative difference may or may not be modest depending on the chemical system under consideration. However, most importantly for the present work, all the miscibility trends discussed in the main text remain qualitatively the same, and thus the virial results are reliable and adequate at the level of accuracy of interest in the present study.

(33) Rubinstein, M.; Colby, R. H. *Polymer Physics*; Oxford University Press: Oxford, 2003.

6.8 Figures

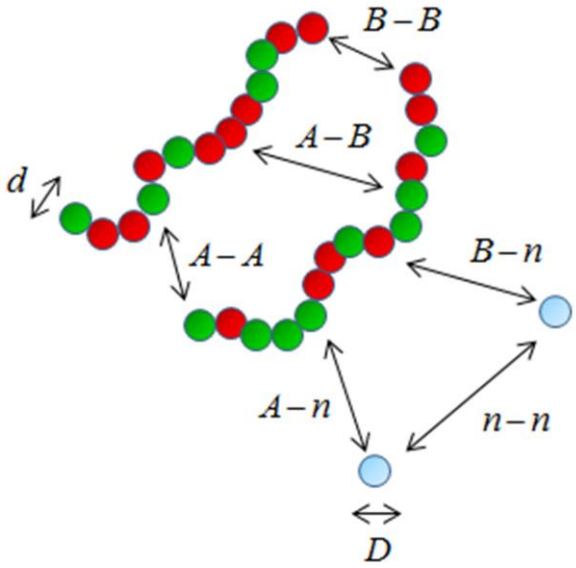

Figure 6.1 Conceptual cartoon of dilute fullerenes in a *AB* random copolymer melt.

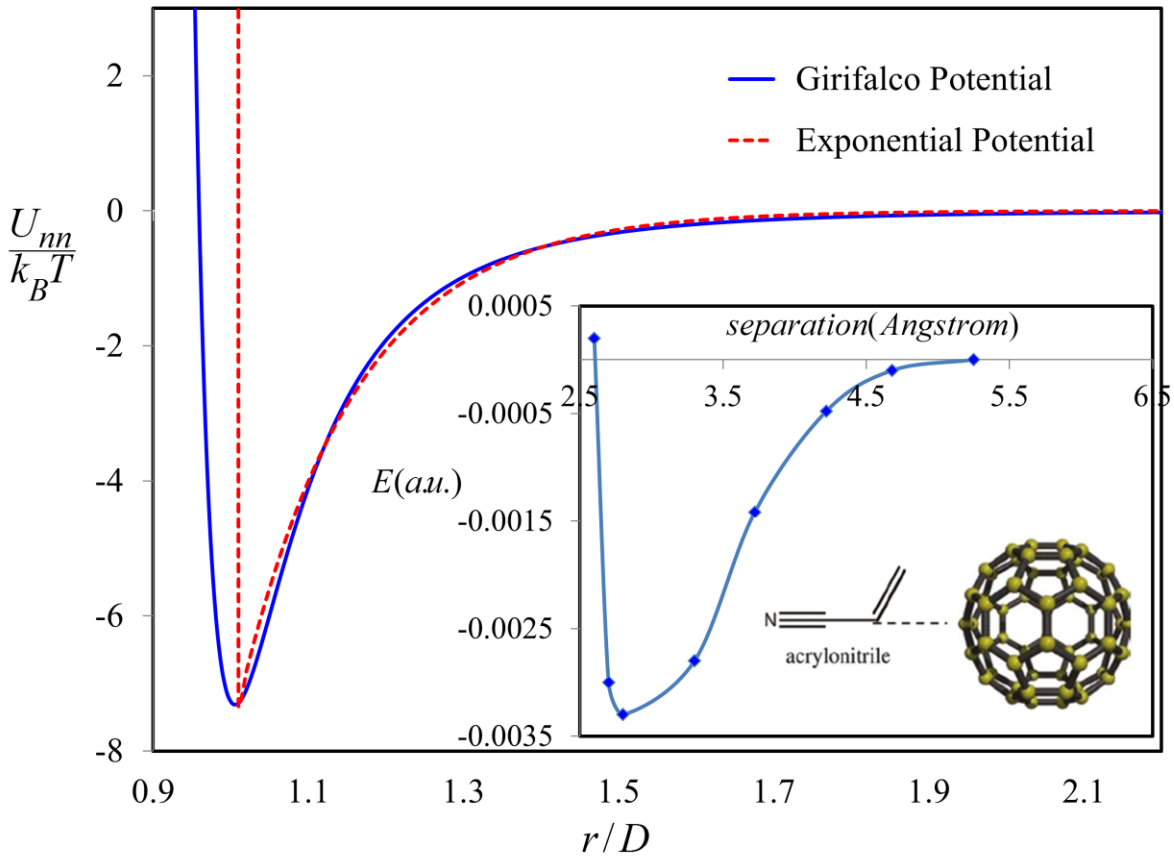

Figure 6.2 Direct interaction potential (units of thermal energy, T = 440*K*) between two C_{60} molecules in vacuum as a function of the dimensionless separation based on Eq(10); a hard core plus exponential tail fit is also shown. Inset: Computational chemistry computed potential energy curve for AN – C_{60} with the C – C bond of AN aligned to the center of the hexagon on C_{60}.

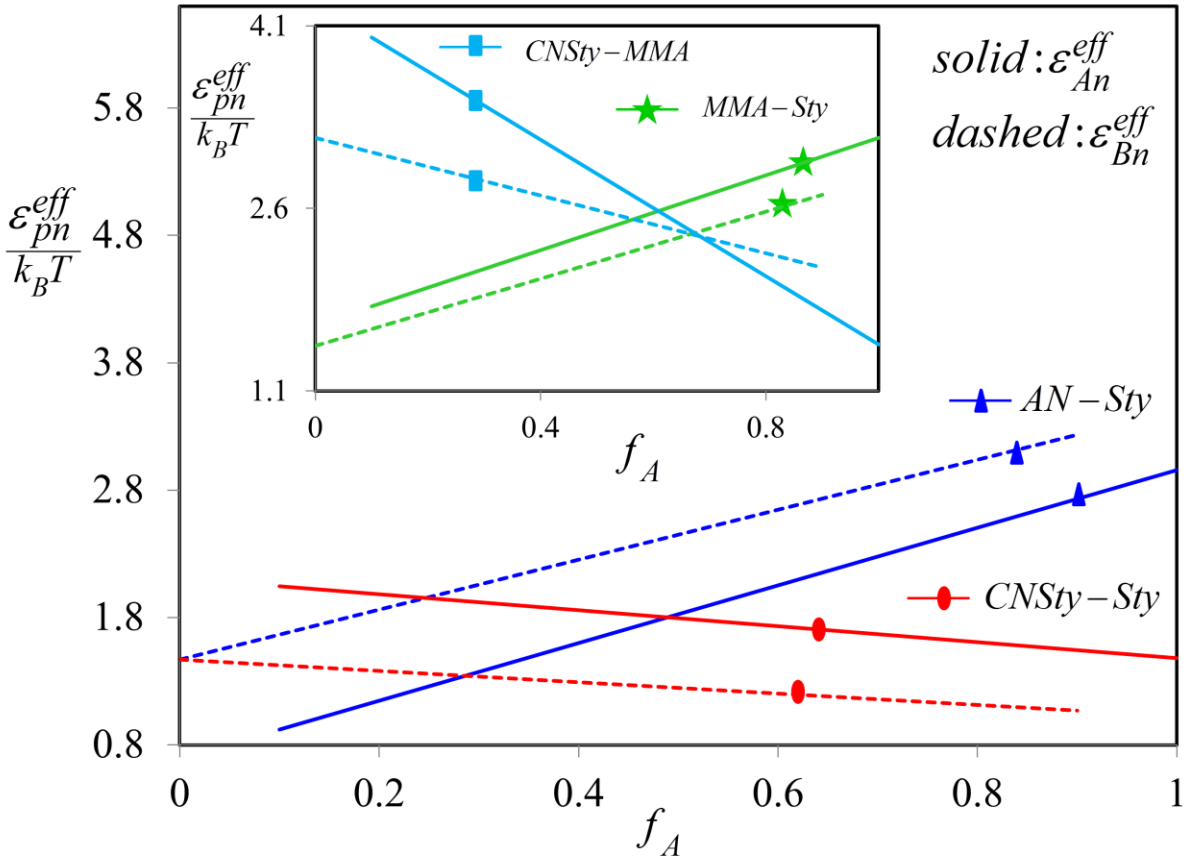

Figure 6.3 The effective pair attraction strength at 440*K* between the *A* (solid) and *B* (dashed) monomers and C_{60} as a function of (A-B) RCP composition for AN-Sty and CNSty-Sty, and (inset): MMA-Sty and CNSty-MMA.

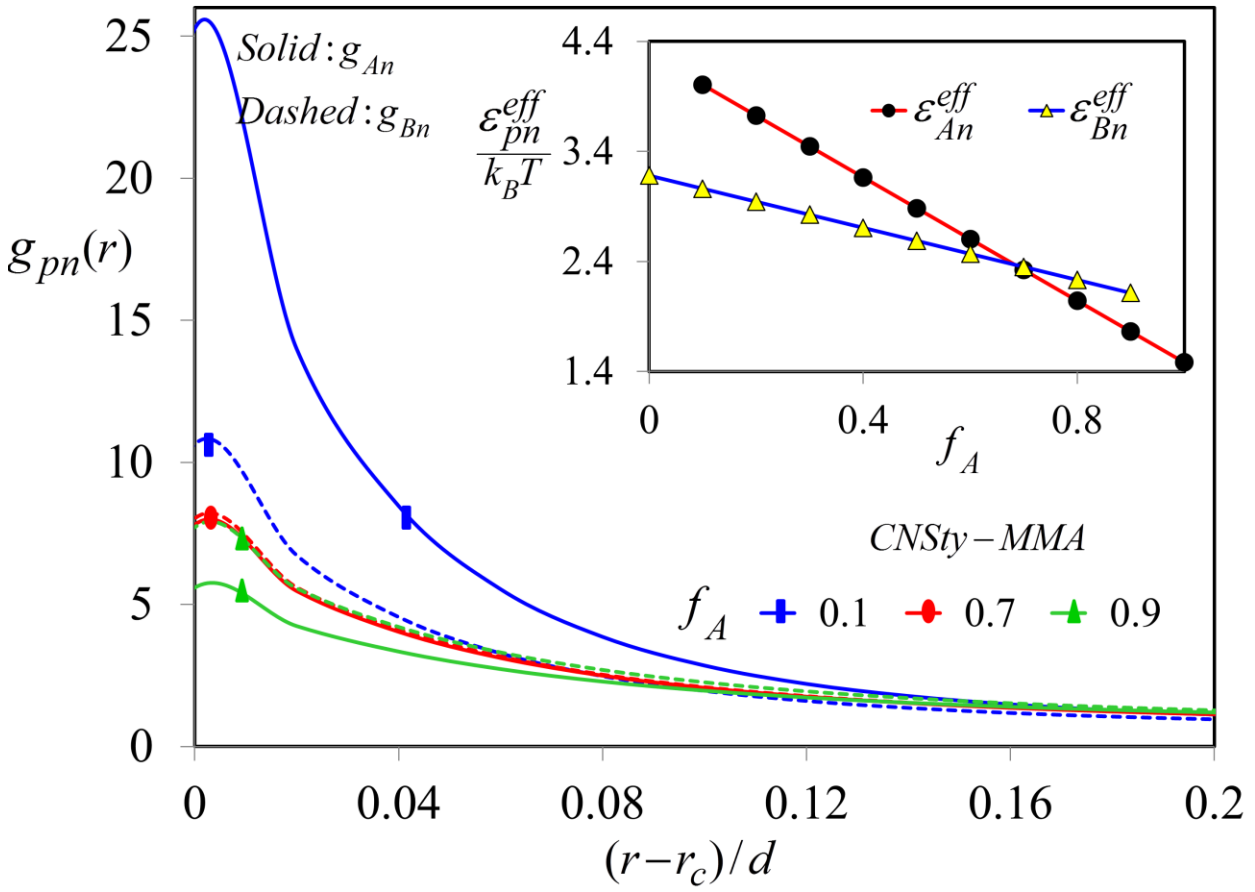

Figure 6.4 *A* (solid) and *B* (dashed) monomer–particle pair correlation functions in random copolymer melt of CNSty-MMA at 440K at the indicated compositions f_A (from top to bottom) of 0.1, 0.7, 0.9. Inset: effective pair attraction strengths between CNSty (*A*) and C_{60}, and MMA (*B*) and C_{60} as a function of RCP composition. The distance of closest approach between a monomer and a particle is defined as $r_c = (D+d)/2$

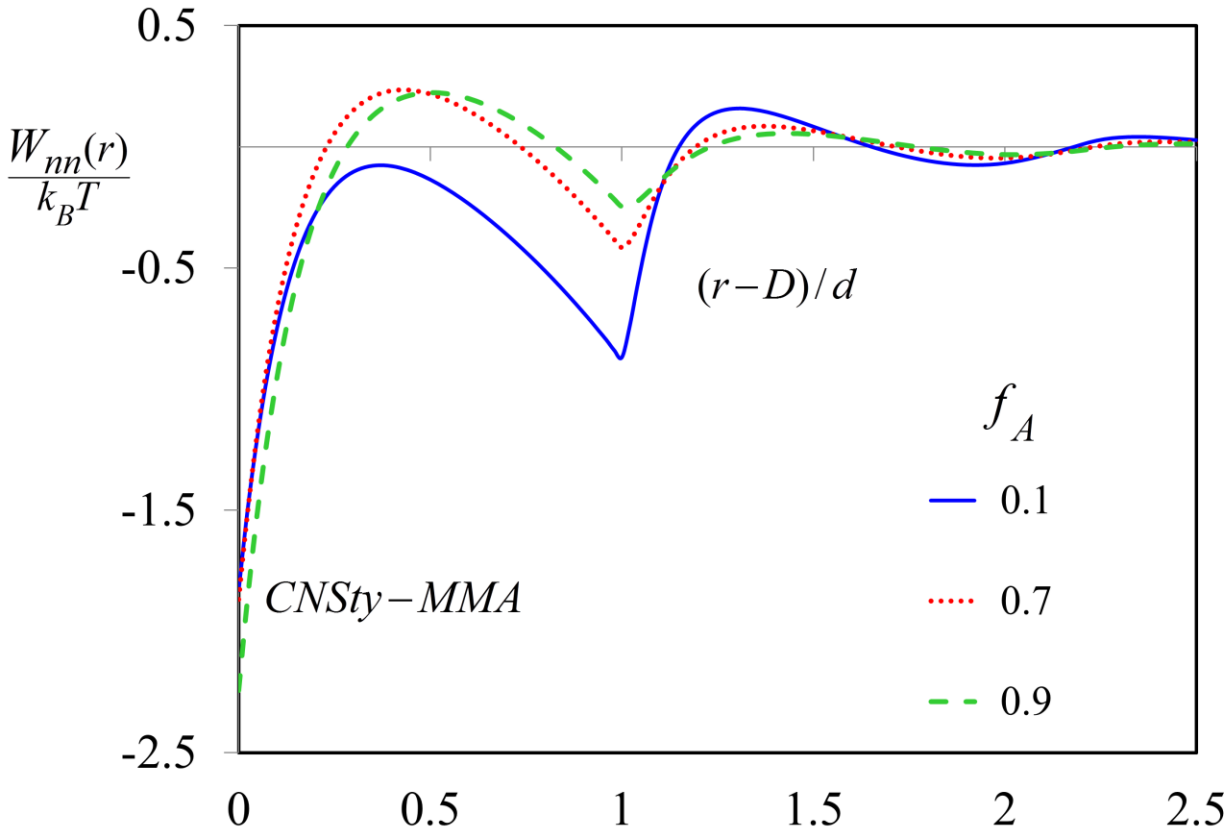

Figure 6.5 Fullerene potential-of-mean-force as a function of dimensionless inter-surface separation in CNSty-MMA at the indicated compositions f_A and T = 440*K*.

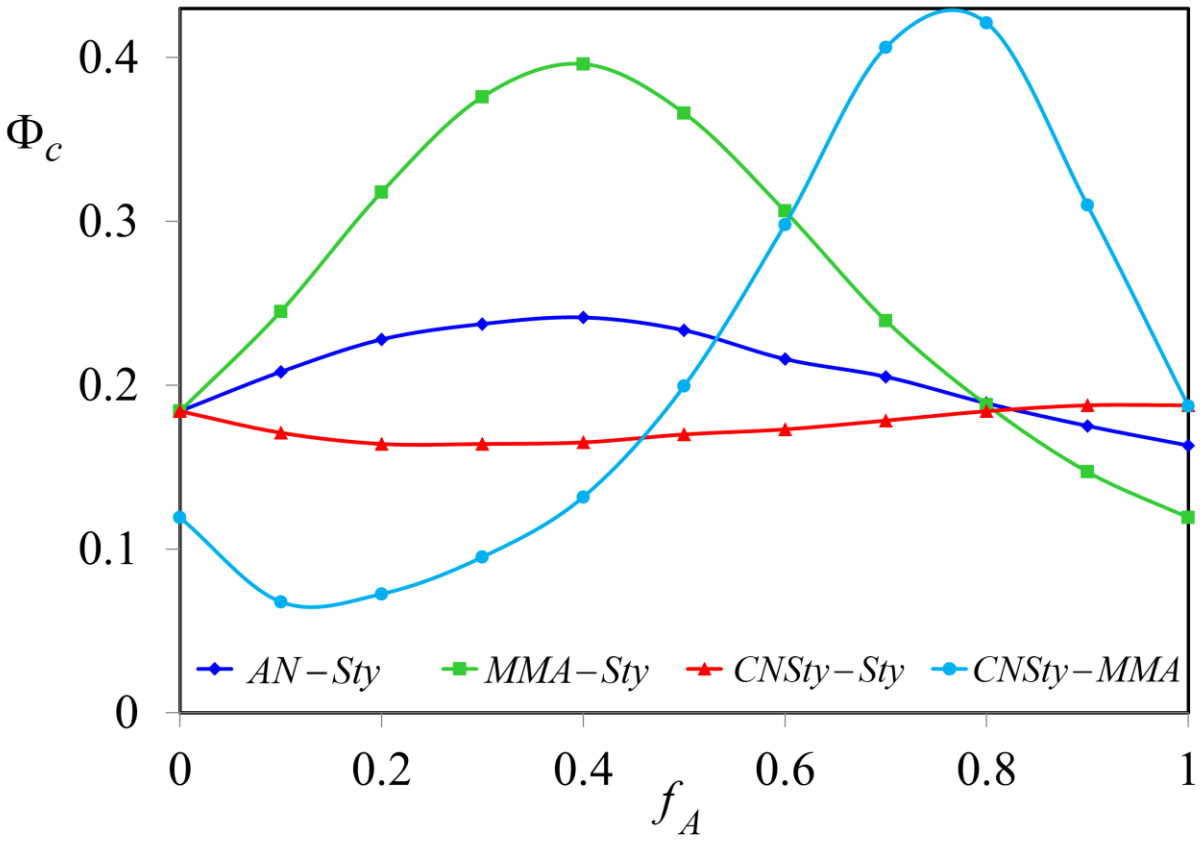

Figure 6.6 Fullerene spinodal volume fraction as a function of composition for T = 440*K* and the indicated copolymer melts.

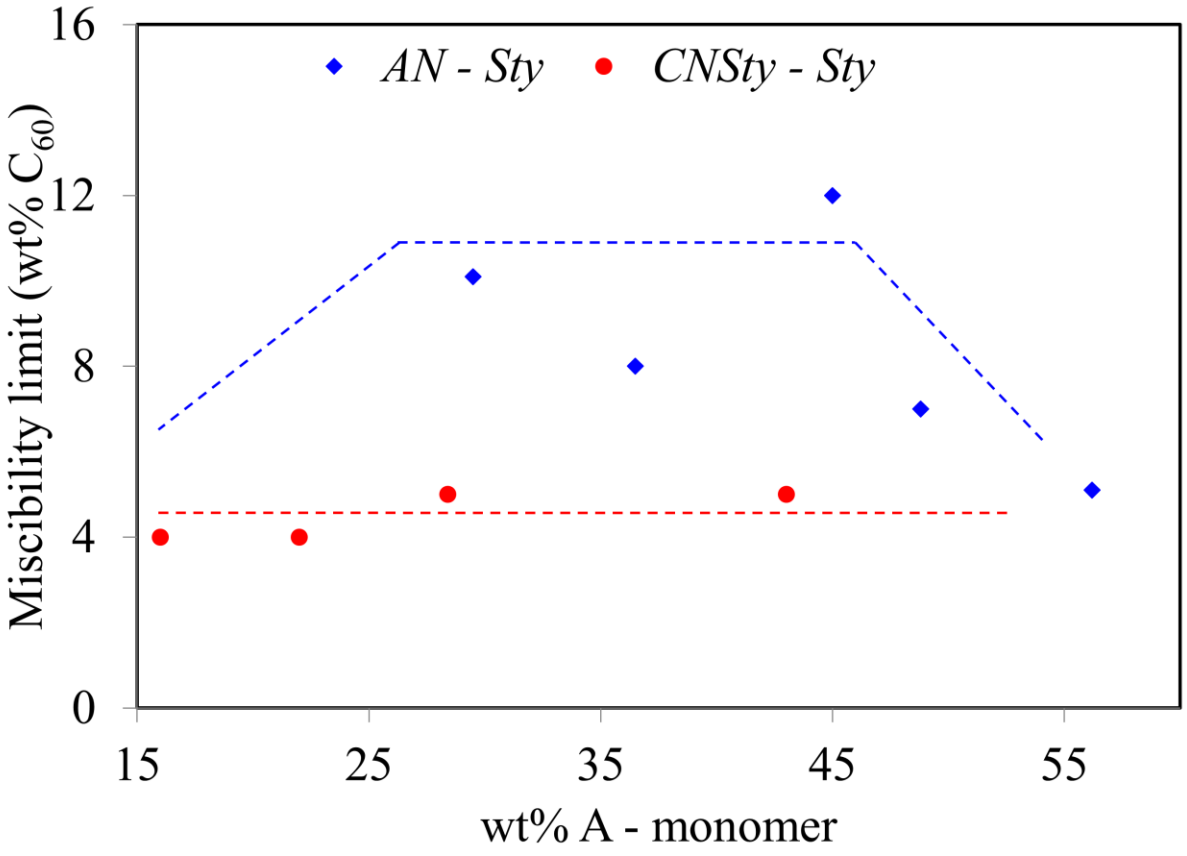

Figure 6.7 Experimental[16] miscibility limit of C_{60} in AN-Sty and CNSty-Sty random copolymer melts. Dashed lines are guide to the eye. In the pure Styrene melt the miscibility limit is ~ 4%.

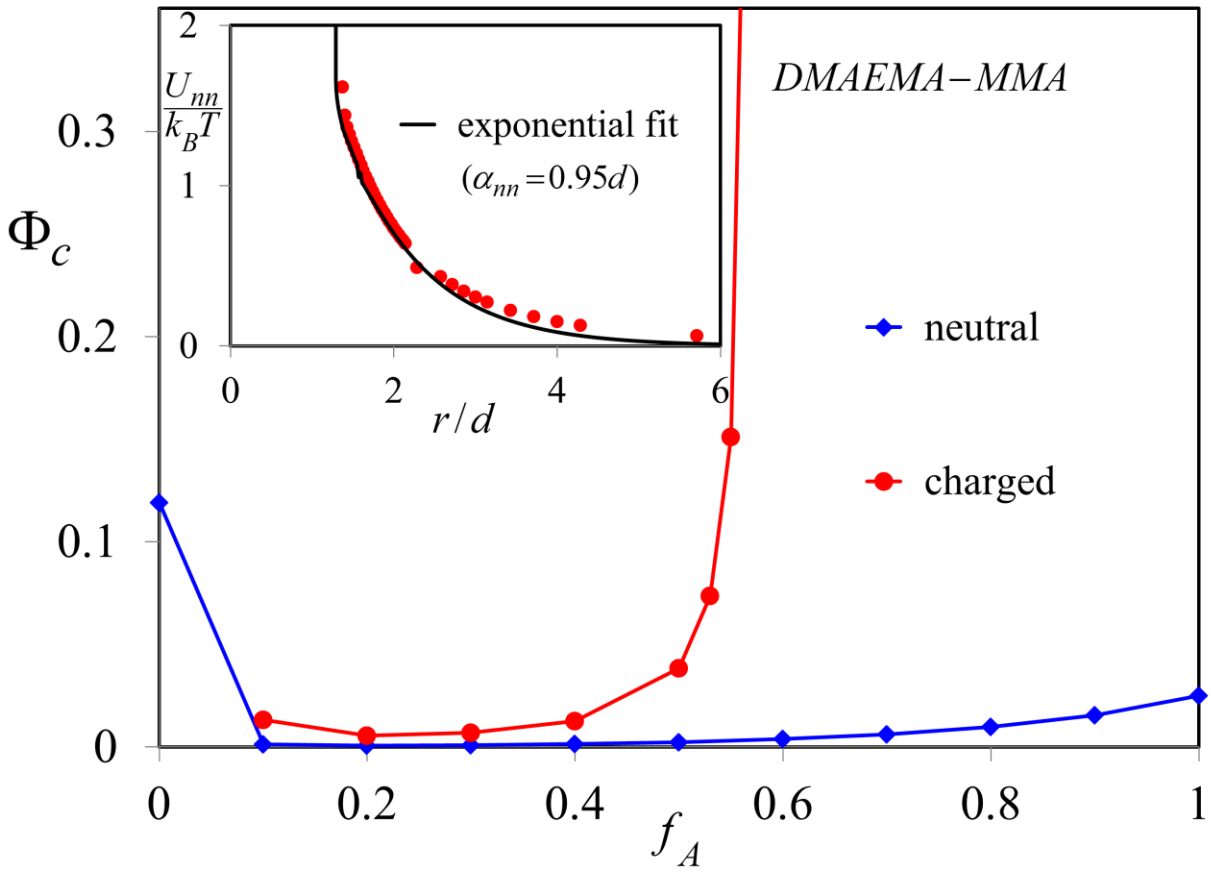

Figure 6.8 Fullerene miscibility limit volume fraction as a function of composition at 440K in a DMAEMA-MMA melt of neutral C_{60} (blue) and fullerene anions (red) screened by a matrix dielectric of constant 6. Inset shows the repulsive energy (in k_BT) between fullerene anions using a dielectric constant of 6. The smooth curve is the exponential fit used in the PRISM calculations with parameters ε_{nn} = 1.38 and α_{nn} = 0.95D.

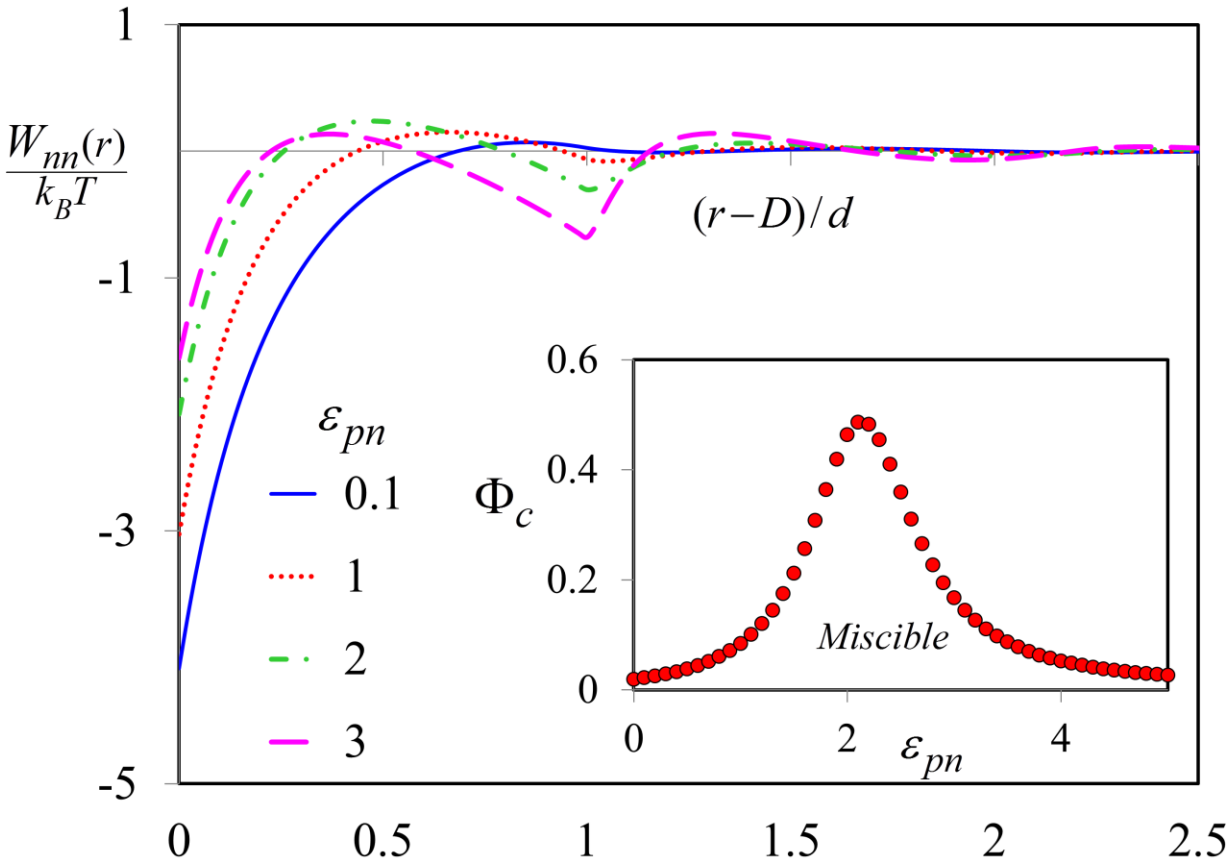

Figure 6.9 Fullerene PMF in a homopolymer melt at the indicated polymer-particle attraction strengths (α_{pn} = 0.12d) and T = 440K. Inset shows the spinodal curve.

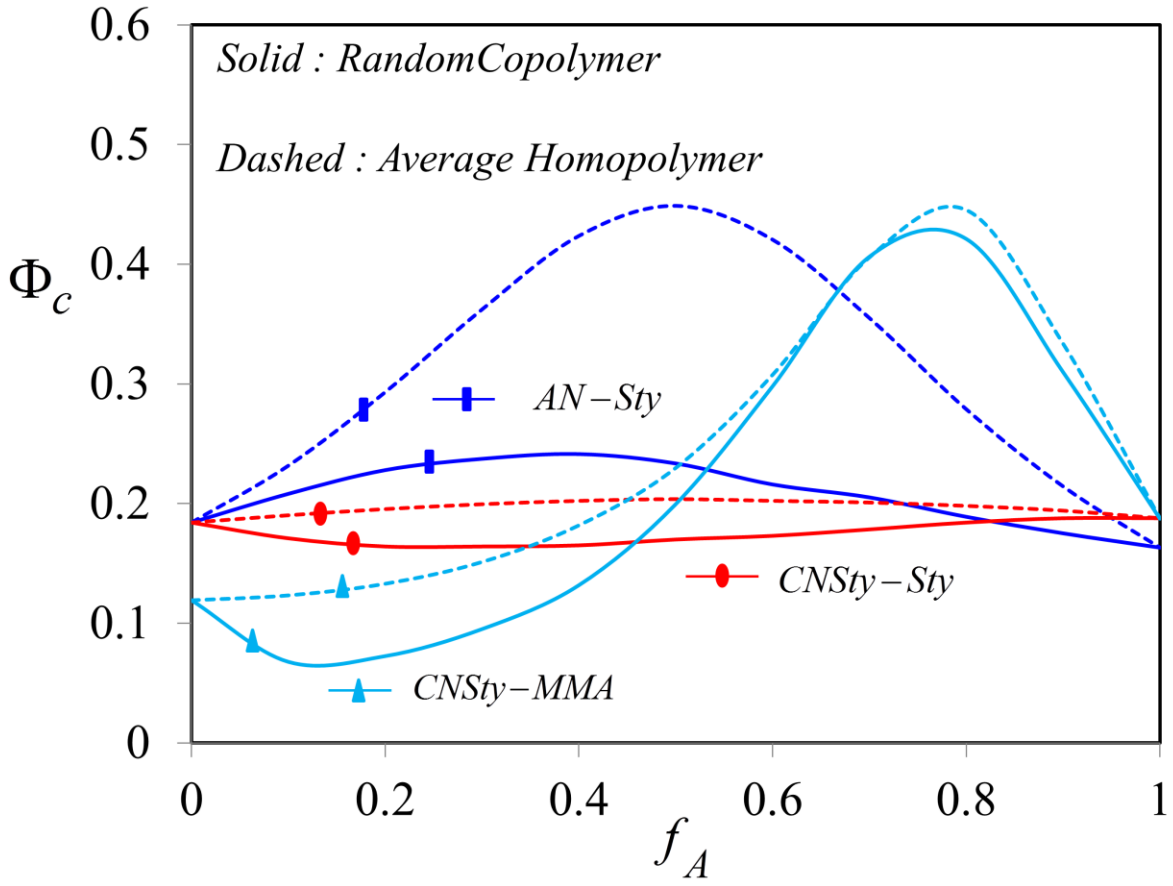

Figure 6.10 Fullerene miscibility limit volume fraction as a function of composition in AN-Sty, CNSty-Sty and CNSty-MMA (solid), and the corresponding results based on the composition-weighted average homopolymer model (dashed).

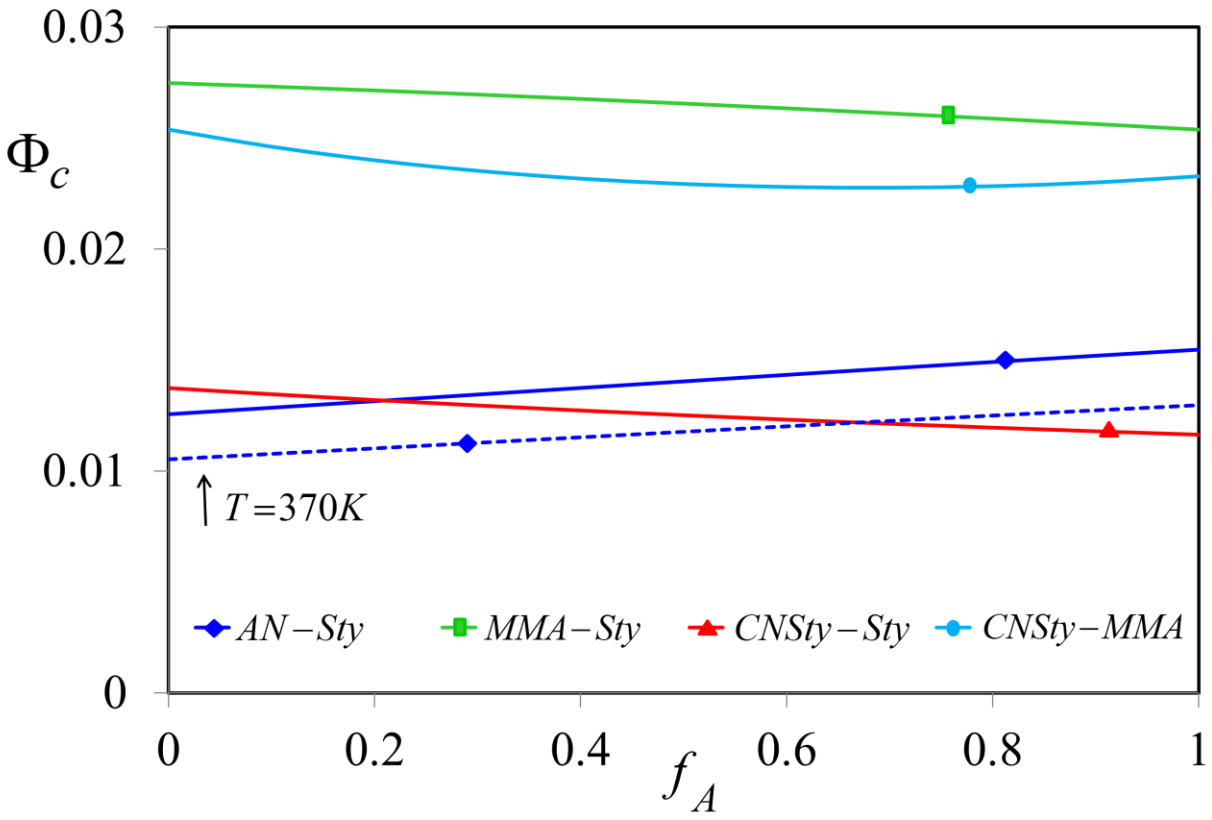

Figure 6.11 Miscibility limit of fullerenes predicted by Flory–Huggins theory in the indicated copolymer melts at 440*K*. Dashed line is the result in the AN-Sty melt at 370*K*.

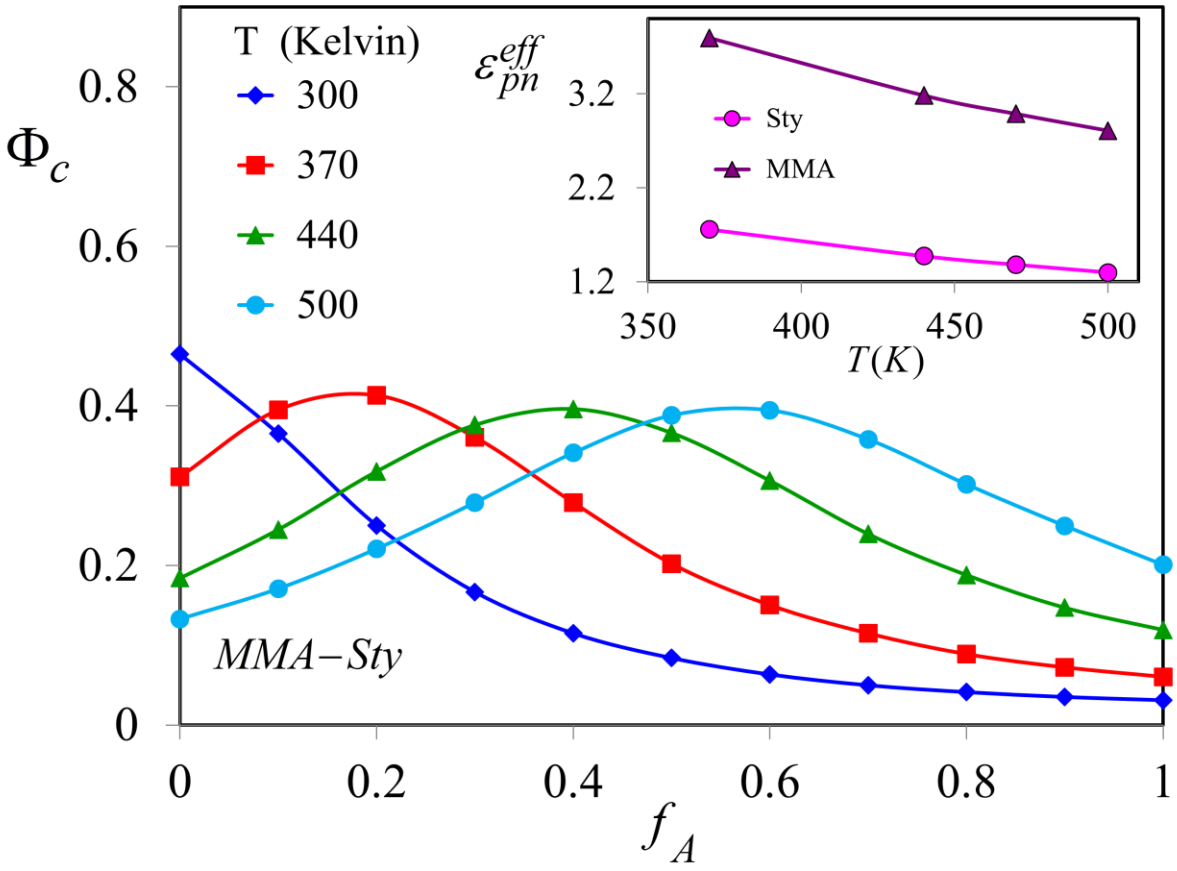

Figure 6.12a Miscibility limit volume fraction of fullerenes in (a) MMA-Sty as a function of composition at the indicated temperatures. The inset shows the effective pair attraction strengths between Sty and C_{60} and MMA and C_{60} as a function of temperature.

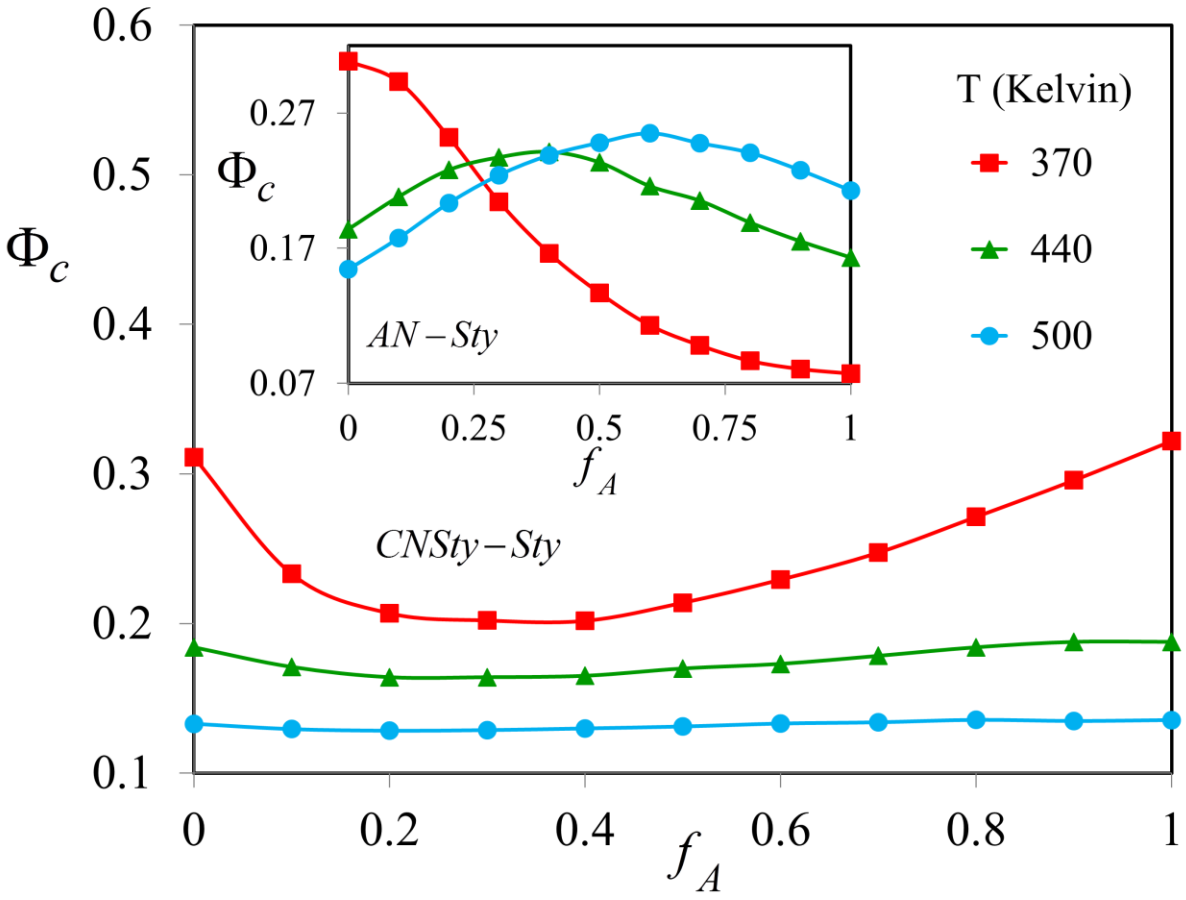

Figure 6.12b Miscibility limit volume fraction of fullerenes in CNSty-Sty (main) and AN-Sty (inset) as a function of composition at the indicated temperatures.

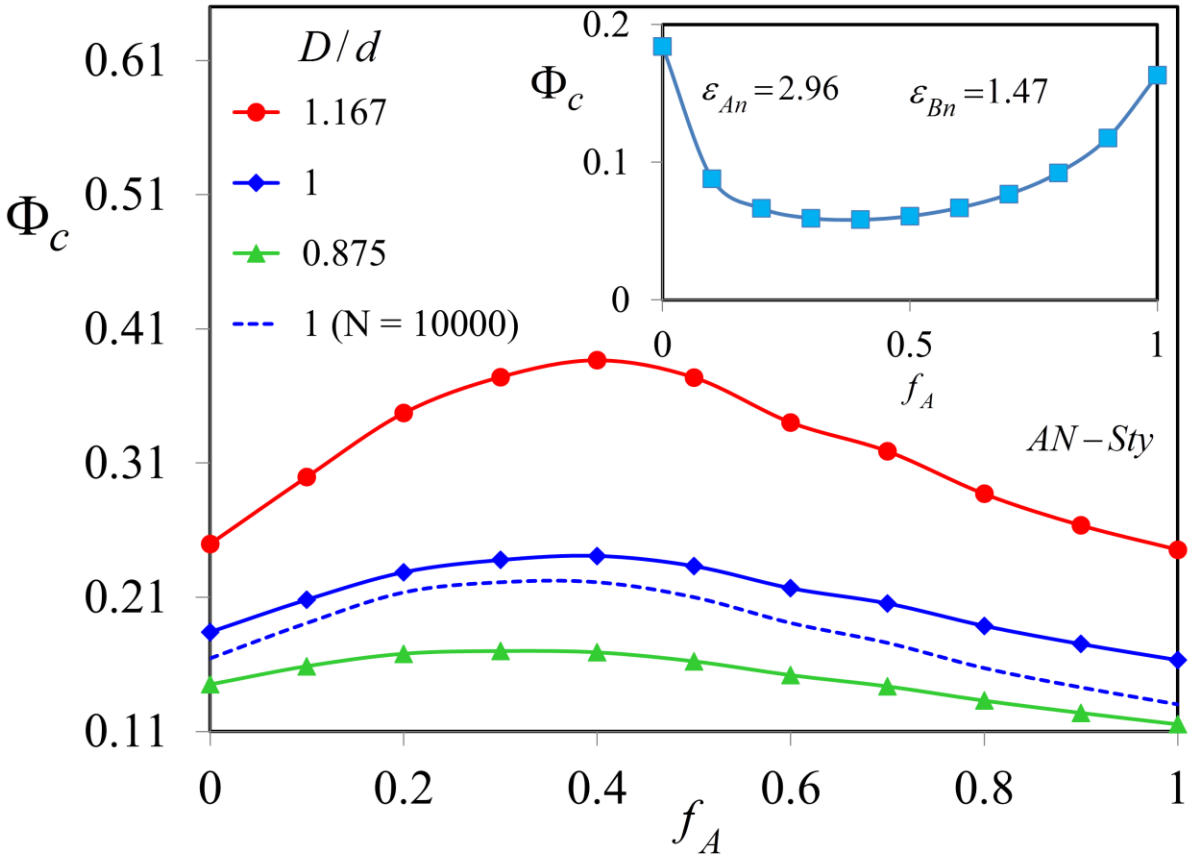

Figure 6.13 Miscibility limit volume fraction of fullerenes at 440*K* in AN-Sty for random copolymers of chain length *N* = 100 (solid) and *N* = 10000 (dashed) at the indicated values of size asymmetry ratio *D/d*; all other parameters are fixed at their reference model values. Inset shows the miscibility limit of fullerene in the AN-Sty melt with D/d=1 and *N* = 100 but at fixed, composition-independent values ε_{An}^{eff} and ε_{Bn}^{eff} of 2.96 and 1.47k_BT, respectively.

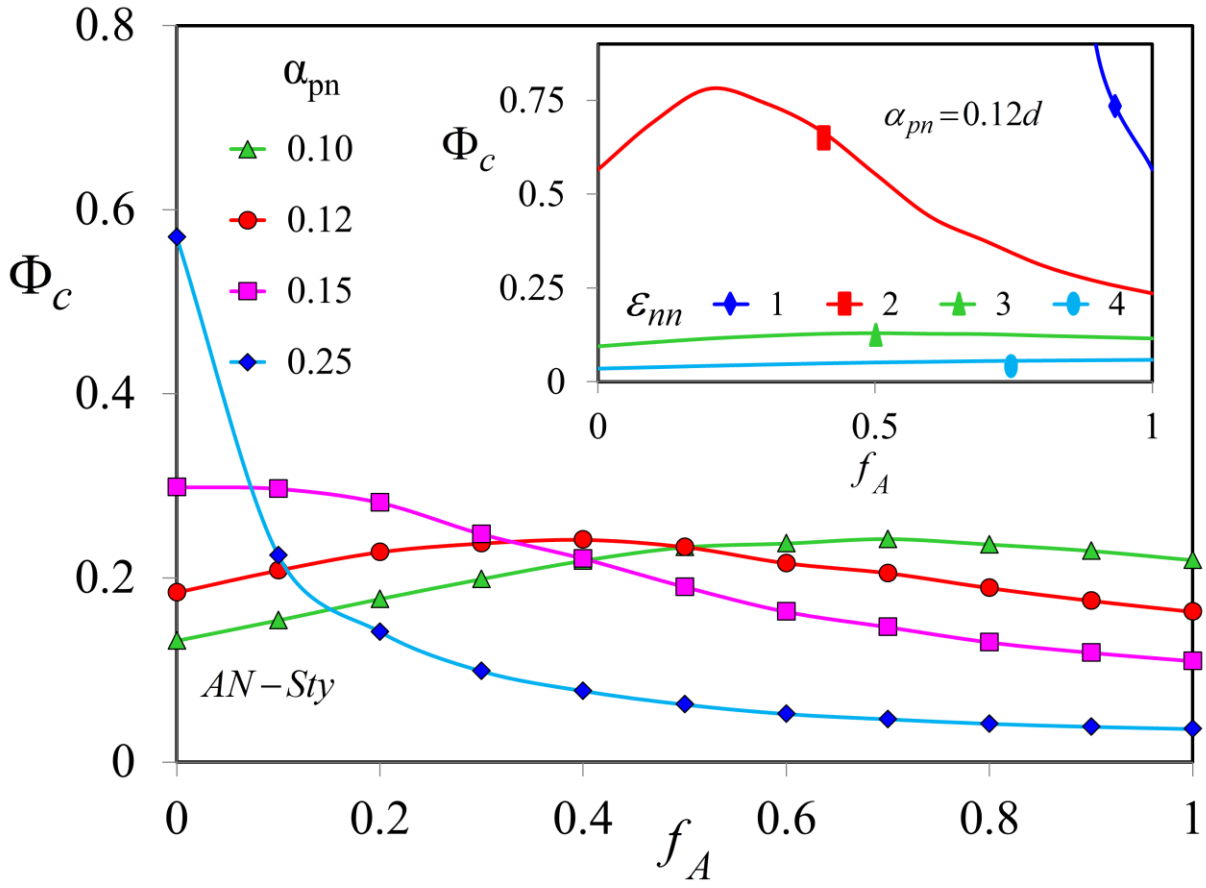

Figure 6.14 Fullerene miscibility limit volume fraction at 440K in AN-Sty as a function of composition for the indicated polymer-particle attraction ranges. Inset: Miscibility limit results in AN-Sty with $\alpha_{pn} = 0.12d$ as a function of direct particle-particle attraction.

Monomers	**AN**	**Sty**	**MMA**	**CNSty**	**DMAEMA**	**C_{60}**
AN	2.32	4.58	2.55	3.71	4.30	5.28
Sty	4.58	6.54	5.16	6.99	7.74	8.01
MMA	2.55	5.16	3.63	4.81	5.06	6.81
CNSty	3.71	6.99	4.81	7.62	7.47	9.10
DMAEMA	4.30	7.74	5.06	7.47	5.73	10.69

Table 6.1 Monomer-monomer and monomer-C_{60} pair attraction strengths (in units of k_BT at 440K) computed using the Amber force field.

Copolymer	T = 440K				T = 370K			
	RCP	*R=1*	*R=5*	*R=10*	*RCP*	*R=1*	*R=5*	*R=10*
AN-Sty	0.23	0.46	0.44	0.40	0.14	0.31	0.28	0.18
CNSty-Sty	0.17	0.21	0.21	0.21	0.21	0.35	0.35	0.34
MMA-Sty	0.37	0.42	0.42	0.41	0.20	0.23	0.22	0.21
CNSty-MMA	0.20	0.23	0.22	0.21	0.09	0.11	0.10	0.07

Table 6.2 **C**ritical nanoparticle volume fraction of fullerenes in the indicated multiblock copolymers of block length R = 1, 5, and 10 at two different experimentally-realizable temperatures. Results for the corresponding random copolymer are also shown.

CHAPTER 7

EQUILIBRIUM STRUCTURE AND MISCIBILITY OF SOFT NANOPARTICLES IN CHEMISTRY-MATCHED POLYMER MELTS

7.1 Introduction

Nanogels are nanoscopic cross-linked polymeric particles that have recently received the attention of many researchers due to their ease of preparation and control of surface morphology (fluctuation amplitude or fuzziness) and overall degree of softness. These particles can be synthesized using micro-emulsion polymerization techniques and are characterized using NMR, size exclusion chromatography, differential scanning calorimetry and different small angle scattering techniques[1-4]. The surface fuzziness and overall softness of such particles can be tuned by varying the cross-linking density[5, 6] as well as changing external parameters like temperature (for thermo-responsive polymers)[7], pH, solvent quality, etc. Higher degree of cross-linking results in a near-smooth particle which when dissolved in a polymer matrix of similar chemistry results in agglomeration due to entropic depletion attraction. Weaker cross-linking results in particles with irregular, fluctuating surfaces that are expected to help mitigate the unfavorable consequences of depletion and promote dispersion via penetration of matrix polymer chains into the surface region of the soft particles. Such behavior was observed experimentally by Mackay et al who employed intramolecularly cross-linked polystyrene nanoparticles of diameter ~ 5-7 nm

and demonstrated improved miscibility in chemically matched polystryene melt[8]. It was also observed that when these particles were added to entangled melts, the viscosity decreased, in stark violation of the Stokes-Einstein continuum ideas[9]. Fundamental understanding of these observations has not been achieved.

To fundamentally understand the above-mentioned phenomenon, a systematic structural and chemical characterization of such particles is essential. For a theoretical analysis, the most basic step is to first calculate the bare effective potential between the center-of-mass (CM) of the soft fluctuating particles in vacuum. Their non-uniform and fluctuating nature makes this a challenging task. The soft repulsive Hertzian pair potential[10] is often used as a highly simplified inter-particle potential for microgels. It is believed to be realistic within a pair-decomposable potential energy description when particle deformation is 10% or less[11]. The Hertzian potential is highly coarse grained and contains only one length scale, the effective particle diameter, and one energy scale determined by the tunable single particle modulus which is controlled largely by the internal polymer cross-linking density. A real polymeric nano/microgel, depending upon the amount of cross-linking, is defined by multiple length scales of which the core radius and the mean width and density profile of the fuzzy, fluctuating surface region are critical. This necessitates the construction of an effective CM-level potential that accounts for the latter aspects, as recently experimentally deduced using small angle neutron scattering (SANS) by Holley et al[1]. Holley and coworkers reported the synthesis and characterization of polystyrene nanogels exhibiting a graded interface and tunable softness with radii $R_p \leq 10nm$. These nanoparticles, cross-linked with divinyl benzene (DVB), were synthesized using batch and semi-batch radical microemulsion polymerization techniques. Three different nanoparticle

morphologies were identified based on modeling of the single particle SANS profiles: (1) fuzzy nanoparticles with fluctuating chain ends, (2) smooth homogeneous particles with very weak surface undulations, and (3) particles with an inhomogeneous core and ill-defined interface. A schematic illustration of these three type of particles is shown in figure 7.1a. The authors show that the size of the polystyrene nanoparticles, the segmental chain distribution at the particle interface, and the softness of the particles can be readily controlled through DVB concentration and synthetic (batch vs. semi-batch) methodology. Detailed SANS analysis allowed the determination of structural parameters such as the particle radius of gyration R_g, size of the cross-linked core R_c, average chain conformation, average mesh size of the network, and width of the fuzzy fluctuating interface τ.

Motivated by the experimental advances discussed above, we aim to develop a general theory for soft nanoparticles that explicitly takes the key two length scales into consideration to construct an effective interaction that can be used as the starting point to predict equilibrium structure and phase behavior in a manner that directly exploits the single particle form factors measured by SANS for real nanogel particles.

7.2 Methodology

7.2.1 Model

SANS allows the determination of single particle structural parameters like the radius of gyration R_g, average chain (strand) conformation, size of the crosslinked core R_c, width of the 'fuzzy' interfacial layer τ, etc[1, 12-17, 18-23]. A soft fuzzy sphere can be effectively perceived as composed of a well-defined core of size R_c (diameter $D = 2R_c$), containing a homogeneous

distribution of crosslinks with a soft fuzzy layer (of thickness τ) at the interface that is representative of dangling chain ends and loops as shown in figure 7.1b. As special example, we consider in detail in sections 7.6 and 7.7 the four particles studied by Holley and workers in ref [1]. The quantitative structural parameters associated with each of these particles (NP1, NP2, NP3 and NP3A) are tabulated in Table 7.1. Particles NPz (z = 1-3) were synthesized using batch microemulsion polymerization as opposed to semi-batch microemulsion polymerization that was employed for particle NP3A.

The azimuthally-averaged and calibrated SANS intensity I(q) for dilute particles in deuterated solvent can be analyzed by using

$$I(q) \propto P(q)S(q) \tag{7.1}$$

where P(q) and S(q) are the form factor and structure factor, respectively. The form factor represents the interference of neutrons scattered from different parts of the same object and therefore statistically quantifies at the pair correlation level the shape and softness of the object. The form factor for a fuzzy particle was modeled by Richtering et al[1, 24, 25] by convoluting the form factor of a homogeneous sphere of radius R_c with an exponentially decaying function:

$$P_f(q) = [\frac{3(sin(qR_c) - qR_c\cos(qR_c))}{(qR_c)^3} e^{-\tau^2 q^2/2}]^2 = |F(q)|^2 \tag{7.2}$$

where F(q) is the amplitude of scattered intensity and the total radius of the particle is $R_p = R_c + 2\tau$ (figure 7.1). The radial density profile Γ(r) can then be obtained by taking an inverse Fourier Transform of the amplitude. Thus,

$$\Gamma(r) = \frac{1}{(2\pi)^3}\frac{4}{3}\pi R_c^3 \int F(q) e^{-i\vec{q}.\vec{r}} d\vec{q} \tag{7.3}$$

Using the F(q) from eqn 7.2, an analytic expression for radial density is obtained:

$$\Gamma(r) = \frac{1}{2\sqrt{\pi} r}\left[\sqrt{2}\tau e^{\frac{-(r^2+R_c^2)}{\tau^2}}\left(e^{\frac{(r-R_c)^2}{2\tau^2}} - e^{\frac{(r+R_c)^2}{2\tau^2}}\right) + \sqrt{\pi} r\left(erf\left(\frac{r+R_c}{\tau\sqrt{2}}\right) - erf\left(\frac{r-R_c}{\tau\sqrt{2}}\right)\right)\right] \qquad (7.4)$$

and

$$\Gamma(0) = erf\left(\frac{R_c}{\tau\sqrt{2}}\right) - \frac{R_c}{\tau}\sqrt{\frac{2}{\pi}} e^{-\frac{R_c^2}{2\tau^2}} \qquad (7.5)$$

Now, consider a hard sphere of size R such that its radial profile is given by a step function

$$\begin{aligned} \rho(r) &= \rho_0 \Theta(r-R) \\ &= \rho_0 \quad , \quad r \le R \\ &= 0 \quad , \quad r > R \end{aligned} \qquad (7.6)$$

Our goal is to capture the radial profile of a fuzzy particle by allowing the hard sphere to fluctuate, i.e., vary its radius according to some distribution, unknown yet, such that the radial density profile of the fluctuating particle is equivalent to that of the true soft particle. Let the normalized distribution be P(r). When the particle radii are sampled according to this distribution, the averaged radial profile is

$$\langle \rho(r) \rangle = \int_0^\infty \rho(r) P(R) dR = \rho_0 \int_r^\infty P(R) dR \qquad (7.7)$$

Enforcing the constraint, $\Gamma(r) = \langle \rho(r) \rangle$, one obtains $P(r) = -\frac{1}{\rho_0}\frac{d\Gamma(r)}{dr}$.

Thus,

$$\rho_0 = \Gamma(0) = erf\left(\frac{R_c}{\tau\sqrt{2}}\right) - \frac{R_c}{\tau}\sqrt{\frac{2}{\pi}} e^{-\frac{R_c^2}{2\tau^2}} \qquad (7.8)$$

and
$$P(r) = -\frac{1}{\rho_0}\left[\begin{array}{l} -\left(\frac{1}{\tau^2\sqrt{\pi}} + \frac{1}{2\sqrt{\pi}r^2}\right)\left\{\begin{array}{l} \sqrt{2}\tau e^{\frac{-(r^2+R_c^2)}{\tau^2}}\left(e^{\frac{(r-R_c)^2}{2\tau^2}} - e^{\frac{(r+R_c)^2}{2\tau^2}}\right) \\ +\sqrt{\pi}r\left(erf\left(\frac{r+R_c}{\tau\sqrt{2}}\right) - erf\left(\frac{r-R_c}{\tau\sqrt{2}}\right)\right)\end{array}\right\} \\ +\frac{1}{2\sqrt{\pi}r}\left(\begin{array}{l} \frac{\sqrt{2}r}{\tau}\left\{e^{\frac{-(r+R_c)^2}{2\tau^2}} - e^{\frac{-(r-R_c)^2}{2\tau^2}}\right\} \\ +\frac{\sqrt{2}}{\tau}e^{\frac{-(r^2+R_c^2)}{\tau^2}}\left\{(r-R_c)e^{\frac{(r-R_c)^2}{2\tau^2}} - (r+R_c)e^{\frac{(r+R_c)^2}{2\tau^2}}\right\} \\ +\sqrt{\pi}\left(1+\frac{2r^2}{\tau^2}\right)\left\{erf\left(\frac{r+R_c}{\tau\sqrt{2}}\right) - erf\left(\frac{r-R_c}{\tau\sqrt{2}}\right)\right\}\end{array}\right)\end{array}\right] \tag{7.9}$$

When the particle radii are sampled from this distribution, the same radial profile as that of a fuzzy particle is obtained.

7.2.2 Intermolecular Site – Site Potentials

In this sub-section, we individually consider the three potentials – particle-particle, particle-monomer, monomer-monomer.

Particle – particle : To compute the inter-particle pair interaction, two fluctuating hard spheres, each fluctuating according to the distribution P(r), are brought from infinity to a distance r. The fraction of accepted configurations are calculated as

$$\begin{aligned} f_{accepted}(r) &= \int_0^\infty\int_0^\infty \exp(-\beta U(R_1,R_2))P(R_1)P(R_2)dR_1dR_2 \\ &= \int_0^\infty\int_0^\infty \Theta(r-(R_1+R_2))P(R_1)P(R_2)dR_1dR_2 \end{aligned} \tag{7.10}$$

In equation (7.10) the “no overlap” criterion has been enforced as in routinely done for hard spheres – i.e., reject the configurations that result in overlap and count only the non-overlap

configurations. Now, as the particles are brought closer and the tails of their densities start overlapping, there will come a point at which the total density is equal to the core density of the particle. To account for excluded volume effects, our simple physical idea is that the particles can be pushed into each other only till that point. For these fuzzy particles, R_c is the separation at which the density drops to roughly half its core value, which is taken as the cutoff for the particle-particle interactions and equation 7.10 is rewritten as :

$$f_{accepted}(r) = \text{constant} \times \int_{R_c}^{\infty} \int_{R_c}^{\infty} \Theta(r - (R_1 + R_2)) P(R_1) P(R_2) dR_1 dR_2 \tag{7.11}$$

Akin to a simple Boltzmann picture, we define the effective interaction between two fluctuating particles as:

$$U_{nn}(r) = -k_B T \ln f_{acc}(r) \tag{7.12}$$

Monomer – particle : In the same spirit as equation (7.10), the fraction of accepted configurations for monomer-filler interactions is given as

$$f_{accepted}(r) = \int_{0}^{\infty} \Theta(r - (r_{mon} + R_1)) P(R_1) dR_1 \tag{7.13}$$

Note that the cutoff is set for the particle-particle interactions (equation (7.11)) taking into account excluded volume, but this does not enter for the monomer – particle potential because a monomer is small compared to the core radius and we assume it can, in principal, penetrate into the core of the soft particle. Then, $U_{pn}(r) = -k_B T \ln f_{acc}(r)$ defines the effective interactions between a monomer and a particle.

Monomer – monomer: We consider an ideal athermal melt where the monomer-monomer interactions are hard core:

$$\begin{aligned} U_{mm}(r) &= \infty \quad , \quad r \le d \\ &= 0 \quad , \quad r > d \end{aligned} \tag{7.14}$$

By assuming hard core (diameter *d*) monomer-monomer interactions, one can easily isolate the effect of the surface irregularity on the dispersion of soft particles in a homopolymer melt via the effective monomer-particle and particle-particle potentials[26-31].

The above coarse-grained methodology is adopted to try and circumvent the high complexity of the system that exists on the microscopic scale if a nanogel or other soft particle is described at the monomer level including all its degrees of freedom. The real detailed surface morphology and chemistry of the particles have been removed from explicit consideration retaining only the averaged pair structure amenable to scattering measurements, the form factor or the radial density profile.

Next, using the above effective CM potentials in PRISM theory, we study the equilibrium structure of their polymer nanocomposites, from which the miscibility can be predicted as a function of (1) degree of fuzziness τ / d , (2) particle core radius R_c / d , (3) matrix packing fraction η_t and (4) matrix polymer chain length. All results below have been calculated in the *dilute two particle limit* where, based on prior work, the virial analysis of miscibility is expected to be accurate up to a critical volume fraction of $\Phi_c \le 0.2$.

7.3 Single Particle Properties

Figure 7.2 shows the radial density profile of a particle of core radius R_c = 2.5 at various degrees of fuzziness. The fuzziness is quantified by τ which is the half-width of the interfacial soft layer. Note that for τ = 0, i.e., a hard sphere (dashed black curve), the profile is a step function as it must be for a smooth homogeneous spherical particle. As the fuzziness increases, and the sharp cutoff at R_c is replaced by an exponential decay of radial density, with the density dropping to half its core value at ~R_c for all values of τ. It is for this reason that R_c is adopted as the cutoff distance for particle-particle interactions.

Figure 7.3 shows the normalized probability distribution from which the radius of the fluctuating hard sphere is sampled. When the softness is as small as $\tau / d = 0.1$, the distribution function is sharply centered around R_c. As the fuzziness increases, the distribution function at ~R_c decreases in height and spreads on either side to encompass a wider range of radii. As the particles become softer, ($\tau / d \geq 1.5$), the natural cut off at r/d=0 skews the distribution function with less sampling of smaller radii and enhanced sampling of larger distances.

Figures 7.4 and 7.5 show the particle – particle and monomer – particle effective pair interaction potentials, respectively, for a core size of R_c = 2.5. The hard core potentials (both m-n and n-n) for a hard sphere (τ = 0) transform into soft potentials as the width of the soft interfacial layer increases. With increasing surface fuzziness, the particle-particle interaction $U_{nn}(r)$ becomes softer monotonically, and it diverges at contact ($D = 2R_c$) since, by construction, two fluctuating soft particles cannot interpenetrate beyond this point. A monomer, on the other hand, can explore the interiors of a soft particle and thus the monomer-particle interaction does not diverge at the distance of closest approach defined as $r_c = (2R_c + d)/2$. As τ increases from zero to 1.5, $U_{mn}(r)$ changes from a hard core to a soft potential. However,

beyond $\tau / d = 1.5$, the potential trend reverses and becomes more repulsive. Mathematically, this originates from the skewed nature of the fluctuating radius probability distribution function where, for sufficiently large fuzziness, the smaller radii are sampled less than the larger ones.

7.4 Spatial Correlation Functions in a Monomer Solvent

This section studied the spatial correlations between a particle and a solvent sphere ($g_{mn}(r)$) and between two particles ($g_{nn}(r)$). For the large majority of the ensuing discussion, we focus on the monomeric fluid limit (N=1) for three reasons – (1) The N=1 model represents a broad range of soft colloidal systems dissolved in small molecules solvents that are of high interest to experimentalists. (2) The rich physics that is found for N=1 is qualitatively also present for the more complicated polymer chain melt problem addressed in section 7.5. (3) The form factor that is central to the methodology adopted in this chapter has been extracted experimentally in solvent matrices and, their validity in a more physically different environment of a polymer melt remains unknown. In the dilute particle limit, two fluid volume fractions are considered, $\eta_t = 0.226$ and 0.4, which are representative of concentrated solutions and melts, respectively.

The cross pair correlation function quantifies the statistical spatial organization of the solvent around the particle. Figure 7.6 shows it for R_c = 2.5 and $\eta_t = 0.226$. For hard spheres, the closest distance of contact between a monomer and a particle is $r_c = (2R_c + d)/2$ which is where the dashed black curve peaks[26, 30,32], and for all smaller distances $g_{mn}(r)$ is zero. However, as the particle becomes fuzzier, solvent molecules penetrate inside the particle core. The $g_{mn}(r)$ curve therefore develops a tail region at small separations implying increased probing of the interior of the nanogel. Because of the soft particle interface, monomers do not strongly layer in a fashion

similar to that around hard impenetrable surfaces. The value of the $g_{mn}(r)$ peak decreases with increasing τ and the most prominent peak is completely obliterated for all $\tau \geq 0.5d$, i.e., when the fuzzy layer is of the order of a monomer diameter. For all such soft particles (τ/d ≥ 0.5), at distances greater than r_c, the oscillations around the random value of unity disappear indicating a lack of solvation shell packing of matrix molecules around the particles. For τ as high as 1*d*, the fuzzy layer is nearly as large as the core radius and extreme penetration inside the nanogel is observed. However, the longer range correlation hole deepens for $\tau / d = 2$ and the matrix particles are now excluded from the deeper interiors of the soft particle. This follows from the fact that the monomer-particle potential for $\tau / d = 2$ is more repulsive compared to the result for smaller values of τ / d.

Figure 7.7 compares the monomer-particle correlation function for two limiting values of surface softness at two different matrix packing fractions. When the nanogel is tightly cross-linked ($\tau / d = 0.05$), $g_{mn}(r)$ peaks at $r = r_c$ followed by oscillations on monomer scale indicative of the layering tendency of the matrix around the particle. At higher matrix fluid density of $\eta_t = 0.4$, the peak height increases from 1.83 to 2.98 with enhanced oscillations. At a higher value of $\tau / d = 2$, the correlation hole feature of $g_{mn}(r)$ persists for both densities. However, there is more penetration of the monomers for the higher packing fraction.

Figure 7.8 shows the interparticle radial distribution function, $g_{nn}(r)$, for R_c = 2.5 in a solvent of $\eta_t = 0.4$. For a smooth particle in a concentrated solution with oscillatory packing correlations, when two particles are brought close, the preferred local packing of the matrix is frustrated, thereby raising the excess (entropic) free energy of the liquid leading to strong contact

aggregation (depletion)[33]. Thus, we see an enormous peak of $g_{nn}(r)$ at contact for a hard sphere in figure 7.8 (dashed black). Introducing slight softness ($\tau / d = 0.1$) drastically reduces the peak value from 6290 to 8.5, while shifting the point at which the peak appears from 5*d* to 5.065*d* due to the fluctuating interfacial layer between the particles. When $\tau / d = 0.5$, the peaks *completely* disappear and are replaced by a local correlation hole. This trend continues up to $\tau / d = 1.5$. For $\tau / d > 1.5$, the peak in $g_{nn}(r)$ re-appears at a surface separation of 0.5*d*. The lack of oscillations in the $g_{mn}(r)$ curve indicates that there is not much layering. In fact for $\tau / d > 1.5$, the cross correlation function shows that the monomers do not penetrate any deeper into the soft particle. Rather, the fuzzy fluctuating layer acts as a bridge between particles, i.e., the particles share their interfacial layers.

The effective interaction between the two particles mediated is given by the particle-particle potential of mean force per eqn 2.8. Figure 7.9 shows the PMF for a core size of $R_c = 2.5$ and fluid packing fraction $\eta_t = 0.226$. For hard spheres there is strong contact aggregation. Increasing the interfacial fuzzy layer suppresses this depletion attraction corresponding to decreasing the minimum at contact. For $\tau = 1$, the PMF becomes completely repulsive, which is a signature of total dispersion. For τ greater than 1, the PMF behavior reverses and a long-ranged attractive potential emerges of magnitude slightly greater than its depletion analog in hard spheres with a range of the order of the fuzzy layer width, 2τ.

Figure 7.10 shows the solvent mediated PMF for the same particle in a liquid of packing fraction $\eta_t = 0.4$. For the hard sphere-like particles in the depletion regime, increasing $\eta_t = 0.226$ to 0.4 leads to more attractive potentials, in accordance with conventional depletion

features[26, 27, 33-37]. This trend, however, reverses in the "very soft" regime, with the $\tau / d = 2$ system presenting a striking example. In a fluid of $\eta_t = 0.4$, the PMF for particles of fuzziness $\tau / d = 2$ is ~ -1k_BT at contact which is a reduction of a factor of 3.5 as compared to $\eta_t = 0.226$ (figure 7.9). Therefore, the solvent mediated potentials for the very soft particles become more repulsive upon increasing of fluid density. This feature is reminiscent of the rough hard sphere trends discussed in Chapter 4[38].

7.5 Miscibility

In the virial approach, spinodal miscibility is determined by the normalized second virial coefficient $\overline{B}_2$ of equation 2.11. This problem is studied as a function of four variables: (1) Fuzziness τ, (2) particle core size R_c ,(3) total matrix fluid packing fraction η_t ,and (4) chain degree of polymerization N. Figures 7.11 and 7.12 show the variation of miscibility with respect to these parameters.

1) Fuzziness τ. Figure 7.11 plots the second virial coefficients for various core sizes as a function of τ / d. Increasing the fuzziness triggers a transformation of $\overline{B}_2$ from negative to positive, implying increasing softness makes the system more miscible. For a core size $R_c = 5$, the system is completely miscible in the window $0.25 \le \tau \le 2$. Beyond $\tau / d = 2$, the second virial coefficients again become negative signifying impending phase separation. The same trend is observed even when the particle size is decreased or increased to $R_c = 2.5$ and 10. *Therefore, miscibility of these soft particles is a non-monotonic function of interfacial fuzziness.* This is a non-trivial and rather surprising result. We believe this is a consequence of the complex interplay

of the three potentials (m-m, m-n, n-n) where the monomer-particle potential is more repulsion at higher τ / d (see Figure 7.4).

2) Core size R_c. The effect of the particle core size is also shown in figure 7.11. The window of miscibility is the smallest for $R_c = 10$ as physically expected since the ratio of τ / R_c for this system is the smallest, making it "harder" than the smaller core particles. As the core size is decreased from $R_c = 10$ to 5, the miscibility window widens indicating improved dispersability in both the depletion (small τ / d) and soft regimes. Decreasing R_c further to 2.5, however, does not continually improve the stability. Improved miscibility is predicted in the depletion regime, but the opposite behavior is predicted in the "soft" regime for $\tau / d \geq 1.5$. For the latter regime, the miscibility variation is highly non-monotonic with $R_c = 5$ showing the best dispersion qualities. The complete miscibility window is also the widest for $R_c = 5$.

3) Solvent packing fraction η_t. The red dashed curve of figure 7.11 is the second virial coefficient results for $R_c = 5$ nanogels in a solvent of increased density $\eta_t = 0.4$. Following the PMF trend, increasing η_t destabilizes the system in the "depletion" regime ($\tau / d \leq 0.1$) but improves dispersion in the "soft" regime, consequently widening the miscibility window.

4) Polymer chain length N. Under iso-compressible melt conditions ($S_0 = 0.17$) as discussed in Chapters 2 and 3, increasing the polymer size monotonically destabilizes the PNC. As shown in figure 7.12 for a particle of core size $R_c = 2.5$, miscibility is reduced in both the low and high τ / d regimes. The miscibility window is the widest for the monomeric fluid of N = 1 and progressively narrows with increasing N. Surprisingly, chain length does not have any effect in the dispersed states of $\tau / d = 0.5$ and 1. The reason for enhanced miscibility in a soft particle

is the ability of the polymer to penetrate the fuzzy layer of the particles. Increasing the degree of polymerization makes it difficult for the polymers to configure themselves in between the particles owing to increased constraints. This decreases the miscibility of the particles.

Table 7.2 shows the spinodal solubility limit Φ_c for particles of core radius $R_c = 5$ at varying amounts of softness in both monomeric solvents and polymer melts. Φ_c is the critical volume fraction beyond which spinodal phase separation occurs. Prior work on smooth particles in homopolymer melt[30] show that the solubility limits based on virial analysis in quantitatively accurate up to $\Phi_c \leq 0.2$. A homogeneously smooth hard sphere of radius $R_c = 5$ has solubility limits of 11.6% and 1.3% in solvents of N=1 and 100, respectively. As the surface fuzziness is increased, the particle solubility increases initially and then drops when $\tau / d > 2$. The window of miscibility, defined as the range in which the particles are always dispersed, is roughly $0.1 \leq \tau / d \leq 2$ for the monomeric fluid and $1 \leq \tau / d \leq 2$ for the polymer melt. It is surprising that when the fuzziness is of the order of a monomer diameter ($2\tau / d = 1$), the particle spinodal solubility is as high as 30% in the polymer matrix, an increase of a factor of 23 compared to that of the smooth sphere.

7.6 Miscibility Predictions for Specific Experimental Nanogel Systems

This section makes predictions for the four specific soft nanoparticles systems considered in ref [1], NP1, NP2, NP3, and NP3A. As shown in Table 7.1, Holley and coworkers varied the DVB monomer cross-linking density to obtain nanogels of different core sizes and degrees of fuzziness. The lowest crosslinking density of 0.81 mol% yielded the "fuzziest" particle with $\tau / R_c \approx 0.73$ while tight crosslinking with semi-batch microemulsion polymerization gave a smooth soft gel that lacked significant interfacial layer ($\tau / R_c \approx 0.1$). A special feature of

choosing these particular soft particles is that the radius of gyration of all the four is approximately fixed at 10 *nm*, i.e., $R_p = R_c + 2\tau \simeq 10nm$.

Figure 7.13 shows the monomer-particle pair correlation function for the four sets of particles at $\eta_t = 0.4$. The most noticeable feature for all the particles is the lack of a sharp peak at the core radius. A weak vestige of solvent layering is present for NP3A which has the narrowest fuzzy layer τ / d, while only a correlation hole feature is observed for NP1, NP2 and NP3. Quantitatively, NP2 allows maximum penetration of the monomer followed by NP1 and NP3. However, note that the $g_{mn}(r)$ curves for NP2 and NP3 attain the random value of unity at r ~ R_c, while this is attained for NP1 at a larger separation of $r \simeq 1.8R_c$ corresponding to the deepest correlation hole. This feature has major implications for the particle PMF as shown in figure 7.14. One sees that the PMF of NP2, NP3 and NP3A are completely repulsive in a monomeric fluid at $\eta_t = 0.4$. Given that NP2 and NP3 also have fuzzy layers, the corresponding PMFs show a weak, long-ranged repulsive tail. For NP1, a strong attraction of -4.7k_BT is observed with a spatial range of order the correlation hole ($\sim 1.8R_c$).

Experiments on the dispersion properties of these particles are presently underway at Oak Ridge National Laboratory (ORNL) for unentangled polymer melts for which the corresponding mapped chain length is N ~ 100 – 1000[39]. We, therefore, study in figure 7.15 the PMF for particles NP3 and NP3A at different chain lengths under iso-compressible melt conditions (S_0 fixed at 0.17). The general feature is that as the chain length is increased, the attraction minimum deepens. For NP3A, the PMF changes from purely repulsive to weakly attractive upon increasing N from 1 to 10. For both particles, the change in PMF minima with increasing N hints at a

possible saturation behavior in the long chain limit as has been observed for smooth hard spheres in polymer melts[33].

We now make testable miscibility predictions for the four nanogel particles at different polymer chain lengths. Table 7.3 show that NP1 is immiscible and NP3A is miscible at all N. This seems counter-intuitive since NP1 is the softest and NP3A is relatively the hardest particle. However, this follows the trend of figure 7.11 where one sees that a fuzzy layer of the order of monomer diameter, $2\tau / d = 1$, yields a positive second virial coefficient for particles of all core sizes $R_c \leq 10$. Figure 7.11 also showed that, depending upon the core size, particles with soft layers much less than 0.5d behave as "hard" particles. Similarly, in the limit of very high degree of fuzziness, the miscibility trend changes back to destabilization. This is the reason why NP1 is predicted to be immiscible at all chain lengths. For both NP2 and NP3, the nanoparticles are totally miscible for N = 1 and their miscibility drops with increasing N. The spinodal solubility limit of NP2 is only slightly better than NP3. Therefore, even though all the four particles have the same effective radius of gyration, their solubility limits are very different.

The biggest take home message from our calculations is that the "effective fuzziness" (τ / R_c) defined by Holley et al[1] is not the only parameter that controls the degree of miscibility. Miscibility of soft particles is determined by the size of the core relative to the monomer diameter (which primarily controls the dispersion properties of smooth hard particles) in addition to the degree of fuzziness. This makes the problem more complicated and can lead to non-intuitive, not easily guessed trends. Based on our present model and calculations, particles with an interfacial fuzziness of $2\tau / d = 1$ should not be viewed as smooth homogeneous spheres as suggested by Holley et al[1]. Rather, the particle fuzziness needs to be much less than $2\tau / d = 1$ to

be deemed ‘hard’. Of course, this is a preliminary theoretical study and future work is required to establish the robustness of our conclusions.

7.7 Importance of Radial Density Profile

The particle form factors of the ORNL soft nanoparticles were obtained by SANS analysis (data fitting) over a limited range of wave vector. Thus, a natural question arises concerning how unique the deductions about the true particle radial density profile are based on limited small angle scattering data fit to a specific single particle form factor model. An alternative form factor has been proposed by Pedersen and Richtering[7, 40] to describe soft particles with a graded interface. The radial profile is described with a symmetric form based on a parabolic shape:

$$\begin{aligned}
\Gamma(r) &= 1 && r \le (R_c - \tau) \\
&= 1 - \frac{1}{2}\frac{\left[(r - R_c) + \tau\right]^2}{\tau^2} && R_c - \tau < r \le R_c \\
&= \frac{1}{2}\frac{\left[(R_c - r) + \tau\right]^2}{\tau^2} && R_c < r \le (R_c + \tau) \\
&= 0 && r > (R_c + \tau)
\end{aligned} \tag{7.15}$$

This form factor is well-suited for analyzing scattering data of particles of core-shell morphology. In this section we repeat the calculations of the previous sections using this parabolic radial profile to: (a) check the robustness of our results, and (b) test whether the theoretical predictions of miscibility trends are sensitive to relatively small changes of the nanoparticle surface characteristics.

The parabolic radial density profile is shown in figure 7.16 where increasing fuzziness results in density reduction. The difference between this profile and the exponential profile of figure 7.2 becomes significant starting at $\tau / d = 1$. The main difference is that for the exponential profile the core density decreases immediately with growing r and the point at which it drops by

half is not strictly R_c but slightly less than R_c. Using the method described in section 7.2, the effective potentials are constructed and equilibrium structure and miscibility predictions are made using PRISM theory.

Figure 7.17 shows the monomer-particle pair correlation function of a particle of radius $R_c = 2.5$ in a solvent of total packing fraction $\eta_t = 0.226$. While the qualitative features are the same as before (figure 7.6), the peak heights differ quantitatively due to the differences in the radial density profile. We also note that increasing τ results in enhanced penetration in a monotonic manner, unlike the behavior in figure 7.6.

Figure 7.18 shows the corresponding PMF between two particles of core radius $R_c = 2.5$ in a monomeric fluid of $\eta_t = 0.226$ at various degrees of fuzziness. The attractive feature, indicating (near) contact aggregation, is reduced as the particle softness grows, and the PMF becomes repulsive for $\tau / d = 0.5$. Interestingly, using this new form factor, the PMFs do not become attractive again at higher values of τ. This is also reflected in figure 7.19 where, for $R_c = 2.5$, increasing τ results in the reduced second virial coefficient changing from negative to positive, before saturating at the bare hard sphere value of unity. This is in sharp contrast with the previous set of calculations in figure 7.11 where for a particle of size $R_c = 2.5$, the second virial coefficients for $\tau / d = 2$ and 2.5 were -5 and -8000, respectively. The trend for $R_c = 5$ is similar to that of $R_c = 2.5$, though for $\tau / d > 2$ there is a weak hint of a turn over as also seen in figure 7.11. The inset to figure 7.19 shows how the $\overline{B}_2$ dependence on τ / d depends on polymer chain length under iso-compressible melt conditions. For $\tau / d < 0.5$, increasing N destabilizes the system in a depletion-like manner[33]. For $\tau / d \geq 0.5$, the inter-particle potentials and miscibilities are predicted to be unperturbed by the melt chain length.

Finally, we make predictions for the four particles using the parabolic radial density profile. The results are quite different from what those in Table 7.3 using the exponential radial density profile. All four particles are completely miscible for short chains (N=1 and 10). For the longer chains, the miscibility trends are complex. The particle with the softest interface, NP1, is the most miscible, though it is only slightly more so than the "hardest" particle NP3A. Among the four particles, least miscibility is predicted for NP2 and NP3. This again reiterates the fact that the absolute softness of the particles, quantified by τ / d, is not the sole determinant of the dispersion properties. The softness in conjunction with the core radius impact miscibility, making the problem rather complex and subtle.

Broadly, we conclude that the non-monotonic change of miscibility with softness is a feature that persists even with a slightly different form factor. Even though the two radial density profiles of equation 7.4 and 7.15 are not qualitatively different, their modest quantitative differences do modify the predictions of PRISM theory. This emphasizes the importance of experimentally measuring the particle form factor to very high accuracy and over as large a range of wavevector as possible in order to better establish the real space radial density profile of soft nanoparticles.

7.8 Summary

We have studied the equilibrium structure of cross-linked nanogels in a chemistry-matched solvent or polymer melt using PRISM theory. An analytical expression for the particle-particle and particle-monomer potentials was derived using experimental scattering intensity information that is a function of the particle core size and degree of surface fuzziness. Our approach is a general technique within the simplifying framework of averaging over all surface irregularities

and fluctuations to give a center-of-mass level potential. At this point, our guess is that this methodology will be valid as long as the amount of fuzziness is less than the core radius or even less, and the surface morphology is irregular and disordered unlike the ordered surface roughness discussed in Chapter 4.

Our results throw light on some of the recent experimental observations of improved cross-linked nanoparticle miscibility in chemically similar polymer melt. Dramatic changes are noted in the single particle-monomer spatial correlation functions upon variation of surface softness. This leads to an unexpected non-monotonic change of the particle potential of mean force as a function of fuzziness. Going from a homogeneously smooth to a graded interfaced particle, the miscibility of the particles is improved and a window of miscibility is predicted where the particles are completely dispersed. However, making the particles very soft does not monotonically improve the stability of the PNC as the longer soft layer can also interdigitate in each other, destabilizing the system.

The miscibility is also an unexpected function of the particle core radius with $R_c = 5$ yielding maximum miscibility. The solvent density has opposing effects on the particle miscibility depending on the amount of softness of the particle. Higher packing fraction results in a stronger attractive PMF for the harder particles, while for the softer particles the miscibility is improved for higher η_t. Increasing the polymer chain length monotonically destabilizes the system, but long polymers can still display full miscibility provided the amount of surface fuzziness is optimal.

7.9 References

1. D.W. Holley, M. Ruppel, J.W. Mays, V.S. Urban, D. Baskaran, *Polymer*, **55**, 58-65, 2014.
2. H. G. Schild, *Prog. Polym. Sci.*, **17**, 163, 1992.
3. B. R. Saunders, B. Vincent, *Adv. Colloid Interface Sci.*, **80**, 1, 1999.
4. A. Guillermo, J. P. Cohen Addad, J. P. Bazile, D. Duracher, A. Elaissari, C. Pichot, *J. Polym. Sci., Part B: Polym. Phys.*, **38**, 889, 2000.
5. X. Wu, R. H. Pelton, A. E. Hamielec, D. R. Woods, W. McPhee, *Colloid Polym. Sci.*, **272**, 467, 1994.
6. W. McPhee, K. C. Tam, R. Pelton, *J. Colloid Interface Sci.*, **156**, 24, 1993.
7. I. Berndt, J. S. Pedersen, P. Lindner, W. Richtering, *Langmuir*, **22**, 459-468, 2006.
8. M. E. Mackay, A. Tuteja, P. M. Duxbury, C. J. Hawker, B. V. Horn, Z. Guan, G. Chen, R. S. Krishnan, *Science*, **311**, 1740, 2006.
9. M. E. Mackay, T. T. Dao, A. Tuteja, D. L. Ho, B. Van Horn, H.-C. Kim, C. J. Hawker, *Nat. Matls.*, **2**, 762-766, 2003.
10. J. R. Seth, M. Cloitre, R. T. Bonnecaze, *J. Rheology*, **50**, 353, 2006; **52**, 1241, 2008.
11. For excellent recent reviews of microgel suspensions, see: M. Cloitre, in "Microgel based Materials", H. Wyss, A. Fernandez de las Nieves, J. Mattson and D. A. Weitz Eds; Wiley-VCH, 2010; R. Bonnecaze, M.Cloitre, *Adv. Polym. Sci.*, **236**, 117, 2010.
12. M. Shibayama, T. Tanaka, C. C. Han, *J. Chem. Phys.*, **97**, 6829, 1992.
13. M. Shibayama, T. Tanaka, C. C. Han, *J. Chem. Phys.*, **97**, 6842, 1992.
14. M. Shibayama, *Macromol. Chem. Phys.*, **199**, 1, 1998.
15. S. J. Mears, Y. Deng, T. Cosgrove, R. Pelton, *Langmuir*, **13**, 1904, 1997.

16. H. M. Crowther, B. R. Saunders, S. J. Mears, T. Cosgrove, B. Vincent, S. M. King, G. E. Yu, *Colloids Surf.*, **152**, 327, 1999.

17. B. R. Saunders, H. W. Crowther, G. E. Morris, S. J. Mears, T. Cosgrove, B. Vincent, *Colloids Surf.*, **149**, 57, 1999.

18. A. Fernandez-Barbero, A. Fernandez-Nieves, I. Grillo, E. Lopez-Cabarcos, *Phys. Rev. E*, **66**, 051803, 2002.

19. N. Dingenouts, C. Norhausen, M. Ballauff, B. Bunsenges, *Phys. Chem.*, **102**, 1594, 1998.

20. N. Dingenouts, C. Norhausen, M. Ballauff, *Macromolecules*, **31**, 8912, 1998.

21. S. Seelenmeyer, I. Deike, N. Dingenouts, S. Rosenfeldt, C. Norhausen, M. Ballauff, T. Narayanan, *J. Appl. Crystallogr.*, **33**, 574, 2000.

22. N. Dingenouts, S. Seelenmeyer, I. Deike, S. Rosenfeldt, M. Ballauff, P. Lindner, T. Narayanan, *Phys. Chem. Chem. Phys.*, **3**, 1169, 2001.

23. S. Seelenmeyer, I. Deike, S. Rosenfeldt, C. Norhausen, N. Dingenouts, M. Ballauff, T. Narayanan, P. Lindner, *J. Chem. Phys.*, **114**, 10471, 2001.

24. M. Stieger, W. Richtering, J. S. Pedersen, P. Lindner, *J. Chem. Phys.*, **120**, 6197-6206, 2004.

25. J. Dubbert, T. Honold, J. S. Pedersen, A. Radulescu, M. Drechsler, M. Karg, W. Richtering, *Macromolecules*, **47**, 8700–8708, 2014.

26. J. B. Hooper, K. S. Schweizer, *Macromolecules*, **38**, 8858-8869, 2005.

27. J. B. Hooper, K. S. Schweizer, *Macromolecules*, **39**, 5133-5142, 2006.

28. L. M. Hall, B. J. Anderson, C. F. Zukoski, K. S. Schweizer, *Macromolecules*, **42**, 8435–8442, 2009.

29. S. Y. Kim, L. M. Hall, K. S. Schweizer, C. F. Zukoski, *Macromolecules*, **43**, 10123–10131, 2010.

30. L. M. Hall, A. Jayaraman, K. S. Schweizer, *Curr. Opin. Solid State Mater. Sci.*, **14**, 38, 2010.

31. D. Banerjee, M. D. Dadmun, B. Sumpter, K. S. Schweizer, *Macromolecules*, 2013, **46**, 8732-8743.

32. L. M. Hall, K. S. Schweizer, *J. Chem. Phys.*, **128**, 234901, 2008.

33. D. Banerjee and K. S. Schweizer, *J. Chem. Phys.*, **142**, 214903, 2015.

34. S. Asakura, F. Oosawa, *J. Chem. Phys*., **22**, 1255, 1954.

35. S. Asakura, F. Oosawa, *J. Polym.Sci*., **33**, 183, 1958.

36. A. Vrij, *Pure Appl. Chem*., **48**, 471, 1976.

37. A. Yethiraj, C. K. Hall, R. Dickman, *J. Colloid Interface Sci*., **151**, 102, 1992.

38. D. Banerjee*, J. Yang*, K. S. Schweizer, *Soft Matter*, to be submitted, August 2015 (*Equal Contribution).

39. Private Communication.

40. I. Berndt, J. S. Pedersen, W. Richtering, *J. Am. Chem. Soc.*, **127**, 9372-9373, 2005.

7.10 Figures

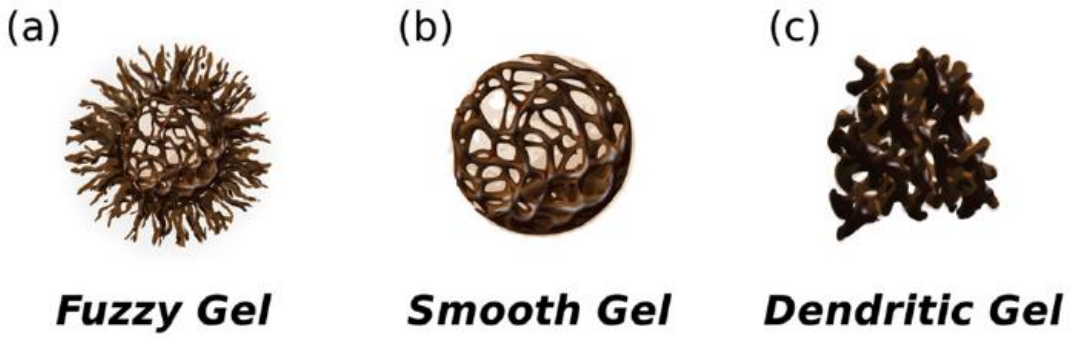

Figure 7.1a Schematic of different types of cross-linked nanoparticles depending on the crosslinking density. Figure reproduced from ref [1].

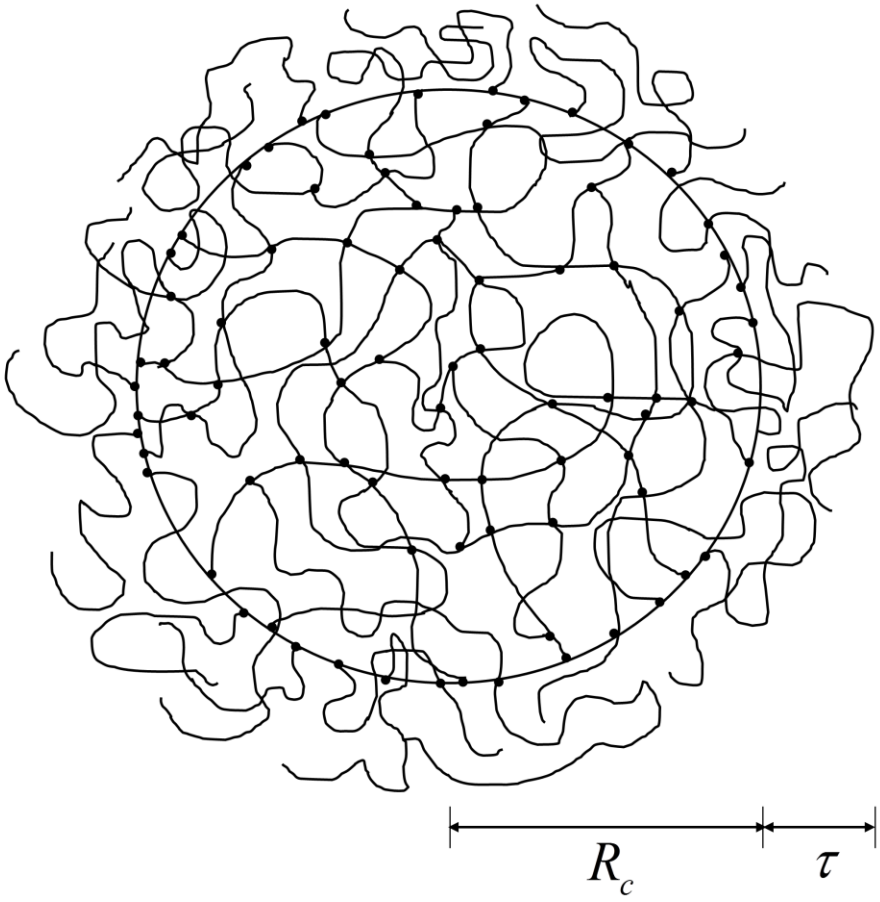

Figure 7.1b Schematic of the model soft fuzzy cross-linked nanogel.

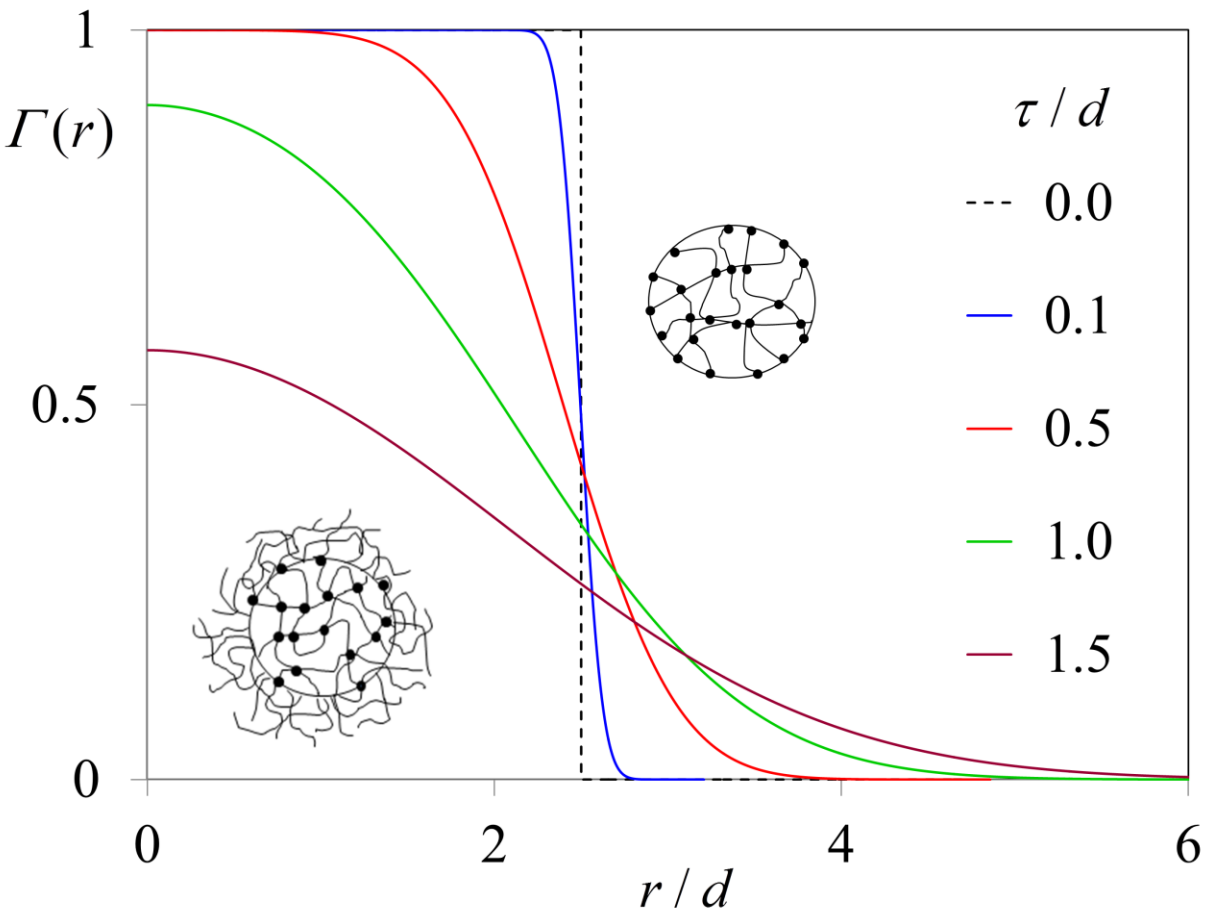

Figure 7.2 Radial density profile of a particle with core $R_c = 2.5$ (diameter $D = 2R_c$) at various degrees of fuzziness.

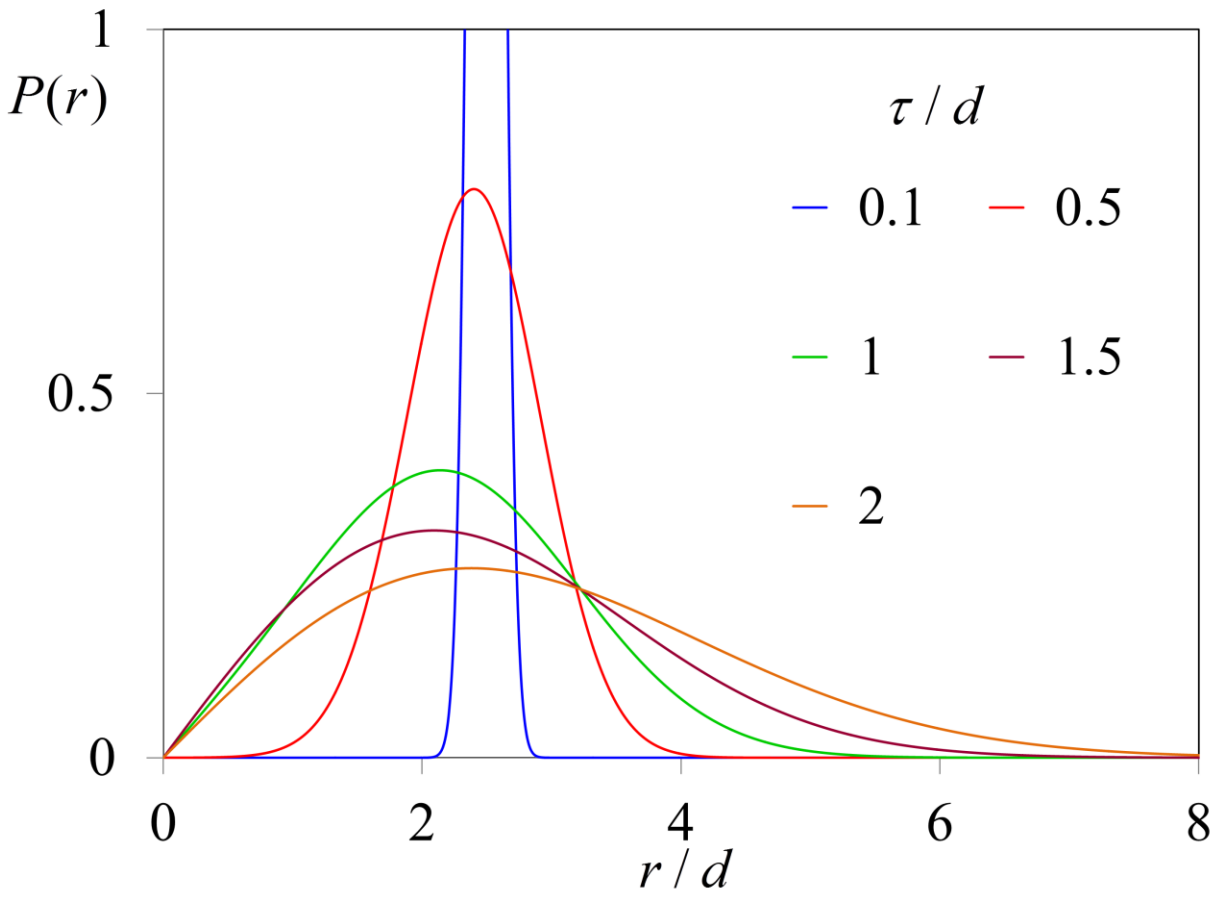

Figure 7.3 Probability distribution function for a particle with core $R_c = 2.5$ at various degrees of fuzziness.

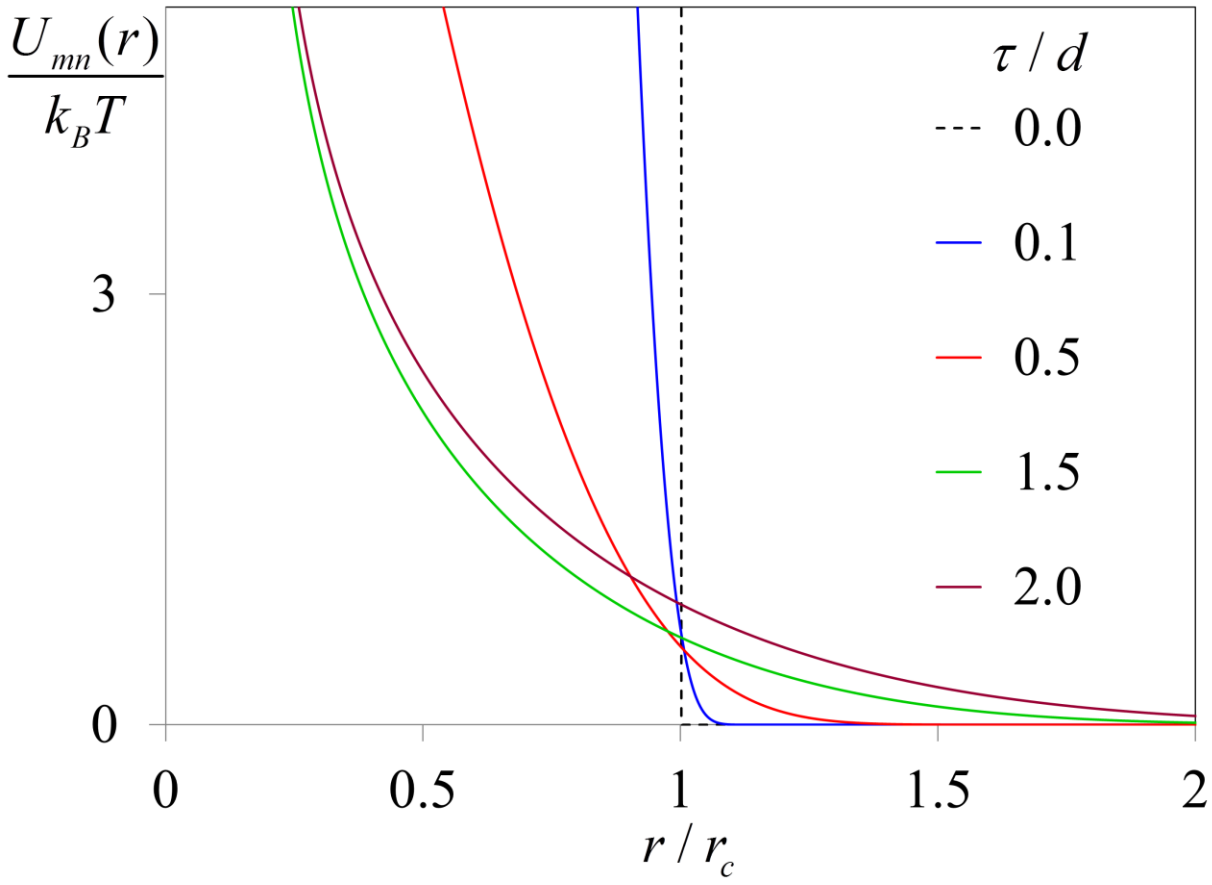

Figure 7.4 Effective interaction between a nanogel of core radius $R_c = 2.5$ and a monomer at various degrees of fuzziness ($r_c = (D+d)/2$).

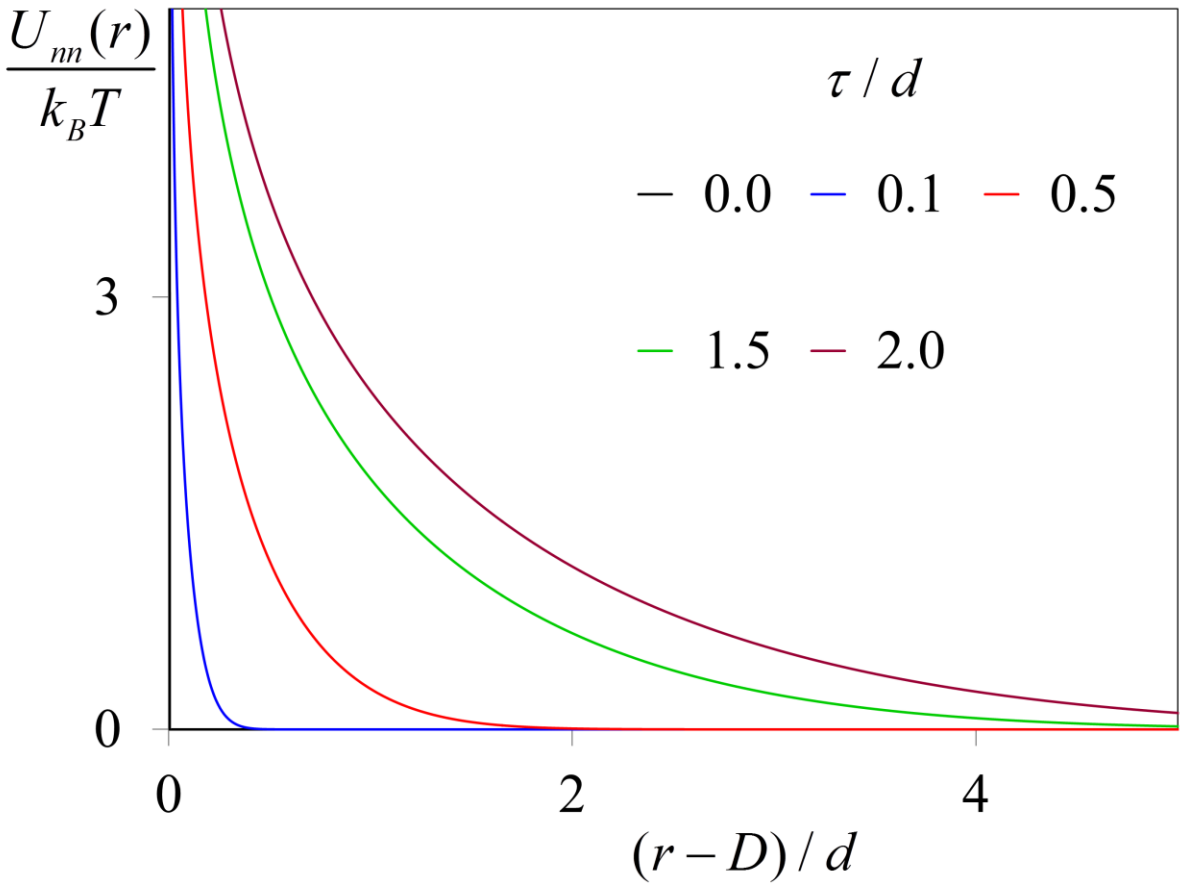

Figure 7.5 Effective interaction between two nanogels of core radius $R_c = 2.5$ at various degrees of fuzziness.

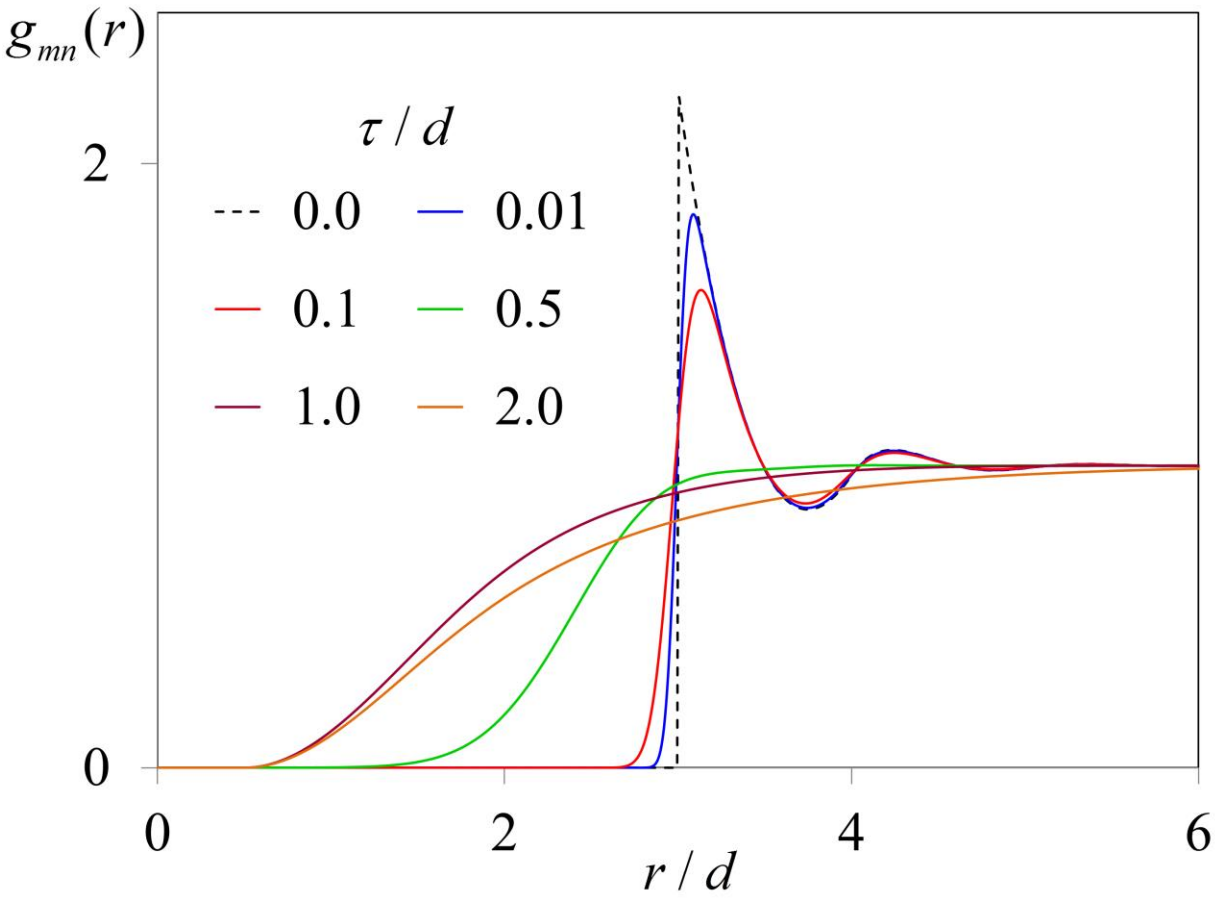

Figure 7.6 Cross correlation function for dilute soft particles of size $R_c = 2.5$ at various degrees of fuzziness and total packing fraction $\eta_t = 0.226$.

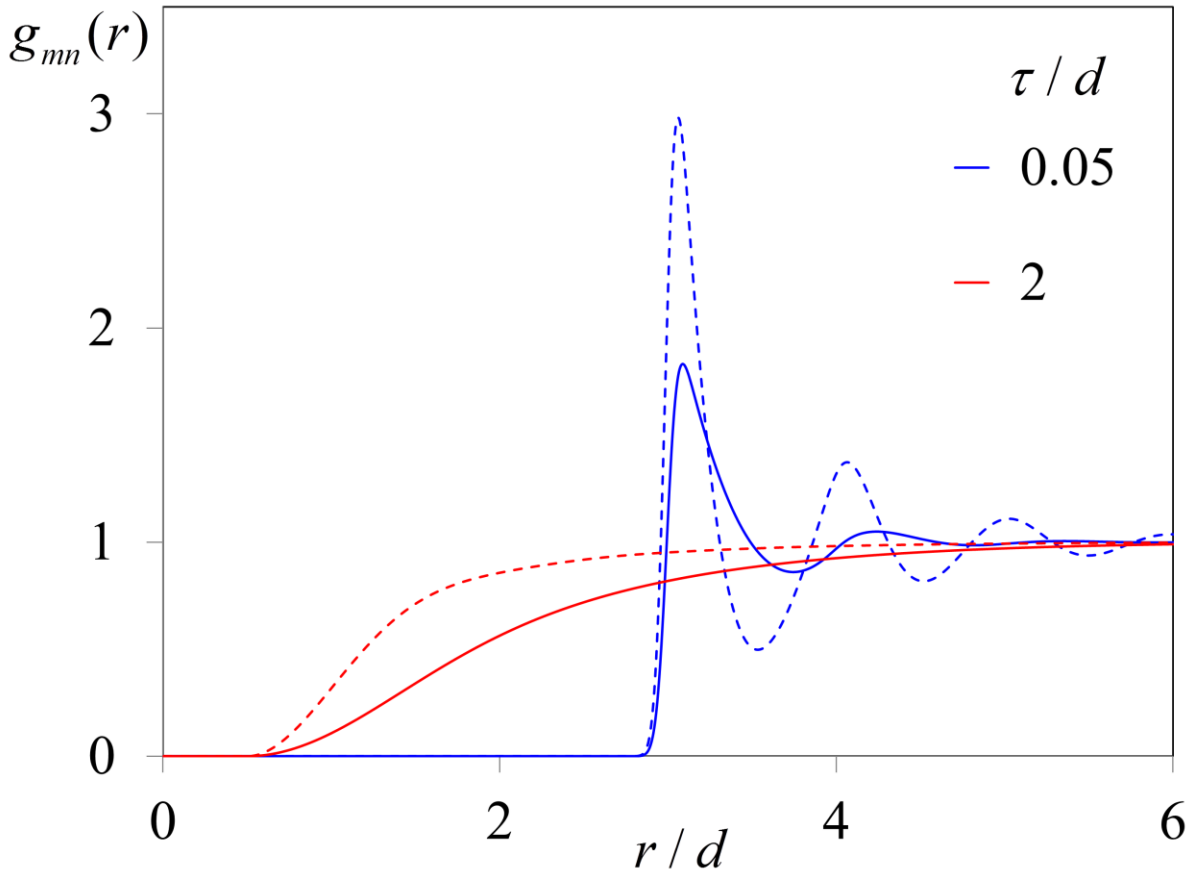

Figure 7.7 Cross correlation function for dilute soft particles of size $R_c = 2.5$ at the indicated degrees of fuzziness at packing fractions $\eta_t = 0.226$ (solid) and 0.4 (dashed).

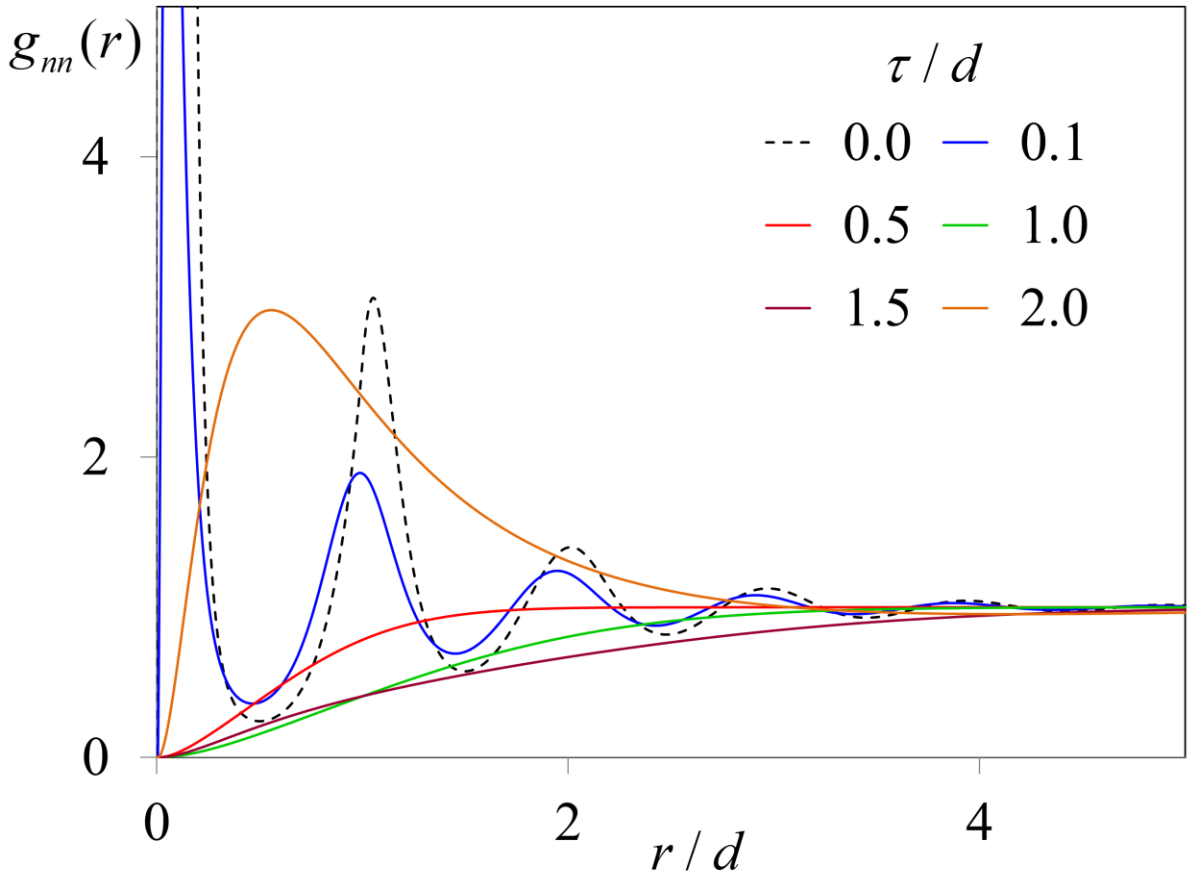

Figure 7.8 Particle-particle correlation function for dilute soft particles of size $R_c = 2.5$ at various degrees of fuzziness and total packing fraction $\eta_t = 0.4$. The peak heights for $\tau / d = 0$ and 0.1 are 6290 and 8.5, respectively.

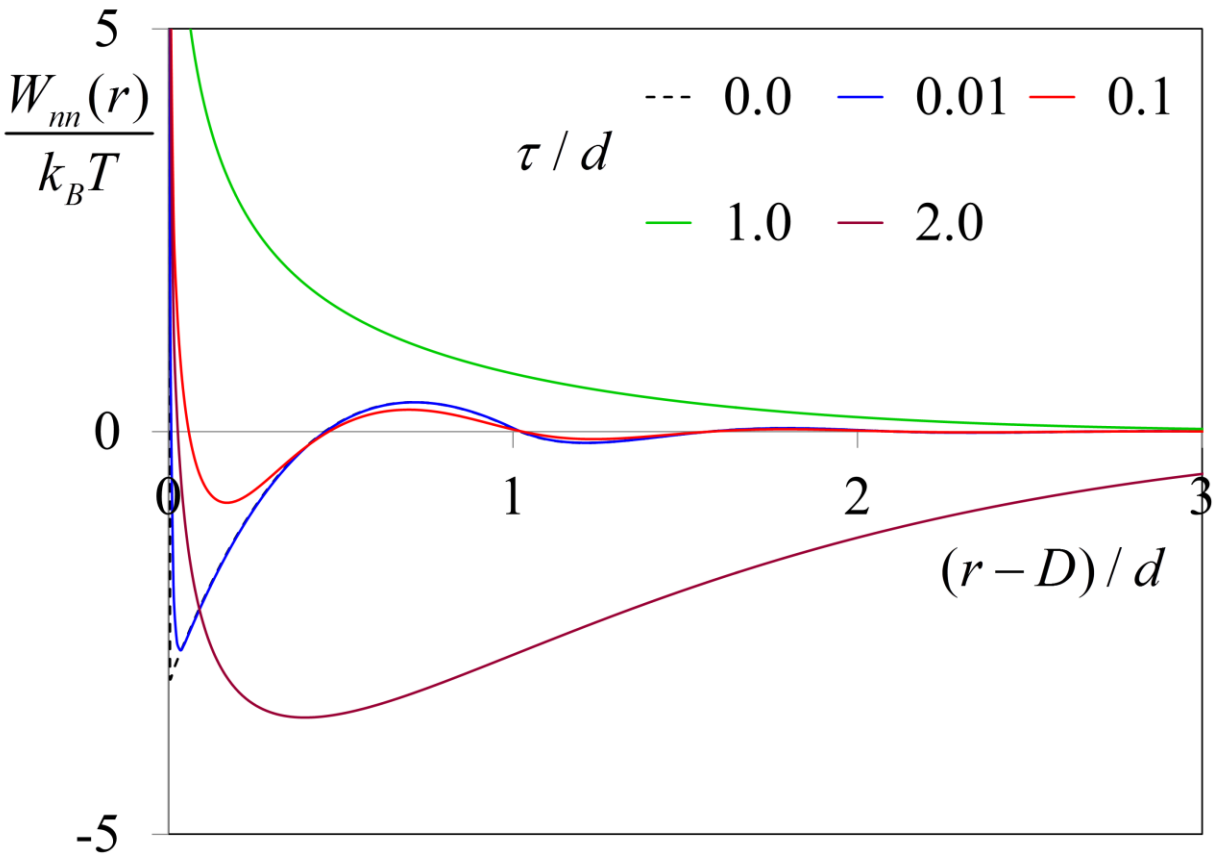

Figure 7.9 Potential of mean force between dilute soft spheres of size $R_c = 2.5$ at at various degrees of fuzziness in a monomeric solvent of total packing fraction $\eta_t = 0.226$.

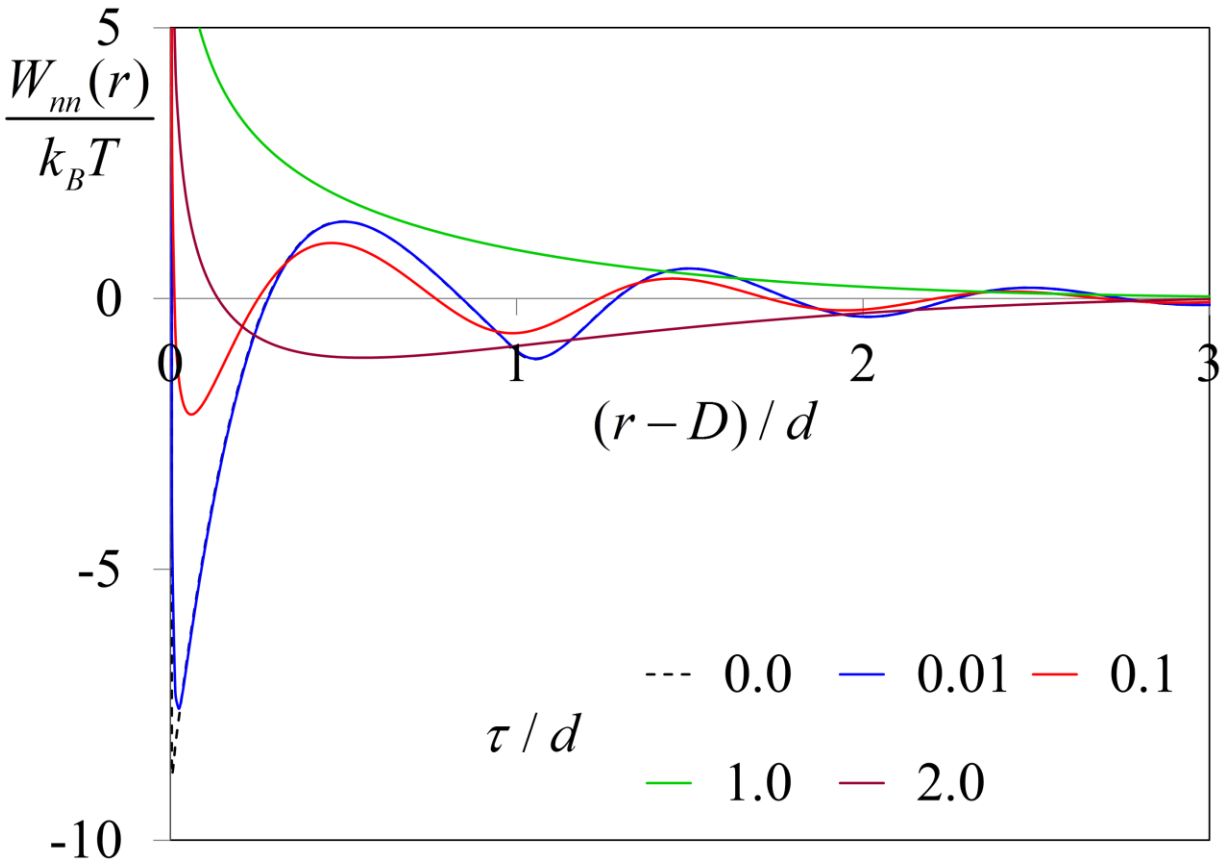

Figure 7.10 Potential of mean force between dilute soft spheres of size $R_c = 2.5$ at at various degrees of fuzziness in a monomeric solvent of total packing fraction $\eta_t = 0.4$.

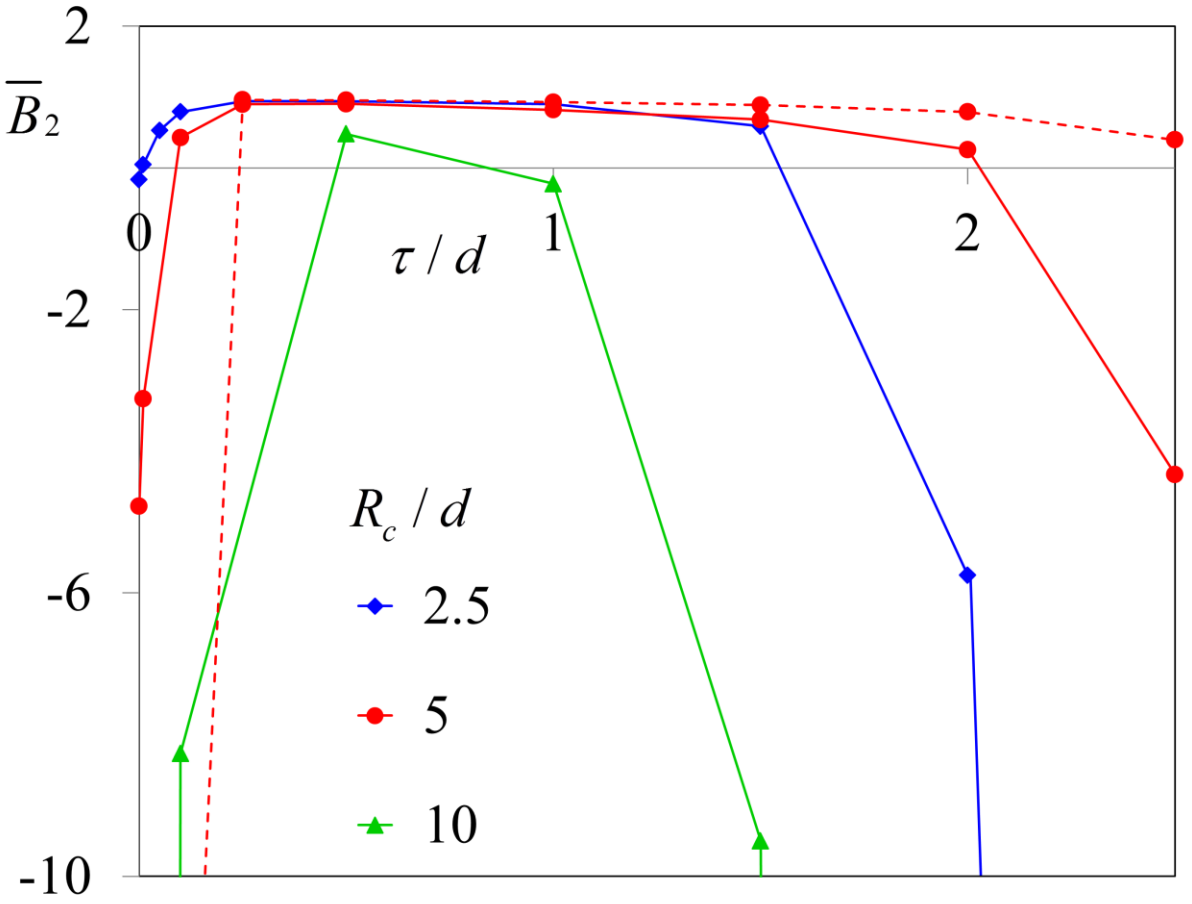

Figure 7.11 Normalized second virial coefficient for soft particles of different core sizes in a monomeric solvent (N=1) of total packing fraction $\eta_t = 0.226$ (solid) and 0.4 (dashed).

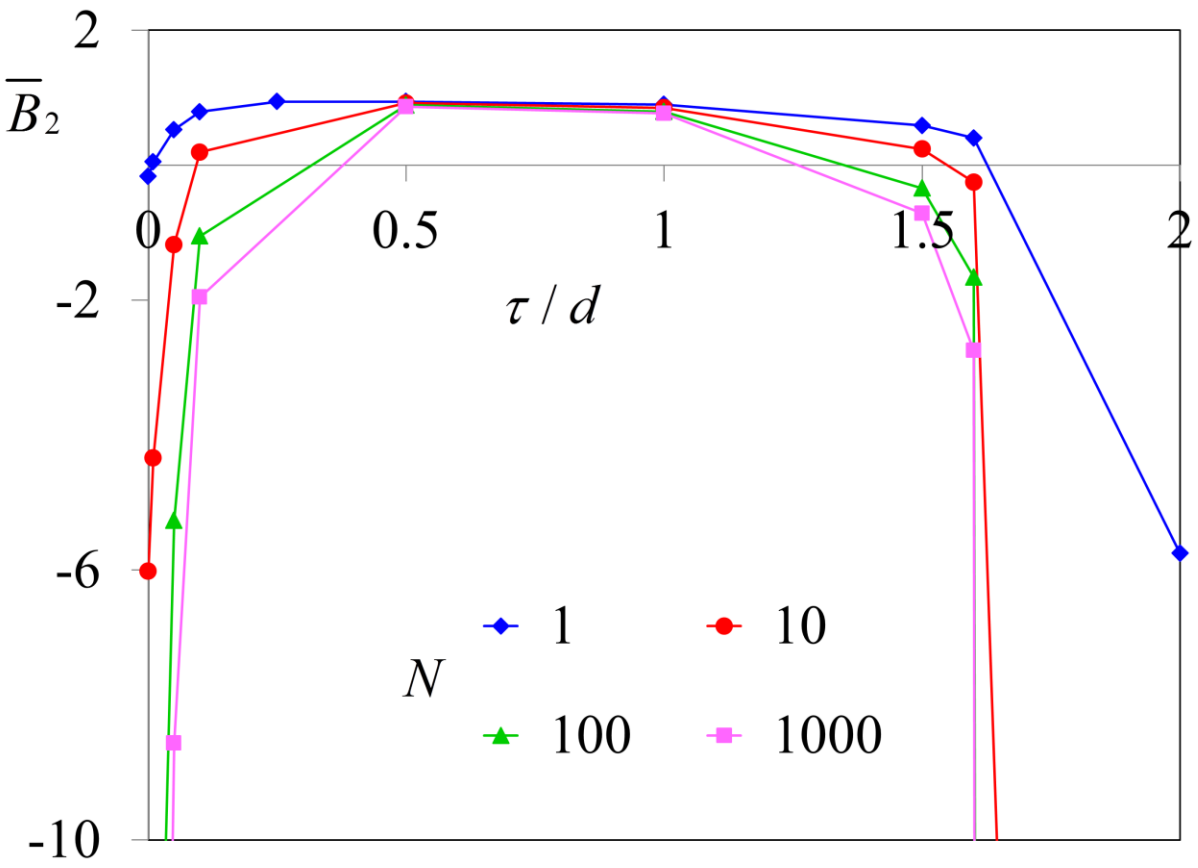

Figure 7.12 Normalized second virial coefficient for soft particles of size $R_c = 2.5$ as a function of surface fuzziness in a polymer melt of various chain lengths and fixed matrix liquid dimensionless compressibility $S_0 = 0.17$.

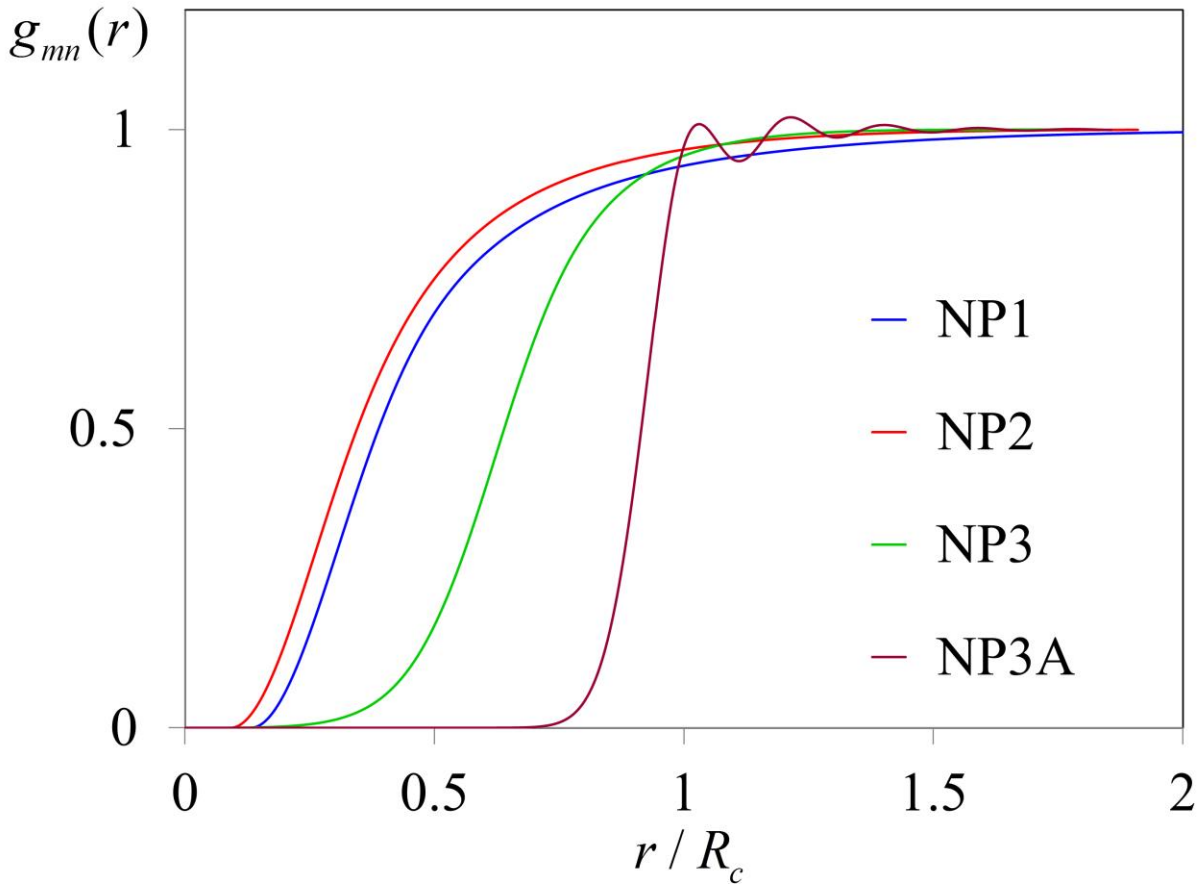

Figure 7.13 Cross correlation function for the indicated soft particles in a solvent of N = 1 and total packing fraction $\eta_t = 0.4$.

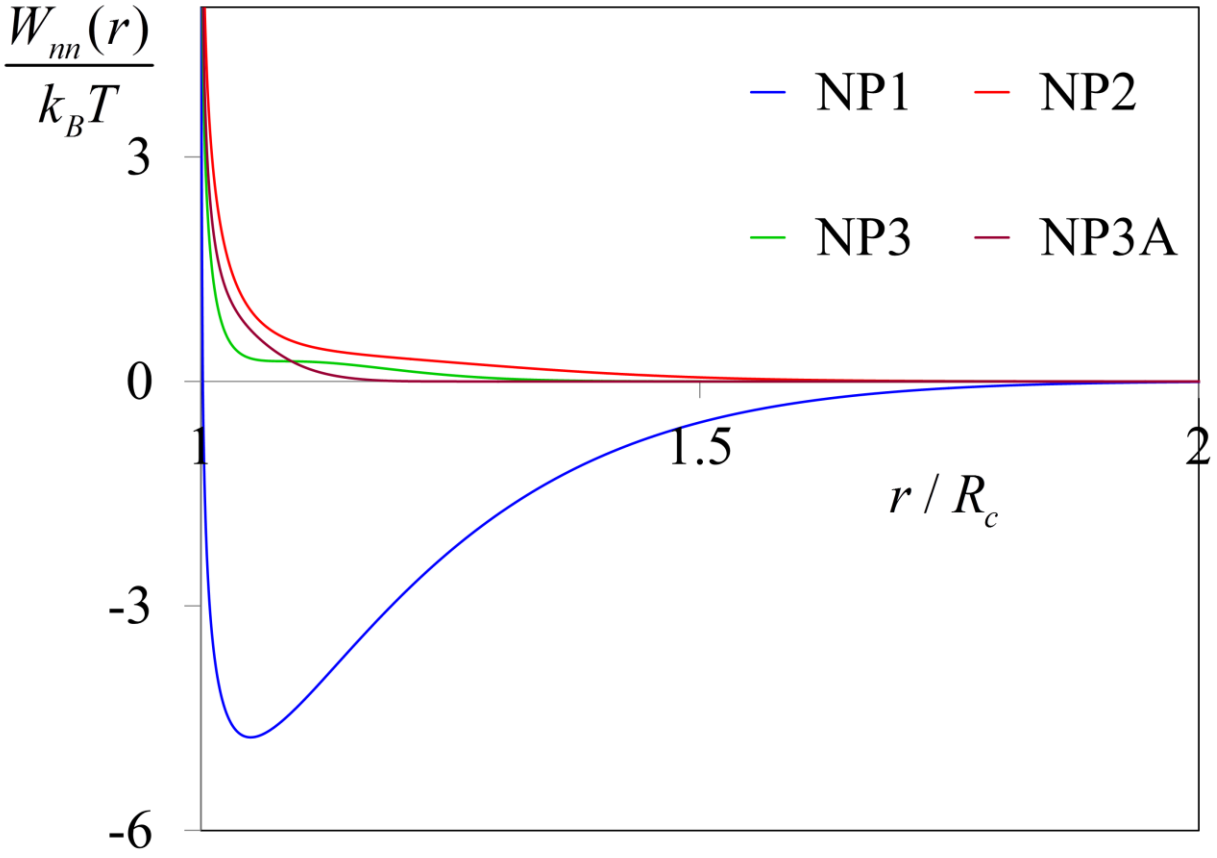

Figure 7.14 Potential of mean force for the indicated soft particles in a solvent of N = 1 and total packing fraction $\eta_t = 0.4$.

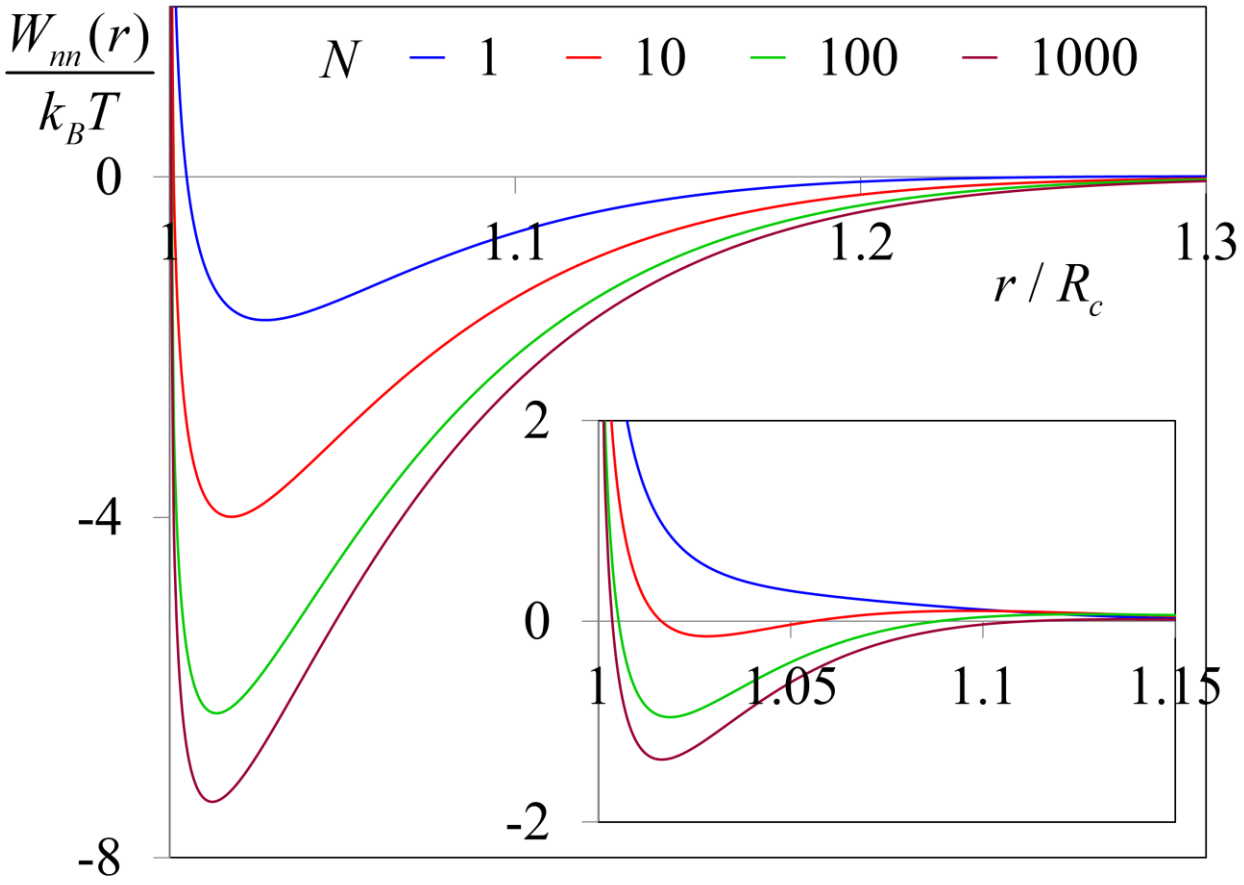

Figure 7.15 Potential of mean force for NP3 (main) and NP3A (inset) at the indicated chain lengths in an iso-compressible polymer melt ($S_0 = 0.17$).The axes labels for the inset are the same as the main plot.

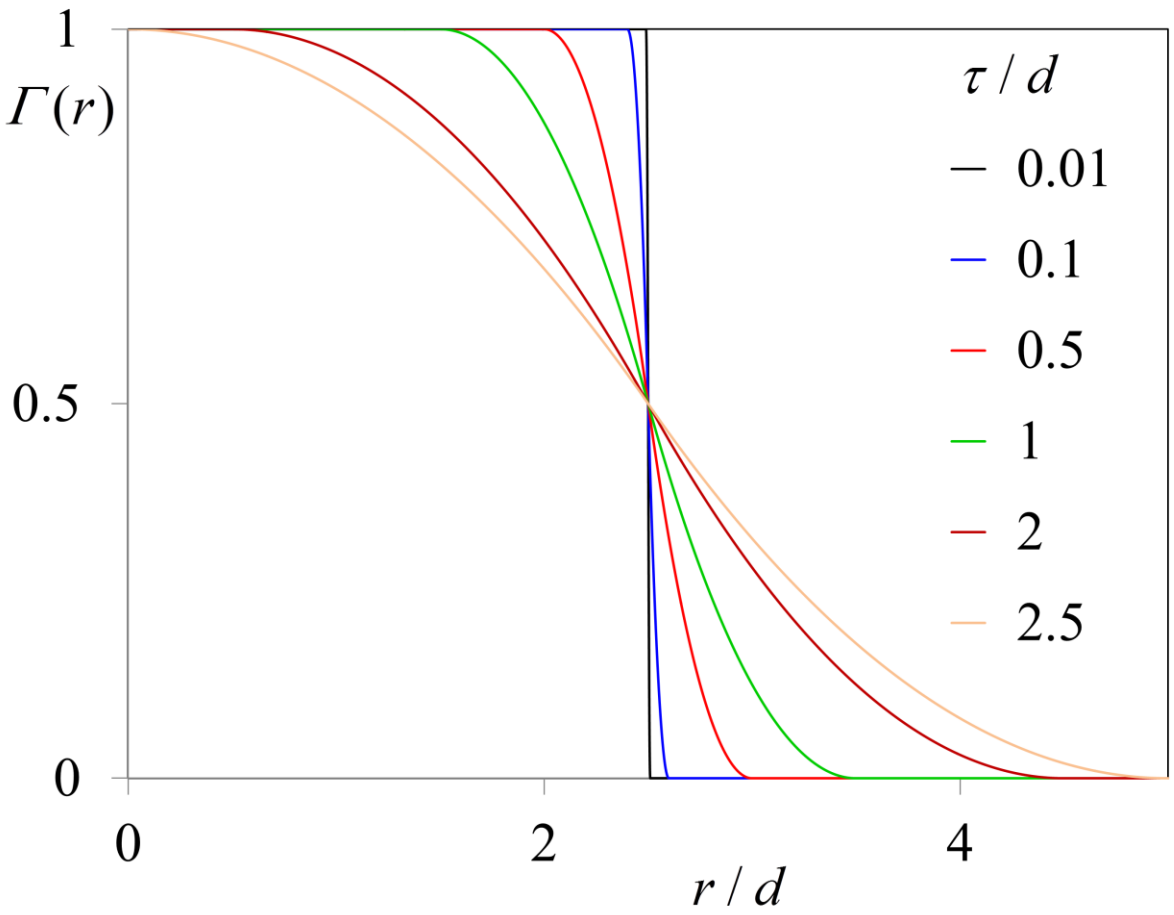

Figure 7.16 Parabolic radial density profile of a particle with core $R_c = 2.5$ at various degrees of fuzziness.

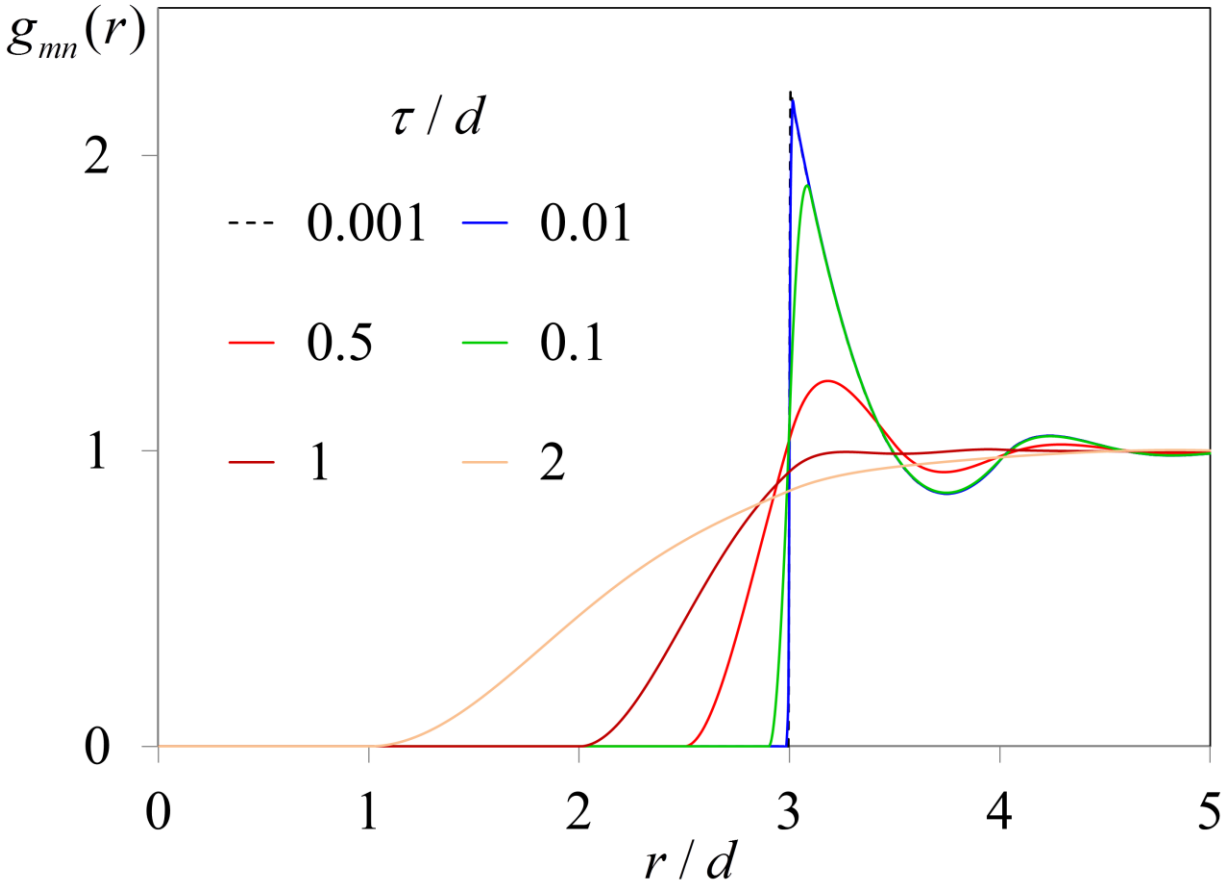

Figure 7.17 Cross correlation function for dilute soft particles of size $R_c = 2.5$ at various degrees of fuzziness (and using parabolic radial density profile) and total packing fraction $\eta_t = 0.226$.

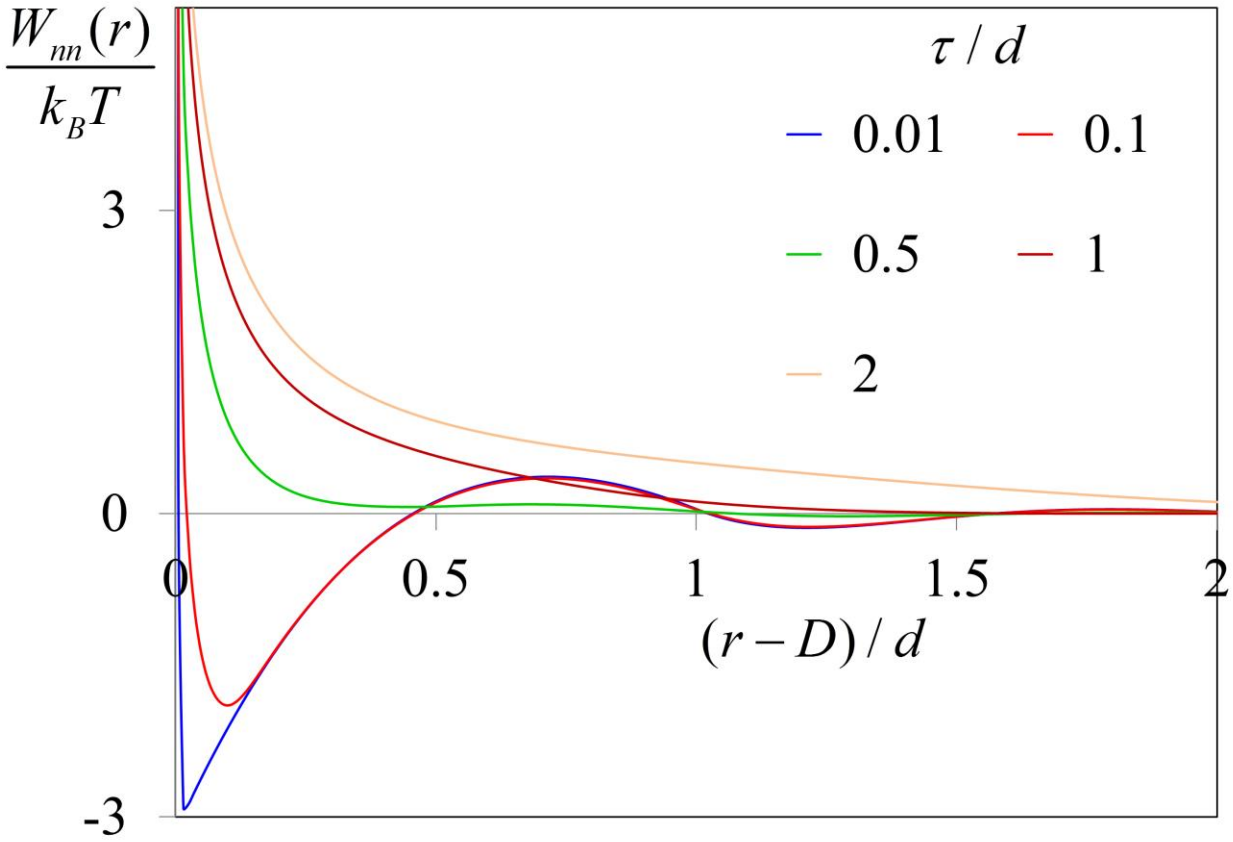

Figure 7.18 Potential of mean force between dilute soft spheres of size $R_c = 2.5$ at various degrees of fuzziness (using parabolic radial density profile) in a monomeric solvent of total packing fraction $\eta_t = 0.226$.

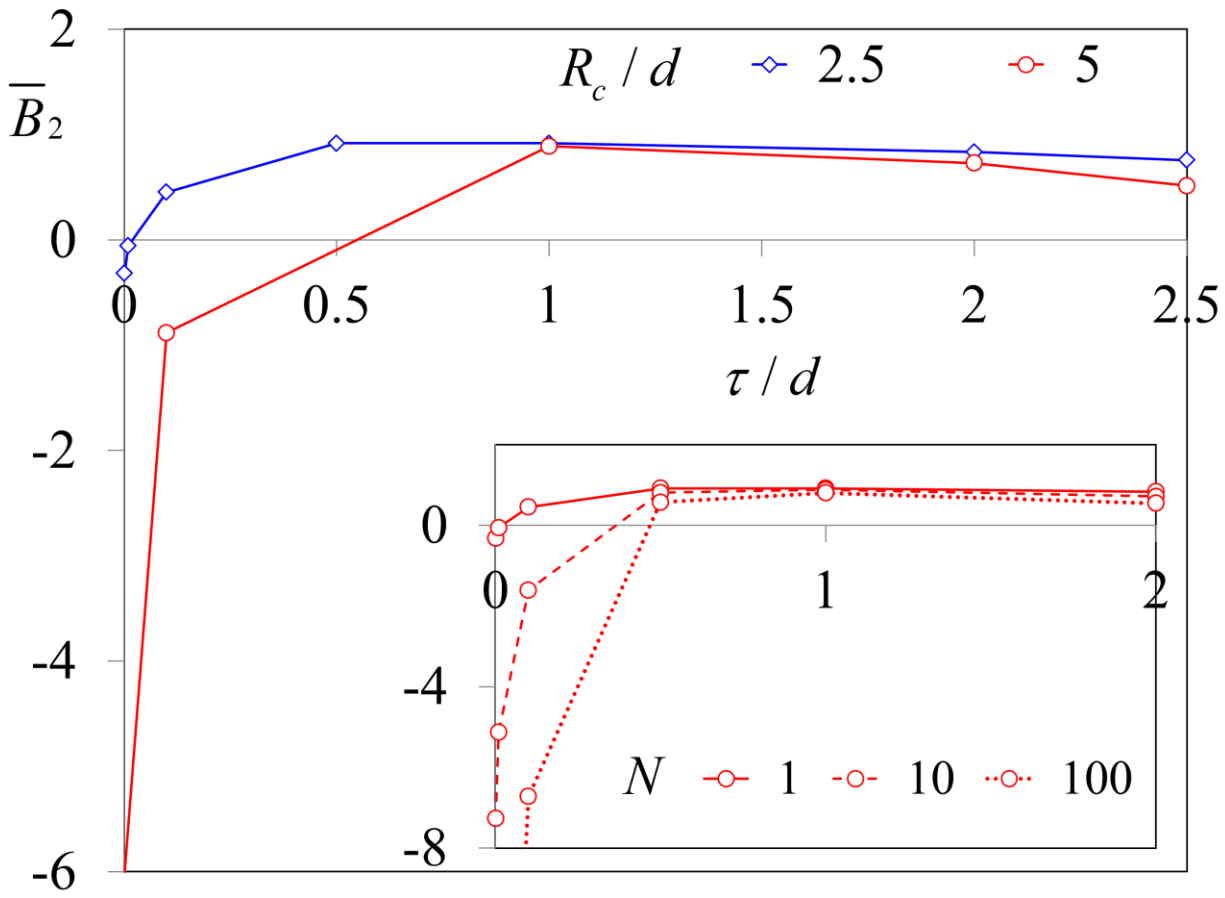

Figure 7.19 (Main) Normalized second virial coefficient for soft particles of different core sizes (using parabolic radial density profile) in a monomeric solvent (N=1) of total packing fraction $\eta_t = 0.226$. (Inset) $\overline{B}_2$ for particles of core $R_c = 2.5$ at different chain lengths under iso-compressible melt conditions. The axes labels for the inset are the same as the main plot.

Sample	crosslinking density [mol%]	R_c [nm]	τ [nm]
NP1*	0.81	3.8	2.77±0.1
NP2*	1.91	5.49	2.13±0.1
NP3*	4.60	7.16	1.51±0.3
NP3A+	4.60	5.12	0.51±0.3

Table 7.1 Molecular properties of cross-linked PS nanogels synthesized using batch* and semi-batch+ microemulsion polymerization techniques. Data reproduced from ref [1].

τ / d	Φ_c	
	N = 1 $(\eta_t = 0.226)$	N = 100 $(\eta_t = 0.4)$
0	0.116	0.0127
0.01	0.170	0.018
0.1	miscible	0.059
0.5		0.297
1		miscible
1.5		
2		
2.5	0.128	0.000214

Table 7.2 Spinodal solubility limits Φ_c for particles of core radius $R_c = 5$ at various degrees of fuzziness in the indicated iso-compressible polymer melts. Systems with solubility limit of $< 10^{-4}$ are deemed immiscible while those with > 0.5 are assumed miscible.

Sample	Φ_c			
	N = 1 ($\eta_t = 0.226$)	N = 10 ($\eta_t = 0.317$)	N = 100 ($\eta_t = 0.4$)	N = 1000 ($\eta_t = 0.4355$)
NP1	immiscible			
NP2	miscible	0.12	0.015	0.007
NP3	miscible	0.1	0.01	0.004
NP3A	miscible			

Table 7.3 Spinodal solubility limits Φ_c for the 4 indicated samples in iso-compressible polymer melts. Systems with solubility limit of < 10^{-3} are deemed immiscible while those with > 0.5 are assumed miscible.

Sample	Φ_c			
	N = 1 ($\eta_t = 0.226$)	N = 10 ($\eta_t = 0.317$)	N = 100 ($\eta_t = 0.4$)	N = 1000 ($\eta_t = 0.4355$)
NP1	miscible		0.12	0.056
NP2			0.086	0.035
NP3			0.1	0.034
NP3A			0.11	0.04

Table 7.4 Spinodal solubility limits Φ_c for the 4 indicated samples in iso-compressible polymer melts using the parabolic radial density profile. Systems with solubility limit of < 10^{-3} are deemed immiscible while those with > 0.5 are assumed miscible.

CHAPTER 8

CONCLUSIONS AND POSSIBLE FUTURE DIRECTIONS

8.1 Concluding Comments

The over-arching goal of this thesis is to study the fundamental equilibrium structural characteristics of polymer nanocomposites (PNC) and identify the materials design conditions under which improved miscibility can be attained by changing the chemical and/or physical features of the individual components. In the absence of attraction between the polymer and a smooth spherical particle, entropy-dominated depletion forces result in strong polymer-mediated attraction at contact between the nanoparticles[1-6]. Broadly, in this dissertation we have theoretically established techniques of countering polymer-particle phase separation using two general routes – (1) incorporating monomer chemical heterogeneity and manipulating polymer architecture and differential wettability, and (2) engineering the surface morphology and "softness" of the nanoparticle.

The Polymer Reference Interaction Site Model (PRISM) liquid state theory[7, 8] has been used throughout the thesis. In many cases, the theory predicts high sensitivity to the chemical details and the bare effective potential (in vacuum) between the different components. Therefore, going beyond the simple case of hard spheres in homopolymer melts[5, 8, 9, 10], we have addressed new, multi-faceted fundamental physics issues and developed design rules for realizing novel

equilibrium polymer nanocomposites with chemical, architectural, and/or particle surface complexity.

Chapter 3 studied in great depth entropic depletion phenomenon under isobaric melt conditions over an unprecedented wide range of polymer-particle size ratios (R_g / D), particle-monomer size ratios (D/d) and chain lengths N^6. Chapter 4 established how incorporating deterministic roughness on a particle surface can mitigate depletion attraction via a competition of new excess entropic mechanisms[11]. The use of rough 'raspberry' particles can either enhance or suppress dispersion depending upon surface topography. A similar theme was established in Chapter 7 for soft cross-linked nanoparticles with fluctuating or fuzzy surfaces[12]. The softness results in partial interpenetration of solvent molecules or polymer chains in the interior of the networked particle, which can even fully destroy depletion attraction.

Prior work has established the role of polymer-particle interfacial attraction on the thermodynamic miscibility of hard spheres in homopolymer melts. Depending upon the interaction, the polymer can form a layer around the nanoparticle leading to steric stabilization or induce phase separation due to bridging and formation of polymer-particle complexes[5, 8, 9, 10]. Going beyond a chemically homogeneous polymer, the role of chemical heterogeneity (in AB copolymers), monomer sequence, and differential adsorption strength on the equilibrium structure of PNCs has been explored in this thesis. Specifically, melts of random copolymer (RCP)[13] and alternating block copolymer (MBCP)[14] were considered in chapters 5 and 6, respectively. For some of the chemical systems, the miscibility of fullerenes is shown to be optimum at an intermediate RCP composition which is greater than that given by either of the

two limiting homopolymers akin to what has been observed experimentally[15]. Replacing the disordered randomness in the monomer sequence by an ordered MBCP leads to even richer structures and novel miscibility features that depend on the size of the particle relative to the block contour length.

8.2 Future Direction

Concerning possible future work, much remains to be done in the context of the rough and soft particles. For the rough raspberry particles, all the calculations have been performed at maximum surface bump coverage which is an additional parameter that can be tuned for more control over the structure. Our model also assumes monodisperse surface corrugation which does not capture experimental realism in some cases. It would be straight forward to incorporate polydispersity in bead size as well as randomness in the placement of corrugation on the surface. For both the rough and soft particles, another direction is to break chemical symmetry and allow local interfacial attractions between the surface beads and monomers.

Given the vast amount of available experimental data on many dynamical phenomena related to soft particle fluids, a straight forward extension of our model is to study the equilibrium structure of such fluids (pair correlation functions $g(r)$ and static structure factor $S(k)$) at very high concentrations as a function of the particle size and fuzziness. Motivated by experiments[16, 17], this problem has been tentatively addressed in the past[18, 19] but the role of particle size and softness on the variation of the equilibrium structures has never been systematically understood. Finally, the ability to compute structural correlations for rough

particles can provide crucial input to developing force-level theories for the slow dynamics and kinetic arrest in suspensions composed non-smooth surface particle suspensions.

The presented work on the copolymer based PNCs is an initial study. All the calculations have been in the dilute nanoparticle limit, and future studies are required to explore in detail the role of many-body effects on structure and thermodynamics. It remains to be determined how the strong coupling between the block length, particle size and chemical heterogeneity is modified when there is a strong direct attraction between the particles. Finally, it would be interesting to study how a copolymer of variable sequence and chemical heterogeneity mediates interactions between non-spherical particles like rods and disks.

8.3 References

(1) S. Asakura, F. Oosawa, *J. Chem. Phys*. **22**, 1255, 1954.

(2) S. Asakura, F. Oosawa, *J. Polym.Sci*., **33**, 183, 1958.

(3) A. Vrij, *Pure Appl. Chem*., **48**, 471, 1976.

(4) A. Yethiraj, C. K. Hall, R. Dickman, *J. Colloid Interface Sci*., **151**, 102, 1992.

(5) J. B. Hooper, K. S. Schweizer, *Macromolecules*, **38**, 8858, 2005.

(6) D. Banerjee and K. S. Schweizer, *J. Chem. Phys.*, **142**, 214903, 2015.

(7) K. S. Schweizer, J. G. Curro, *Adv. Chem. Phys.*, **98**, 1, 1997.

(8) L. M. Hall, A. Jayaraman, K. S. Schweizer, *Curr. Opin. Solid State Mater. Sci.*, **14**, 38, 2010.

(9) J. B. Hooper, K. S. Schweizer, *Macromolecules*, **39**, 5133-5142, 2006.

(10) L. M. Hall, K. S. Schweizer, *Soft Matter*, **6**, 1015, 2010.

(11) D. Banerjee*, J. Yang*, K. S. Schweizer, *Soft Matter*, to be submitted, August 2015 (*Equal Contribution).

(12) D. Banerjee, K. S. Schweizer, manuscript in preparation.

(13) D. Banerjee, M. D. Dadmun, B. Sumpter, K. S. Schweizer, *Macromolecules*, **46**, 8732, 2013.

(14) D. Banerjee and K. S. Schweizer, *J. Polym. Sci. Part B: Polym. Phys*, **53**, 1098-1111, 2015.

(15) S. Teh, D. Linton, B. Sumpter, M. D. Dadmun, *Macromolecules*, **44**, 7737-7745, 2011.

(16) Z. Zhang, N. Xu, D. Chen, P. Yunker, A. M. Alsayed, K. B. Aptowicz, P. Habdas, A. J. Liu, S. R. Nagel, A. G. Yodh, *Nature*, **459**, 230-233, 2009.

(17) C. N. Likos, *Phys. Rep.*, **348**, 267, 2001; A. Jusufi, M. Watzlawek, H. Lowen , *Macromolecules*, **32**, 4470, 1999.

(18) J. Yang, K. S. Schweizer, *Euro Phys. Lett.*, **90**, 66001, 2010.

(19) J. Yang, K. S. Schweizer, *J. Chem. Phys.*, **134**, 204908, 2011.

APPENDIX A

DEPLETION IN SEMI-DILUTE POLYMER SOLUTIONS

A natural question is whether all the qualitative features of the nanoparticle PMF in polymer melts persist in semidilute solutions. We examine this question based on the analytic Gaussian thread model and numerical full PRISM calculations for segments of nonzero size.

A.1 Gaussian Thread Polymer Limit

It is instructive to first recall the exact analytic solution of the pure polymer liquid PRISM equations in the limit that chains are a priori replaced by infinitely thin (d→0) Gaussian random walk threads or space curves[1, 2]. Here the site-site interchain hard core constraint is enforced only at a point, $r = 0$, where $g_{pp}(r = 0) = 0$, corresponding to a literally zero inter-site contact value. Fuchs[3] has derived that this Gaussian thread limit emerges rigorously from the full solution of PRISM theory for nonzero volume segments in the asymptotic semidilute limit of $N \to \infty, \eta_t \to 0$ but $\eta_t / \eta^* \neq 0$, where η^* is the dilute-semidilute crossover packing fraction which scales as $\eta^* \propto N^{-1/2}$ for ideal coils. The predictions of the thread limit of PRISM theory agree well with experimentally-verified scaling and field theory ideas in semidilute polymer solutions where oscillatory packing correlations are absent[1, 4, 5]. The specific results for the pure polymer liquid are:

$$\omega_p(k) = \left(N^{-1} + k^2 \sigma^2 / 12 \right)^{-1} \tag{A.1}$$

$$g_{pp}(r) = 1 + \frac{3}{\pi \rho_p \sigma^2 r}\left(e^{-r/\xi_\rho} - e^{-r\sqrt{2}/R_g}\right) \tag{A.2}$$

$$\xi_\rho^{-1} = \sqrt{2}R_g^{-1} + \frac{\pi}{3}\rho_p\sigma^2 \tag{A.3}$$

$$S_{pp}(k) = \omega_p(k) + \rho_p h_{pp}(k) = \frac{12\left(\xi_\rho/\sigma\right)^2}{1 + k^2\xi_\rho^2} \quad , \quad S_{pp}(r) \propto \frac{e^{-r/\xi_\rho}}{r} \tag{A.4}$$

Here, σ is the statistical segment length and $R_g^2 = N\sigma^2/6$. Note the monotonic, Yukawa decay of the real space collective density fluctuations on the density correlation or mesh length that monotonically decreases with polymer density. The Fourier signature of this behavior is a Lorenztian static structure factor peaked at k=0. These features agree with experiment and simulation in semidilute solutions up to ~30-40% polymer volume fraction[1, 6, 7]. Beyond that, they incur qualitative errors since the density correlation length approaches the monomer size and local oscillatory packing correlations emerge in both $S_{pp}(r)$ and $g_{pp}(r)$ on lengths scales that can extend to ~3-4 monomer diameters[1, 6, 7]. Simultaneously, $S_{pp}(k)$ qualitatively changes to a shape at small wavevectors that increases, not decreases, with k, and at large wavevectors is oscillatory.

The interchain site-site pair correlation function of eqn (A.2) has two parts : (i) a local decay on the density correlation length scale, and (ii) a long range component called the correlation hole on the R_g scale[8] which is a consequence of long range chain connectivity and excluded volume interactions. The latter feature is universally present irregardless of whether the d→0 limit is taken, while the former is modified in a nonuniversal manner at high densities[1].

If a hard sphere (radius R) is immersed in this thread polymer liquid, the monomer-particle correlation function has been derived to be[4]:

$$g_{pn}(r) = 1 - \frac{R}{r} e^{-(r-R)/\xi_\rho}, \quad r > R \tag{A.5}$$

Note that the polymer density vanishes at the sphere surface, and the correlations are controlled entirely by the density correlation length with no long range component. The corresponding depletion potential between two spheres follows as[4]:

$$\beta W_{nn}(r) = -\ln g_{nn}(r) = \frac{\pi}{3} \rho_p \sigma^3 \frac{R^2}{r\sigma} e^{-(r-D)/\xi_\rho} \quad , r > D \tag{A.6}$$

Its functional form is a monotonically decaying attraction with no long range component.

In concentrated solutions and melts, the thread model incurs qualitative errors which include: (a) no oscillatory correlations in $S_{pp}(r)$ nor (locally) $g_{pp}(r)$, (b) the correct trend is the density correlation length now increases with polymer density versus decreasing as predicted by eqn (A.3), and (c) the strict connection between $S_{pp}(k=0)$ and ξ_p implied in eqn (A.4) fails[6, 7]. These deviations from the thread model results are defining physical features of a dense liquid or concentrated solution.

A.2 Numerical PRISM calculations in the semi-dilute regime

Figure A.1 (main frame) shows that in a semidilute polymer solution, the static structure factor (main frame of Fig. A.1) is monotonically decreasing at low wavevector in contrast with the melt–like structure factor (S_0 = 0.5), and no strong oscillations at high wavevectors due to real

space local packing correlations are present (see inset). The site-site interchain distribution function in semidilute solution increases monotonically with separation but does have a nonzero, albeit small, contact value. In both melts and semidilute solutions there is a long range correlation hole that extends to r ~ R_g.

The d→0 thread model does exhibit many of the same qualitative features for $g_{pp}(r)$ and $S_{pp}(k)$ found based on numerical PRISM calculations in the semidilute regime. This includes the key scaling relations for the mesh length $\left(\xi_\rho \propto \left(\rho_p \sigma^2\right)^{-1}\right)$ and dimensionless compressibility $\left(S_0 \propto \left(\xi_\rho / \sigma\right)^2\right)$ which follow from longer wavelength correlations. However, the thread model misses the nonzero contact value of $g_{pp}(r)$ and the weak oscillations at higher wavevectors of $S_{pp}(k)$ due to the d→0 simplification.

Figure A.2 shows PMF calculations for nanoparticles of size asymmetry D/d = 80 and fixed N = 1000 at both melt and semidilute-like densities. At melt-like compressibilities (S_0 = 0.1-0.5), as shown in section 3.3, the PMF is highly oscillatory on the monomer diameter scale followed by a long-ranged repulsive tail. However, at lower semidilute densities (higher dimensionless compressibilities) the inner local barrier of regime II *disappears* and is replaced by a PMF that monotonically increases from contact, attains a shallow maximum, and then slowly decays to zero on the R_g length scale. This barrier (not to be confused with the amplitude parameter α in melts) is reduced with decreasing polymer concentration and nearly vanishes at low polymer densities. We note that at $\eta_t = 0.05$ ($S_0 = 81$) the mesh length is $\xi_\rho \simeq 3.5d$.

Figure A.3 shows the variation of the barrier height with chain length at fixed $\eta_t = 0.2$ (very close to the semidilute-concentrated crossover) where N grows from 50 to 10^4 corresponding to S_0 increasing from 1.5 to 4.2. Note that here the iso-compressible strategy adopted for melts is not employed since the focus is on the long-ranged repulsion of the PMF which persists with or without the calibration strategy. For the calculations in Figure A.3, the dimensionless parameters R_g/R and S_0 both increase as N grows. The barriers scale linearly with particle size D/d (not shown), and broaden, shift to larger separation, and decrease in amplitude with increasing chain length, ultimately disappearing for very long chains consistent with the approach to the Gaussian thread limiting behavior. The absence of the inner barrier (regime II of melts) in the numerical PRISM calculations performed in the semidilute regime is intuitive given the absence of monomer-scale packing oscillations in $g_{pp}(r)$ and $g_{pn}(r)$ in semidilute solutions.

The above trends of the PRISM results for the PMF in semidilute solutions are qualitatively consistent with recent self-consistent mean field theory results[9]. The latter work argued that the long range repulsion is due to chain end segregation effects. Specifically, chain ends are depleted less near the hard particle surface than interior segments leading to a net mismatch between the nonzero chain end and total segmental concentrations near a repulsive surface, resulting in the long range repulsion. From this perspective, it is not surprising that the PRISM thread model misses the long range part of the PMF given it assumes zero contact density of polymer at the particle surface. We note that in numerical PRISM theory all explicit chain end effects are absent (pre-averaged at the start), and thus our mechanism for the long range repulsive tail in semidilute solution is not obviously identical to that of ref [9].

A.3 References

(1) K. S. Schweizer, J. G. Curro, *Adv. Chem. Phys.* **98**, 1, 1997.

(2) K. S. Schweizer, J. G. Curro, *Chem. Phys.* **149**, 105, 1990.

(3) M. Fuchs, *Z. Phys. B* **103**, 521, 1997.

(4) A. P. Chatterjee, K. S. Schweizer, *J. Chem. Phys.* **109**, 10464, 1998.

(5) A. P. Chatterjee, K. S. Schweizer, *Macromolecules* **31**, 2353, 1998.

(6) J. B. Hooper, K. S. Schweizer, T. G. Desai, R. Koshy, P. Keblinski,. *J. Chem. Phys*. **121**, 6986, 2004.

(7) R. Koshy, T. Desai, P. Keblinski, J. Hooper, K. S. Schweizer, *J. Chem. Phys.* **119**, 7599, 2003.

(8) P. G. de Gennes, *Scaling Concepts in Polymer Physics* (Cornell University Press, Ithaca, 1979).

(9) A. A. Shvets, A. N. Semenov, *J. Chem. Phys*. **139**, 054905, 2013.

A.4 Figures

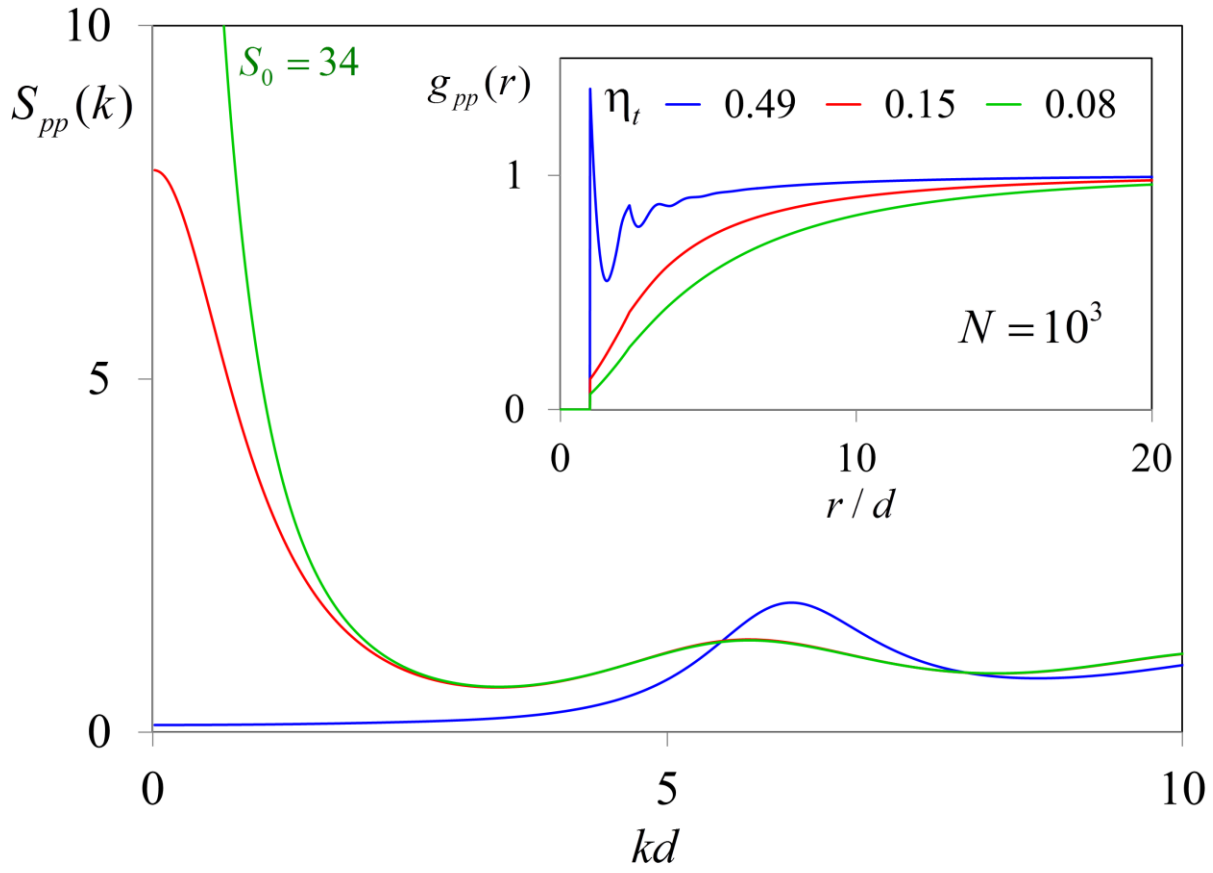

Figure A.1. (Main) The dimensionless polymer collective static structure factor at various packing fractions for a chain length N=1000. The mesh size $\xi_\rho \simeq 3.5d$ for $\eta_t = 0.05$, and is predicted to decrease as a power law in semidilute solution, $\xi_\rho \propto \sigma\, \eta_t^{-1}$, until the concentrated regime is entered where[6, 7] $\xi_\rho \approx d$. (Inset) The corresponding interchain site-site pair correlation function, $g_{pp}(r)$

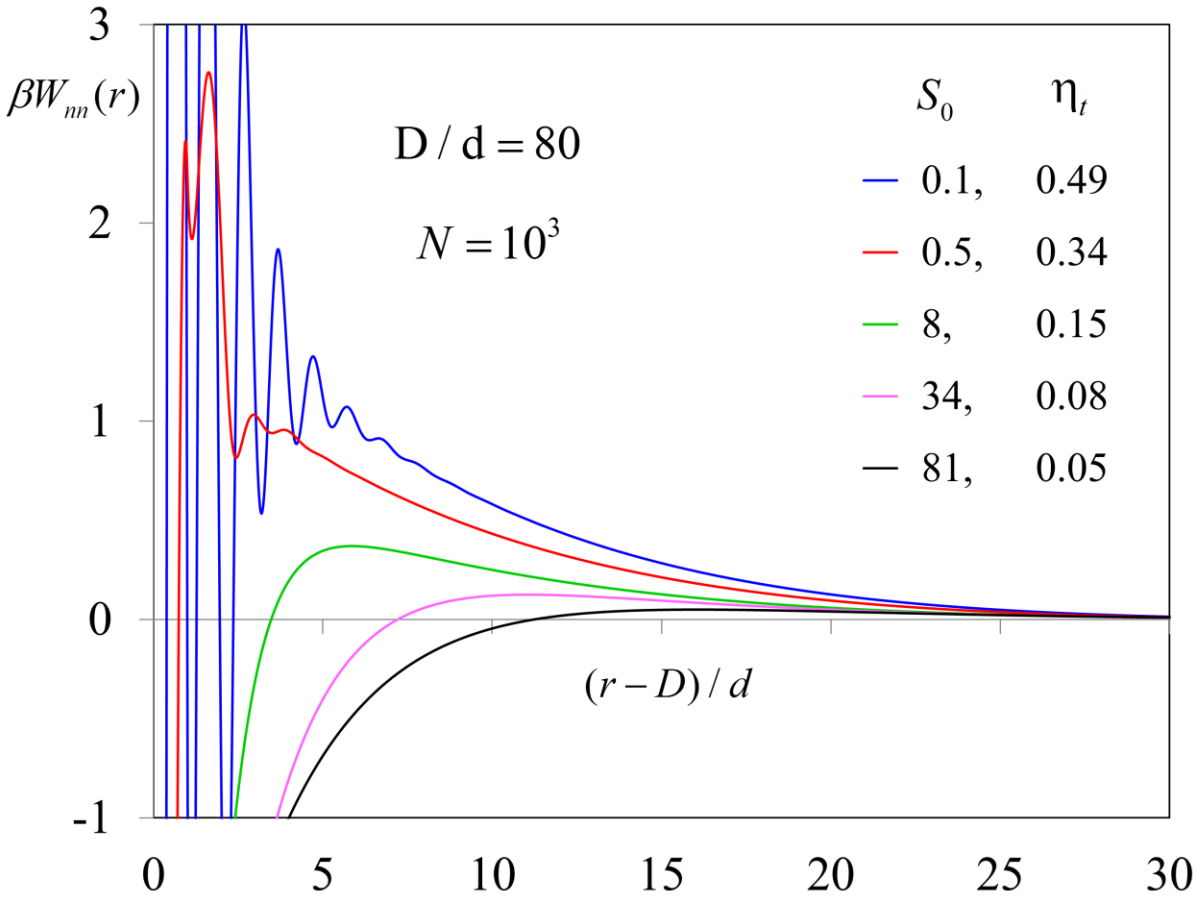

Figure A.2. The long-ranged repulsive tail region of the potential of mean force for D/d = 80 and N = 1000 under melt (S_0 = 0.1, 0.5) and semidilute conditions (S_0 = 8, 34, 81) conditions.

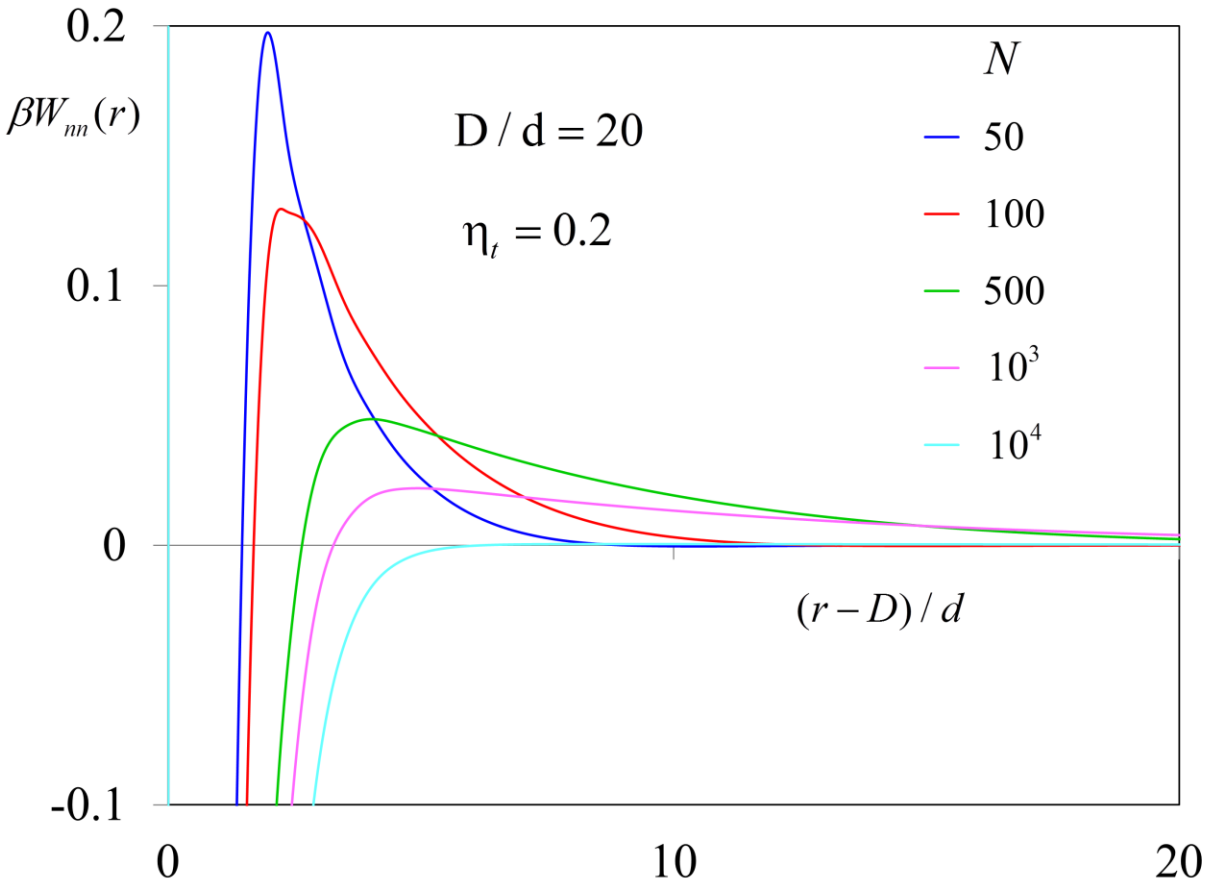

Figure A.3. Potential of mean force in a dense semidilute solution of $\eta_t = 0.2$ with D/d = 20 at the indicated chain lengths.

APPENDIX B

COMPUTATIONAL CHEMISTRY CALCULATIONS AND ROLE OF NON-UNIVERSAL PARAMETERS

B.1 Calculation of Interaction Potentials

All electron density functional theory calculations were used to develop initial insight into the extent of molecular interactions between an interacting monomeric unit and C_{60}[1]. The potential energy curve shown in the inset of Figure 6.2 was obtained using this approach. We also calibrated the results against a number of classical force fields which indicated that the AMBER force field can provide a reasonable accuracy for the relative attraction strengths[2]. Based on this calibration, and the fact that the classical force field approach is considerably more computationally efficient, we opted to use the AMBER force field to estimate the attraction strengths (binding energies) for all the different monomer and C_{60} interactions that are reported in Table 6.1.

B.2 Role of Non-universal Parameters

Section 6.4.2 summarized our findings concerning the influence of nonuniversal parameters and model simplifications on the miscibility predictions in the main text. Here we present some technical details underlying our statements.

In reality, the persistence lengths of the polymers that are copolymerized are not exactly the same, nor are their dimensionless isothermal compressibilities ($S_0 = \rho k_B T \chi_T$) in the

corresponding homopolymer melts due to equation-of-state effects. To explore the miscibility consequences of these factors, the reduced persistence length (local aspect ratio) for the freely-jointed chain model was changed from l/d = 1.2 to other typical values of 1.1 or 1.3[3]. The latter are also representative of the polymers we study based on the experimental characteristic ratios and monomer volumes. Based on equation-of-state data, realistic values of the dimensionless isothermal compressibility for Acrylonitrile and Styrene at 440K are approximately 0.2 and 0.3, respectively, compared to the single value used in the main text of S_0 = 0.25. The characteristic ratios of RCPs can be modeled as a composition average of the parent homopolymers[4, 5], and we adopt this simple model also for the dimensionless isothermal compressibility,

$$S_0 = f_A * (S_0)_A + (1 - f_A) * (S_0)_B \tag{B.1}$$

$$l/d = f_A * (l/d)_A + (1 - f_A) * (l/d)_B \tag{B.2}$$

Since S_0 changes via η_t, the total packing fraction also varies with composition.

The spinodal curve of C_{60} in Acrylonitrile-Styrene (AN-Sty) has been re-calculated wherein *all* the parameters, effective interactions, local aspect ratio l/d, S_0, and η_t, are varied as functions of composition. To within the resolution of the presented figures, an identical result is found (not plotted) as compared to Figure 6.6 which was based on the fixed "reference values" of l/d, S_0 and η_t. Hence, the non-monotonic variation of filler solubility with f_A is robust to these changes of the model. Since we wish to study qualitative trends, this exercise suggests it is not essential to vary l/d, S_0 and η_t with copolymer composition. However, the inset of Figure B.1 shows that the downward concavity of the spinodal curve reverses to an upward concavity when effective interactions are not varied with composition. Hence, including the physical effect that

monomers interact with the filler in an effectively composition-dependent manner is essential at zeroth order.

The nanoparticle-to-monomer diameter ratio was fixed at D/d = 1 in the main text. For the monomers of interest, we estimate $d \sim 0.6 - 0.8$ *nm*, and thus D/d can modestly deviate from unity. Figure B.1 presents miscibility calculations that change this ratio to D/d = 1.167 and D/d = 0.875 in the AN-Sty melt. Trends are not modified qualitatively, and the non-monotonic behavior persists. Figure B.1 also shows that increasing N from 100 to 10,000 results in only a small reduction of fullerene miscibility, as expected.

The spatial range of the interfacial attraction, α_{pn}, was held fixed at $0.12d$ in the main text. The main frame of Figure B.2 shows an example of the effect of changing this parameter on the miscibility of C_{60} in a AN-Sty melt. When α_{pn} is as small as $0.1d$, a slight hint of an intermediate copolymer composition (~70%) achieving the best miscibility emerges. The downward concavity becomes more pronounced as α_{pn} is increased to $0.12d$ with the miscibility peak shifting from $f_A = 0.7$ to 0.4. However, the concavity does not grow continuously by increasing the spatial range. When $\alpha_{pn} = 0.15d$, the miscibility of C_{60} in pure *B*-homopolymer melt (Sty, $f_A = 0$) increases to nearly 30% and no intermediate composition achieves better dispersion than the homopolymer. Thus, the spatial range is important since the distinctive non-monotonic spinodal curve occurs only when $0.1d \leq \alpha_{pn} \leq 0.15d$. However, significantly, our computational chemistry calculations do find this range describes all the monomers studied here, and it is nearly independent of chemistry. Of course, the spatial attraction ranges for *A* and *B* monomers need not be exactly the same. To address this, another C_{60}–AN-Sty melt system was studied with $\alpha_{An} = 0.14d$ and $\alpha_{Bn} = 0.12d$. Qualitatively the non-monotonic miscibility trend

remained the same, but there are some quantitative changes such as the maximum miscibility increases to 32% at a 50% copolymer composition (plot not shown).

Finally, the inset of Figure B.2 shows the sensitivity of the dispersion trends for the AN-Sty system to the magnitude of the direct fullerene attraction. As expected, miscibility decreases (increases) if the direct attraction grows (weakens) relative to the $\varepsilon_{nn} = 2.5k_BT$ value used in the main text. However, the most crucial trend, a concave down non-monotonic form of the spinodal curve that indicates an intermediate RCP composition gives the best fullerene miscibility, is still obtained in the window of $2 \le \beta\varepsilon_{nn} \le 4$, which is realistic based on our estimates in section 6.2.2.

B.3 References

(1) S. Teh, D. Linton, B. Sumpter, M. D. Dadmun, *Macromolecules*, **44**, 7737-7745, 2011.

(2) C. D. Sherrill, B. Sumpter, M. O. Sinnokrot, M. S. Marshall, E. G. Hohenstein, R. C. Walker, I. R. Gould, *J. Computational Chemistry*, **30**, 2187-2193, 2009.

(3) K. S. Schweizer, J. G. Curro, *Adv. Chem. Phys.*, **98**, 1-142, 1997.

(4) W. H. Stockmayer, L. D. Moore, M. Fixman, B. N. Epstein, *J. Polym. Sci.*, **16**, 517-530, 1955.

(5) T. Kotaka, T. Tanaka, H. Ohnuma, Y. Murakami, H. Inagaki, *Polym. J.*, **1**, 245-259, 1970.

B.4 Figures

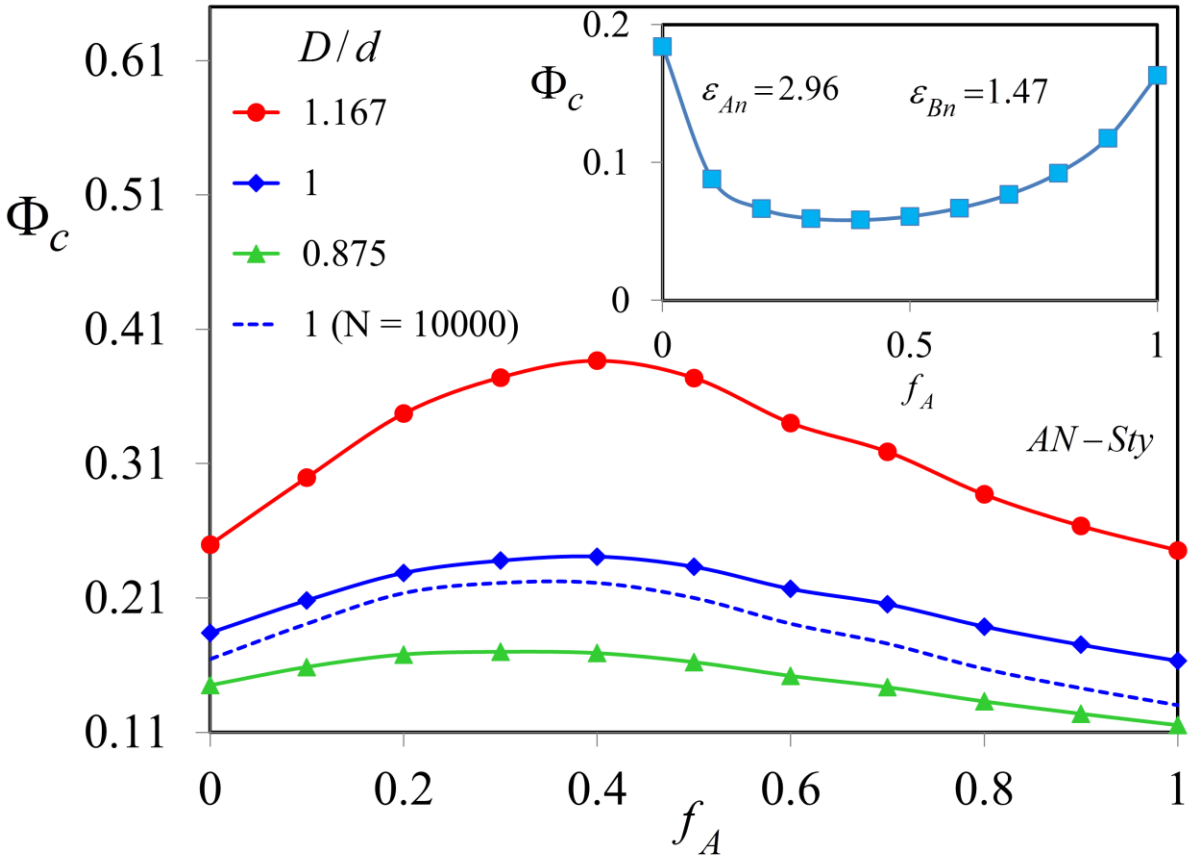

Figure B.1 Miscibility limit volume fraction of fullerenes at 440*K* in AN-Sty for random copolymers of chain length *N* = 100 (solid) and *N* = 10000 (dashed) at the indicated values of size asymmetry ratio *D/d*; all other parameters are fixed at their reference model values. Inset shows the miscibility limit of fullerene in the AN-Sty melt with D/d=1 and *N* = 100 but at fixed, composition-independent values ε_{An}^{eff} and ε_{Bn}^{eff} of 2.96 and 1.47k_BT, respectively.

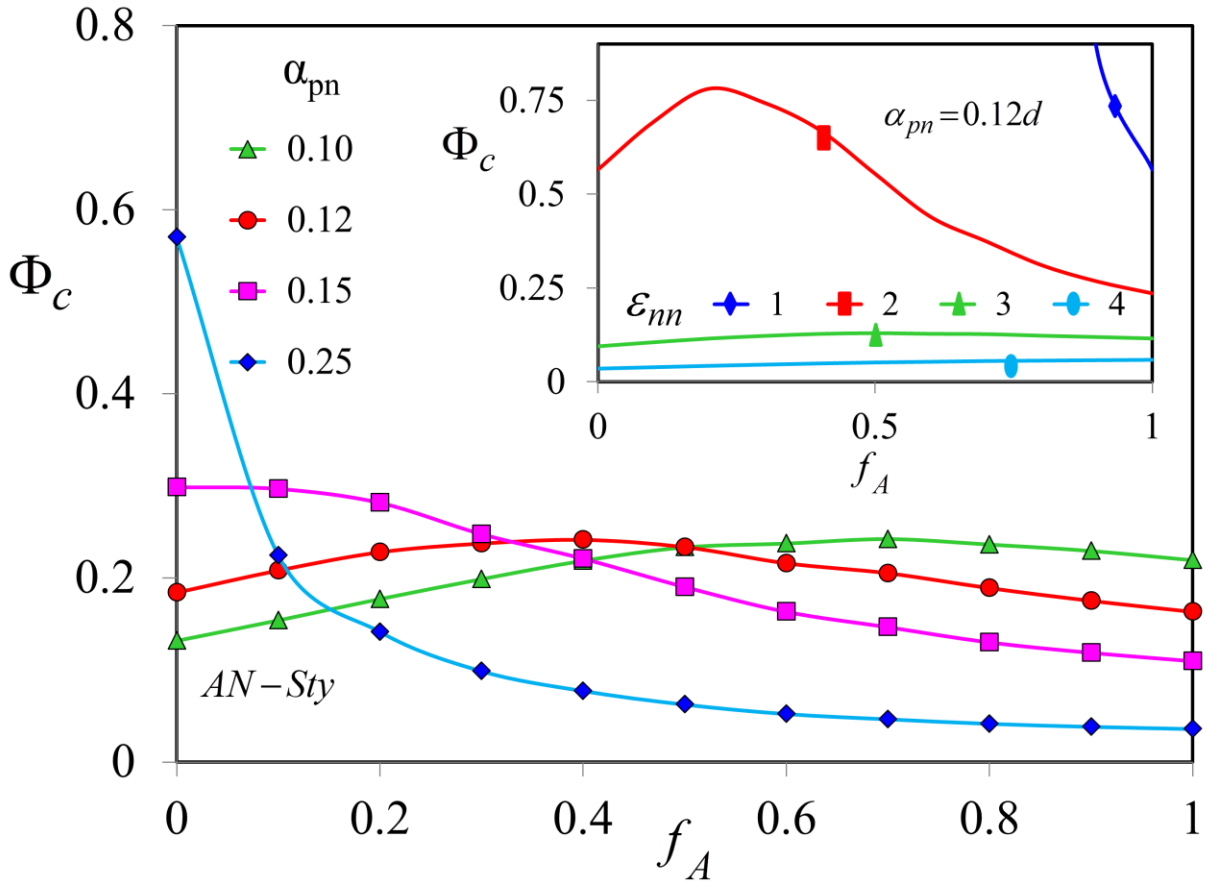

Figure B.2 Fullerene miscibility limit volume fraction at 440K in AN-Sty as a function of composition for the indicated polymer-particle attraction ranges. Inset: Miscibility limit results in AN-Sty with $\alpha_{pn} = 0.12d$ as a function of direct particle-particle attraction.